Ontwikkeling van theoretische technieken voor de accurate bepaling van spectroscopische grootheden gebruikmakend van geavanceerde elektronische structuurmethoden

Development of Theoretical Tools to Accurately Determine Spectroscopic Properties Using Advanced Electronic Structure Methods

Andy Van Yperen-De Deyne

Promotoren: prof. dr. ir. V. Van Speybroeck, prof. dr. ir. K. Hemelsoet, prof. dr. M. Waroquier
Proefschrift ingediend tot het behalen van de graad van
Doctor in de Ingenieurswetenschappen: Toegepaste Natuurkunde

Vakgroep Toegepaste Fysica
Voorzitter: prof. dr. ir. C. Leys
Faculteit Ingenieurswetenschappen en Architectuur
Academiejaar 2013 - 2014

UNIVERSITEIT GENT

ISBN 978-90-8578-721-1
NUR 910, 928
Wettelijk depot: D/2014/10.500/67

This research was conducted at the Center for Molecular Modeling.

You can know the name of a bird in all the languages of the world, but when you're finished, you'll know absolutely nothing whatever about the bird… So let's look at the bird and see what it's doing — that's what counts.
Richard P. Feynman

Leden van de examencommissie

Voorzitter

prof. dr. ir. Luc Taerwe (Universiteit Gent)

Leescommissie

prof. dr. Benoît Champagne (Université de Namur)
prof. dr. Stefaan Cottenier (Universiteit Gent)
prof. dr. ir. Henk Vrielinck (Universiteit Gent)
prof. dr. Michel Waroquier (Universiteit Gent, *copromotor*)

Overige Leden

dr. Andrew Beale (Unversity College of London)
dr. Hendrik De Cooman (Karel de Grote Hogeschool)
prof. dr. ir. Karen Hemelsoet (Universiteit Gent, *copromotor*)
dr. Ewald Pauwels (Universiteit Gent)
dr. dr. Danny Vanpoucke (Universiteit Gent)
prof. dr. ir. Veronique Van Speybroeck (Universiteit Gent, *promotor*)

Contents

List of Figures

List of Tables

List of Abbreviations

ACF	Autocorrelation function
AIMD	*Ab Initio* Molecular Dynamics
AMFI	Atomic Mean-Field
CASSCF	Complete Active Space Self Consistent Field
CI	Configuration Interaction
CP	Coupled-Perturbed
DFT	Density Functional Theory
EPR	Electron Paramagnetic Resonance
ϵPS	Excitation energy (ϵ) Power Spectrum
GGA	Generalized Gradient Approximation
HF	Hartree-Fock
HK	Hohenberg-Kohn
HRPD	High-Resolution Power Diffraction
IF	Infrared
KS	Kohn-Sham
LBE	Lead-Bismuth Eutectic
LDA	Local Density Approximation
MD	Molecular Dynamics
MRCI	Multi Reference Configuration Interaction
MYRRHA	Multi-purpose hYbrid Research Reactor for High-tech Applications
NMR	Nuclear Magnetic Resonance
PBC	Periodic Boundary Conditions
PES	Potential Energy Surface
PS	Power Spectrum
QRO	Quasi-Restricted Orbitals
QM	Quantum Mechanical
SCF	Self-Consistent Field
SCR	Selective Catalytic Reduction
SEARCH	Safe ExploitAtion Related CHemistry
SO	Spin-Orbit

SOMF	Spin-Orbit Mean-Field
SON	Spin-Orbit-Nucleus
SOO	Spin-Other-Orbit
SS	Spin-Spin
SSO	Spin-Same-Orbit
UV/Vis	ultraviolet and visual
VPS	Velocity Power Spectrum
ZFS	Zero-Field Splitting
ZORA	Zeroth Order Regular Approximation

Voorwoord

Dit doctoraatsproefschrift draagt slechts één naam, maar de inhoud kon enkel tot stand komen door de steun van en samenwerking met vele andere mensen. Hiervoor is een woord van dank zeker op zijn plaats.

Eerst en vooral wil ik prof. Michel Waroquier en prof. Veronique Van Speybroeck bedanken om mij de kans te geven een doctoraat aan te vangen in een boeiend vakgebied en voor hun wetenschappelijke ondersteuning. Daarnaast wil ik hen bedanken voor de omkadering en infrastructuur die een computationele groep nodig heeft om succesvol te zijn. Ze hebben mij ook de mogelijkheid geboden om mijn kennis te verbreden naar andere spectroscopische technieken — naast EPR – waardoor de nauwe samenwerking met prof. Karen Hemelsoet onstond. Ik ben Karen dankbaar voor mij te motiveren wanneer nodig, de hulp om artikels een trapje hoger te krijgen en mij te betrekken bij andere interessante onderwerpen. Het is pas met de hulp van deze drie promotoren, elk met hun eigen sterkte, dat het mij gelukt is dit proefwerk neer te kunnen leggen.

Ook een groot woord van dank voor dr. Ewald Pauwels om in eerste instantie de dagelijkse begeleiding van mij op te nemen en mij, reeds sinds mijn laaste Masterjaar, rond te leiden in de wereld van het moleculaire modeleren en van de computationele EPR. Ook de praatjes met Ewald en Hendrik hebben veel bijgebracht, zowel op het wetenschappelijke als persoonlijke.

Wetenschappelijk onderzoek verrichten wordt veel aangenamer als je ook omringd bent door leuke mensen. In eerste instantie zijn daar de bureaugenoten die meeleven op de momenten van frustratie en de momenten van opluchting bij het halen van een deadline - bedankt hiervoor Nooriya, Daria, Michaël en Danny! Bij uitbreiding zorgt het hele CMM voor een aangename werksfeer met leuke babbels en passend wetenschappelijk advies. Bedankt Thierry, Sebastian, An, Toon, Kim, Stefaan, Marc, Matthias V., Matthias D.G., Brecht, Stijn, Dimitri, Jeroen, Kristof, Sam, Steven, Bart, Jan, Kevin, Lennart, Hannelore, Saron, Kurt, Louis, Dietmar, Julianna, Thomas, Diederik, Diederica, David, Ward en Wim. Een speciaal woordje voor deze laatste twee die

door hun praktische (Wim) en computer (Ward) ondersteuning zoveel werk lichter maken!

Uiteraard zijn er ook mensen buiten het CMM die belangrijk waren om dit onderzoek te kunnen voeren. Ik ben dan ook de experimentele collega's van de EMR groep van onze universiteit — dr. Hendrik De Cooman, prof. Henk Vrielinck en prof. Freddy Callens — erg dankbaar voor de samenwerking en het inzicht over de experimentele kant van EPR. I would also like to thank the experimental colleagues dr. Upakul Deka, dr. Inez Lezcano-Gonzalez, dr. Andrew Beale and prof. Bert Weckhuysen from the University of Utrecht, for the fruitful collaboration. I am also grateful for the short but very pleasant collaboration with Siv Aalbergsjø and prof. Einar Sagstuen. Ook het HPC team van de UGent verdient hier een woord van dank voor hun dagelijkse ondersteuning bij problemen met de supercomputer.

Naast het wetenschappelijke, dragen ook de persoonlijke momenten gedurende de laatste vijf jaar bij tot dit werk. Ik ben mijn vrienden en familie zeer erg dankbaar voor de leuke momenten die nodig zijn om het werk eens los te kunnen laten.

Mijn ouders ben ik ook ongelooflijk dankbaar voor hun onvoorwaardelijke steun, de kansen en vrijheid die ze mij gaven om te doen wat ik wil, maar ook om mijn nieuwsgierigheid telkens aan te wakkeren, iets wat zeker bijgedragen heeft tot op z'n minst de aanzet van een doctoraat.

Uiteraard is de steun op het thuisfront enorm belangrijk. Anneli, héél erg bedankt om zoveel: naar mij te luisten op de moeilijke momenten, mijn zin te laten doen, uw advies, mij te herinneren dat ik mij ook wel eens mag ontspannen, alle praktische zaken mee te regelen, na te lezen, ... Maar bovenal voor de mooie jaren die we samen al doorbrachten. Ik kijk uit naar de volgende uitdagingen die we samen aangaan!

Andy Van Yperen-De Deyne
Gent, 26 augustus 2014

Samenvatting

Spectroscopie is de studie van de interactie tussen elektromagnetische golven en materie. Het is een zeer breed begrip en kan voor talloze doeleinden ingezet worden: van de structuurbepaling van DNA tot de analyse van sterrenstelsels lichtjaren van ons verwijderd. De kennis die gedurende vele jaren bekomen werd door middel van verschillende spectroscopische technieken, kan moeilijk onderschat worden. In het bijzonder is er een sterke relatie tussen kwantummechanica en spectroscopie. Verschillende observaties binnen de spectroscopie hadden nood aan een onderliggende theorie, waaruit eerst de kwantumtheorie van Bohr en vervolgens de golfmechanica van Schrödinger voortvloeide.

Een kwantummechanische beschrijving impliceert onder meer dat in atomaire en moleculaire systemen de energie gekwantiseerd is, waardoor enkel díe elektromagnetische straling met de juiste frequentie kan interageren met het bestudeerde systeem. Zulke gekwantiseerde energieniveaus kunnen gerelateerd worden met verscheidene fysische processen. De interactie tussen het magnetisch moment van kernen en elektronen met externe magnetische velden, rotaties en vibraties van een molecule en elektronische energieniveaus zijn uitermate belangrijk voor moleculaire spectroscopie.

In dit doctoraatswerk wordt er gebruik gemaakt van geavanceerde theoretische berekeningen om inzicht te krijgen in verschillende spectroscopische processen op moleculaire systemen. Door de evolutie op het gebied van computerkracht en door de ontwikkeling van bijzonder efficiënte methodes, zoals **dichtheidsfunctionaaltheorie (DFT)**, is het mogelijk om ook voor complexe systemen de hypotheses uit experimenten te toetsen aan de hand van theoretische voorspellingen. Zulke theoretische *ab initio* berekeningen zijn noodzakelijk wanneer de opgemeten spectra complex zijn of verscheidene hypotheses tot zeer gelijkaardige resultaten kunnen leiden.

Met DFT kunnen, mits voldoende computerkracht en voldoende vereenvoudiging, systemen tot maximaal enkele duizenden atomen doorgerekend worden. Meer gangbaar zijn systemen van tientallen tot enkele honderden ato-

men. Dit komt overeen met een lengteschaal van enkele nanometers, een typische lengteschaal waar kwantummechanische effecten inderdaad een belangrijke rol spelen. Het praktische gebruik van DFT impliceert dat parametrizatie noodzakelijk is. In dit werk worden ook geavanceerdere golffunctietechnieken gebruikt — *Complete Active Space Self Consistent Field* (CASSCF) en *Multi Reference Configuration Interaction* (MRCI) — waarvoor geen parametrizatie nodig is en dus meer fundamenteel zijn. De computationele kost is weliswaar navenant, waardoor enkel zeer kleine systemen binnen de mogelijkheden van deze geavanceerde golffunctie gebaseerde methoden liggen.

De theoretische inbreng is ook zeer complementair aan experimentele inzichten. De gedetailleerde geometrische structuur en bijhorende elektronische configuraties vormen de basis van berekeningen, terwijl de spectroscopische grootheden een afgeleide hiervan is. Dit staat in contrast met de experimentele aanpak, waarin de geometrie en elektronische structuur wordt afgeleid uit de spectroscopische grootheid. Daarenboven is een computerexperiment nauwkeurig te controleren en kunnen omgevingsfactoren uitgeschakeld worden, in tegenstelling tot vele experimentele technieken. In dit werk staat de link tussen een kwantummechanische (QM) beschrijving en verscheidene spectroscopische technieken centraal.

De eerste techniek die besproken wordt, is **Elektronische Paramagnetische Resonantie (EPR)**. EPR is een zeer krachtige techniek om systemen met ongepaarde elektronen — en dus netto spin ($S \geq 1/2$) — te karakteriseren. De interactie tussen zulke ongepaarde elektronen en een extern magnetisch veld resulteert in een energieopsplitsing, die zowel theoretisch als experimenteel bestudeerd kan worden. De mate van opsplitsing hangt af van de grootte van het magnetisch veld en zijn oriëntatie ten opzichte van het systeem, de nucleaire magnetische momenten in de omgeving van het ongepaard elektron en de onderlinge elektron-elektron magnetische interactie. Het — vaak complexe — spectrum kan gekarakteriseerd worden aan de hand van hyperfijntensoren (interactie met de magnetische momenten van de atoomkernen), g-tensor (interactie met magnetisch veld) en de nulveldsplitsing tensor (interactie tussen elektronenspins).

Deze tensoren kunnen computationeel bepaald worden, onder meer aan de hand van DFT-methoden, maar de toepassing ervan werd tot voor kort gelimiteerd tot geïsoleerde (gasfase) systemen. De uitbereiding naar periodieke codes werd pas vrij recent mogelijk. Binnen de programma's waar enkel systemen in de gasfase kunnen doorgerekend worden, wordt ondertussen de spin-baankoppeling veel accurater bepaald, waardoor die methodes er nog steeds significant beter in slagen om experimentele resultaten te reproduceren. Het is niet evident de twee-deeltjes natuur van sommige spin-

baan interacties accuraat in rekening te brengen binnen het DFT-formalisme. Vandaar dat er in CP2K en andere codes sommige g-tensor correcties foutief werden uitgerekend of helemaal niet in rekening werden gebracht. In dit werk werden benchmarkberekeningen uitgevoerd op diatomaire systemen en op een NaCl-kristal met rhodiumdefecten. De resultaten hiervan wijzen op deze tekortkomingen. De studie over de rhodium defecten in NaCl-kristallen werd uitgevoerd in samenwerking met de Elektron Magnetische Resonantie (EMR) groep van de Universiteit Gent (Vakgroep Vastestofwetenschappen), in het bijzonder met prof. Henk Vrielinck en prof. Freddy Callens.

In dit doctoraatswerk werden deze tekortkomingen geremedieerd door de bijdrage van de twee-deeltjes spin-baan interactie tot de g-tensor grondig te analyseren. Een wiskundige relatie tussen de twee-elektron-spin-baan (SSO) en de spin-andere-baan (SOO) interacties biedt de oplossing om het probleem, eigen aan de DFT-methode, te omzeilen. Het concept werd geïmplementeerd in de periodieke code (CP2K) en resulteerde in een duidelijk betere overeenkomst met referentieberekeningen. Daarenboven blijkt de Coulombbijdrage tot de SOO niet verwaarloosbaar voor hoge spin systemen, zoals in de literatuur eerder verondersteld werd.

Een tweede onderzoeksonderwerp betreft de combinatie van **UV/Vis spectroscopie** en **vibrationele spectroscopie**. De meest frequente methode om elektronische excitatie-energieën te bepalen, komt overeen met zuivere vertikale transities, waarbij men zelden rekening houdt met de nulpuntsvibratie, *i.e.* de moleculaire vibraties van het systeem op het absolute nulpunt. In realiteit worden UV/Vis metingen echter vaak op kamertemperatuur opgemeten en is een dergelijke vertikale excitatie niet volledig representatief. Een mogelijke manier om zulke temperatuurseffecten in rekening te brengen is via **Moleculaire Dynamica** (MD). In deze techniek worden de bewegingsvergelijkingen van Newton voor de atomen opgelost en wordt stapsgewijs een traject van moleculaire configuraties met bijhorende snelheden opgebouwd. Hiermee genereert men stelselmatig een ensemble van geometrieën.

De gemiddelde elektronische excitatie-energie berekend tijdens een MD-simulatie wijkt af van de statische vertikale excitatie-energie en resulteert in een beduidend betere overeenkomst met experimentele gegevens. De flexibiliteit van de molecule heeft blijkbaar een invloed op de excitatie-energie voor de elektronen, maar een methode om na te gaan welke beweging hiervoor grotendeels verantwoordelijk is, was niet beschikbaar. In dit doctoraatsproefschrift wordt een methode uitgewerkt, gebaseerd op Fourier transformaties, om de bewegingen te identificeren die de grootste invloed hebben op de excitatie-energie. De methode maakt gebruik van het principe van een vibrationele vingerafdruk: elke moleculaire vibratie heeft een karakteristieke frequentie. Tegelijkertijd correspondeert elk van deze vibraties met een vi-

brationele coördinaat. Als de spectrale dichtheid, gerelateerd aan de Fourier transformatie, van deze vibrationele coöordinaat berekend wordt, verschijnt een sterke piek op de karakteristieke frequentie.

Wanneer de elektronische excitatie-energie berekend wordt gedurende de MD-simulatie, kan een tijdsafhankelijk signaal van deze excitatie-energieën opgesteld worden. De spectrale dichtheid van dit signaal (ϵPS) bevat opnieuw een spectrum opgebouwd uit karakteristieke frequenties van de moleculaire vibraties: hun vibrationele vingerafdrukken. Drie verschillende vibrationele modes werden onderscheiden: (i) de vingerafdruk is afwezig in het ϵPS, (ii) de vingerafdruk is aanwezig op de originele frequentie of (iii) op het dubbele van de originele frequentie. Enkel de laatste categorie draagt bij tot het verschil tussen een statische excitatie-energie (*i.e.* berekend voor het geometrische minimum) en de dynamische waarde, uitgemiddeld over het MD-traject. Deze methode werd gevalideerd voor drie koolwaterstofverbindingen. Daarenboven werd ook een complexere molecule, nl. de halochrome kleurstof ethyloranje bestudeerd.

De expertise in verband met het bepalen van vibrationele spectroscopie aan de hand van MD werd ook gebruikt ter ondersteuning van experimenteel onderzoek, binnen de selectieve katalytische reductie van schadelijke stikstofoxides naar onschadelijk stikstof en water aan de hand van Cu-SSZ-13. Er werd een zeer goede overeenkomst met de experimentele resultaten bekomen en de hypotheses over NH_3 geadsorbeerd op zowel Lewis en Brønsted zure sites konden bevestigd worden. Dit werk werd uitgevoerd in samenwerking met dr. Andrew Beale en prof. Bert Weckhuysen van de Anorganische Chemie en Katalyse groep van de Universiteit van Utrecht.

Een tweede toepassing van MD als nuttige methode betreft de geautomatiseerde generatie van radicalen in rhamnose kristallen. De methode volgt het ionizatieproces en dus de vorming van de radicalen. De procedure staat toe de menselijke bias bij het bepalen van radicalaire structuren te elimineren en is breder inzetbaar. Dit onderzoek werd uitgevoerd in samenwerking met de Vakgroep Fysica van de Unversiteit van Oslo, in het bijzonder met Siv Aalbergsjø en prof. Einar Sagstuen.

Ten derde werd, als een zijproject, de stabiliteit van polonium componenten bestudeerd. Deze toepassing heeft geen relatie met spectroscopie, maar bouwt voort op de ervaring met elektronische structuurmethoden en relativistische effecten. Dit onderzoek is deel van het SEARCH project die de veiligheid van een Lood-Bismuth Eutecticum (LBE) als koelmiddel bij vierde generatie kernreactoren bestudeert. Binnenin dit LBE zal polonium gevormd worden door neutronenvangst door bismuth atomen. Een oplijsting van de mogelijke poloniummolecules met atomen aanwezig dichtbij het LBE opper-

vlak, is een eerste stap richting het ontwerp van filter-materialen, nodig om de atmosfeer boven het LBE te zuiveren.

Summary

Spectroscopy is the study of the interaction between electromagnetic waves and matter. The concept is very broad and can be applied for various applications going from structural determination of DNA to analysis of very distant galaxies. The knowledge gained by spectroscopy can hardly be underestimated. In particular, there is a close relation between quantum mechanics and spectroscopy. Several observations within spectroscopy forced theoretical physicists to come up with a more fundamental theory to describe matter, which evolved from the quantum theory of Bohr to the wave quantum mechanics.

This theory gives evidence of the existence of quantized energy levels for atomic and molecular systems, allowing only electromagnetic waves with specific frequencies to interact with the studied system. Such quantized energy levels can be related to different physical processes. The interaction between the magnetic moment of nuclei and electrons with external magnetic fields, rotations and vibrations of a molecule and electronic energy levels are most important for molecular spectroscopy.

In this doctoral work, advanced theoretical calculations are used to gain insight in different spectroscopic processes at the molecular level. Due to the evolution of computer power and development of efficient methods such as **Density Functional Theory (DFT)** it is nowadays possible to test the hypothesis of experiments by theoretical predictions for complex systems. Such theoretical calculations are necessary when the measured spectra are complicated or multiple hypotheses can lead to similar observations.

If sufficient computer power is available and sufficient approximations are introduced, DFT can handle up to several thousands of atoms. Systems with few tens to few hundreds of atoms are more common. This is in correspondence with the length scales on which quantum mechanical effects play an essential role. The practical use of DFT requires parametrization, which yield an approximation. In this work, also more advanced wavefunction techniques are used — Complete Active Space Self Consistent Field (CASSCF)

and Multi Reference Configuration Interaction (MRCI) — which are more fundamental and don't suffer from a possible bias due to parametrization. The computational cost of these methods is however limiting the system size which can be studied, allowing only (very) small molecules to be calculated.

A theoretical viewpoint often complements experimental insight. Detailed geometrical structures and electronic configurations are the fundamentals of these calculations and provide a clear view on the molecular processes. Additionally, a computer experiment can be controlled very precisely and environment effects can be avoided when desirable, in contrast to most experimental techniques. In this thesis the link between a quantum mechanical (QM) description and multiple experimental techniques is the central topic.

Firstly, **Electron Paramagnetic Resonance (EPR)** is discussed. EPR is a very powerful technique to characterize systems with unpaired electrons which have a net spin. The interaction between such unpaired electrons and an external magnetic field results in an energy splitting which can be studied by microwaves. The size of this energy splitting obviously depends on the applied magnetic field and its orientation with respect to the system but also on the nuclear magnetic moments surrounding the unpaired electron and mutual electron-electron interactions. The spectrum — often quite complex — is typically characterized with the help of three distinct EPR properties: the g-tensor (interaction with magnetic field), hyperfine tensors (interaction with magnetic moments of the nuclei) and the zero-field splitting (interaction between electron spins).

The tensors can computationally be determined, amongst others, within the framework of DFT. The use of DFT was however for a long period in time restricted to isolated (gas phase) systems. Extension to periodic codes became available quite recently via CP2K and some other periodic DFT codes. The accuracy of these codes fully lies within the expectation, taking into account the approximations used for this implementation. For the gas phase based calculations however, the spin-orbit operator can be calculated more accurately, resulting in a better experimental agreement. It is not trivial to include the two-particle nature of the spin-orbit interactions in a DFT formalism. Therefore, these corrections to the g-tensor were incorrectly implemented or even neglected in the periodic codes. Benchmark calculations on diatomic systems and on a NaCl crystal with rhodium defects, included in this work, give evidence for these shortcomings. The study of the rhodium defect in NaCl was performed with the experimental partners of the Electron Magnetic Resonance (EMR) group of Ghent University (Department of Solid State Sciences), in particular prof. Henk Vrielinck and prof. Freddy Callens.

In the frame of this PhD, a solution to these problems was found by an in-

depth investigation of the two-particle spin-orbit interaction and its influence on the g-tensor. A mathematical relation between the most important contributions of the two-electron spin-same-orbit (SSO) and spin-other-orbit (SOO) interactions offered solution to the problem. The concept was implemented in the periodic code CP2K and clearly improved the results with respect to the reference calculations. Additionally, it was found that the Coulomb-contribution to the SOO is not negligible for high spin systems, as was originally proposed in literature.

The combination of **UV/Vis spectroscopy** and **Vibrational spectropy** was subject of a second research topic. In previous studies, the excitation energy was calculated via a static computation on the optimized ground state, often even neglecting the zero point vibrational energy. Such a vertical excitation is however not always representative for the actual UV/Vis measurements, especially at higher temperatures. A possible solution to incorporate such temperature effects is through **Molecular Dynamics (MD)**. This technique solves the classical equations of motions for the nuclei and a trajectory of molecular configurations with corresponding velocities is created. An ensemble of geometries is therefore generated. The averaged electron excitation energy obtained during such a MD simulation differs from the static vertical excitation energy. Most often the obtained dynamic value is in a better agreement with experimental data. The flexibility of the molecule apparently influences the electron excitation, however a method to isolate the responsible motions was not available.

In this doctoral work such a method was developed. The method is based on the principle of a vibrational fingerprint: each molecular vibration has a characteristic frequency and each of these vibrations correspond with a vibrational coordinate. If the power spectrum (related to the Fourier transform) of this vibrational coordinate is calculated, a large peak at this characterizing frequency occurs. When the excitation energy is calculated at various snapshots generated during the MD simulation, also a time-dependent signal of this excitation energy is found. Calculating the power spectrum of this signal results in a spectrum containing the characterizing frequencies of the molecular vibrations. They left their vibrational fingerprint in the so-called ϵPS. Three different vibrational modes were distinguished: (i) the fingerprint is not present in the ϵPS, (ii) the fingerprint is present at its original location or (iii) at twice the original frequency. Only the last category contributes to the difference between the static excitation energy (*i.e.* calculated for the geometrical minimum) and the averaged value from the MD trajectory. The method was validated for three hydrocarbon compounds. Moreover, also a more complicated molecule, in particular the halochromic dye ethyl orange, was investigated to identify the dominant motions causing the shift

in excitation energy when comparing the dynamic and static approach.

This expertise related to vibrational spectroscopy with MD simulations was furthermore employed to support experimental research at a metal exchanged zeolite — Cu-SSZ-13. This zeolite acts as a catalyst for the selective catalytic reduction of harmful nitrogen monoxides to harmless nitrogen and water. Structural information concerning the adsorption of guest molecules onto the framework or metal was obtained, analyzed and compared to experimental findings. Secondly, also the vibrational structure of this system was determined using MD simulations. Very good agreement with experimental results were obtained, confirming the hypothesis that NH_3 is adsorbed on both Lewis and Brønsted acid sites. The theoretical data assisted in the assignment of the infrared spectra of the adsorbed complexes. This part of the research was conducted in collaboration with dr. Andrew Beale and prof. Bert Weckhuysen (Inorganic Chemistry and Catalysis Group, Utrecht University).

Another application of MD as a very useful tool concerns the automated generation of radical species in rhamnose crystals. The method follows the ionization process and the formation of the radicals. The procedure helps to remove the human bias in predicting the radical structures and is widely applicable. This research was conducted in collaboration with the Department of Physics of the University of Oslo, in particular with Siv Aalbergsjø and prof. Einar Sagstuen.

Thirdly, as a side project, the stability of polonium compounds has been investigated. For this research, experience with electronic structure methods and relativistic effects was put into practice. This research is part of the SEARCH project to investigate safety issues when using a Lead-Bismuth Eutectic (LBE) as coolant in fourth generation reactors. Within this LBE, polonium will be formed through neutron caption by bismuth atoms. A list of the possible molecules formed with Po and other atoms present near the LBE surface is a first step in the design process of filter materials, which will be used to clean the LBE cover gas.

Part I

Development of Theoretical Tools to Accurately Determine Spectroscopic Properties Using Advanced Electronic Structure Methods

Chapter 1

General Introduction

Spectroscopy encompasses the study of the interaction between electromagnetic waves and matter. Modern research in physical science, astrophysics, material characterization, (bio-)chemical technology and medical sciences highly rely on spectroscopy as a valuable tool to discover the laws of physics. It has enormously influenced our knowledge in all of these topics and multiple researchers were honoured with a Nobel prize for their contributions to spectroscopy, both at a theoretical and at an experimental level.[1] Examples vary from the award for physics going to Zeeman and Lorentz in 1902 "*in recognition of the extraordinary service they rendered by their researches into the influence of magnetism upon radiation phenomena*" [2], lying at the fundamentals of magnetic resonance spectroscopy, up to Ertl as laureate for the prize in chemistry in 2007 "*for his studies of chemical processes on solid surfaces*" [3], in which spectroscopy played a crucial role.

The first spectroscopic observations were done with visual light. The true start of spectroscopy as a scientific tool could be appointed to optics experiments of Newton, in the second half of the 17th century, in which it was shown that sunlight can be dispersed into a continuous set of colors.[4] The work of Joseph von Fraunhofer during the early 1800s may be regarded as groundbreaking in the field of experimental spectroscopy. With the advent of dispersive spectrometers he observed the appearance of a number of dark features in the spectrum of the Sun.[5] They are caused by absorption by chemical elements present in the solar atmosphere.[6] Since then, spectroscopy has steadily grown in importance as a precise scientific technique for characterization in chemistry, physics and astronomy.

The observations of Balmer and later of Lyman, Paschen and many others, that electromagnetic emission of light by hydrogen atoms occurs in series of narrow spectrum lines, directly lead to the Bohr model of quantum the-

ory for hydrogen.[7, 8, 9] In this way, spectroscopy highly contributed to the discovery of the atomic structure and in its turn to the development of quantum mechanics.[10] This theoretical framework was very often challenged by experimental findings and refined during the first part of the 20th century.[11, 12, 13] The spectroscopic techniques described in this work all rely on the principle of quantized energy levels for atomic and molecular structures. During spectroscopic measurements, transitions between such quantized energy levels are induced and/or observed.

During the last century, a wide variety of different spectroscopic techniques were developed. They are typically ordered by the frequency (wavelength) of the electromagnetic waves, used to characterize the probed object. Figure 1.1 displays an overview of the electromagnetic spectrum and the corresponding molecular effect. The link to the quantized energy levels on different energy scales is given in Figure 1.2 In the following, we describe shortly the main spectroscopic techniques.

Nuclear Magnetic Resonance (NMR) The spectroscopic technique which requires the lowest energy (related to the lowest frequencies) is magnetic resonance spectroscopy, in particular NMR.[14] In NMR, the intrinsic magnetic moment of the nuclei (if any) interacts with an external magnetic field, causing energy levels to split and allowing transitions between them. The technique is often used for structural determination and is known to the wide public as magnetic resonance imaging (MRI), as used for medical purposes.

Electron Paramagnetic Resonance (EPR) Similar to NMR, Electron Paramagnetic Resonance (EPR) or Electron Spin Resonance (ESR), relies on the magnetic resonance principle.[15, 16, 17, 18] However, in EPR spectroscopy, the magnetic moment of the unpaired electrons interact with the external magnetic field, indicated in the right part of Figure 1.2. The use of EPR is thus limited to systems with radicals or transition metals, however the technique is very sensitive and even small amounts of unpaired electrons can be detected. Besides, the amount of information obtained from EPR experiments about the radical/transition metal environment can be very high.

Rotational spectroscopy This technique relies on the discretization of the rotational energy for molecules as in the case of the rigid rotor (see Figure 1.2, green arrow). There is no external probe. Only polar molecules are *microwave active*, since rotation of such molecules results in a change of dipole moment. Energy transitions between rotational energy levels occur at microwave frequencies.[19]

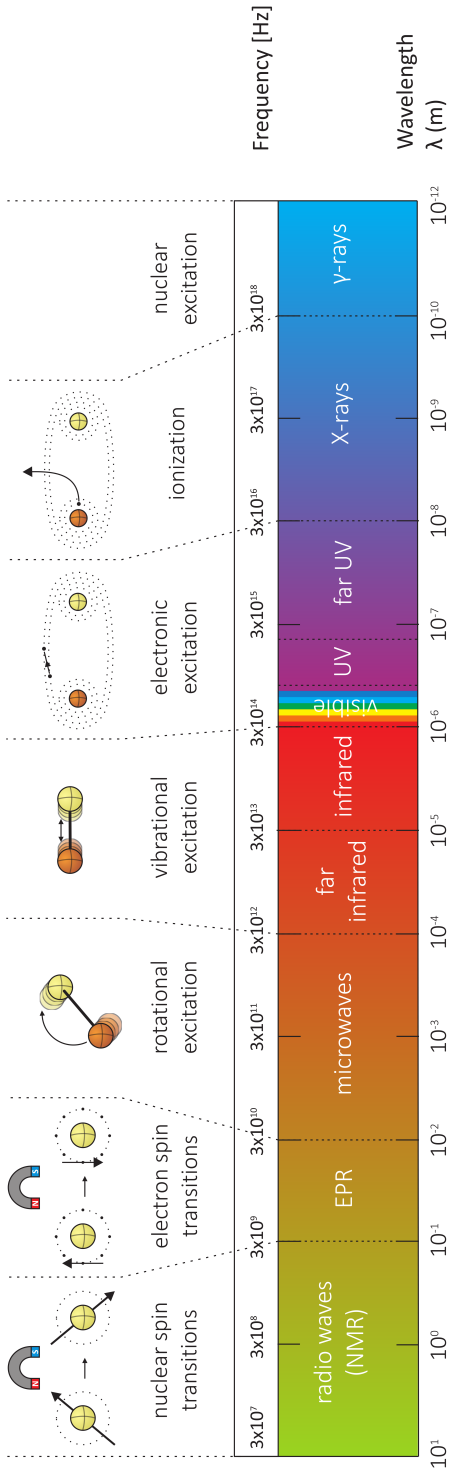

Figure 1.1: The electromagnetic spectrum and multiple spectroscopic techniques indicated at their frequency range.

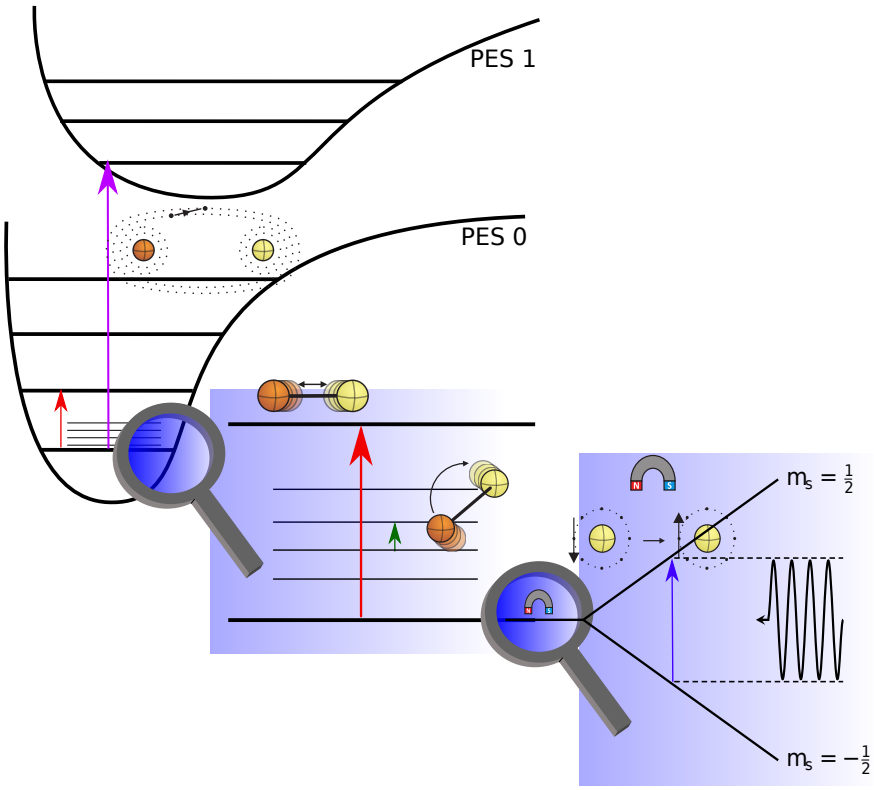

Figure 1.2: The link between various spectroscopic field and the discretization of quantized energy levels for a generic diatomic molecule. Potential energy surfaces for the electronic ground state (PES 0) and the first excited state (PES 1) are depicted in function of the internuclear distance. Transitions between both PES are linked to UV/Vis (indicated in purple) and fluorescence. Vibrational and rotational transitions are presented centrally on the figure, indicated by red and green transitions respectively. Finally, when an magnetic field is applied, the interaction with the electron spin is taken into account, as is the case in EPR spectroscopy (transition indicated in blue).

Vibrational spectroscopy Information on molecular vibrations can experimentally be gained by a large variety of techniques. Two techniques are briefly discussed here since they are most widely used in literature: infrared (IR) and Raman spectroscopy. Both techniques exploit the quantization of vibrational energy, characteristic for specific motions of the system at hand as indicated by the red arrow in Figure 1.2. Certain frequency regions are used as fingerprint for related bond vibrations (*e.g.* C–H, O–H, C–C, C=C, ...), making vibrational spectroscopy an excellent tool for material characterization.[20, 21] Such fingerprints are indicated in the IR spectrum of biphenyl shown in Figure 1.3.

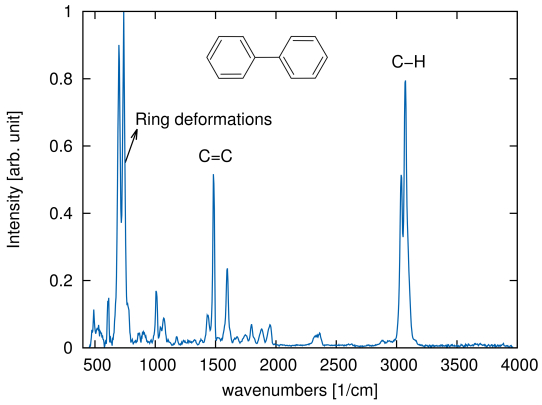

Figure 1.3: IR spectrum of biphenyl with indication of several fingerprint regions. Data from NIST Standard Reference Database 69: *NIST Chemistry WebBook*.

The IR technique measures direct transitions between vibrational energy levels, either by absorption or emission of a photon. These transitions are allowed for vibrational excitations that change the dipole moment (*IR active*).

In contrast, Raman spectroscopy relies on inelastic Rayleigh scattering in which some electrons fall back to another vibrational level, in contrast to the majority which get scattered elastically. This difference between elastic and inelastic scattering therefore contains information concerning the vibrational structure of the studied system. The selection rules for these transitions rely on a change in polarizability due to the vibrational excitation (*Raman active*).

UV/Vis and fluorescence spectroscopy Observations which lie in the visible or ultraviolet region are typically linked to transitions of valence electrons. Excitations of the ground state to an excited state belong to the field

of UV/Vis spectroscopy (see Figure 1.2, indicated by the purple transition). Complementary, de-excitations are observed in fluorescence experiments.[20, 22] Such electron excitations play an essential role in conjugated systems. Typically π or non-bonding electrons are excited to higher anti-bonding molecular orbitals. These techniques are widely used to characterize solutions of transition metal ions, (highly) conjugated organic compounds such as dyes.[23, 24]

The amount of conjugation is an essential element which determines the color by a high degree, as indicated in Figure 1.4 in which the UV/Vis spectrum of different acenes is plotted. Changing the environment of the studied compound can alter the amount of conjugation, which in turn will influence the observed spectrum. For example, the protonation of one of the aromatic rings in the acenes during a reaction in a zeolite has direct influence on the color of the solution.[25, 26]

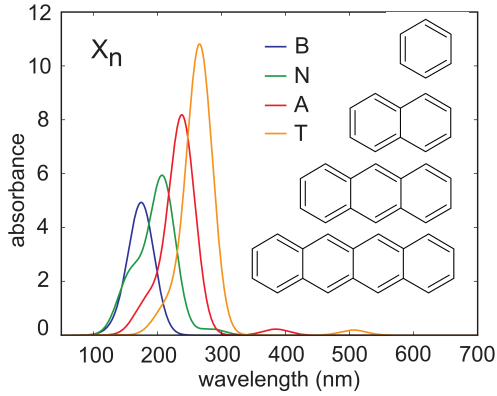

Figure 1.4: UV/Vis spectra of benzene, naphtalene, antracene and tetraceen. Data is retrieved from Ref. [25].

X-ray spectroscopy Also X-rays will induce electronic transitions but they correspond to much higher energies. Absorbing X-rays results in transitions of electrons from the inner shell to unoccupied orbitals (XANES) or to the vacuum (EXAFS). X-ray emission spectroscopy (XES) relies on the replacement of an electron from the outer shells to the created hole in the inner shell. The released energy is then emitted as an X-ray photon with a characteristic wavelength of the studied atom.

Electromagnetic waves with even higher energy will affect nuclear levels. These techniques were not considered in this work which focusses on *molecular* spectroscopy.

The information obtained from different spectroscopic techniques can be combined and can largely contribute in understanding the phenomena occurring at the nanoscale. In addition, theoretical calculations can sustain the experimental hypothesis or provide insights in the observed spectra which can become very complex. *Ab initio* molecular modeling is nowadays considered a powerful tool to analyze spectra.[27] We have known a rapid development of spectroscopic techniques to examine very complex molecular systems.[28] Theoretical models have also evolved to a level that should be able to predict accurate spectroscopic properties, with the support of the current availability of powerful computer resources.

Several advanced electronic structure methods are available but not all are computationally feasible due to the immense computational cost. Density Functional Theory (DFT) offers a viable alternative and gains an increasing popularity in the last decades.[29] DFT is now widely used in diverse research fields going from biosystems to material design. The theory of DFT relies on the Hohenberg-Kohn theorem, stating that the ground state density fully determines the system.[30] It implies that any property of the system — and in particular thus also spectroscopic properties — can in principle be expressed as a functional of the density.

In this doctoral work special focus is given on EPR, UV/Vis and vibrational spectroscopy. Although these three items are well described theoretically and although adequate computational models are available, there are still issues that merit additional model development to improve the outcome and to enlarge their applicability.

In particular, g-tensor calculations by means of DFT-based methods lack an adequate description of exchange terms in the spin-orbit interaction. At the start of this thesis, no model was available to treat specifically high-spin states in periodic codes.

Theoretical methods, which are able to reproduce reliable spectroscopic properties in most of the cases, exist and even comprise the most advanced wavefunction methods like coupled-cluster theory and time-dependent density functional theory (TD-DFT).[31, 32, 33, 34] They all approach the problem from a static viewpoint, from the energetically most favorite configuration at zero Kelvin. On the other hand, dynamical approaches like Molecular Dynamics (MD) match better the real working conditions during the experimental measurements, as the spectroscopic properties are derived after averaging over an ensemble of configurations encountered during the MD run.[35, 36, 26, 25] Dynamical methods incorporate vibrational motions on the potential energy surface (PES) and take into account temperatures and anharmonic effects in a very natural way. The influence of individual vibra-

tional modes on this averaged property, was investigated in detail in this PhD research.

All improvements on the existing models require a good knowledge of the underlying mechanisms of the three spectroscopic techniques under study in this thesis. Moreover, the most suitable way — static or dynamic method — to predict theoretical values of spectroscopic properties is an important aspect.

In Figure 1.5 a summary of the different items under discussion in this PhD is presented, with highlights on the major methods involved in the studied subjects.

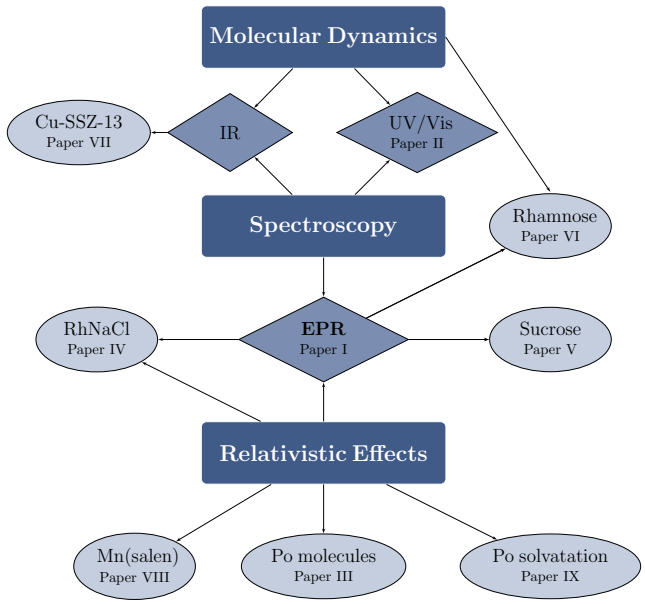

Figure 1.5: Overview of research topics in this doctoral thesis

Electron Paramagnetic Resonance

Computation of EPR parameters with the help of DFT-based methods has been done for more than 17 years with alternating success. At the beginning the calculations were restricted to gas phase molecules, *e.g.* ADF[37], ORCA[38], MagRespect[39], ... For defect structures in solid states, cluster models — in which the solid is approximated by a limited number of atoms — are not sufficient to properly describe the molecular environment of the defect. Since EPR very often concerns defects in crystals, use of peri-

odic codes is the most ideal, as periodic boundary conditions (PBC) are built in, allowing to simulate an infinite crystal with a select number of atoms in the unit cell. Many research consortia have constructed their own periodic code (CP2K[40], VASP[41], QuantumEspresso[42], ...) and in some of them, modules have been implemented enabling the calculation of EPR properties.[43, 44, 45] Seminal work in the development of periodic EPR codes has been done by Pickard and Mauri.[43] Unfortunately their computation is strongly implementation dependent and there is no unambiguous procedure to include the diverse contributions to the g-tensor. These factors make an assessment of different periodic codes to predict EPR properties a nearly unfeasible task. Despite several arguments favoring the use of periodic codes most groups still rely on cluster models.[46, 47, 48] This is mainly due to the much better implementation of spin-orbit corrections than in periodic codes. DFT codes using PBC are typically density based and described by plane waves, while the most accurate spin-orbit methods (AMFI, SOMF) are well suited for atomic based basis sets.[49, 50] In **Paper I**, the theory of g-tensor corrections arising from two-body spin-orbit interactions has been revisited and a protocol has been proposed to compute the spin-orbit matrix elements in periodic DFT with the same accuracy as in standard cluster codes. This has been extensively examined for a set of small molecules. The algorithm, developed for the spin-orbit g-tensor corrections, turns out to be also applicable to treat high spin systems, as additional terms appear, which were not present in previous methods, even for gas phase calculations.

Molecular Dynamics as a tool for vibrational spectroscopy

MD is a widely used tool to incorporate the dynamical behavior of a nanoscale system. At every timestep, the forces are calculated on every atom, leading to an updated velocity and position at the next timestep according to the equations of motion of Newton.[51, 52, 53] If the total time of the MD simulation is sufficiently long, an ensemble of slightly adapted geometries is created. In this way, molecular vibrations are taken into account, enabling opportunities to determine IR and Raman spectra from these calculations. In practice, the Velocity Power Spectrum (VPS) has been used extensively throughout many parts of this work.

Excited state spectroscopy

Time-Dependent Density Functional Theory (TD-DFT) has become the most popular technique to calculate electronic transitions in a computational feasible way.[32, 33, 34] Averaging the electronic transition energy for the ge-

ometries generated in an MD simulation results in a better agreement with experimental data compared to the excitation energy computed in a static way on an optimized geometry.[35, 36, 26] This indicates that it is very important to account for the flexibility of the molecule. Further insight can be gained by unravelling the molecular motions causing this significant change in the excitation energies.

Polonium

As a side project in this PhD thesis, the stability of various polonium compounds has been investigated. Expertise with respect to relativistic effects and advanced wavefunction based methods, built up in previous topics, was indispensable for this topic. This research fits in the framework of the European SEARCH project, in which the safety of liquid Lead-Bismuth Eutectic (LBE) as coolant in fourth generation nuclear reactors is investigated.[54] Under operation conditions, neutron capture by the LBE will lead to formation of a notable amount of highly radioactive polonium-210. Experiments investigating the LBE under operation or accident conditions are very expensive due to the pollution of the equipment and the high safety measures to be taken into account. Therefore, computer experiments are very valuable in order to get insight in the behavior of Po in and near the LBE. In particular the solubility of polonium in LBE and the evaporation and formation of Polonium-containing molecules were investigated.

The main goal of this doctoral dissertation is to give a valuable contribution to improve the accuracy of *ab initio* predictions of spectroscopic properties. This is achieved by new model development to readdress shortcomings in the literature or by development of new analysis methods, making use of existing tools. In all cases, principles of quantum mechanics and interacting many particle physics remain central.

The PhD thesis is composed of two parts. In Part I some chapters are devoted to a general description of the different molecular modeling tools used in this work. A lot of attention is given on the derivation of the spin-orbit interaction and the methodology how to deal with it in the evaluation of spin-orbit corrections terms to the g-tensor, and other EPR properties. Suggestions are given how to incorporate them in existing codes such as CP2K. These methods were used on a sucrose crystal which was experimentally measured

by collaborators of the EMR-group of the Department of Solid State Sciences of the Ghent University. Chapter 4 focusses on the vibrational spectroscopy obtained from molecular dynamics. Some vibrational motions have a direct impact on the fluctuations of electronic excitation energies. In Chapter 5 two applications are discussed for which MD simulations are used for different purposes: (i) the vibrational structure of copper holding catalyst materials (in collaboration with the Inorganic Chemistry and Catalysis group of the Utrecht University, dr. A. Beale, prof. B. Weckhuysen), (ii) the exploration of radical formation in rhamnose during radiation (in collaboration with the Department of Physics of the University of Oslo, prof. E. Sagstuen). Finally, in Chapter 6, the stability of some Polonium compounds has been examined. This research topic can be regarded as a side project, not really related to the central theme of this PhD work (spectroscopy) but which requires an extensive knowledge of high level wavefunction methods including relativistic effects and to some extent related with the relativistic effects encountered in the g-tensor corrections.

In Part II a list of all publications is taken up, making part of this doctoral dissertation. All scientific results are incorporated in these papers, and will not be discussed in separate chapters.

Chapter 2

Methods

Initiated by the first hypothesis of energy quanta by Max Planck, the theory of quantum mechanics has changed the opportunities and the challenges for physicists. The wave character for electrons had large repercussions regarding the understanding of spectroscopy and chemistry. For the field of quantum chemistry in particular, it forms the basis to understand and predict fundamental properties of molecules. Further developments by Paul Dirac combined quantum theory with special relativity, leading to a natural introduction of the concept "spin", as already proposed *ad hoc* by Wolfgang Pauli. This is an important keystone to understand the interaction of electrons and magnetic fields and therefore forming the basics of EPR. The introduction of relativistic effects in quantum chemistry did also become essential to describe elements with very high atomic number for which both scalar relativistic effects and spin-dependent effects contribute largely.

Due to the high degree of freedom in atomic and molecular systems — the many body problem — there is no analytical solution for the Schrödinger wave equation. Approximate methods at several levels were developed during the last century, simplifying the many body problem and the inclusion of relativistic effects.[55, 56] In this Chapter, the techniques used in the following Chapters and in the included papers are discussed. The stage is set by introducing general concepts widely used in molecular modeling, starting from wave function and density based methods. Subsequently, the most important relativistic effects for several purposes are introduced. Next, coupled perturbed equations are derived following a linear response approach. Closely related, the linear response approach for time-dependent density functional theory is briefly introduced and also overview of molecular dynamics is given. Finally, the programs which are extensively used in this work are highlighted.

2.1 Quantum Chemistry Methods

A molecule can be characterized by its nuclear configuration and number of electrons. In this perspective, following non-relativistic Hamiltonian corresponds to this picture [57]

$$\begin{aligned}\hat{H} = &-\sum_A \frac{\nabla_A^2}{2M_A} + \sum_{A\neq B} \frac{Z_A Z_B}{|\boldsymbol{R}_A - \boldsymbol{R}_B|} \\ &-\sum_i \frac{\nabla_i^2}{2} + \sum_{i\neq j} \frac{1}{|\boldsymbol{r}_i - \boldsymbol{r}_j|} - \sum_{i,A} \frac{Z_A}{|\boldsymbol{R}_A - \boldsymbol{r}_i|}\end{aligned} \tag{2.1}$$

In this work we always assume the Born-Oppenheimer approximation to be valid and hence consider the nuclei to be classical point charges, decoupled from the electronic wave problem. This approximation is justified by the large differences between the nuclear and electronic mass and is widely used in quantum chemistry.[31]

2.1.1 Wavefunction Based Methods

The main challenge to quantum chemistry is to solve the Schrödinger equation [10]

$$\text{Time-dependent :} \qquad \hat{H}\,|\Psi(t)\rangle = i\hbar\frac{\partial}{\partial t}\,|\Psi(t)\rangle \tag{2.2}$$

$$|\Psi(t)\rangle = \sum_n c_n \exp(-\frac{i}{\hbar}E_n t)\,|\Psi_n\rangle \tag{2.3}$$

$$\text{Time-independent :} \qquad \hat{H}\,|\Psi_n\rangle = E\,|\Psi_n\rangle \tag{2.4}$$

The most straightforward methods are wavefunction based methods in which the static wavefunction Ψ_n is expressed as a single Slater Determinant (Hartree-Fock) in function of single particle wavefunctions ϕ_i or as a sum of Slater Determinants to include correlation (post-Hartree-Fock).

I. Hartree-Fock

In Hartree-Fock, the *ansatz* for the stationary wavefunction is a single Slater Determinant, *i.e.* the antisymmetric sum of product wavefunctions.

$$\Psi^{SD}(\boldsymbol{r}_1, \ldots, \boldsymbol{r}_N) = |\phi_1\phi_2\ldots\phi_N| \tag{2.5}$$

This *ansatz* results in a set of coupled equations

$$\hat{h}_{HF} |\phi_j\rangle = \epsilon_j |\phi_j\rangle \tag{2.6}$$

The single particle Hamiltonian $\hat{h}_{HF}$ consists of a kinetic energy term and a mean field which depends on all other orbitals ϕ_i. It therefore requires self consistency (SC) to obtain a set of orbitals ϕ_j^{SC}, producing the central field $\hat{h}_{HF}^{SC}$ that has these same orbitals ϕ_j^{SC} as eigenfunctions.[55, 58]

Due to the restriction to the single Slater Determinant *ansatz*, the exact wavefunction cannot be found. The true ground state energy is more bound than the HF energy. The difference between the HF and the exact solution is called the electron correlation energy. Additionally, HF is unable to describe degeneracy as present in very symmetrical molecules.

II. Complete Active Space

A first step to include electron correlation and hence correctly describe bond breaking is the Complete Active Space Self-Consistent Field (CASSCF) approach. For this multi configurational (MC) method, the wavefunction is expanded in multiple Slater Determinants and both the single particle orbitals within each Slater Determinant Ψ_k^{SD} and their coefficients c_k are unknown variables which have to be determined.[31]

$$\left|\Psi^{MC}\right\rangle = \sum_k c_k \left|\Psi_k^{SD}\right\rangle \tag{2.7}$$

For this method, the electronic orbitals are categorized in three sub-spaces

- Fully occupied *Internal orbitals*
- Partially occupied *Active orbitals*
- Empty *Virtual orbitals*

The Slater Determinants $\left|\Psi_k^{SD}\right\rangle$ differ in the occupation of the active orbitals, as schematically indicated in Figure 2.1.

This approach includes so-called static correlation, resulting in a wavefunction that approaches the exact solution closer compared to Hartree-Fock and that overcomes problems in describing highly symmetrical systems and dissociation of molecules. The remaining difference in energy between an

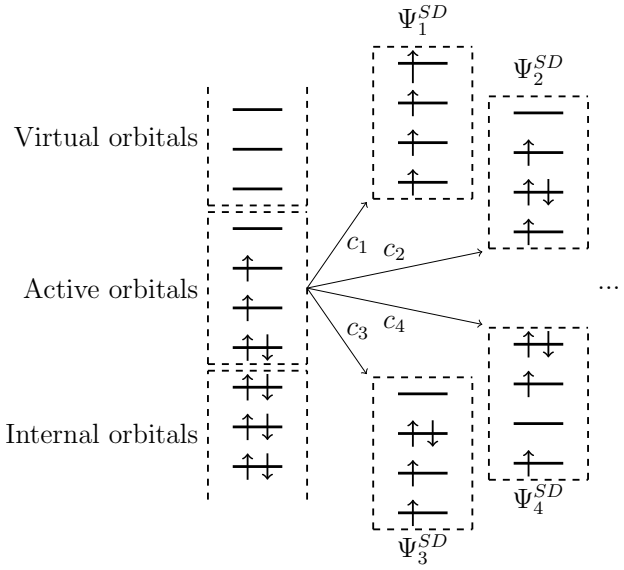

Figure 2.1: Schematic representation of the CASSCF approximation. The partition into internal, active and virtual orbitals is represented (left hand side of the Figure). The exact wavefunction is expanded in multiple Slater Determinants $\left|\Psi_k^{SD}\right\rangle$, for which the occupation of the active orbitals is different (right hand side of the Figure).

exact solution and this CASSCF result is called dynamic correlation, which can be described using more advanced methods (see III.).[31]

It is important to note that CASSCF cannot be considered as a black-box method. The choice of the active orbitals, the number of active electrons as well as the number of states $\left|\Psi_k^{SD}\right\rangle$ should be well-thought. If not, the symmetry could be broken, resulting in inaccurate wavefunctions and energies. In the simple case of one isolated atom for example, all orbitals with same quantum numbers should be treated at the same level. An obvious choice is to place the valence electrons in an active space and core electrons are then treated as internal (see Figure 2.1). If the active space is not properly chosen, the symmetry gets broken by the incorrect selection of active orbitals and electrons rather than by the symmetry of the system. The same holds for the number of calculated states. If the system is degenerate and only one state is calculated, the degeneracy will be lost.

III. Multi-Reference Configuration Interaction

When a Full Configuration Interaction (Full CI) wavefunction is dominated by a single reference Hartree-Fock state, one could express the full wavefunction as a linear combination of this reference state and single, double and higher excitations relative to that state[1].[31]

$$\left|\Psi^{FCI}\right\rangle = \left(1 + \sum_{\alpha,\mu} \hat{X}_{\mu,\alpha} + \sum_{\mu,\nu,\alpha,\beta} \hat{X}_{\mu,\nu,\alpha,\beta} + \dots\right) \left|\Psi^{HF}\right\rangle \tag{2.8}$$

$$\hat{X}_{\mu,\alpha} = x_{\mu,\alpha}\hat{c}_\mu^\dagger \hat{c}_\alpha \tag{2.9}$$

$$\hat{X}_{\mu,\nu,\alpha,\beta} = x_{\mu,\nu,\alpha,\beta}\hat{c}_\mu^\dagger \hat{c}_\nu^\dagger \hat{c}_\alpha \hat{c}_\beta \tag{2.10}$$

Very often this summation is truncated at the double or triple excitations (CCSD, CCSDT), for limiting the computational efforts.

Using the CASSCF wavefunction (Eqn. 2.7) as a starting point, the Multi-Reference Configuration Interaction (MRCI) includes dynamic correlations by including excitations in a similar fashion as the single reference CI case.

$$\left|\Psi^{MRCI}\right\rangle = \left(1 + \sum_{\mu,\alpha} \hat{X}_{\mu,\alpha} + \sum_{\mu,\nu,\alpha,\beta} \hat{X}_{\mu,\nu,\alpha,\beta} + \dots\right) \sum_k c_k \left|\Psi_k^{SD}\right\rangle \tag{2.11}$$

The computational cost of this method is however very high, making it only applicable for sufficiently small systems.

A key point to consider is that the energy in these calculations is not size-extensive [59], *i.e.* the energy of two non-interacting fragments in two isolated calculations does not correspond with the same setup where the fragments are sufficiently separated. Size-extensivity can only be reached if the compound system is equal to the direct product of the fragment spaces. Since the direct product of the fragment spaces contain triple and quadruple excitations, these are not systematically included in the MRCI expansion.

2.1.2 Density Functional Theory

In contrast to wavefunction based methods as described above, Hohenberg and Kohn proposed a theory which uses the density as key quantity.[29, 30]

[1] In Equations 2.9 and 2.10, creation ($c^\dagger$) and annihilation (c) operators in second quantization are used. In this way Equation 2.9 represents the annihilation of an electron from an occupied orbital α and addition of an electron to an unoccupied orbital μ in the Hartree-Fock wavefunction $\left|\Psi^{HF}\right\rangle$

In fact, the Hohenberg-Kohn theorem states that there is a one-to-one correspondence between the ground state density of an N-electron system ρ and the external potential $v_{ext}(\boldsymbol{r})$. Therefore, any property that can be derived from the external potential is a functional of the ground state density. This implies that the total energy can also be written as a functional of the density ρ.

$$E[\rho] = \langle \Psi[\rho] | \, \hat{T} + \hat{V}_{ext} + \hat{V}_{ee} \, | \Psi[\rho] \rangle \tag{2.12}$$

$$E[\rho] = T[\rho] + V_{ext}[\rho] + V_{ee}[\rho] \tag{2.13}$$

$$E[\rho] = T_s[\rho] + V_{ext}[\rho] + E_H[\rho] + E_{xc}[\rho] \tag{2.14}$$

From a practical point of view, this Density Functional Theory (DFT) is only useful if some approximations are used to construct a practical workflow. Mostly the Kohn-Sham (KS) scheme is employed [60], since it reduces the abstract density problem to a scheme very similar to wave function methods. Herein a fictitious system of non-interacting electrons with wavefunction φ_j is introduced with the same density as the real system of interacting electrons. The energy is then rewritten as a sum of a kinetic energy T_s of non-interacting electrons, an external potential V_{ext}, a Hartree energy E_H and the Exchange-Correlation energy E_{xc}. While all other terms don't pose a problem to evaluate, the exchange-correlation energy is unknown and multiple approximations are introduced during the last decades.

I. LDA

Historically the first approximation was inspired on the Thomas-Fermi homogeneous electron gas model[61, 62], for which the kinetic energy is a functional of the density only. Dirac included an exchange contribution[63, 29]

$$E_x^D = -C_x \int \rho^{\frac{4}{3}}(\boldsymbol{r}) \mathrm{d}\boldsymbol{r}, \qquad C_x = \frac{3}{4}\left(\frac{3}{\pi}\right)^{1/3} \tag{2.15}$$

This forms the exchange part of the local density approximation (LDA), valid for systems with slow-varying densities. The Xα formulation of Slater to approximate the non-local part of the Fock operator by a local one[64], is exactly this LDA if correlation is neglected and a scaling factor $\alpha = \frac{2}{3}$ is used.[29]

$$v_{X\alpha} = -\frac{3}{2}\alpha \left(\frac{3}{\pi}\rho(\boldsymbol{r})\right)^{1/3} \tag{2.16}$$

In **Paper I**, this type of exchange interaction is used to calculate spin-orbit coupling matrix elements.

II. Extended Density Functionals

Further development of the DFT was obtained by including non-local dependencies of the density, such as its gradient ($\nabla\rho$) for the generalized gradient approximation (GGA) and the Laplacian ($\Delta\rho$) for meta-GGA functionals. Use of the Kohn-Sham orbitals and their exchange interaction lead to hybrid GGA functionals. Double hybrid functionals have an additional term corresponding with a Møller-Plesset like perturbation correction term.[31, 65]

In this PhD thesis some widely used functionals were chosen for the applications. The focus of this work was not on a details functional performance study. The interested reader is referred to dedicated literature works on this topic. The chosen functionals include some GGA functionals such as PBE and BLYP and some hybrid functionals like PBE0 and B3LYP.

2.2 Relativistic Quantum Mechanics: Dirac Equation

Previous methods focused on the solution of the non-relativistic many particle problem. For organic systems this is often sufficient. However, in the case of heavy elements relativistic effects play a dominant role and can therefore not be neglected (row 4 in the periodic table to be on the safe side, for row 6 inclusion of relativistic effects is not optional). In 1928 Paul Dirac unified the quantum theory as proposed by Schrödinger and special relativity. As a result, he obtained the one-particle time-dependent Dirac equation, here given in the familiar Schrödinger form

$$\hat{H}_D \left|\Psi_D\right\rangle = i\hbar\frac{\partial}{\partial t}\left|\Psi_D\right\rangle \tag{2.17}$$

in which $\left|\Psi_D\right\rangle$ are Dirac-spinors, *i.e.* vector-valued wavefunctions and $\hat{H}_D$ is the Dirac Hamiltonian. For particles in an electromagnetic field the Dirac Hamiltonian is expressed as [56]

$$\hat{H}_D = c\boldsymbol{\alpha}\cdot\boldsymbol{\pi} + \beta mc^2 + q\phi \tag{2.18}$$

in which the minimal substitution is applied $\boldsymbol{\pi} = \boldsymbol{p} - \frac{q}{c}\boldsymbol{A}$[66], the Dirac matrices $\boldsymbol{\alpha} = (\alpha_1, \alpha_2, \alpha_3)$ and β, and the external field ϕ are introduced.

$$\alpha_i = \begin{pmatrix} 0 & \sigma_i \\ \sigma_i & 0 \end{pmatrix} \qquad\qquad \beta = \begin{pmatrix} 1_2 & 0 \\ 0 & -1_2 \end{pmatrix} \tag{2.19}$$

in which 1_2 is a two-by-two unity matrix and σ_i are the Pauli matrices

$$\sigma_1 = \begin{pmatrix} 0 & 1 \\ 1 & 0 \end{pmatrix} \qquad \sigma_2 = \begin{pmatrix} 0 & -i \\ i & 0 \end{pmatrix} \qquad \sigma_3 = \begin{pmatrix} 1 & 0 \\ 0 & -1 \end{pmatrix} \tag{2.20}$$

From this definition, it follows that $|\Psi_D\rangle$ represents a spinor with four components, which simultaneously describes an electron (with positive energy, *large components*) and a positron (with negative energy, *small components*). For chemistry, only the electron is considered valuable to describe molecules and therefore simplifications are recommended. Using a Foldy-Wouthuysen transformation — *i.e.* a unitary transformation of the Dirac space — the decoupling of the positron and electron can be obtained up to any order of c^{-1}. [67]

2.2.1 Dirac-Coulomb-Breit Hamiltonian in an External Field

When extending this description to multiple electrons, Coulomb interactions between the electrons are obviously necessary. Inclusion of spin-spin interaction is less intuitive, however mandatory to have a full description of the system. In particular for spin-dependent properties, these interactions will have significant contributions. These spin-spin interactions were first introduced by Breit [68] and together with the Dirac and Coulomb term, they form the Dirac-Coulomb-Breit Hamiltonian ($\hat{H}_{DCB}$)

$$\begin{aligned} \hat{H}_{DCB} = &\sum_i \hat{H}_{D,i} + \sum_i q_i \phi_i + \frac{1}{2} \sum_{i \neq j} \frac{q_i q_j}{r_{ij}} \\ &- \frac{1}{4} \sum_{i \neq j} \frac{q_i q_j}{r_{ij}} \left(\boldsymbol{\alpha}_i \cdot \boldsymbol{\alpha}_j + \frac{(\boldsymbol{\alpha}_i \cdot \boldsymbol{r}_{ij})(\boldsymbol{\alpha}_j \cdot \boldsymbol{r}_{ij})}{r_{ij}^2} \right) \end{aligned} \tag{2.21}$$

In order to describe only the two electrons, decoupling of the two positrons is needed. With a similar but much more complex method than the Foldy-Wouthuysen transformation — the Chraplyvy-Barker-Glover[69, 70, 71] reduction — the $\hat{H}_{DCB}$ can be transformed into following Hamiltonian, split up in a one-and two particle Hamiltonians ($\hat{H}_i$ and $\hat{H}_{ij}$ respectively).[72, 18][2]

$$\hat{H} = \sum_i \hat{H}_i + \frac{1}{2} \sum_{i \neq j} \hat{H}_{ij} \tag{2.22}$$

[2]Atomic units were used in which $\alpha = c^{-1}$, with α the fine structure constant, and the charge of an electron is put to one ($e = 1$).

$$\hat{H}_i = \alpha^{-2} + \frac{\boldsymbol{\pi}_i^2}{2} - \frac{\alpha^2}{8}\boldsymbol{\pi}_i^4 - \phi_i + \frac{\alpha}{2}(\boldsymbol{\sigma}_i \cdot \boldsymbol{B}) + \frac{\alpha^2}{4}\boldsymbol{\sigma}_i \cdot (\boldsymbol{E} \times \boldsymbol{\pi}_i) + \frac{\alpha^2}{8}\nabla_i \cdot \boldsymbol{E} - \frac{\alpha^3}{4}(\boldsymbol{\sigma}_i \cdot \boldsymbol{B})\boldsymbol{\pi}_i^2 - \frac{\alpha^4}{8}(\boldsymbol{\sigma}_i \cdot \boldsymbol{B})^2 \quad (2.23)$$

$$\begin{aligned}\hat{H}_{ij} =& \frac{1}{r_{ij}} - \frac{\alpha^2}{4r_{ij}^3}\left[\boldsymbol{\sigma}_i \cdot (\boldsymbol{r}_{ij} \times \boldsymbol{\pi}_i) - \boldsymbol{\sigma}_j \cdot (\boldsymbol{r}_{ij} \times \boldsymbol{\pi}_j)\right] \\ &+ \frac{\alpha^2}{2}\frac{1}{r_{ij}^3}\left[\boldsymbol{\sigma}_i \cdot (\boldsymbol{r}_{ij} \times \boldsymbol{\pi}_j) - \boldsymbol{\sigma}_j \cdot (\boldsymbol{r}_{ij} \times \boldsymbol{\pi}_i)\right] \\ &+ \frac{\alpha^2}{4}\frac{1}{r_{ij}^3}\boldsymbol{\sigma}_i \cdot \boldsymbol{\sigma}_j - \frac{3}{4}\alpha^2\frac{1}{r_{ij}^5}\left(\boldsymbol{\sigma}_i \cdot \boldsymbol{r}_{ij}\right)\left(\boldsymbol{\sigma}_j \cdot \boldsymbol{r}_{ij}\right) - \frac{2\pi}{3}\alpha^2\delta(\boldsymbol{r}_{ij})\boldsymbol{\sigma}_i \cdot \boldsymbol{\sigma}_j \\ &- \frac{\alpha^2}{2}\frac{1}{r_{ij}}\boldsymbol{\pi}_i \cdot \boldsymbol{\pi}_j - \frac{\alpha^2}{2}\frac{1}{r_{ij}^3}\left(\boldsymbol{\pi}_i \cdot \boldsymbol{r}_{ij}\right)\left(\boldsymbol{r}_{ij} \cdot \boldsymbol{\pi}_j\right) - \pi\alpha^2\delta(\boldsymbol{r_{ij}}) \quad (2.24)\end{aligned}$$

For most practical purposes such as molecular calculations, these interactions are categorized in two effects: scalar relativistic and spin-orbit coupling.

2.2.2 Scalar Relativistic Contributions

These contributions are independent of the vector property *spin*, which explains the label *scalar*. For the single particle Hamiltonian (Eqn. 2.23) only some terms are retained (not containing any spin variable):

$$\hat{H}^{sr} = \alpha^{-2} + \frac{p^2}{2} - \frac{\alpha^2 p^4}{8} + \frac{\alpha^2}{8}\nabla \cdot \boldsymbol{E} - \phi \quad (2.25)$$

These terms correspond respectively to a constant mass term, the original kinetic energy, the mass-velocity term, the Darwin term and the potential energy potential.

This corresponds to the quantum mechanical equivalent of a Taylor expansion for the special relativistic energy expression.

$$E = \sqrt{m_e^2c^4 + p^2c^2} + V = \frac{1}{\alpha^2}\left(\sqrt{1 + \alpha^2p^2}\right) + V \text{ [a.u.]} \quad (2.26)$$

For regular potentials this approach is valid if the velocity is much smaller than the speed of light. For Coulombic potentials however, problems arise.

There will always be a region where $E - V = T = \frac{p^2}{2m_e}$ will become very large, in particular near the nucleus. For that region, this expansion is invalid and the mass-velocity term as first order perturbation is incorrect[73, 74].

An interesting point of view about this approach is that it starts from a free electron, on which the potential is only a perturbation. This is not the case when the electrostatic potential of the nucleus is considered, since it is very large (in absolute value) near the nucleus. Indeed, this approximation is only valid for small values of $\frac{p^2}{2m_0^2c^2} = \frac{E-V}{m_0c^2}$, which is not the case near the nucleus.

As an alternative to this Foldy-Wouthuysen transformation, one can follow the regular expansion, leading to the zeroth order regular approximation (ZORA) for the scalar relativistic effects. Classically one gets

$$\begin{aligned} E &= \alpha^{-2}\sqrt{1+\alpha^2p^2} - \alpha^{-2} + V \\ &= \alpha^{-2}\frac{(\sqrt{1+\alpha^2p^2}-1)(\sqrt{1+\alpha^2p^2}+1)}{\sqrt{1+\alpha^2p^2}+1} + V \\ &= \frac{\alpha^{-2}p^2}{\left(\alpha^{-2}\sqrt{1+\alpha^2p^2}+\alpha^{-2}\right)} + V \qquad (2.27) \\ &= \frac{\alpha^{-2}p^2}{(E-V)+2\alpha^{-2}} + V \\ &= \frac{\alpha^{-2}p^2}{(2\alpha^{-2}-V)(1+\frac{E}{2\alpha^{-2}-V})} + V \qquad (2.28) \end{aligned}$$

This results in zeroth order in

$$E \approx \frac{p^2\alpha^{-2}}{(2\alpha^{-2}-V)} + V \qquad (2.29)$$

The quantum mechanical equivalent is more complex and inherently contains the spin-orbit coupling. Except for the original implementation in ADF, most traditional codes have only this scalar variant available.

This method, first proposed by van Lenthe[73] in a two-component fashion, corresponds to the scalar part of the Hamiltonian derived by Chang, Pelissier and Durand. It has one major drawback, since it is not gauge invariant to the potential energy V, *i.e.* the total energy is not linear in V. In this thesis preference is given to the modified ZORA Hamiltonian[75] with a suitable model potential, solving this issue. Including these scalar relativistic effects demands the use of an adapted basis set.

2.2.3 Spin-Orbit Coupling

Secondly, the spin-orbit interaction is very often considered to be a main concern when relativistic effects become important. The reduction of the full Dirac equation to two-component equations leads to following Breit-Pauli spin-orbit Hamiltonians (H^{BP}), which can be derived from the Eqns. 2.23 and 2.24:

$$\hat{H}_{SON} = \sum_i \frac{g'\alpha^2}{4} \sum_A Z_A \boldsymbol{s}_i \cdot \frac{(\boldsymbol{r}_i - \boldsymbol{R}_A) \times \boldsymbol{p}_i}{|\boldsymbol{r}_i - \boldsymbol{R}_A|^3} \tag{2.30}$$

$$\hat{H}_{SSO} = -\sum_i \sum_{j \neq i} \frac{g'\alpha^2}{4} \boldsymbol{s}_i \cdot \frac{(\boldsymbol{r}_i - \boldsymbol{r}_j) \times \boldsymbol{p}_i}{|\boldsymbol{r}_i - \boldsymbol{r}_j|^3} \tag{2.31}$$

$$\hat{H}_{SOO} = -\sum_i \sum_{j \neq i} \frac{\alpha^2}{4} \boldsymbol{s}_i \cdot \frac{(\boldsymbol{r}_j - \boldsymbol{r}_i) \times \boldsymbol{p}_j}{|\boldsymbol{r}_i - \boldsymbol{r}_j|^3} \tag{2.32}$$

which represent respectively the coupling of the electron spin and

(i) the orbit of the electron with respect to the nucleus (spin-orbit-nucleus, SON)

(ii) the orbit of this electron with respect to another electron (spin-same-orbit, SSO)

(iii) the orbit of another electron with respect to the first electron (spin-other-orbit, SOO)

In these expressions Z_A is the nuclear charge and $g' = 2g_e - 2$ with g_e the free electron g-factor.

The direct calculation of the two-electron Hamiltonian matrix elements requires the evaluation of four-center integrals which is computationally very demanding. Several approximations have therefore been suggested. They will be discussed in Chapter 3 and are the subject of **Paper I**.

2.2.4 Other Relativistic Corrections

The spin-dependent relativistic corrections are essential to describe the EPR experiment properly and are therefore highlighted. The Zeeman term shows the interaction between the spin of an electron and the external magnetic field. It has a relativistic correction via the Zeeman Kinetic Energy (ZKE).

Secondly, also the spin-spin interaction is essential for high spin systems which exhibits zero field splitting (ZFS).

$$\hat{H}_{SS} = \frac{\alpha^2}{8} \sum_{i,j} \frac{\boldsymbol{\sigma}_i \cdot \boldsymbol{\sigma}_j}{r_{ij}^3} - 3\frac{(\boldsymbol{\sigma}_i \cdot \boldsymbol{r}_{ij})\,(\boldsymbol{\sigma}_j \cdot \boldsymbol{r}_{ij})}{r_{ij}^5} \tag{2.33}$$

In fact this is the zeroth order term that causes the ZFS and dominates in organic systems such as porphyrine. For transition metal ions, the spin-orbit coupling is a much more dominant contribution to the ZFS. Overall this interaction is considered to be very small compared to binding energies, which will be shown in the paper about Polonium.

The orbit-orbit interactions are rarely taken into account.

2.3 Coupled Perturbed SCF Equations

Coupled Perturbed Equations can be applied to calculate various molecular properties.[76] In particular, we derive here the Coupled Perturbed equations for property Λ which can be formulated as a second derivative of the total electronic energy E, with respect to two parameters λ and λ' (see Eqn. 2.34).[50, 77] Examples are forces and frequencies, NMR shielding tensor, g-tensor, hyperfine tensor, ... [76]

$$\Lambda = \left.\frac{\partial^2 E}{\partial\lambda\partial\lambda'}\right|_{\lambda=0=\lambda'} \tag{2.34}$$

According to the Hellmann-Feynman theorem[78, 79], Eqn. 2.34 can be rewritten as

$$\begin{aligned}\Lambda =& \frac{\partial}{\partial\lambda}\left[\langle\Psi|\left.\frac{\partial\hat{H}}{\partial\lambda'}\right|_{\lambda'=0}|\Psi\rangle\right]_{\lambda=0} = \left[\langle\Psi|\left.\frac{\partial^2\hat{H}}{\partial\lambda\partial\lambda'}\right|_{\lambda=0=\lambda'}|\Psi\rangle\right. \\ &\left. + \left[\frac{\partial}{\partial\lambda}\langle\Psi|\right]_{\lambda=0}\left.\frac{\partial\hat{H}}{\partial\lambda'}\right|_{\lambda'=0}|\Psi\rangle + \langle\Psi|\left.\frac{\partial\hat{H}}{\partial\lambda'}\right|_{\lambda'=0}\left[\frac{\partial}{\partial\lambda}|\Psi\rangle\right]_{\lambda=0}\right]\end{aligned} \tag{2.35}$$

The second order derivative of the full Hamiltonian in the first term poses no problem to evaluate. The other two contributions however, depend on the variations of the wavefunction Ψ on the external parameter λ. Applying linear response theory, a coupled set of equations is derived to evaluate the first order changes of the wavefunction due to the perturbations. The linear response theory can be applied to any energy eigenvalue problem, whether it is the HF or the KS equation. We therefore prefer to outline the procedure

in the case of a general self-consistent field (SCF) operator $\hat{F}$, encompassing both approaches

$$\hat{F} = \hat{h} + \hat{V}_C + \hat{K} + \hat{V}_{xc} \tag{2.36}$$

for which $\hat{h}$ is the single particle Hamiltonian grouping all one-body terms, $\hat{V}_C$ the electron-electron Coulomb potential (direct term), $\hat{K}$ the exchange Coulomb potential, most conveniently defined through its matrix elements[3] and $\hat{V}_{xc}$ the DFT exchange correlation potential.

The SCF secular equation obeys:

$$\hat{F}\psi_\alpha = \epsilon_\alpha \psi_\alpha \tag{2.37}$$

and yields as solutions the single-particle molecular orbital energies ϵ_α of both the occupied and unoccupied spin orbitals ψ_α.

Now a perturbation $\lambda\hat{h}_\lambda$ is introduced in the SCF operator: $\hat{F} \to \hat{F}(\lambda) = \hat{F} + \lambda\hat{h}_\lambda$, with λ an adiabatic parameter. The perturbation causes a linear response of the orbital energies and spin orbitals:

$$\epsilon_\alpha(\lambda) = \epsilon_\alpha^{(0)} + \lambda\epsilon_\alpha^{(1)} + O(\lambda^2) \tag{2.38}$$

$$\psi_\alpha(\lambda) = \psi_\alpha^{(0)} + \lambda\psi_\alpha^{(1)} + O(\lambda^2) \tag{2.39}$$

$$\hat{F}(\lambda) = \hat{F}^{(0)} + \lambda\hat{F}^{(1)} + O(\lambda^2) \tag{2.40}$$

Keeping only the first order terms in λ, Eqn. 2.37 becomes:

$$(\hat{F}^{(0)} - \epsilon_\alpha^{(0)})\psi_\alpha^{(1)} + (\hat{F}^{(1)} - \epsilon_\alpha^{(1)})\psi_\alpha^{(0)} = 0 \tag{2.41}$$

Solutions of the unperturbed secular equation (Eqn. 2.37) form a complete and orthogonal set of wavefunctions, spanning the space of occupied spin orbitals $\alpha, \beta, \gamma, \ldots$ and unoccupied spin orbitals $\mu, \nu, \xi, \ldots$. Due to the orthogonality of both spaces, one may assume that the correction $\psi_\alpha^{(1)}$ due to the perturbation lies in the space of the unoccupied spin orbitals:

$$\psi_\alpha^{(1)} = \sum_{\mu\in\sigma} U_{\alpha\mu}\psi_\mu^{(0)} \tag{2.42}$$

This expansion can be substituted in Eqn. 2.37, which needs the evaluation of the first order perturbed SCF operator $\hat{F}^{(1)} = \left.\frac{\partial\hat{F}(\lambda)}{\partial\lambda}\right|_{\lambda=0}$.

[3] $\langle\alpha|\hat{K}|\gamma\rangle = -\sum_\beta n_\beta \langle\alpha\beta|\frac{1}{r_{12}}|\beta\gamma\rangle$ with n_β the occupation number of the $\beta \equiv (b, m_b)$ molecular orbitals

In DFT the SCF operator $\hat{F}$ in Eqn. 2.37 is a functional of the density ρ and hence the derivative of each term of $\hat{F}$ with respect to the λ requires the computation of the derivative of the density. It is the key expression in the further elaboration of Eqn. 2.41, which then turns out to decompose in coupled perturbed equations.

$$\begin{aligned}
&\frac{\partial}{\partial\lambda}\rho_\sigma(\boldsymbol{r})\bigg|_{\lambda=0} \\
&= \sum_\alpha n_\alpha \frac{\partial}{\partial\lambda}\left[\left(\psi_\alpha^{(0)}(\boldsymbol{r}) + \lambda\psi_\alpha^{(1)}(\boldsymbol{r})\right)^* \left(\psi_\alpha^{(0)}(\boldsymbol{r}) + \lambda\psi_\alpha^{(1)}(\boldsymbol{r})\right)\right]_{\lambda=0} \\
&= \sum_\alpha n_\alpha \left[\psi_\alpha^{(0),*}\psi_\alpha^{(1)} + \psi_\alpha^{(1),*}\psi_\alpha^{(0)}\right]_{\lambda=0} \\
&= 2\sum_{\alpha,\mu} n_\alpha \psi_\alpha^{(0)}\psi_\mu^{(0)}\,\mathrm{Re}(U_{\alpha\mu})
\end{aligned} \tag{2.43}$$

In the above expressions, the unperturbed wavefunctions are assumed to be real-valued (*i.e.* $\psi_\alpha^{(0)} \in [\mathbb{R} \to \mathbb{R}]$) and n_α is the occupation number of orbital α.

All derivatives of the perturbed SCF operator

$$\hat{F}^{(1)} = \hat{h}_\lambda + \frac{\partial V_C}{\partial\lambda}\bigg|_{\lambda=0} + \frac{\partial K}{\partial\lambda}\bigg|_{\lambda=0} + \frac{\partial V_{XC}}{\partial\lambda}\bigg|_{\lambda=0} \tag{2.44}$$

can be evaluated through use of Eqn. 2.43 or similar derivations. Their explicit expressions can be found in the work of F. Neese.[80]

We illustrate the procedure with the direct Coulomb operator $\hat{V}_C$:

$$\frac{\partial}{\partial\lambda}V_C(\boldsymbol{r}) = \frac{\partial}{\partial\lambda}\int\frac{\rho(\boldsymbol{r})}{|\boldsymbol{r}-\boldsymbol{r}'|}\mathrm{d}\boldsymbol{r}' = 2\sum_{\alpha,\mu} n_\alpha\,\mathrm{Re}(U_{\alpha\mu})\int\frac{\psi_\alpha^{(0)}(\boldsymbol{r}')\psi_\mu^{(0)}(\boldsymbol{r}')}{|\boldsymbol{r}'-\boldsymbol{r}|}\mathrm{d}\boldsymbol{r}' \tag{2.45}$$

The first order secular equation (Eqn. 2.41) can be written as (using the orthogonality of the occupied and unoccupied orbitals):

$$\begin{aligned}
&\left\langle\psi_\mu^{(0)}\right|(\hat{F}^{(0)} - \epsilon_\alpha^{(0)})\left|\psi_\alpha^{(1)}\right\rangle + \left\langle\psi_\mu^{(0)}\right|(\hat{F}^{(1)} - \epsilon_\alpha^{(1)})\left|\psi_\alpha^{(0)}\right\rangle = 0 \\
&\sum_\nu U_{\alpha\nu}\left\langle\psi_\mu^{(0)}\right|(\hat{F}^{(0)} - \epsilon_\alpha^{(0)})\left|\psi_\nu^{(0)}\right\rangle \\
&\quad + \left\langle\psi_\mu^{(0)}\right|\hat{h}_\lambda + \frac{\partial V_C}{\partial\lambda} + \frac{\partial K}{\partial\lambda} + \frac{\partial V_{XC}}{\partial\lambda}\left|\psi_\alpha^{(0)}\right\rangle = 0
\end{aligned} \tag{2.46}$$

We used the orthogonality of the occupied and unoccupied orbitals.

$$\left\langle \psi_{\mu}^{(0)} | \psi_{\alpha}^{(0)} \right\rangle = 0 \tag{2.47}$$

The above expression (Eqn. 2.46) is essentially a set of coupled equations and can be written in matrix form for the real and imaginary part of the unknown $U_{\beta\nu}$

$$\boldsymbol{M'} \cdot Re(\boldsymbol{U}) = Re(\boldsymbol{h_\lambda}) \tag{2.48}$$
$$\boldsymbol{M''} \cdot Im(\boldsymbol{U}) = Im(\boldsymbol{h_\lambda}) \tag{2.49}$$

The derivatives to λ of the operator $\hat{F}$ also contain the expansion coefficients $U_{\alpha\mu}$ through the density dependence (*e.g.* $\hat{V}_C$) and therefore have a contribution to the matrices $\boldsymbol{M'}$ and $\boldsymbol{M''}$. It can be shown that for LDA and GGA functionals, only the imaginary part is non-zero and the real part of expansion coefficients $\boldsymbol{U}$ becomes important for hybrid functionals.

2.4 Time-Dependent Density-Functional Theory

Although DFT has proven to be a very successful approach for ground state properties, the theory is fundamentally unable to describe excited states. Several attempts to describe excited states with DFT can be found in literature and the use of time-dependent density functional theory (TD-DFT) has recently gained much popularity.[33] The Runge-Gross theorem lies at the basis of this theory and can be interpreted as an extension of the Hohenberg-Kohn to time-dependent external potentials and time-dependent densities, in the sense that two different time-dependent potentials will lead to two different densities at a moment infinitesimally later.[81, 33] Similar to DFT, also a time-dependent Kohn-Sham scheme can be constructed, allowing a practical implementation to track the density during a period of time in presence of a non-static external field.

TD-DFT is however most popular in its linear response formulation. In the Fourier domain the linear response of a quantum mechanical observable $\hat{R}$ is

$$R_1(\omega) = \chi_{RS}(\omega) F(\omega) \tag{2.50}$$

with $F(\omega)$ the perturbing field and $\chi_{RS}(\omega)$ the frequency-dependent response function. In the Lehmann representation, this is given by [33]

$$\chi_{RS}(\omega) = \lim_{\eta \to 0^+} \sum_{n=1}^{\infty} \left\{ \frac{\left\langle \Psi^{(0)} \right| \hat{R} \left| \Psi_n^{(1)} \right\rangle \left\langle \Psi_n^{(1)} \right| \hat{S} \left| \Psi^{(0)} \right\rangle}{\omega - \Omega_n + i\eta} + \frac{\left\langle \Psi^{(0)} \right| \hat{S} \left| \Psi_n^{(1)} \right\rangle \left\langle \Psi_n^{(1)} \right| \hat{R} \left| \Psi^{(0)} \right\rangle}{\omega + \Omega_n + i\eta} \right\} \tag{2.51}$$

in which $\left| \Psi_n^{(1)} \right\rangle$ represents the nth excited state, corresponding to an energy E_n. This response function has poles at the excitation energy $\Omega_n = E_0 - E_n$, which is the property we are mainly interested in.

In the formulation of Casida, based on the linear response time-dependent HF, the perturbed property $R_1(\omega)$ can be found by solving [82, 83]

$$\left\{ \omega \begin{pmatrix} \mathbf{1} & \mathbf{0} \\ \mathbf{0} & -\mathbf{1} \end{pmatrix} - \begin{pmatrix} \boldsymbol{A} & \boldsymbol{B} \\ \boldsymbol{B}^* & \boldsymbol{A}^* \end{pmatrix} \right\} \begin{pmatrix} \boldsymbol{R}_1(\omega) \\ \boldsymbol{R}_1^*(\omega) \end{pmatrix} = \begin{pmatrix} \boldsymbol{F}(\omega) \\ \boldsymbol{F}^*(\omega) \end{pmatrix} \tag{2.52}$$

which can be seen as an extension of the Coupled Perturbed equations (Eqn. 2.46) as proven in Ref. [83].

Due to the structure of Eqn. 2.51, a perturbation with frequency Ω_n will result in an infinite response. The only reasonable response for these frequencies can be found if the perturbation is infinitesimal small ($F(\omega) \to 0$). Therefore the excitation energies Ω_n can be found by solving the following generalized eigenvalue problem

$$\begin{pmatrix} \boldsymbol{A} & \boldsymbol{B} \\ \boldsymbol{B}^* & \boldsymbol{A}^* \end{pmatrix} \begin{pmatrix} \boldsymbol{X}(\omega) \\ \boldsymbol{Y}^*(\omega) \end{pmatrix} = \Omega_n \begin{pmatrix} \mathbf{1} & \mathbf{0} \\ \mathbf{0} & -\mathbf{1} \end{pmatrix} \begin{pmatrix} \boldsymbol{X}(\omega) \\ \boldsymbol{Y}^*(\omega) \end{pmatrix} \tag{2.53}$$

This method is widely implemented in Quantum Chemical codes and was used to calculate the excitation energies of multiple compounds in **Paper II**.

2.5 Molecular Dynamics

A powerful technique to monitor the dynamical behavior of a molecular system is Molecular Dynamics (MD).[52, 53] It follows the nuclear motion during multiple possible conditions, such as a system in equilibrium or in flow. In order to track these motions, the force $\boldsymbol{F}_A$ on each atom A should be

calculated, which then can be used to calculate the acceleration, velocity and new atomic positions. In this way a trajectory of different geometries, with related properties such as velocity or forces, is constructed.

In many cases - especially for treating larger systems - a force field based approach is used to evaluate the force on each single atom. In this view, atoms are represented by point charges, bonds by springs,... This implies parametrization of the many unknowns in such a system, such as the atomic charge, bond constants, equilibrium (dihedral) angles, ... Due to its low cost, it allows to run very long simulations for very large systems which is often desired for long-time processes such as diffusion. It however lacks the ability to reach parts of the potential energy surface (PES) for which the electronic structure changes drastically because of a bias introduced by the parametrization of the many parameters. Examples are reactions, polarization effects,...

Alternatively, *ab initio* molecular dynamics (AIMD) meets these deficiencies since it solves the electronic problem of each geometry on the trajectory on the fly. This implies that the atomic charges are different at each MD step, bond breaking can occur, ...The AIMD exists in different flavors of which Ehrenfest MD (EMD), Born-Oppenheimer MD (BOMD) and Car-Parinello MD (CPMD) are widely known.[53]

In EMD and CPMD the electrons are propagated during the nuclear motion, avoiding to evaluate the electronic problem at each trajectory step, which is needed for BOMD. The drawback is very short time steps for the trajectories. Due to the development of fast methods to evaluate the DFT problem[40, 84, 85], the BOMD method has gained popularity in recent years. It is nevertheless important to point out that in view of its much larger computational cost, the accessible correlation length and relaxation times are much shorter with AIMD compared to classical MD. In this work only AIMD is used and therefore this method will be denoted as MD for convenience.

2.6 Software

In this PhD work a large variety of quantum chemical software was used. The actual wavefunction or DFT calculations were performed using available programs such as CP2K, ORCA, Gaussian, ADF/BAND, QuantumESPRESSO and VASP. For post analysis, in-house packages (MD-Tracks, Yaff, Horton), available software (VMD, GROMACS) and own scripts were used and mostly run on a local desktop. The majority of the simulations performed in view of this PhD research were done with either ORCA (gas phase) or CP2K (periodic), and particular features of both packages are therefore briefly summarized.

2.6.1 ORCA

The ORCA package is a quantum chemical package which is developed with a high focus on spectroscopic properties and open shell properties. The project was started by Frank Neese and is on-going under his supervision.[38, 86] Examples of the available spectroscopic properties are IR and Raman spectroscopy, absorption and fluorescence, NMR, hyperfine tensor, g-tensor, ZFS tensor, circular dichroism spectra, Mössbauer parameters and exchange couplings. A wide variety of standard quantum chemical methods described above are available and applicable for the many spectroscopic properties. For computational efficiency, the wide spread Gaussian Type Orbitals (GTO) are used. These basis sets are isolated on the nucleus and are well suited for describing molecules in the gas phase, *i.e.* the molecule is surrounded by vacuum. Another advantage is the availability of relativistic effects, such as the DKH and ZORA method for scalar relativistic calculations and spin-orbit and spin-spin interactions on a quasi-degenerate perturbation theory level (Davidson diagonalization) for the MRCI and CASSCF calculations. In contrast to most other codes in which only one method for the spin-orbit coupling is implemented (Z_{eff} in Gaussian, V_{eff} in ADF and CP2K, ...), a large variety is available in ORCA and MagRespect.

2.6.2 CP2K

This periodic code is freely available under the GPL licence and created by a team of developers, with main contributors being Jürg Hutter, Matthias Krack, Teodoro Laino and Joost VandeVondele.[40, 87]. CP2K is suited for a wide variety of methodologies, going from full quantum mechanic simulations at a hybrid functional level down to using classical mechanics simulations. Also a large variety of other features is present in CP2K, such as EPR and NMR calculations, transition state methods (NEB), Monte Carlo simulations and especially Molecular Dynamics (MD). Due to the periodicity build in this code, it is very well suited to include long-range effects. Description of an isolated molecule is less convenient, however with the use of a box which is sufficiently large, good agreement with non-periodic codes can be achieved. Description of this large vacuum is however computationally quite demanding, but for reference comparison to established non-periodic codes, it was essential.

In this dissertation mainly QM simulations were performed. For these calculations two descriptions of the density are given: one in the real space by periodically repeated GTOs and another in reciprocal space, giving rise to a plane wave basis set. Both representations are connected by the three

dimensional Fourier transform and have each their benefits, such as an easily defined kinetic energy in the reciprocal space on the one side, the electron-electron interaction easily calculated using periodic GTOs on the other side.

Another key feature of CP2K is its excellent scaling with respect to increasing computer power. Multiple efforts have been made to obtain a linear scaling method, allowing huge systems to be calculated at a full QM level, opening opportunities for the use of the Tier-1 cluster of the Flemish Supercomputer Centre (Vlaams Supercomputer Centrum, VSC).

Chapter 3

EPR Properties

Electron Paramagnetic Resonance (EPR) is a Magnetic Resonance technique which is very powerful to investigate defects in solids which contain unpaired electrons and are therefore paramagnetic. During Magnetic Resonance experiments, transitions between energy levels which depend on the strength of an external magnetic field are induced. EPR relies directly on the observations of Stern and Gerlach[88] that a beam of particles (*e.g.* silver atoms) in a magnetic field splits up in several distinct beams. In particular for EPR, these energy levels are determined by the magnetic moment $\boldsymbol{\mu}$ of the unpaired electrons. An external magnetic field $\boldsymbol{B}$ will interact with μ and the spin-degeneracy will be lifted.

The experimental observed spectrum is afterwards fitted to an effective spin Hamiltonian with several tensorial parameters

$$\hat{H}_S = \sum_N \left(\boldsymbol{S} \cdot \boldsymbol{A}_N \cdot \boldsymbol{I}_N\right) + \mu_B \boldsymbol{S} \cdot \boldsymbol{g} \cdot \boldsymbol{B} + \boldsymbol{S} \cdot \boldsymbol{D} \cdot \boldsymbol{S} \tag{3.1}$$

- $\boldsymbol{g}$ is the g-tensor, which describes the coupling between the electronic spin system and a constant external magnetic field and is therefore an anisotropic extension of the Zeeman effect
- $\boldsymbol{A}_N$ is the hyperfine tensor of rank 2 describing the coupling between the electronic spin S and the nuclear spin I_N of nucleus N
- $\boldsymbol{D}$ is the Zero-Field Splitting tensor and only present for high spin systems ($S > \frac{1}{2}$), representing the electronic spin-spin interactions within the system.

Each of these tensor properties consists of multiple contributions and often linear response theory is needed to calculate them from *ab initio* methods.

3.1 Calculation of EPR Properties

In this first part the different contributions to the various tensors are given from an *ab initio* point of view. The focus lies at the g-tensor, since it has a prominent presence in the EPR related papers included in this work.

3.1.1 g-tensor Calculation

Following the structure of the effective spin Hamiltonian (Eqn. 3.1), the g-tensor is defined as a second order property[1]

$$g_{rs} = \frac{2}{\alpha} \frac{\partial^2}{\partial B_r \partial S_s} \left\langle \Psi \right| \hat{H} \left| \Psi \right\rangle \Big|_{\boldsymbol{B}=0=\boldsymbol{S}} \tag{3.2}$$

which has the same structure as Eqn. 2.34 and uses the full Hamiltonian $\hat{H}$ defined in Eqn. 2.22. The indices r and s represent general Cartesian coordinates. The ground state Ψ is an explicit function of the external magnetic field $\boldsymbol{B}$ and double perturbation theory is applied to evaluate the second order derivative. Using the Hellmann-Feynman theorem for Eqn. 3.2, one gets to the following perturbation series

$$\begin{aligned} g_{rs} = & \frac{2}{\alpha} \left[\left\langle \Psi^{(0)} \right| \frac{\partial^2 \hat{H}}{\partial B_r \partial S_s} \Big|_{\boldsymbol{B}=\boldsymbol{0}=\boldsymbol{S}} \left| \Psi^{(0)} \right\rangle \right. \\ & \left. + \left\langle \Psi^{(1)}_{B_r} \right| \frac{\partial \hat{H}}{\partial S_s} \Big|_{\boldsymbol{S}=\boldsymbol{0}} \left| \Psi^{(0)} \right\rangle \Big|_{\boldsymbol{B}=\boldsymbol{0}} + \left\langle \Psi^{(0)} \right| \frac{\partial \hat{H}}{\partial S_s} \Big|_{\boldsymbol{S}=\boldsymbol{0}} \left| \Psi^{(1)}_{B_r} \right\rangle \Big|_{\boldsymbol{B}=\boldsymbol{0}} \right] \end{aligned} \tag{3.3}$$

In the evaluation of the matrix elements of the derivatives of the Hamiltonian with respect to the magnetic field and spin projection, the spin-field reduction procedure[89] is used to handle the derivative with respect to the spin operator $\hat{S}_s$. In this approach, the spin quantization axis is assumed to coincide with each component of the spin operator in turn.

The Hamiltonian terms that contribute to Eqn. 3.3 are selected from the full Hamiltonian expression outlined in Chapter 1 (Eqn. 2.22) and can be categorized in first and second order contributions in this expression.

(i) First order terms Only terms of Hamiltonian $\hat{H}$ (Eqn. 2.22) linear in both $\boldsymbol{S}$ *and* linear in $\boldsymbol{B}$ will contribute:

[1] Note that in atomic units the Bohr magneton μ_B equals $\frac{\alpha}{2} = \frac{1}{2c}$

- the Zeeman term (Z):

$$\hat{H}_Z = \alpha \sum_i \boldsymbol{s}_i \cdot \boldsymbol{B} = \alpha \boldsymbol{S} \cdot \boldsymbol{B} \tag{3.4}$$

yielding[2]

$$g_{rs}^Z = g_e \delta_{rs} \tag{3.5}$$

- the Zeeman Kinetic Energy term:

$$\hat{H}_{ZKE} = -\frac{\alpha^3}{2} \sum_i (\boldsymbol{s}_i \cdot \boldsymbol{B}) \hat{p}_i^2 \tag{3.6}$$

yielding

$$\Delta g_{r,s}^{ZKE} = -\alpha^2 \delta_{rs} \left[\sum_{i \in \alpha} \langle \psi_i | \, \hat{p}^2 \, | \psi_i \rangle - \sum_{i \in \beta} \langle \psi_i | \, \hat{p}^2 \, | \psi_i \rangle \right] \tag{3.7}$$

where the first summation runs over all spin-up orbitals (α) and the second over the spin-down orbitals (β).

Note that the Zeeman term reduces to the free-electron value $g_e = 2.0023193$ and that both terms are isotropic (*i.e.* direction independent). [3]

(ii) Second order terms According to Eqn. 3.3 now only terms linear in $\boldsymbol{S}$ and without dependence of the magnetic field should be considered from the relativistic two-body Hamiltonian (Eqn. 2.22). These correspond to the spin-orbit interactions from Eqns. 2.30, 2.31 and 2.32.

The influence of the magnetic field is indirect by considering the ground state wavefunction $|\Psi\rangle$ as an explicit functional of the external magnetic field $\boldsymbol{B}$. This wavefunction interacts through the orbital-Zeeman interaction $\hat{H}_{OZ}$,

[2] When quantumelectrodynamical corrections are taken into account

[3] Because this trivial contribution is present for every g-tensor, the essential information lies in the deviation from it, noted as Δg.

$$\boldsymbol{g} = g_e \mathbf{1} + \Delta \boldsymbol{g} \tag{3.8}$$

In some cases, such as **Paper IV**, the notation δg is used. Depending on the application or size of this deviation, it is sometimes preferred to express Δg in *ppt, parts-per-thousand*.

appearing after minimal substitution ($\boldsymbol{\pi} \rightarrow \boldsymbol{p} + \alpha \boldsymbol{A}$) in the kinetic energy operator (Eqn. 2.23)[80]:

$$\hat{H}_{OZ} = \frac{\alpha}{2} \sum_i \boldsymbol{B} \cdot \boldsymbol{l}_i \tag{3.9}$$

It is precisely this term that perturbs the ground state $\left|\Psi^{(0)}\right\rangle$ through the one electron orbitals $\psi_\alpha^{(0)}$. The r-component of the magnetic field (B_r) acts as the perturbation parameter and following Eqn. 3.9 the perturbation operator (h_λ in Eqn. 2.44) becomes $\frac{\alpha}{2} \sum_i (\hat{l}_r)_i$. The linear response single particle orbitals to this perturbation are denoted here as $\left|\psi_{\alpha,B_r}^{(1)}\right\rangle$ and, following the coupled perturbed approach of Chapter 1, can be expressed as a linear combination of unoccupied, unperturbed single particle orbitals:

$$\left|\psi_{\alpha,B_r}^{(1)}\right\rangle = \frac{\alpha}{2} \sum_\mu U_{\alpha\mu} \left|\psi_\mu^{(0)}\right\rangle \tag{3.10}$$

The ground state wavefunction $|\Psi\rangle$ can now be constructed from the perturbed wavefunctions $|\psi_\alpha\rangle = \left|\psi_\alpha^{(0)}\right\rangle + B_r \left|\psi_{\alpha,B_r}^{(1)}\right\rangle$ (see Eqn. 2.39), resulting in a similar linear response equation

$$|\Psi\rangle = \left|\Psi^{(0)}\right\rangle + B_r \left|\Psi_{B_r}^{(1)}\right\rangle + O(B_r^2) \tag{3.11}$$

from which the linear response of the ground state wavefunction $|\Psi\rangle$ is now given by

$$\left|\Psi_{B_r}^{(1)}\right\rangle = \sum_\alpha \sum_\mu U_{\alpha\mu} \hat{c}_\mu^\dagger \hat{c}_\alpha \left|\Psi^{(0)}\right\rangle \tag{3.12}$$

in second quantization. To simplify the notation, the unperturbed single particle wavefunctions will be denoted only by their label $|\alpha\rangle$ or $|\mu\rangle$ for occupied and unoccupied levels respectively.

Using this expression in Eqn. 3.3 results in

$$g_{rs}^{OZ/SO} = \frac{2}{\alpha} \sum_{\alpha\mu} U_{\alpha\mu} \left\langle \Psi^{(0)} \right| \left. \frac{\partial \hat{H}_{SO}}{\partial S_s} \right|_{\boldsymbol{S}=0} \hat{c}_\mu^\dagger \hat{c}_\alpha \left|\Psi^{(0)}\right\rangle + c.c. \tag{3.13}$$

$$= \frac{2}{\alpha} \sum_{\alpha\mu} U_{\alpha\mu} \left\langle \alpha \right| \hat{\Gamma}^{SO} \left| \mu \right\rangle + c.c. \tag{3.14}$$

with the spin field reduced total spin-orbit operator written as in mean field $\hat{\Gamma}^{SO}$ form

$$\hat{\Gamma}^{SO} = \hat{\Gamma}^{SON} + \hat{\Gamma}^{SSO} + \hat{\Gamma}^{SOO} \tag{3.15}$$

As the SSO and SOO spin-orbit operators are two-body operators, many approximations needs to be introduced to reduce them to single-particle operators. In the most advanced method, a mean-field is derived along the same lines as applied in the evaluation of a Hartree-Fock mean field. This method is discussed more in detail in Section 3.2.

In case of a non-hybrid functional, the coefficients $U_{\alpha\mu}$ can be expressed as [50]

$$U_{\alpha\mu} = \frac{\alpha}{2} \frac{\langle \mu | \hat{l}_r | \alpha \rangle}{\epsilon_\mu - \epsilon_\alpha} \tag{3.16}$$

This results in a sum-over-state (SOS) expression, related to second order perturbation theory

$$\Delta g_{rs}^{OZ/SOC} = \sum_\alpha \sum_\mu \left[\frac{\langle \alpha | \hat{l}_r | \mu \rangle \langle \mu | \hat{\Gamma}^{SO} | \alpha \rangle}{\epsilon_\mu - \epsilon_\alpha} + c.c. \right] \tag{3.17}$$

Additionally, some gauge-correction contributions for $\Delta \boldsymbol{g}$ are needed to take into account the inconsistency between the atomic orbitals in the expansion of the KS orbitals and the gauge origin of the vector potential $\boldsymbol{A}$. They are particularly present in the diamagnetic terms, obtained by applying the minimal substitution in the two-body spin-orbit terms. Multiple approaches exist to circumvent these issues, such as using the Gauge-Including-Atomic-Orbitals (GIAO), individual gauge origin for localized orbitals (IGLO), continuous set of gauge transformations (CSGT)[90].

Summary Multiple contributions should be included to accurately determine the g-tensor.

$$\boldsymbol{g} = g_e \mathbf{1} + \Delta g^{ZKE} \mathbf{1} + \Delta \boldsymbol{g}^{OZ/SOC} + \Delta \boldsymbol{g}^{gauge} \tag{3.18}$$

3.1.2 Hyperfine Tensor Calculation

The hyperfine tensor of nucleus N describes the interaction between the spin of the nucleus and the spin of the electron.

$$\hat{H}_S^N = \boldsymbol{S} \cdot \boldsymbol{A_N} \cdot \boldsymbol{I}_N \tag{3.19}$$

To obtain this, a generalization of Eqn. 2.24 is needed which doesn't focus on the electron-electron interactions, but on the nucleus-electron interactions.

The hyperfine tensor of nucleus N can than be defined as

$$A_{N,rs} = \frac{\partial^2}{\partial I_{N,r} \partial S_s} \langle \Psi | \hat{H} | \Psi \rangle \tag{3.20}$$

Similar to the g-tensor (Eqn. 3.3), several parts can be distinguished.

(i) First order term Most often, only the first order terms are taken into account, especially for organic molecules (*e.g.* in **Paper VII** and Refs. [89, 91, 92, 93] The isotropic hyperfine coupling is caused by the Fermi contact interaction of nucleus N[89]:

$$\hat{H}_N^{FC} = \frac{4\pi}{3} \alpha^2 g_e g_N \mu_N \sum_i \delta(\boldsymbol{r}_{iN}) \boldsymbol{I}_N \cdot \boldsymbol{s}_i \tag{3.21}$$

where g_N is the nuclear g-factor and μ_N the nuclear magnetic momentum. This leads to the isotropic contribution of the hyperfine interaction

$$A_N^{iso} = \frac{4\pi}{3} \alpha^2 g_e g_N \mu_N \frac{1}{\langle S_z \rangle} \left(\sum_{i \in \alpha} \langle \psi_i | \, \delta(r_N) \, | \psi_i \rangle - \sum_{i \in \beta} \langle \psi_i | \, \delta(r_N) \, | \psi_i \rangle \right) \tag{3.22}$$

in which μ_N is the nuclear magneton and g_N the nuclear g-value. Secondly, the spin-dipole interaction also contributes to the hyperfine [89]

$$\hat{H}_N^{SD} = \frac{1}{2} \alpha^2 g_e g_N \mu_N \sum_i \frac{3(\boldsymbol{r}_{iN} \cdot \boldsymbol{I}_N)(\boldsymbol{r}_{iN} \cdot \boldsymbol{s}_i) - \boldsymbol{I}_N \cdot \boldsymbol{s}_i r_{iN}^2}{r_{iN}^5} \tag{3.23}$$

$$A_{N,rs}^{dip} = \frac{1}{2} \alpha^2 g_e g_N \mu_N \frac{1}{\langle S_z \rangle} \sum_i \langle \psi_i | \, \frac{1}{r_N^3} \delta_{rs} - 3 \frac{r_{N,r} r_{N,s}}{r_N^5} \, | \psi_i \rangle \tag{3.24}$$

Both contributions can be calculated with knowledge of only the Kohn-Sham orbitals and no additional linear response equations need to be solved. Due to the Fermi-contact term, an all-electron treatment is necessary since pseudopotentials don't contain information about the (spin-)density at the nucleus.

(ii) Second order term Also higher order terms could be included in a similar way as for the g-tensor[94, 95, 96]. In practise, the wavefunction $|\Psi\rangle$ is now perturbed by one of the components of the nuclear spin $\boldsymbol{I}_N$, which is turned on adiabatically with a prefactor λ. The interaction Hamiltonian is now the orbital-nucleus interaction given as[95]

$$\hat{H}_{LI} = \frac{\alpha}{2}\mu_B \sum_N g_N \sum_i \frac{\boldsymbol{l}^A \cdot \boldsymbol{I_N}}{r_{iN}^3} \tag{3.25}$$

This results in perturbed wavefunctions $\left|\Psi_{I_r}^{(1)}\right\rangle$ to be calculated via linear response and for which the spin-orbit matrix elements with the unperturbed wavefunction should be calculated. Again, in the case of pure density functionals, a SOS formulation can be found [96]

$$A_{rs}^{LI/SOC} = \frac{1}{4\langle S_z\rangle}\alpha^4 g_e g_N \sum_h \sum_p \left[\frac{\langle h|\,\hat{l_r}/r_N^3\,|p\rangle\,\langle p|\,\Gamma^{SO}\,|h\rangle}{\epsilon_a - \epsilon_i} + c.c.\right] \tag{3.26}$$

in which again the spin-orbit operator is expressed as a mean-field operator, similar as for the g-tensor.

3.1.3 ZFS Tensor

For systems with spin equal or larger than 1, an energy splitting in absence of an external magnetic field could occur due to the spin-spin interactions of the electrons. This is called the Zero-Field Splitting (ZFS) and is also a tensor property in the effective spin Hamiltonian

$$\hat{H}_S = \boldsymbol{S} \cdot \boldsymbol{D} \cdot \boldsymbol{S} \tag{3.27}$$

The explicit definition can then be written as

$$D_{rs} = \frac{\partial^2}{\partial S_r \partial S_s}\,\langle\Psi|\,\hat{H}_{full}\,|\Psi\rangle \tag{3.28}$$

Again the same partitions as above can be introduced

(i) First order term These contributions are similar to those of the hyperfine interaction, but now the electron spin is used twice. Due to the

Pauli exclusion principle for fermions, the Fermi contact interaction does not contribute, leaving only the dipole interaction. [18, 97, 98, 89]

$$D_{rs} = \frac{1}{2}\frac{\alpha^2}{S(2S-1)} \left\langle \Psi^{(0)} \right| \sum_{i \neq j} \frac{r_{ij}^2 \delta_{rs} - 3\left(r_{ij}\right)_r \left(r_{ij}\right)_s}{r_{ij}^5} \times \left\{ 2 s_{zi} s_{zj} - s_{xi} s_{xj} - s_{yi} s_{yj} \right\} \left| \Psi^{(0)} \right\rangle \tag{3.29}$$

(ii) Second order terms The wavefunction $|\Psi\rangle$ is now perturbed by the spin-orbit interaction itself, which requires again an external adiabatic parameter λ.[99, 100] Differently from the linear response in the case of the g-tensor and hyperfine tensor, now the perturbation Hamiltonian depends on the spin, resulting in a perturbed single particle wavefunction $\left|\psi_i^{\tau(1)}\right\rangle$ which contains a contribution of its own spin τ *and* a contribution from the opposite spin τ'[100]

$$\left|\psi_\alpha^{\tau(1)}\right\rangle = \sum_{\mu \in \tau} U_{\alpha\mu}^{\tau} \left|\psi_\mu^{\tau(0)}\right\rangle + \sum_{\mu \in \tau'} U_{\alpha\mu}^{\tau'} \left|\psi_\mu^{\tau'(0)}\right\rangle \tag{3.30}$$

For this reason, the perturbed state $\left|\Psi_{h_r^{SOC}}^{(1)}\right\rangle$ is not the same spin state as the unperturbed ground state wavefunction $\left|\Psi^{(0)}\right\rangle$. Therefore, in a SOS represtation, the ZFS can be written as three contributions, and — as derived in Ref. [101] and verified in Ref. [72] — those three contributions have different prefactors. The three contributions differ by means of the intermediate state, which is either the same spin ($\boldsymbol{D}^{(0)}$), higher spin ($\boldsymbol{D}^{(+1)}$) or lower spin ($\boldsymbol{D}^{(-1)}$).

$$D_{rs}^{(0)} = -\frac{1}{S^2} \sum_b \Delta_b^{-1} \left\langle \Psi_S^{(0)} \right| \sum_i \Gamma_{i,r}^{SO} \left| \Psi_S^{(1)} \right\rangle \left\langle \Psi_S^{(1)} \right| \sum_i \Gamma_{i,s}^{SO} \left| \Psi_S^{(0)} \right\rangle \tag{3.31}$$

$$D_{rs}^{(+1)} = \frac{-1}{(S+1)(2S+1)} \sum_b \Delta_b^{-1} \left\langle \Psi_S^{(0)} \right| \sum_i \Gamma_{i,r}^{SO} \left| \Psi_{S+1}^{(1)} \right\rangle \left\langle \Psi_{S+1}^{(1)} \right| \sum_i \Gamma_{i,s}^{SO} \left| \Psi_S^{(0)} \right\rangle \tag{3.32}$$

$$D_{rs}^{(-1)} = \frac{-1}{S(2S-1)} \sum_b \Delta_b^{-1} \left\langle \Psi_S^{(0)} \right| \sum_i \Gamma_{i,r}^{SO} \left| \Psi_{S-1}^{(1)} \right\rangle \left\langle \Psi_{S-1}^{(1)} \right| \sum_i \Gamma_{i,s}^{SO} \left| \Psi_S^{(0)} \right\rangle \tag{3.33}$$

With $\sum_b$ the sum over all excited states b and $\Delta_b = E^{(0)} - E^{(1)}$.

3.2 Spin-Orbit Coupling

Spin-orbit coupling contributes largely to the different EPR properties defined above. In **Paper I**, the goal was to improve the spin-orbit contribution implemented in the CP2K program, in order to improve the g-tensor for high-spin systems. For this we focussed on the calculation of the spin-other-orbit interaction in particular, since the approach of Pickard and Mauri showed to underestimate this contribution (see **Paper I**), especially when compared to the approach used by Neese [50].

In **Paper I** we applied the new model for spin-orbit coupling for g-tensor calculations. However, this operator could be used to calculate the hyperfine tensor as well, however the largest improvement is expected for the ZFS. For the latter both the matrix elements as the perturbed wavefunction are influenced by the spin-orbit operator.

3.2.1 Spin-Orbit Mean-Field for the Two-Electron SO Terms

In the first Chapter, a differentiation is made between the various types of spin-orbit interactions. The spin-orbit-nucleus interaction $\hat{H}_{SON}$ (Eqn. 2.30) is a one-body interaction and poses no particular problem in the evaluation of the matrix element $\langle p| \hat{\Gamma}^{SO} |h\rangle$. The two other terms, the spin-same-orbit $\hat{H}_{SSO}$ (Eqn. 2.31) and spin-other-orbit $\hat{H}_{SOO}$ (Eqn. 2.32), are two-particle interactions, making the further analytical elaboration more complex. In the spin-orbit mean-field (SOMF) method[49] the key ingredient is the introduction of a mean field $\hat{\Gamma}^{SO}$, defined following the lines applied in interacting many-particle problems:

$$\langle \alpha| \hat{\Gamma}^{SO} |\gamma\rangle = \sum_{\beta \in occ} \langle \alpha\beta| \hat{V}^{SO} |\gamma\beta\rangle_{as} \tag{3.34}$$

We respect the following notation: small Greek letters are associated to spin-orbitals ($\alpha \equiv (a, m_a)$), while the spatial orbitals are denoted by the corresponding Latin letter.

Two-body interactions can be best treated within the second quantization formalism:

$$\frac{1}{2}\sum_{ij} \hat{H}_{ij} \rightarrow \frac{1}{4}\sum_{\alpha\beta\gamma\delta} \langle \alpha\beta| V_{12} |\gamma\delta\rangle_{as} \hat{c}^{\dagger}_{\alpha}\hat{c}^{\dagger}_{\beta}\hat{c}_{\delta}\hat{c}_{\gamma} \tag{3.35}$$

with the antisymmetric matrix element $\langle \alpha\beta| V_{12} |\gamma\delta\rangle_{as} = \langle \alpha\beta| V_{12} |\gamma\delta\rangle - \langle \alpha\beta| V_{12} |\delta\gamma\rangle$.

The two-body interaction should first be made symmetric with the interchange of i and j. The spin-same and spin-other-orbit operators (Eqn. 2.31 and Eqn. 2.32 respectively) are therefore rewritten in symmetric form:

$$V_{ij}^{SSO} = -\frac{g'}{4}\left(\boldsymbol{s}_i \cdot \boldsymbol{L}_i + \boldsymbol{s}_j \cdot \boldsymbol{L}_j\right) \tag{3.36}$$

$$V_{ij}^{SOO} = -\left(\boldsymbol{s}_i \cdot \boldsymbol{L}_j + \boldsymbol{s}_j \cdot \boldsymbol{L}_i\right) \tag{3.37}$$

with the pseudo-orbital momentum operator $\hat{L}_1$ equivalent to $-2g^{SOC}(1,,2)$ from Ref. [50].

$$\boldsymbol{L}_1 = \frac{\alpha^2}{r_{12}^3}\left(\boldsymbol{r}_{12} \times \boldsymbol{p}_1\right) \tag{3.38}$$

Note that some matrix elements of $\boldsymbol{L}_1$ show some particular properties, which are useful in the further elaboration:

$$\langle ab|\, \boldsymbol{L}_1\, |cd\rangle = -\langle cb|\, \boldsymbol{L}_1\, |ad\rangle \tag{3.39}$$

$$= +\langle ad|\, \boldsymbol{L}_1\, |cb\rangle \tag{3.40}$$

such that $\langle ab|\, \boldsymbol{L}_1\, |ad\rangle = 0$.

Just like in Hartree-Fock, the mean-field concept, expressed in Eqn. 3.34, implies that the non-interacting wavefunction (in our case the Kohn-Sham (KS) Slater determinant) is a good approximation for the true wavefunction. The single-particle states in the diverse matrix elements may be regarded as the KS orbitals.

In the following we will derive the mean-field for both SSO and SOO operators, which can be used in the $\Delta\boldsymbol{g}^{OZ/SOC}$, $\Delta\boldsymbol{A}^{LI/SOC}$ and second order terms to $\boldsymbol{D}$.

I. Spin-Same-Orbit

The two separate matrix elements of V_{12}^{SSO}, required to deduce the spin-orbit mean-field operator $\hat{\Gamma}^{SSO}$ are given by

$$\langle h\alpha|\, V_{12}^{SSO}\, |p\alpha\rangle = -\frac{g'}{4}\Big[\langle m_h|\, \boldsymbol{s}\, |m_p\rangle \cdot \langle ha|\, \boldsymbol{L}_1\, |pa\rangle + \langle m_a|\, \boldsymbol{s}\, |m_a\rangle \cdot \langle ha|\, \boldsymbol{L}_2\, |pa\rangle\, \delta_{m_{s_p} m_{s_a}}\Big] \tag{3.41}$$

$$= -\frac{g'}{4}\langle m_h|\, \boldsymbol{s}\, |m_p\rangle \cdot \langle ha|\, \boldsymbol{L}_1\, |pa\rangle \tag{3.42}$$

since $\langle ha|\, \boldsymbol{L}_2\, |pa\rangle = \langle ah|\, \boldsymbol{L}_1\, |ap\rangle = 0$. Similar we get following expression for the exchange part

$$\begin{aligned}\langle h\alpha|\, V_{12}^{SSO}\, |\alpha p\rangle = -\frac{g'}{4}\big[&\langle m_h|\, \boldsymbol{s}\, |m_a\rangle \cdot \langle ha|\, \boldsymbol{L}_1\, |ap\rangle\, \delta_{m_a m_p} \\ &+ \langle m_a|\, \boldsymbol{s}\, |m_p\rangle \cdot \langle ha|\, \boldsymbol{L}_2\, |ap\rangle\, \delta_{m_a m_h}\big]\end{aligned} \tag{3.43}$$

The mean-field $\hat{\Gamma}^{SSO}$ is then easily defined as

$$\begin{aligned}\langle h|\, \hat{\Gamma}^{SSO}\, |p\rangle = &-\frac{g'}{4}\sum_{a\in occ}\langle ha|\, L_{1,z}\, |pa\rangle \\ &+\frac{g'}{8}\sum_{a\in occ}\left(\langle ha|\, L_{1,z}\, |ap\rangle + \langle ah|\, L_{1,z}\, |pa\rangle\right)\end{aligned} \tag{3.44}$$

II. Spin-Other-Orbit

A similar calculation is performed for the SOO interaction:

$$\begin{aligned}\langle h\alpha|\, V_{12}^{SOO}\, |p\alpha\rangle &= -\left[\langle m_h|\, \boldsymbol{s}\, |m_p\rangle \cdot \langle ah|\, \boldsymbol{L}_1\, |ap\rangle + \langle m_a|\, \boldsymbol{s}\, |m_a\rangle \cdot \langle ha|\, \boldsymbol{L}_1\, |pa\rangle\right] \\ &= -\langle m_a|\, \boldsymbol{s}\, |m_a\rangle \cdot \langle ha|\, \boldsymbol{L}_1\, |pa\rangle\end{aligned} \tag{3.45}$$

The exchange part is now given by

$$\begin{aligned}\langle h\alpha|\, V_{12}^{SOO}\, |\alpha p\rangle = -\big[&\langle m_h|\, \boldsymbol{s}\, |m_a\rangle \cdot \langle ah|\, \boldsymbol{L}_1\, |pa\rangle\, \delta_{m_a m_p} \\ &+ \langle m_a|\, \boldsymbol{s}\, |m_p\rangle \cdot \langle ha|\, \boldsymbol{L}_1\, |ap\rangle\, \delta_{m_a m_h}\big]\end{aligned} \tag{3.46}$$

Finally we obtain for the mean-field $\hat{\Gamma}^{SOO}$

$$\langle h|\, \hat{\Gamma}^{SOO}\, |p\rangle = \frac{1}{2}\sum_{b\in occ}\left(\langle ah|\, L_{1,z}\, |pa\rangle + \langle ha|\, L_{1,z}\, |ap\rangle\right) \tag{3.47}$$

valid for systems with total spin $\frac{1}{2}$.

Note that the exchange SOO contribution is exactly twice the exchange contribution of the SSO terms

$$\sum_{\alpha\in occ}\langle h\alpha|\, V_{12}^{SOO}\, |\alpha p\rangle = 2\sum_{\alpha\in occ}\langle h\alpha|\, V_{12}^{SSO}\, |\alpha p\rangle \tag{3.48}$$

This property agrees with the result of Neese [50] and others [49]. Finally the spin-orbit mean field $\hat{\Gamma}^{SO}$ is then obtained as

$$\langle h|\, \hat{\Gamma}^{SO}\, |p\rangle = -\frac{1}{2}\sum_{a\in occ}\langle ha|\, L_{1z}\, |pa\rangle + \frac{3}{4}\sum_{a\in occ}\left(\langle ha|\, L_{1z}\, |ap\rangle + \langle ah|\, L_{1z}\, |pa\rangle\right) \tag{3.49}$$

3.2.2 Extension to High Spin Systems

In **Paper I** an extension to high spin systems is introduced for the spin-other-orbit contribution, which is neglected in literature[49, 50]. The SOO contribution arises from the fact that the direct Coulomb term is non-vanishing due to the presence of more then one half-occupied orbitals. To include this in DFT, information of these single occupied orbitals can be found in the spin density $\rho_\uparrow - \rho_\downarrow$. Similar to above, it is the gradient of this density which is especially useful in the calculation of the spin-orbit matrix elements. For further details and derivation, see **Paper I** and its appendix.

3.2.3 Effective Potential

A second approximation which is very commonly applied, uses the fact that the gradient of a Coulombic potential has the same radial dependence (*i.e.* $\boldsymbol{r}/r^3$) as the spin-orbit coupling. The spin-orbit coupling with respect to the nucleus can indeed exactly be represented by

$$\hat{H}_{SON} = \sum_i \frac{g'\alpha^2}{4} \boldsymbol{s}_i \cdot (\boldsymbol{\nabla}_i v_{ext} \times \boldsymbol{p}_i) \tag{3.50}$$

if the external potential is caused only by the Coulombic interaction of the nuclei: $v_{ext} = -\sum_{N,i} \frac{Z_N}{|\boldsymbol{r}_i - \boldsymbol{R}_N|}$. Within DFT, the extension to include the spin-same-orbit coupling is straightforward

$$\hat{H}_{SON} + \hat{H}_{SSO} = \sum_i \frac{g'\alpha^2}{4} \boldsymbol{s}_i \cdot (\boldsymbol{\nabla}_i (v_{ext} + v_{ee} + v_{xc}) \times \boldsymbol{p}_i) \tag{3.51}$$

where v_{ee} is the Coulomb repulsion for electrons and v_{xc} is the exchange-correlation potential. This does *not* include the spin-other orbit interaction since (2.32) cannot be derived from a Coulomb-like expression. Several solutions have been suggested

(i) Neglect the SOO contribution (referred to as V_{eff}).

(ii) Replacement of the SOO contribution by the SSO part, scaled by a factor -3 [50] (referred to as $V_{eff,SOO}$). In **Paper I** we suggest using this approach in order to get more accurate results in much better correspondence to the SOMF approach. For further details, see **Paper I**.

(iii) Assumption that the SOO *describes the screening of the external field B by the induced electronic currents, as experienced by the unpaired electron* as was suggested by Pickard and Mauri [43, 89]. This allows the contribution to the g-tensor to be written as

$$\Delta g_{xy}^{SOO} = \frac{1}{S} \int B_y^{1,s}(\boldsymbol{r}) \left[\rho_\alpha - \rho_\beta\right] \mathrm{d}\boldsymbol{r} \tag{3.52}$$

in which $\boldsymbol{B}^{1,s}$ is the magnetic field induced by the electronic currents when a magnetic field with unit magnitude is applied in the x direction. (referred to as $V_{eff,PM}$).

3.2.4 Effective Nuclear Charge (Z_{eff})

The most convenient and simple approach is to consider the two-electron spin-orbit Hamiltonian terms as screening terms for the one-electron H_{SON} contribution. One could neglect those two-electron contributions and compensate for them using an effective nuclear charge $Z_{A,eff}$ or introduce a similar screening factor $\xi(r)$ [102, 80]. Therefore equation (2.30) is rewritten as

$$\hat{H}_{SO,\xi} = \sum_i \frac{g'\alpha^2}{4} \sum_A \xi(r_i) \boldsymbol{s}_i \cdot (\boldsymbol{r}_i - \boldsymbol{R}_A) \times \boldsymbol{p}_i \tag{3.53}$$

usually further approximated as

$$\hat{H}_{SON} = \sum_i \frac{g'\alpha^2}{4} \sum_A Z_{A,eff} \boldsymbol{s}_i \cdot \frac{(\boldsymbol{r}_i - \boldsymbol{R}_A) \times \boldsymbol{p}_i}{|\boldsymbol{r}_i - \boldsymbol{R}_A|^3} \tag{3.54}$$

This simple approximation is available in several packages including Gaussian and ORCA.

In **Paper I** the influence of the SOO on g-tensor for small, transition metal holding molecules is calculated. It became clear that the Pickard and Mauri approach, as implemented in CP2K and GIPAW, resulted in a SOO contribution which is few orders too small. The results are improved if a proper scaling factor is used for the exchange contribution of the SSO to include also the SOO. As a reference, SOMF calculations in ORCA were performed with similar basis set and the same functional. Also the influence of the new derived contribution is determined for high spin systems and it is shown that it is non-negligible for the high spin states.

In **Paper V** the new SOO scaled variant was used with improved result to the experimental g-values and orientations.

3.3 Defects in NaCl

Before the implementation, defect structures in NaCl solid were investigated. For this intrinsically periodic system, CP2K seems very suited due to the incorporation of dual plane wave and Gaussian type orbitals. In **Paper IV** the hyperfine, quadrupole and g-tensors of a rhodium centre in a NaCl crystal were calculated with both cluster models and periodic calculations.

This system was of interest mainly because of its resemblance with rhodium defects in AgCl, used in photographic films. The Rh^{3+} defects act as efficient and deep electron traps[103, 104, 105]. When irradiated, Rh^{2+} or Rh^{+} centres with possible vacancies are created due to electron capture. In **Paper IV** the focus lies on Rh^{2+} defects which have been detected with 0, 1 or 2 vacancy positions (denoted as $[RhCl_6]^{4-}$.*n*Vac with $n = 0, 1, 2$. The situation without vacancies is presented in Figure 3.1. The very accurate experimental data for the multiple vacancies, allows us to put EPR calculations of transition metals via DFT on the test.

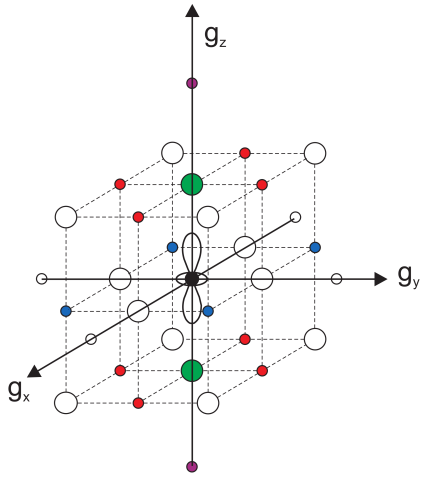

Figure 3.1: Rhodium defect in NaCl crystal, without cationic vacancies

As described above, one particular way of categorizing DFT codes is by the presence of periodic boundary conditions (PBC). If a solid state needs to be described in a DFT program without PBC, a selected number of atoms should be chosen to form the cluster model. Similar to what can be found in literature for alkali halides[106, 107], cluster models are constructed using atoms within a certain radius of the defect. The size of such a cluster was deter-

mined by the balance between accuracy and computational feasibility. With ORCA, single point calculations for clusters up to 185 atoms were possible, while for ADF only 125 atoms could be included in one calculation. Geometry optimization with these clusters were instable leading to deformed clusters or unconverged wavefunctions, leading to unrealistic Rh^{2+} environments.

Therefore, geometry optimizations were performed using PBC, by means of CP2K. These calculations don't suffer from the cluster effects described above. **Paper IV** was the first to examine the accuracy of the g-tensor implementation for transition metal systems. The computational cost was found to be very high due to the large periodic unit cell which was necessary in order to minimize the Rh-Rh interaction between periodic images.

3.4 Test Case - Sucrose

In **Paper V** the scaled SOO approach was used to calculate the g-tensor of radiation-induced radicals in solid state sucrose. In this study, Hendrik De Cooman and coworkers of the Electron Magnetic Resonance Research Group determined the g-tensor of the three dominant radicals at room temperature in this structure with very high precision. For this, ENDOR-induced EPR (EIE) was used in order to separate the EPR spectra of the different radicals. The hyperfine tensors for these radicals were subject of previous work[108, 109] where the use of DFT was very successful.

The method from **Paper I** was not yet applied for the flavoprotein radicals in Ref. [92], but rather used in new projects such as this solid state sucrose. Both the original implementation and the new spin-other-orbit correction were performed, in order to compare the two approximations. The results of the three radicals are presented in Tables V.1, V.2 and V.3 appended to **Paper V** in Part II of this dissertation, together with the experimental value for comparison. Rather than an overestimation of δg, now an underestimation is found. Overall, the size of deviation for radical T1 and T2 is smaller, while for T3 the agreement is not improved. The latter should be nuanced, since T2 and T3 are basically the same systems, only differing slightly in the conformations. A geometry optimization was performed on these structures, resulting in T2 and T3 being modelled by the same structure. Therefore it is not unexpected that the agreement with one of both radicals (T2) is much higher than for the other (T3).

Chapter 4

The Vibrational Fingerprint of Spectroscopic Properties via Molecular Dynamics

Very often only static nuclear configurations are used to calculate molecular properties. However, even at the theoretical situation of zero Kelvin, molecules always have an intrinsic vibrational energy. Experiments take place at finite temperature — very often at room temperature — and hence molecules show an even larger vibrational energy. Static calculations are inadequate to take temperature into account and Molecular Dynamics (MD) simulations are well suited to reproduce the experimental measurements.

This Chapter contains a brief introduction to vibrational spectroscopy and how this information can be obtained from Molecular Dynamics (MD). It is followed by a summary of **Paper II**, wherein vibrational spectroscopy is used to gain information about the influence of temperature on spectroscopic properties of a molecular system. This Chapter aims at demonstrating the generality of the approach, while in **Paper II** the focus lies on the excitation energy ϵ.

Vibrational spectroscopy relies on the quantization of energy of a multidimensional potential energy surface (PES), similar to the simplified case of a one dimensional harmonic oscillator. When light is absorbed or emitted by a material in the infrared region (see Figure 1.1)[1], transitions between the quantum levels of PES are measured. Close to its minimum, the multidimensional PES of a nanosystem with N nuclei can be approximated by 3N-6 independent harmonic oscillators (3N-5 for linear molecules), each of them

[1] 750 nm (Near-infrared) up to 1 mm (Far-infrared)

with a characterizing frequency. Determination of these harmonic oscillators is called a Normal Mode Analysis (NMA) and the resulting coordinates are called normal modes. This is often used to predict IR and Raman spectra, however anharmonic effects are not included in this method. In contrast, in *ab initio* MD simulations these anharmonic effects are included naturally since the full potential energy surface can be sampled.

4.1 Fluctuations and Correlation Functions

Since molecules are not rigid structures, their properties — in general denoted as A in the following — are time-dependent ($A(t)$). In most experimental setups, the measured A are averaged values over a time scale in which the geometry of the molecules is changing due to thermal motions. Therefore an observed averaged value can be written as

$$\bar{A}(t_0, \mathcal{T}) = \frac{1}{\mathcal{T}} \int_{t_0}^{t_0+\mathcal{T}} A(t)\mathrm{d}t. \tag{4.1}$$

where t_0 is the time at which the measurement is started and $\mathcal{T}$ its duration. A converged statistical average is obtained if the experiment is sufficiently long[2]

$$\langle A \rangle = \lim_{\mathcal{T}\to\infty} \frac{1}{\mathcal{T}} \int_{0}^{\mathcal{T}} A(t)\mathrm{d}t. \tag{4.2}$$

Within the assumption of ergodicity, this average over time is equivalent to the average over a statistical ensemble.

In Figure 4.1 the difference between the time-dependent signal $A(t)$, its average $\langle A \rangle$ and the static property A_0 at the equilibrium geometry is presented in the case of ethylene for an MD run at 100 K. In this illustrative example the chosen property is the first excitation energy ϵ, for which the static and averaged values are clearly different.

In general a signal $A(t)$ and its delayed signal $A(t+\tau)$ are supposed to be unrelated. However, for small values of delay τ, $A(t+\tau)$ will be close to $A(t)$ and only for larger delays the correlation will be lost. This correlation is expressed in the autocorrelation function (ACF), for property A defined as

$$\langle A(0)A(t) \rangle = \lim_{\mathcal{T}\to\infty} \int_{0}^{\mathcal{T}} A^*(\tau)A(\tau+t)\mathrm{d}\tau. \tag{4.3}$$

[2] $t_0 = 0$ is chosen here for convenience

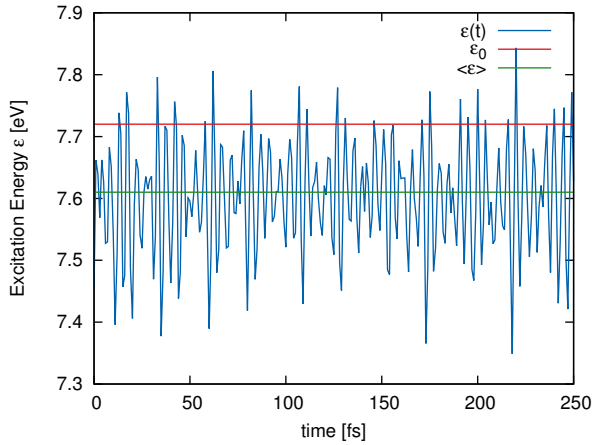

Figure 4.1: The trajectory of the first excitation energy $\epsilon(t)$ of gas phase ethylene in a limited time frame is displayed in blue, the averaged value over the MD simulation in green ($\langle\epsilon\rangle$) and the excitation energy of the optimized structure in red (ϵ_0).

which is basically the cross-correlation of signal $A(t)$ with itself ($(A \star A)(t)$), which is in turn defined as the convolution $(A^*(-\tau) * A(\tau))(t)$.

For $t = 0$, the integrandum of Eqn. 4.3 equals $|A(t)|^2$ and is positive for all t, implying a maximum for the ACF at $t = 0$. This can be proven with the Cauchy-Schwartz inequality.

4.2 Power Spectra

A Power Spectrum (PS), sometimes called spectral density, is defined as the Fourier transform of the ACF

$$I_A(\omega) = \int_{-\infty}^{+\infty} \langle A(0)A(t)\rangle \exp(-i\omega t)\mathrm{d}t. \tag{4.4}$$

The Wiener-Khintchine theorem [110, 111] uses the convolution theorem[112] to reformulate Eqn. 4.4 into a more practical formulation which avoids the explicit calculation of the ACF.

$$
\begin{aligned}
I_A(\omega) &= \int_{-\infty}^{+\infty} \langle A(0)A(\tau)\rangle \exp(-i\omega t)\mathrm{d}t \\
&= \int_{-\infty}^{+\infty} \Big(A^*(-\tau) * A(\tau)\Big)(t) \exp(-i\omega t)\mathrm{d}t
\end{aligned}
$$

$$
\begin{aligned}
I_A(\omega) &= \int_{-\infty}^{+\infty} A^*(-t) \exp(-i\omega t)\mathrm{d}t \int_{-\infty}^{+\infty} A(t) \exp(-i\omega t)\mathrm{d}t \\
&= \left[\int_{-\infty}^{+\infty} A(t) \exp(-i\omega t)\mathrm{d}t\right]^* \left[\int_{-\infty}^{+\infty} A(t) \exp(-i\omega t)\mathrm{d}t\right] \\
&= \left|\int_{-\infty}^{+\infty} A(t) \exp(-i\omega t)\mathrm{d}t\right|^2
\end{aligned} \tag{4.5}
$$

The PS can be characterized by the amplitude of the Fourier transform of the original signal $A(t)$. It is often this PS of a property which is experimentally determined, rather than the ACF itself.

Different PS are frequently used, depending on the choice of the property $A(t)$ which is tracked. If the velocities are tracked ($A(t) = v_i(t)$), the Velocity Power Spectrum (VPS) is retrieved, the PS of the dipole moment is related to the IR spectrum and the Raman spectrum can be linked to the PS of the polarizabilities.[111]

4.2.1 Velocity Power Spectra

The Velocity Power Spectrum (VPS) is obtained as the Fourier transform of the ACF of the particle velocities and can be interpreted as a vibrational density of states (VDOS).[113, 114] This VPS contains all vibrational frequencies and — in contrast to IR and Raman spectra — does not depend on any selection rules.

$$
I_{VPS}(\omega) = \sum_N \int_{-\infty}^{+\infty} \langle \boldsymbol{v}_N(0)\boldsymbol{v}_N(\tau)\rangle \exp(-i\omega t)\mathrm{d}t \tag{4.6}
$$

Here $\boldsymbol{v}_N$ represents the velocity of atom N with components $r = x, y, z$. Using Eqn. 4.5, a more practical expression can be obtained

$$
I_{VPS}(\omega) = \sum_{N,r} \left|\int_{-\infty}^{+\infty} v_{N,r}(t) \exp(-i\omega t)\mathrm{d}t\right|^2 . \tag{4.7}
$$

The VPS is therefore characterized by the sum of the Fourier transformations of every velocity component of every atom. Eqn. 4.7 makes it clear that the VPS will have a high intensity for the frequencies with which the atoms are moving, *i.e.* the frequencies of their velocities.

During MD simulations the real PES is sampled. In this way, anharmonic effects are naturally inbedded in the computed vibrational spectra when applying this approach. In **Paper II** and **Paper VII** the vibrational structure of molecular systems and a catalytic material are respectively studied using this approach.

4.2.2 Infrared Spectra

IR spectroscopy highly relies on the vibrational structure of the system. MD simulations can be used to express the IR spectrum by means of the Fourier transform of the dipole ($\boldsymbol{\mu}$) ACF with the proper prefactor.[110, 115, 111]

$$I_{IR}(\omega) = \frac{2\pi\omega\left[1-\exp(-\frac{\hbar\omega}{k_BT})\right]}{3\hbar cn}\int_{-\infty}^{+\infty}\langle\boldsymbol{\mu(0)}\cdot\boldsymbol{\mu(t)}\rangle\exp(-i\omega t)\mathrm{d}t \quad (4.8)$$

with $\hbar$ is the Planck constant, k_B the Boltzmann constant, T the temperature, c the speed of light and n the refraction index of the material. In the classical limit of $\hbar \to 0$ and using Eqn. 4.5 again, this gets reduced to [110, 111]

$$I_{IR}(\omega) \approx \frac{2\pi\omega^2}{3cnk_BT}\int_{-\infty}^{+\infty}\langle\boldsymbol{\mu(0)}\cdot\boldsymbol{\mu(t)}\rangle\exp(-i\omega t)\mathrm{d}t \quad (4.9)$$

$$\approx \frac{2\pi}{3cnk_BT}\sum_r\left|\omega\int_{-\infty}^{+\infty}\mu_r(t)\exp(-i\omega t)\mathrm{d}t\right|^2 \quad (4.10)$$

$$\approx \frac{2\pi}{3cnk_BT}\sum_r\left|\int_{-\infty}^{+\infty}\frac{\mathrm{d}\mu_r(t)}{\mathrm{d}t}\exp(-i\omega t)\mathrm{d}t\right|^2 \quad (4.11)$$

This can be transfered back to the Fourier transform of the ACF from the derivative of the dipole moment $\boldsymbol{\mu}$, however Eqn. 4.11 is more useful.

4.2.3 Raman Spectra

It is also possible to calculate the Raman spectra as a Fourier transform of the polarizability tensor ($\boldsymbol{\alpha}$) ACF.[116, 111, 110] The polarizability consists of an isotropic ($\alpha_{iso}(t) = Tr(\boldsymbol{\alpha}(t))$ and an anisotropic part ($\boldsymbol{\alpha}_{ani}(t)$),

$$\boldsymbol{\alpha}(t) = \alpha_{iso}(t)\boldsymbol{I} + \boldsymbol{\alpha}_{ani}(t). \quad (4.12)$$

The Raman cross section intensity is proportional to

$$I_{Raman}(\omega) \propto \int_{-\infty}^{+\infty} \exp(-i\omega t)\langle\alpha_{iso}(0)\alpha_{iso}(t)\rangle \mathrm{d}t + \int_{-\infty}^{+\infty} \exp(-i\omega t)\frac{2}{15}\langle Tr[\alpha_{ani}(0)\cdot\alpha_{ani}(t)]\rangle \mathrm{d}t. \quad (4.13)$$

In the published papers (**Paper II** and **Paper VII**), the focus lies on the VPS since it is widely used and rather well established. The VPS contains all vibrational frequencies, while the IR and Raman spectra only show peaks at frequencies belonging to allowed transitions. Especially in **Paper II**, this is essential since the VPS is used to extract vibrational information for *all* vibrational modes. In **Paper VII**, the VPS is employed instead of Eqn. 4.8 to avoid problems which can occur if the dipole moment $\boldsymbol{\mu}$ shows large discontinuous fluctuations which results in a large amount of noise Moreover the intensities of the IR spectrum have been shown to be barely reliable.[117]

4.3 Vibrational Coordinates

4.3.1 General Scheme

To fully understand the vibrational power spectra it is essential to assign motions to each peak in the VPS.

A first option is to define internal coordinates and calculate the corresponding spectrum. This typically results in a spectrum with limited peaks which can be used to decompose the VPS and assign a motion to each vibrational peak [118, 119]. These internal coordinates can be very simple and easy to determine, however their corresponding spectra might contain multiple peaks.[118] In contrast, there are situations in which more complex internal coordinates are chosen specifically for the system at hand, resulting in a very localized calculated spectrum. However, the method to define these coordinates is not generally applicable.[119]

Despite these previous research efforts, it would still be very desirable to have a more robust method, applicable for any system and resulting in very localized spectra for all newly defined coordinates. A set of internal coordinates for which all power spectra are perfectly isolated, showing no overlap with other peaks, are called “vibrational coordinates” in this work. Although the isolation of the power spectra of the vibrational coordinates is very complex

and not perfect in general, the method described below allowed us to decompose the power spectra of interest (see **Paper II**).

Martinez et al.[120] have proposed a theoretical framework which allows to construct, in principle, such vibrational coordinates. A matrix $\boldsymbol{I}^{\dot{x}(\omega)}$ is constructed containing velocity correlation functions.

$$\left[\boldsymbol{I}^{\dot{x}}(\omega)\right]_{ij} = \int_{-\infty}^{+\infty} \langle \dot{x}_i(0)\dot{x}_j(\tau)\rangle \exp(-i\omega t)\mathrm{d}t$$

For any linear combination of the coordinates x_i, say $A = \sum_i a_i x_i$ (*e.g.* the spectrum of an internal coordinate), the power spectrum is written as

$$I_A(\omega) = \int_{-\infty}^{+\infty} \left\langle \dot{A}(0)\dot{A}(t) \right\rangle \exp(-i\omega t)\mathrm{d}t = \boldsymbol{a}^T \cdot \boldsymbol{I}^{\dot{x}}(\omega) \cdot \boldsymbol{a}. \tag{4.14}$$

The goal is to find a linear combination A for which $I_A(\omega)$ is localized in the frequency domain. In fact, 3N independent linear combinations should be determined to maintain the number of dimensions. These new vibrational coordinates are labeled $Q_i(t)$, in vector notation this becomes $\boldsymbol{Q} = (Q_1(t), Q_2(t), \ \ldots, Q_{3N}(t))$. This new coordinate system can be transformed into the original by an inverse transformation matrix $\boldsymbol{Z}$.

$$\boldsymbol{x} = \boldsymbol{Z} \cdot \boldsymbol{Q} \tag{4.15}$$

The matrix of power spectra can be constructed for this new coordinate system

$$\boldsymbol{I}^{\dot{q}}_{kl}(\omega) = \int_{-\infty}^{+\infty} \left\langle \dot{Q}_k(0)\dot{Q}_l(\tau) \right\rangle \exp(-i\omega t)\mathrm{d}t \tag{4.16}$$

Martinez et al.[120] defined a cost function $\Omega^{(n)}$

$$\Omega^{(n)} = \sum_k \left(\frac{\beta}{2\pi} \int_{-\infty}^{+\infty} |\omega|^{2n} I^{\dot{q}}_{kk}(\omega)\mathrm{d}\omega - \left(\frac{\beta}{2\pi} \int_{-\infty}^{+\infty} |\omega|^{n} I^{\dot{q}}_{kk}(\omega)\mathrm{d}\omega \right)^2 \right) \tag{4.17}$$

$$\Omega^{(n)} = \sum_k \left(\left\langle \omega^{2n} \right\rangle_k - \left\langle \omega^n \right\rangle_k^2 \right) \tag{4.18}$$

in which $\beta = 1/k_B T$ and $I^{\dot{Q}}_{kk}(\omega)$ is the power spectrum for the coordinate set $\boldsymbol{Q}$, n is a non-zero integer which is free of choice, but restricts the physical interpretation and practical use of the method.

It can be shown that the first part of Eqn. 4.17 is independent of the transformation matrix $\boldsymbol{Z}$ and the minimization of the cost function results in maximizing the second part. This corresponds with solving a generalized eigenvalue problem with following form.

$$\boldsymbol{K}_{\dot{x}}^{(n)} \cdot \boldsymbol{Z} = \boldsymbol{K}_{\dot{x}}^{(0)} \cdot \boldsymbol{Z} \cdot \boldsymbol{\Lambda} \tag{4.19}$$

$$\boldsymbol{K}_{\dot{x}}^{(m)} = \frac{\beta}{2\pi} \int_{-\infty}^{+\infty} |\omega|^m \, I_{kk}^{\dot{x}}(\omega) \mathrm{d}\omega \tag{4.20}$$

The method employed in **Paper II** to find such vibrational modes relies on these principles, but is better known as the Principal Component Analysis (PCA) and is described in the following section.

4.3.2 Principal Component Analysis

A Principal Component Analysis (PCA) is a statistical procedure to find variables, which are uncorrelated, as a linear transformation of a set of correlated variables. The uncorrelated variables are called the *principal components* of the dataset. This technique is often used to find patterns in systems with high dimensionality for which graphical representation is difficult or impossible.[31] A typical characteristic of PCA is that only a few principal components are sufficient to describe the main variations. However, in **Paper II** we used all principal components since they can be linked to vibrational coordinates (see below). Therefore we will use the notation Q_i as principal component in what follows.

Mostly, for the analysis of MD simulations via PCA, a selection of atomic positions is used as correlated variables. In **Paper II** this approach is followed.

In order to find the principal components, the covariance matrix $\boldsymbol{C}$ should be diagonalized. Each element of the covariance matrix is defined as the covariance between two different coordinates x_i and x_j.

$$C_{ij} = cov\Big(x_i(t), x_j(t)\Big) = \left\langle \Big(x_i(t) - \big\langle x_i(t) \big\rangle\Big)\Big(x_j(t) - \big\langle x_j(t) \big\rangle\Big) \right\rangle \tag{4.21}$$

The eigenvectors of this matrix are the principal components Q_k and correspond with an eigenvalue λ_k.

$$\boldsymbol{C} = \boldsymbol{Q} \cdot \boldsymbol{D} \cdot \boldsymbol{Q}^T \tag{4.22}$$

Here the diagonal matrix $\boldsymbol{D} = diag\big(\lambda_1, \lambda_2, \ldots, \lambda_{3N}\big)$ contains the eigenvalues λ_i and $\boldsymbol{Q}$ is a matrix for which the rows are the eigenvectors Q_i, called the principal components.

Martinez et al.[120] have shown in the case of $n = -2$, solving Eqn. 4.19 is equivalent to performing PCA of the positions. This means that PCA minimizes the cost function $\Omega^{(n)}$ resulting — in principle — in coordinates for which the PS $I_Q(\omega)$ is as localized as possible. In practice, this holds for low frequency modes for which these PS indeed result in isolated peaks in the frequency domain. For those modes with high frequency, the PS are composed of multiple peaks which are reoccuring for different modes, as schematically shown in Figure 4.2.

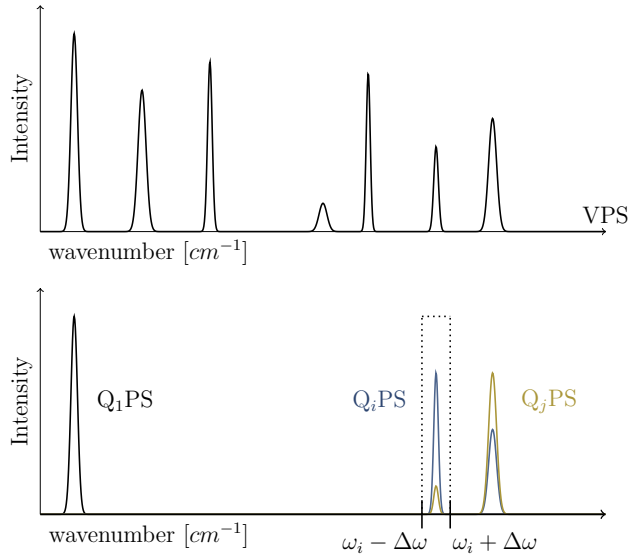

Figure 4.2: Generic scheme of a VPS (top panel) and its decomposition (bottom panel), presented by different colors and a Fourier Filter at ω_i indicated with dotted lines. For the low frequency modes (Q_1PS), often a very suitable coordinate is found, while for higher frequencies, mixing occurs (Q_iPS and Q_jPS).

Mathematically a cost function is minimized in order to localize the PS of the new coordinates. The lack of finding such modes for high frequencies, indicates that some conditions are not met or the cost function is insufficient. The calculated correlation between two such coordinates ($cov(Q_i, Q_j)$) is zero, as required by the PCA analysis. Indeed, this corresponds with an off-diagonal element of the diagonal matrix $\boldsymbol{D}$.

$$D_{ij} = \int Q_i(\tau) Q_j(\tau) \mathrm{d}\tau \tag{4.23}$$

which is very much related to the overlap in Fourier space, according to

Parseval's theorem[121] and assuming real-valued position values Q_i

$$D_{ij} = \int Q_i^*(\tau) Q_j(\tau) \mathrm{d}\tau \tag{4.24}$$

$$= \int \tilde{Q}_i^*(\omega) \tilde{Q}_j(\omega) \mathrm{d}\omega \tag{4.25}$$

where $\tilde{Q}_i(\omega)$ is the Fourier transform of $Q_i(t)$.

This indicates that, if the correlation between two coordinates Q_i is zero, their overlap in Fourier domain should be zero as well. From Eqn. 4.25 and the observation of possible overlap in the I_{Q_i} and I_{Q_j} PS, it becomes clear the overlap in PS can be nonzero for two signals which don't correlate. In a visual representation of the PS, only the magnitude and not the phase of $\tilde{Q}_i$ and $\tilde{Q}_j$ is taken into account, while in the correlation (Eqn. 4.25) the phase can be a determining factor.

In order to find vibrational coordinates which have no overlap of their PS, PCA clearly is not sufficient. To solve this issue, four adapted schemes are here suggested to go beyond the standard PCA of the coordinates.

(i) Using a different n value in Eqn. 4.17 leads to a different cost function. As suggested in Ref. [120], $n = 2$ would result in a scheme equivalent to Normal Mode Analysis (NMA). This was employed in the preparation period of **Paper II**, however, in contrast to $n = -2$, the localization holds for high frequency but is not present at low frequencies.

(ii) The overlap in the Fourier domain (Eqn. 4.25) could be calculated over a selected region $\omega_i - \Delta\omega$ to $\omega_i + \Delta\omega$ (indicated in the bottom panel in Figure 4.2), where ω_i is the frequency of one of the multiple peaks in the PS of Q_i. Performing a PCA on the new correlations result in the desired behavior of the new coordinates (*i.e.* very localized in Fourier domain), however the method is not (yet) generalized. Such a generalization becomes cumbersome if the spectra get more complicated — *e.g.* for larger systems — and other techniques to refine the spectrum could be appropriate.

(iii) Performing a PCA for a selected set of atoms, *e.g.* all atoms from the backbone of the molecule, neglecting the substituents, or treating every substituent seperately. Again the problem lies in the generalization, since such an approach needs chemical intuition in order to divide the molecular structure in relevant structures.

(iv) Using a Fourier filter, placed over the peak of interest at ω. An inverse Fourier transform results in a full trajectory in which the motion corresponding to ω is by far the most dominant. However, the actual coordinate is often mixed and a clear definition remains impossible.

For **Paper II**, it was sufficient to use PCA and the Fourier filtering method, mentioned above, to draw conclusions. Further developments are needed to obtain a general approach that unravels the vibrational fingerprint of realistic systems using MD simulations.

4.4 Electronic Excited State Power Spectrum

In **Paper II** the main interest was to find which geometrical changes cause the difference between an averaged excitation energy $\langle\epsilon\rangle$ and the excitation energy at equilibrium geometry ϵ_0. This effect was observed in multiple research domains dealing with this topic, such as modeling of dyes[26] or intermediate compounds formed during a catalytic process.[25] **Paper II** uses the same setup: first an MD simulation generates a trajectory of geometries, for which subsequently the excitation energy at several snapshots is calculated. The data is thoroughly analyzed in order to assign motions to significant changes in ϵ. For this purpose, the electronic excitation energy power spectrum (ϵPS) is introduced in order to track the changes in excitation energy ϵ during the MD simulation. It is analog to the IR and Raman spectrum defined above, in which the change in dipole moment $\boldsymbol{\mu}$ and change in polarizability $\boldsymbol{\alpha}$ is tracked.

4.4.1 Problem Setting

When a property A is averaged over an MD run, the result is often different from the value at the equilibrium geometry, as described in Section 4.1 and shown in Figure 4.1. In order to explain what is causing this difference, the MD simulations should be analyzed simultaneously with the time-dependent property $A(t)$. In **Paper II** this is done using power spectra and the property which is investigated is the excitation energy $\epsilon(t)$. The excitation energy was calculated for snapshots taken every 10 MD steps, at a TD-DFT level of theory. For the created signal $\epsilon(t)$, the ϵPS is introduced:

$$I_{\epsilon PS} = \int \langle\epsilon(0)\epsilon(t)\rangle \exp(-i\omega t)\mathrm{d}t = \left|\int \epsilon(t)\exp(-i\omega t)\mathrm{d}t\right|^2 \tag{4.26}$$

Since the VPS is linked to vibrational modes of the system, frequencies reoccurring in the ϵPS are essential to understand which motions are influencing the excitation energy.

This power spectrum consists of high intensity peaks at frequencies related to a certain molecular motion. In general, we showed in **Paper II** that three types of motions can be found:

- Inactive motions: no corresponding peak is found
- Linear active motions: at ω_{mode} a peak occurs in ϵPS
- Quadratic active motions: at $2\omega_{mode}$ a peak occurs in ϵPS

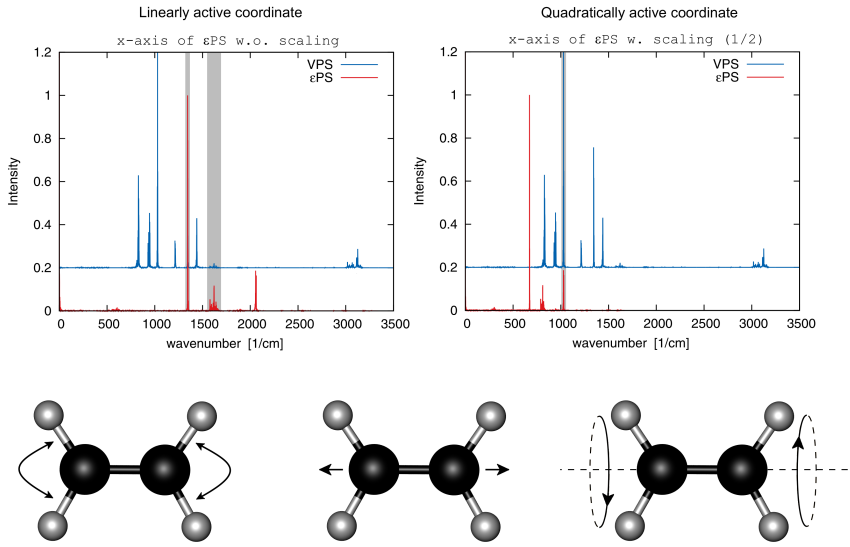

Figure 4.3: Linear and quadratic correspondence between ϵPS and VPS. The selected case study is ethylene. Figures are used from **Paper II**. At the bottom, the corresponding motions are visualized: at left the symmetrical CH_2 scissor mode, in the centre the C–C stretch and at right thee torsion mode.

In the top panels of Figure 4.3 the comparison between the ϵPS and VPS is shown for ethylene at 600K. The top left panel compares both PS without any scaling of the frequency axis, resulting in two peaks, perfectly aligned as indicated with the grey bars.[3] These frequencies correspond to a symmetrical

[3]The peak around 1600 cm^{-1} was further examined and exactly the same envelope is found in the VPS.

scissor motion (Figure 4.3, bottom left) and a carbon-carbon stretch (Figure 4.3, bottom center), respectively. The excitation energy for these motions depends linearly on the vibrational coordinate.

Clearly, slightly above 2000 cm^{-1}, one peak is present in the ϵPS which could not be explained by the direct comparison of both PS. However, if we assume a quadratically dependent motion, *i.e.* $\epsilon \propto Q_i^2$, the frequency at which ϵ is changing will be twice as large as the frequency of the vibrational coordinate Q_i. Therefore, it is useful to scale the frequency scale of ϵPS by a factor $1/2$, as shown in the top right panel in Figure 4.3. Now the agreement is perfect for a mode at $\sim$1000 cm^{-1}, corresponding to the torsion along the carbon-carbon axis (Figure 4.3, bottom right).

A schematic overview of the proposed method is given in Figure 4.4. Note that in the expansion of ϵ in function of the coordinates Q_i, another term is occurring, corresponding with mixing modes. The intensities of these contributions are found to be very low in the ϵPS and this is therefore not further examined.

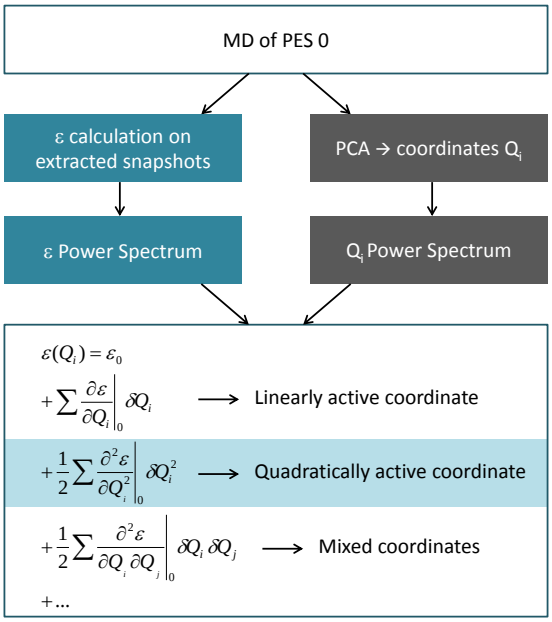

Figure 4.4: Flow scheme for identification of the dominant internal modes responsible for changes in ϵ.

In **Paper II**, four molecules are investigated in detail to validate the proposed method: ethylene, biphenyl, hexamethylbenzene and ethyl orange (see Fig-

ure 4.5). Multiple excited states are taken into account, each leading to a partially different ϵPS and showing the method is more widely applicable. This gives us information about the multiple PES and their differences. The influence of temperature was also investigated, resulting in the scanning of multiple minima in the case of biphenyl, which is impossible when using a NMA based method. For further details, see **Paper II**.

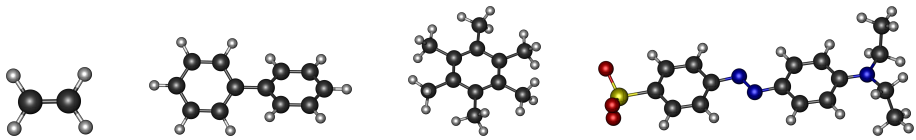

(a) (b) (c) (d)

Figure 4.5: Four molecules investigated in **Paper II**: (a) ethylene, (b) biphenyl, (c) hexamethylbenzene and (d) ethyl orange.

4.4.2 Tracking the Same Transition

When using this procedure for excitation energies, one should be careful and make sure to track the same transition during the MD run. There is no guarantee the first excited state corresponds ith the same orbital transition during the whole length of the MD simulation. For the three test cases in **Paper II** this was not a problem since the first and second excitation energy are well separated.

However, in the case of ethyl orange the difference $\epsilon_1 - \epsilon_2$ is small and the different excited states can cross along the MD trajectory. This results in a different order of the excitations. Transitions corresponding mostly from the HOMO $\rightarrow$ LUMO transition (orbital 88 $\rightarrow$ orbital 89 correspond to an oscillator strength larger than 0.60) have a high oscillator strength and a smaller contribution of the HOMO-1 $\rightarrow$ LUMO transition (87 $\rightarrow$ 89) is in phase. Systematically, the smaller oscillator strength corresponds to the transition dominated by the HOMO-1 $\rightarrow$ LUMO in antiphase with the HOMO $\rightarrow$ LUMO transition. For this reason, it is advised to track the corresponding transitions and hence sorting all excitation energies according to their oscillator strength f (f-sorted) rather then sort them through the excitation energy ϵ (ϵ-sorted).

For the ϵ-sorted trajectories, $\epsilon_1(t)$ and $\epsilon_2(t)$ will never cross, while $f_1(t)$ and $f_2(t)$ are constantly switching. The same information for all datapoints is plotted in a scattering plot in Figure 4.6a,b where we can see a less dense

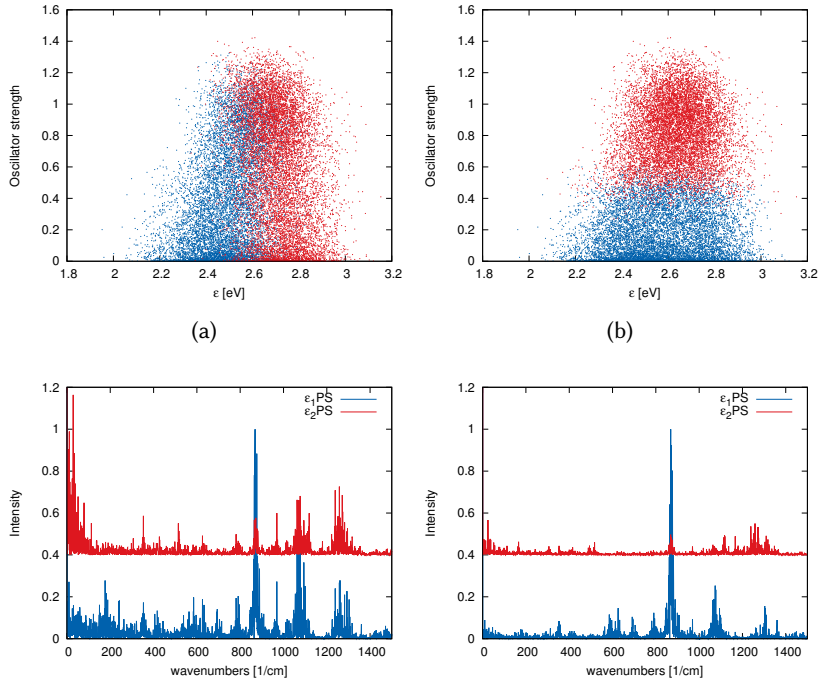

Figure 4.6: Differences between an ϵ-sorted trajectory (a) and a f-sorted one (b) and the consequence regarding the ϵPS in (c) and (d) respectively.

region for $f \approx 0.5$. This indicates that sorting according to f-values will result in two trajectories each corresponding with its own type of transition (HOMO $\rightarrow$ LUMO or HOMO-1 $\rightarrow$ LUMO).

On Figure 4.6 the influence of the sorting methods on the ϵPS becomes clear. The noise on the ϵPS with $f_1 < f_2$ is much smaller. One could suggest to construct an $\langle\epsilon\rangle$PS with an average value taken over ϵ_1 and ϵ_2, since that is the actual value tracked during an experimental observation. This however does not result in clearer spectra.

For other properties A than the excitation energy, this type of problem will not occur if A is uniquely defined. This could require a more specific definition of the property, in order to find a unique signal to analyse. This results in an increase of the PS resolution, as was the case for ϵ for ethyl orange.

Chapter 5

Molecular Dynamics as an Analysis Tool For Various Applications

We discuss here two applications where Molecular Dynamics (MD) acts as an extremely viable and useful tool for gaining information on observables. These applications belong to various research fields and are inspired by experimental partners who needed theoretical support to interpret their experimental results.

The first study concerns the structure of a copper exchanged zeolite which is an ideal catalyst for the Selective Catalytic Reduction (SCR) of nitrogen oxides NO_x. The system was experimentally studied under reaction conditions by our collaborators, the Group of Inorganic Chemistry and Catalysis of prof. Bert Weckhuysen. MD is used as a tool to provide the geometrical structure of the catalyst and the reproduction of the IR spectrum. A second paper in this topic is in preparation and therefore not included in Part II of this work, but the data are included in the present discussion.

The second application is situated in the field of radiation-induced radicals present in organic crystals, sugars, etc. The CMM has a longstanding reputation in the study of EPR properties in radicals induced by radiation of sugars, amino acids and other organic crystals. Present work was in collaboration with the Department of Physics of the University of Oslo, under the lead of prof. Einar Sagstuen.

5.1 Metal-Exchanged Zeolitic Catalyst Material: Cu-SSZ-13

In cooperation with an experimental partner — the Group of Inorganic Chemistry and Catalysis from the University of Utrecht (The Netherlands) — the structure of a copper exchanged zeolite and its catalytical behavior was investigated to gain better insight in the Selective Catalytic Reduction (SCR) of nitrogen oxides (NO_x) from exhaust in diesel engines.

The standard NH_3-SCR reaction reduces NO into N_2 in presence of ammonia and oxygen

$$4\mathrm{NO} + 4\,\mathrm{NH_3} + \mathrm{O_2} \longrightarrow 4\,\mathrm{N_2} + 6\mathrm{H_2O} \tag{5.1}$$

In real life conditions, also NO_2 is present in the exhaust enabling a much faster SCR reaction[122]

$$\mathrm{NO} + \mathrm{NO_2} + 2\,\mathrm{NH_3} \longrightarrow 2\,\mathrm{N_2} + 3\,\mathrm{H_2O} \tag{5.2}$$

SCR uses a catalytic environment to obtain a high selection in NO_x to N_2 reduction. This catalyst is either an oxide material or an ion exchanged zeolite. In particular metal exchanged zeolites show a high efficiency as a catalyst for the SCR. Most widely studied are copper and iron exchanged ZSM-5[123], however these have two major drawbacks. First, at high temperatures and in presence of water vapor — which is the case in car exhausts — the structure is not hydrothermally stable. This is caused by alumina atoms which are removed from their tetrahedral framework positions. In combination with copper migration, copper-alumina clusters can be formed which contaminates the zeolite. Second, at low temperatures hydrocarbons are formed, damaging the zeolite structure.

The introduction of molecular sieves with small pore windows, such as those with a chabazite structure, allows much higher efficiency. Cu-SSZ-13 was studied in the frame of this PhD research since it exhibits excellent SCR-deNO_x behaviour. This is shown in Figure 5.1 which compares the conversion of three copper-exchanged zeolites over a wide temperature range. This shows the Cu-SSZ-13 as most robust and performing very well (between 80% and 100% efficiency) in a temperature range of 230 °C up to 500 °C. Importantly, at high temperature in moist conditions, the efficiency remains very high[124].

Ab initio calculations were performed to gain insight in the molecular environment of copper exchanged chabazite and its interaction with NH_3-SCR

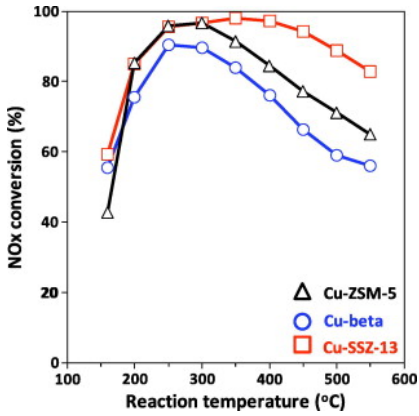

Figure 5.1: Temperature dependence of NO_x conversion for three copper-exchanged zeolite materials, Cu-ZSM-5 (triangles), Cu-beta (circles) and Cu-SSZ-13 (squares). This figure is taken from J. H. Kwak et al.[125]

reagents. The data are compared to experimental findings whenever possible. In **Paper VII**, CP2K was used for molecular dynamics simulations with periodic boundary conditions to predict the structure of the empty Cu-SSZ-13 and that of the zeolite filled with guest molecules like ammonia and nitrogen oxides. In addition theoretical IR spectra have been derived using the Velocity Power Spectrum (VPS) method. This is compared with experimental infrared spectra and results in a very good agreement. Additionally, a Normal Mode Analysis (NMA) was performed with the same setup. In a next study we focus on geometry optimized structures with ammonia and nitrogen oxide molecules which are compared to high-resolution powder diffraction (HRPD). In order to gain insight in the oxidation state of copper, the electron and spin density of the system was partitioned with a Hirshfeld-like method using the code Horton[126], which results in the assignment of a charge and a spin to the copper and surrounding atoms. This paper is presently in preparation. The computational details of this work can be found in **Paper VII**, however the PBE-D3 functional was used to calculate the adsorption energies and atomic charges, rather than the BLYP functional employed in **Paper VII**.

5.1.1 Geometrical Structure of Cu-SSZ-13

The chabazite structure consists of layers of double 6 membered rings (d6r), for which both 6 membered rings (6r, Figure 5.2a indicated in green) contain

6 Si atoms linked by 6 oxygens. Both rings are again linked via an oxygen atom between the Si atoms. The d6r layers are stacked in an ABCA fashion (see Figure 5.2b), with creation of 4 membered rings (Figure 5.2a, indicated in red). Overall a spacious cage is constructed (Figure 5.2a, indicated in yellow) which can be accessed by an 8 ring windows (Figure 5.2a, indicated in blue), allowing guest molecules to migrate through the nanoporous material.

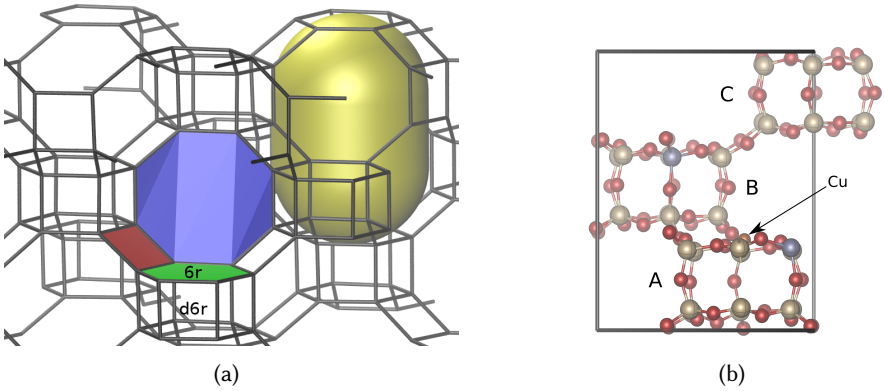

(a) (b)

Figure 5.2: (a) The chabazite structure with the 6 rings indicated in green, 8 ring windows in blue and the 4 rings between the double 6 membered rings colored in red. The large cage in chabazite is indicated by the yellow pill-shaped object. (b) Unit cell of chabazite structure with three d6r shown, with the periodic box plotted in black. The ABCA structure is clearly visible. The copper ion (in orange) is positioned at the centre of the top 6r of the lowest d6r.

As in most catalytically active zeolites, some of the silicon atoms are substituted by tetrahedral surrounded aluminium atoms. These have an oxidation state +3 rather than +4 for silicon, implying that charge compensation is necessary in order to obtain an overall neutral system. For this reason, Brønsted acid sites are formed by adding a proton to one of the framework oxygen atoms. In **Paper VII**, we focussed on positions O(1) and O(2) since they are most stable, due to their close distance to the aluminium defect.

Alternatively, a copper ion can compensate for the charge due to the presence of aluminium in the framework. Two possible oxidation states are found for copper: Cu^{+} and Cu^{2+}. Evidence for Cu^{2+} is found in literature (see further), hence compensating for two framework Al atoms. In the chabazite framework, originally four different positions for copper were suggested: (i) in the centre of a 6r, (ii) in the centre of the d6r, (iii) in the 8r or (iv) in the

centre of the chabazite cage.[127] By XRD experiments, the position in the centre of a 6r was found to be preferred in the empty framework as indicated in Figure 5.2b.[128] This structure was used as a start for all our calculations.

Various aluminium configurations were considered. Overall, only small differences were obtained between the different configurations with one or two Al atoms in the d6r, both geometrical and energetically. For all these configurations, the Cu ion is coordinated with four framework oxygens. The only configuration which is clearly unfavorable and significantly different, is the one where the Cu ion is located in a d6r without Al substitutions. This allowed us to focus on one single Al distribution to model the system, rather than performing calculations for all possible Al distributions.

We have chosen a uniform distribution of the aluminum atoms and in correspondence with a Si/Al ratio of 17, similar to the zeolite studied in the experimental setup (Si/Al ratio between 15 and 22). In practice we have positioned the Al substitutes at two T sites located at different d6r. This resulted at a typical copper coordination with four framework oxygens, in correspondence with literature[129].

Periodic DFT is very well suited to describe this extended system due to its inherent periodicity (**Paper VII** and Ref. [129]), although cluster approaches were used as well [130]. Cluster models might suffer from spin contamination or border effects where spin is located at the edge of the cluster [131]. In our simulations a monoclinic unit cell was used, containing 108 atoms for the empty Cu-SSZ-13 framework (see Figure 5.2b). This unit cell consists of 36 tetrahedral sites (T-sites) which are all equivalent in the case of a pure silicate. This approach allows the inclusion of guest molecules without interaction with their periodic images and the distribution of Al atoms in different d6r.

Alternatively, a rhombohedral unit cell was used by Göltl et al.[129, 132, 133], reducing the number of T-sites by a factor of 3 and describing only one d6r. For this reduced unit cell periodic images of guest molecules or even Al positions are very near and likely to interact. Moreover, a much smaller Si/Al ratio is obtained for this approach since only one d6r is present.

A first step in understanding the SCR process at the nanoscale is understanding the zeolite structure and in particular, the interaction of the Cu cation with NH_3 and NO_x guest molecules.

5.1.2 Adsorption of Guest Molecules: Structural Analysis

In this section, we will describe the adsorption of different complexes on Cu exchanged and on protonated chabazite as present under SCR conditions. Firstly, a single NH_3 molecule is adsorbed on both catalyst models. The

Level of Theory	Cu-SSZ-13	H-SSZ-13 (O(1))	H-SSZ-13 (O(2))
PBE	163.3	156.6	161.1
PBE+D3	207.4	181.3	186.1
B3LYP	150.7	131.5	128.5
B3LYP+D3	183.2	168.3	165.5

Table 5.1: Adsorption energy of NH_3 on Lewis acid site (Cu-SSZ-13) and Brønsted acid sites (H-SSZ-13). All values are expressed in kJ/mol, positive values indicate a more stable bonded system.

adsorption energy is determined and will be used to as a starting point for molecular dynamics simulations. Secondly, the number of NH_3 molecules is gradually increased up to four adsorbed molecules to simulate the high NH_3 load used experimentally.

I. Adsorption of NH_3

Adsorption energies of ammonia were calculated using PBE and B3LYP, either with or without long range dispersive interaction corrections by means of an additional interatomic interaction potential (in particular the D3 correction of Grimme).[134] The motivation for including dispersion corrections is to incorporate the long range interactions between an adsorbed guest molecule at the acid site and the framework at larger distances. In particular for the infrared spectrum of CO adsorbed on Cu in a generic model for zeolites, DFT fails to find the experimentally found blue shift. Nachtigallová et al.[135] suggest that the lack of dispersion in DFT lies at the origin of this discrepancy.

The D3 correction indeed has a systematic effect of $\sim$ 30 kJ/mol for the adsorption of NH_3 on the different acid sites, see Table 5.1. The main conclusion is that NH_3 forms a more tight bond with the Cu ion and this holds for all investigated levels of theory. This agrees with the fact that the catalytic activity is enhanced even if there is no 100% ion exchange and also Brønsted acid sites are present. In that case, the copper ions are very good adsorption sites, suggesting that the reaction will occur on these sites and an increased reactivity is expected.

When ammonia is adsorbed on the Brønsted acid site, NH_4^+ is formed and coordinated towards a framework oxygen (see Figure 5.3a). In the case of the Cu exchanged chabazite, the nitrogen is oriented to the copper and the system is tilted in such a way that one of the hydrogens of NH_3 is oriented towards the framework (see Figure 5.3c).

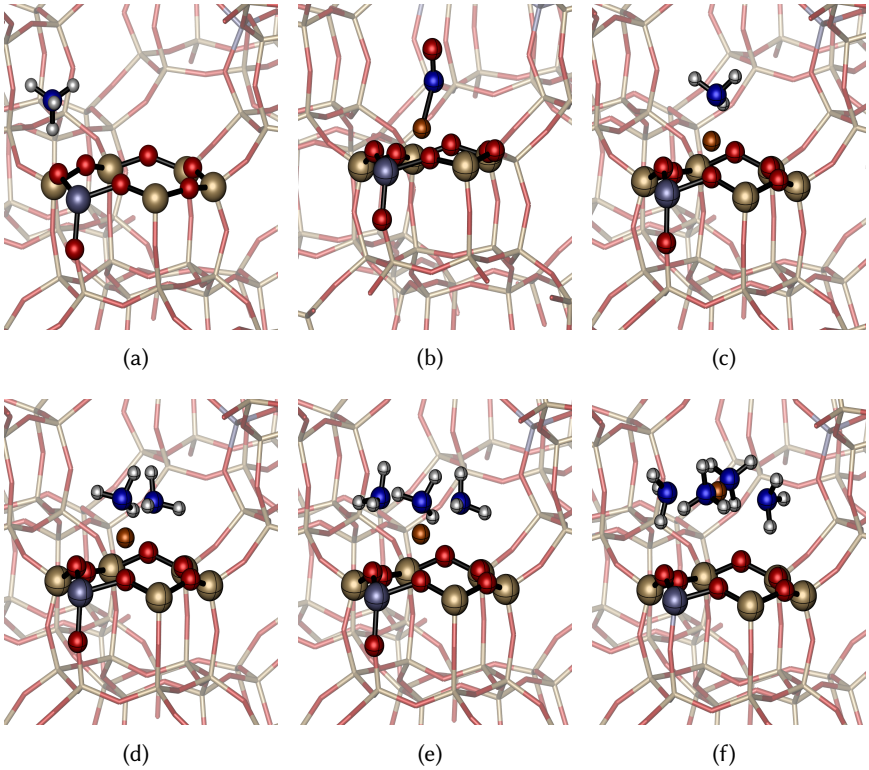

Figure 5.3: Optimized Adsorption geometries for (a) NH_3 on an O(2) position in H-SSZ-13 and (b) NO molecule, (c) one NH_3 molecule, (d) two NH_3 molecules, (e) three NH_3 molecules, (f) four NH_3 molecules on the copper ion in Cu-SSZ-13.

	ΔE [kJ/mol]	d(Cu-6r)	$d(Cu\text{-}O(f))_{close}$	$d(Cu\text{-}N)_{av}$
Cu-SSZ-13	-	0.536	2.042	-
+1 NH_3	207.4	1.672	1.899	1.948
+2 NH_3	145.5	1.831	1.966	2.025
+3 NH_3	72.9	2.157	2.016	2.120
+4 NH_3	98.3	3.558	3.589	2.041
NO		1.273	1.942	1.765

Table 5.2: Energetics and structural information regarding the adsorption of multiple NH_3 molecules and NO molecule on Cu^{2+} in the chabazite zeolite. All calculations are performed using the PBE+D3 level of theory. Distances are expressed in $\mathring{A}$.

To model a high load of NH_3 in the setup, multiple ammonia molecules were included in the geometry calculations. In our simulations, gradually adding NH_3 guest molecules results in a lowering of the number of Cu-framework oxygen (Cu-O(f)) interactions, which are replaced by Cu-N coordinations. This results in a systematical increase of the distance between the copper ion and the plane of the 6r in which the ion was originally located (see Table 5.2). The configurations are displayed in Figure 5.3c-f.

When two ammonia molecules are adsorbed, the copper ion remains highly coordinated: in addition to the two nitrogens, two of the framework oxygens are still oriented towards the copper.

When three ammonia molecules are adsorbed, this coordination towards two O(f) remains (see Figure 5.3e), while this is not the case when four NH_3 molecules are present in the unit cell. In this simulation the closest Cu-O(f) is 3.589 $\mathring{A}$ and a square planar environment is found for $[Cu(NH_3)_4]^{2+}$. For the initial HRPD experiments at low temperatures correspondence between both theory and experiment is found.

The adsorption energy for increasing number of ammonia molecules is also given in Table 5.2. All energies are positive and although there is a descending trend, adding the fourth ammonia molecule is energetically more favorable than the third molecule. This last process is less efficient since the copper ion remains oriented to the framework and the complex is not mobile. Once the fourth ammonia molecule is adsorbed, the complex is detached from the framework and can find its optimum position in the zeolite cage, optimizing the interactions with the framework. This significant difference in types of interactions explains the somewhat surprising increase in adsorption energy in the case of four NH_3 molecules.

II. Adsorption of NO

The adsorption of nitrogen oxide on the Cu^{2+} ion was calculated with the same methodology as for the NH_3 adsorption. The NO molecule is found to be orthogonal to the 6r in which the copper is located, while the copper is still coordinated to three framework oxygens with similar distances as the case for the NH_3 adsorption (see Figure 5.3b).

Multiple spin states were investigated since both the Cu^{2+} ion and the neutral NO molecule have one unpaired electron. Over a wide range of starting geometries and Al distributions, the singlet state was always found to be the most stable. Advanced experiments are currently performed to elucidate the exact position of the Cu ion, which will allow comparison of detailed structural data (*i.e.* bond lengths and angles) between theory and experiment.

5.1.3 Reduction of the Copper Ion: Hirshfeld-I Charges

Multiple references[128, 130, 127, 136] use X-ray spectroscopy to characterize Cu-SSZ-13, both in absorption (XAS and XANES) as in emission (XES) mode.

In the X-ray Absorption Near Edge Structure (XANES) spectra, the X-rays are absorbed by the core electrons, which are most often emitted but sometimes captured in the valence orbitals. Those electrons excited to the valence orbitals show features (pre-edge) near the large absorption peak of emitted electrons (continuum) observed in the X-ray spectra.

When studying Cu-SSZ-13 with this technique, valuable information about the oxidation state of Cu is given by these pre-edge features. For Cu^{+} ten 3d-electrons are present, prohibiting the core electrons to be excited to a 3d orbital. If a higher oxidized Cu is present, Cu^{2+}, one 3d orbital is unoccupied allowing this excitation, corresponding with a peak at 8982.8 eV [130]. Performing such experiments in SCR conditions or with other gasses present, allows tracking the oxidation of the copper ion in the zeolite. Korhonen et al.[137] and Giordanino et al.[130] conclude that in the fresh samples Cu^{2+} is present. At high temperatures the copper ions are partially reduced in presence of NH_3, in correspondence with what was found for Cu-ZSM-5, for which the reduction was complete[138]. This reduction of Cu^{2+} was found to be limited by presence of O_2[130].

To investigate the Cu reduction theoretically, the electron density and spin density was partitioned with the Iterative Hirshfeld (Hirshfeld-I, HI) parti-

	Hirshfeld-I charge		Hirshfeld-I spin charge	
	Cu	N	Cu	N
Cu-SSZ-13	1.37		0.56	
+NO	1.32	0.11		
+1 NH_3	1.39	-1.36	0.64	0.04
+2 NH_3	1.51	-1.30	0.69	0.08
+3 NH_3	1.56	-1.30	0.79	0.05
+4 NH_3	1.47	-1.30	0.64	0.08
+4 NH_3 + H_2O	1.52	-1.30	0.67	0.08

Table 5.3: Hirshfeld-I charge and spin charge for the different systems under study. All values are expressed in e.

tioning scheme[139, 140] using the in-house code Horton[126].[1] The results are given in Table 5.3. Figure 5.4 displays the spin density of the original Cu-SSZ-13 material.

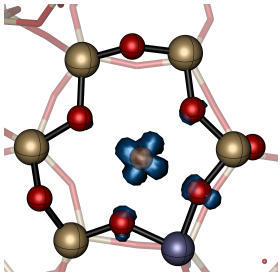

Figure 5.4: Spin density for empty Cu-SSZ-13 material.

The atomic charge of the copper ion is slightly reduced when NO is adsorbed, but adsorption of ammonia molecules induced an opposite effect. Adsorption of multiple NH_3 molecules even increases the Cu charge above the value predicted in the empty zeolite. While electrons are removed from the copper ion, the spin charge is increased. From this we can conclude the spin gets more localized on the copper ion and spin-down electrons must be removed during this process.

Remarkably, the adsorption energy of NH_3 also correlates with the charge on the copper ion. This indicates that the copper ion would tend to the Cu^+

[1] Although the extended Hirshfeld method (Hirshfeld-E, HE)[126] results in very reliable silicon and oxygen atomic charges (*i.e.* +2 and -1 respectively), the accuracy for transition metals was not tested yet. Therefore, the iterative Hirshfeld method (Hirshfeld-I, HI)[140] was chosen in our analysis.

oxidation state if possible. The trend of adsorption energy going from 3 NH_3 to 4 NH_3 is stronlgy correlated with the charges as well (Table 5.3). This will be investigated further.

5.1.4 Infrared Spectroscopy

Infrared spectra were measured during standard SCR conditions by I. Lezcano-Gonzalez and coworkers (see **Paper VII**) for both copper-exchanged (Cu-SSZ-13) and proton exchanged chabazite (H-SSZ-13). The advantages of infrared spectroscopy are the fast acquisition (FTIR) and the possibility to perform the experiment *in situ*. For these experiments the focus lies on fingerprint regions, which are specific for molecular vibrations.

NMA and molecular dynamics calculations were performed on both H-SSZ-13 and Cu-SSZ-13, on which one NH_3 molecule was adsorbed. Resulting frequencies are tabulated in Table 5.4.

For the NMA analysis a partial Hessian analysis was performed where only the relevant portion of the chemically active center was taken into account, *i.e.* the Cu-ion or Brønsted proton, the ammonia molecule and a single six-membered ring. These atoms are highlighted in Figure 5.3a-c. All other framework atoms were fixed to reduce the computational cost. Besides, the global motions lie well below 1200 cm^{-1}, a region which is experimentally not thoroughly investigated.

The molecular dynamics results were used to calculate the VPS, as explained in Chapter 4, in order to mimic the infrared spectrum observed experimentally. The MD results are in very good agreement with experiment and with the NMA predictions, see Table 5.4. Additionally, the formation of extra-framework alumina (EFAl) centres were expected, in analogy with what was found in Cu-ZSM-5. This situation was considered by an $Al(OH)_3$ model system with adsorbed ammonia for which similar MD simulations were performed. The resulting power spectra are presented in Figure 5.5. In the range below $\approx$ 1100 cm^{-1}, typical vibrations associated with zeolite frameworks are found which are hard to distinguish. The main focus is on the regions between 1200 cm^{-1} to 1800 cm^{-1} (Figure 5.5) where the vibrations of the ammonia molecule are expected.

In Figure 5.5, four peaks can be seen. The peak at 1640 cm^{-1} arises in each configuration, but is linked to a mode of ammonia which keeps the dipole moment unaltered. It is therefore present in every VPS since ammonia is present in each configuration. At slightly smaller wavenumber (1600 cm^{-1}) a peak for both the Cu complex and the EFAl can be found. When considering the range of 1240 cm^{-1}, one clear peak is found only for the Cu complex. This

	ν_{exp}	ν_{NMA}		ν_{MD}		Assignment
H-SSZ-13		O(1)	O(2)	O(1)	O(2)	
	1448	-	1480	1432	1455	δ NH_{4as}^{+}
	1393	-	1387	1370	1368	δ NH_{4s}^{+}
Cu-SSZ-13		$[Cu(NH_3)]^{2+}$	$[Cu(NH_3)_4]^{2+}$	$[Cu(NH_3)]^{2+}$	$[Cu(NH_3)_4]^{2+}$	
	1619	1632	1621	1601	1606	δ NH_{4as}^{+}
		1537	-	1535	-	H-bonded δ NH_{4as}^{+}
	1278	1261	1291	1271	1285	NH_3 wagging

Table 5.4: Assignment of IR absorbing bands of ammonia-adsorbed H- and Cu-exchanged SSZ-13 zeolites. Both experimental (ν_{exp}), NMA (ν_{NMA}) and MD (ν_{MD}) results are included for NH_3 adsorbed on two Brønsted acid sites (O(1) and O(2)) or at the Cu ion ($[Cu(NH_3)]^{2+}$). Additionally also the results for a high load of NH_3 was included ($[Cu(NH_3)_4]^{2+}$). All values are expressed in cm^{-1}.

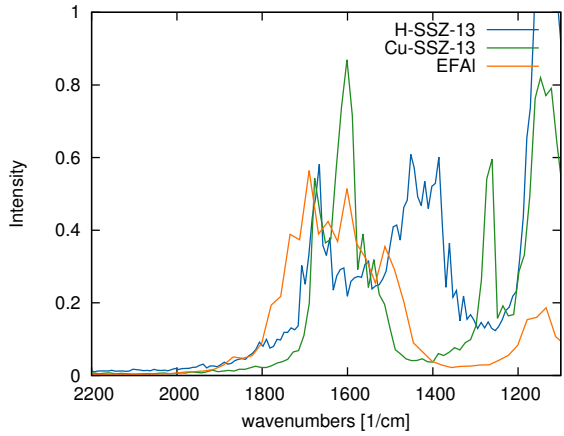

Figure 5.5: Velocity Power Spectra for H-SSZ-13 (blue), Cu-SSZ-13 (green) and EFAl (orange).

can be used as a fingerprint of such a complex being present in the system which is studied.

In contrast, a broad peak from 1350 cm^{-1} to 1450 cm^{-1} is observed only for the Brønsted acid site, which in turn can be regarded as a fingerprint for these sites. These results are in excellent agreement with the experiments performed in **Paper VII**.

As mentioned in literature, the two different Brønsted acid sites result in a shift in the high wavenumber region. This result was also reproduced in our calculations.

5.2 Automated Procedure for Generating Radical Structures Applied on Rhamnose

Radiation defects in organic crystals are very well suited to be studied with EPR experiments.[141, 142, 143] The radical structure, the location of the radical center, has usually been proposed based on intuition, whether or not supported by available EPR measurements (mostly by hyperfine coupling tensors). The possibility of theoretical estimates of these EPR properties for each proposed radical with the help of DFT-calculations, facilitates the search for plausible radical structures. Especially hyperfine tensors are very useful since multiple nuclei near the radical centre can interact with the unpaired electron and provide much more data than a single g-tensor.[93, 91, 144, 108, 109]

The reaction paths bringing the undamaged crystal structures to a radiation-induced radical structure are not easy to unravel and may be very complex. This leads to a situation that not all experimentally observed radical structures can be reproduced. **Paper VI** is the result of a collaboration between the group of prof. Sagstuen (University of Oslo) and the CMM in which it was attempted to remove this bias by scanning the potential energy surfaces (PES) of both the neutral and irradiated system with Molecular Dynamics (MD). As proof of principle, rhamnose single crystal is considered[145, 146, 147] in a periodic supercell (period of 2 in each direction) containing 16 rhamnose molecules with 16 water molecules. For further computational details, we refer to **Paper VI**.

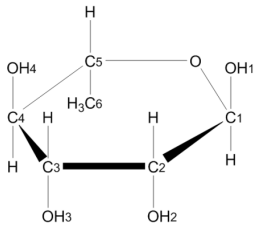

Figure 5.6: Schematic representation of an undamaged rhamnose molecule. Figure courtesy of Siv G. Aalbergsjø.

When such a crystal is irradiated, an electron is removed from a molecule and captured at sufficiently large distance. To mimic this behaviour, both a unit cell with a deficiency and an excess of electrons is considered, leading to cationic and anionic structures. A geometry optimization of such structures, starting from the most stable rhamnose geometry, would lead to at most two radicals in contrast to experiment, where at least five different structures are experimentally detected.[145, 93]

Our approach tries to mimic the conditions as met in experiment by performing MD simulations for both the undamaged as irradiated structures.[148] In order to find a large variety in radicals which can be formed, the PES of the undamaged structure is first sampled, resulting in 10 starting geometries. For each starting geometry 4 different sets of initial velocities were randomly imposed, generating a much larger variety of structures.

Once the radical behaviour was imposed by subtracting or adding an electron, one would expect the spin to be localized on the rhamnose molecules. However, for the first few steps, sometimes even several hundred, the spin is fully delocalized over the unit cell and the density is not representing a radical, as was hoped for. After these initial steps, the spin density does collapse and the spin gets localized on few atoms. This means from that point

on, we start sampling another PES and must have gone through a conical intersection. From this point on, analysis of Mulliken spin densities indicate the spin is indeed fully localized on the radical center.

This process is not occurring fluently but very abrupt with a very large peak in kinetic energy at that point. Such an event is unphysical and considered as an artifact of DFT. Indeed, DFT cannot describe conical intersections properly and when passing through such a point on the PES, it will use the previous wavefunction as initial guess to update it. Therefore, the density varies quite smoothly until the geometry is reaching the edge of the region in which a delocalized density can describe the system, leading to unconverged wavefunctions and very high potential energies. At that moment, a physical density can be found with a related potential energy drop, resulting in a large kinetic energy.

Despite this process being unphysical, the method was able to produce radicals in 67 out of 160 MD simulations. These were obtained without a predefined bias, which was eventually the goal of this work. Indeed a wide variety of radicals were found, including both structures previously discussed and completely new structures. Even some new reaction paths such as ring openings, previously not considered, occurred. For these new structures, geometry optimizations and hyperfine calculations were performed in order to find a match with experiment.

In cases where no radical is formed, some plausible reaction mechanisms preventing this formation are suggested. Firstly, two hydrogen chains are present in the system and play a crucial role in the charge separation, *i.e.* during the deprotonation of a rhamnose molecule this chain absorbs a proton which is then transfered. Due to the limited size of the periodic unit cell, such a transfer can bring a new proton back to the deprotonated site. Such an event is seen in multiple cases. Secondly, a longer MD simulation could finally result in a radical structure.

In **Paper VI** three essentially new configurations are found which were not yet suggested and show good correspondence with experimental hyperfine structures. Four other products which were never discussed before were found, however they show no correspondence with the experimental hyperfine information and are therefore eliminated to serve as a good model for the defect.

This research is the work of PhD candidate Siv G. Aalbergsjø, from the University of Oslo, under supervision of Einar Sagstuen. My input was limited and restricted to supervision of the calculations, data interpretations and contributions to editing the final paper.

Chapter 6

Accurate Electronic Structure Methods for Various Applications

In this Chapter two different topics will be briefly discussed for which benchmarking of DFT results with advanced electronic structure methods was necessary. The systems are very challenging for currently available electronic structure methods. Although for both systems, DFT calculations were essentially used in all resulting publications, advanced wavefunction based electronic structure methods (*i.e.* post-Hartree-Fock) were considered in order to determine the reliability of DFT. In the first topic, the focus lies on the very heavy elements polonium, bismuth and lead, which introduced an additional difficulty related to relativistic effects. Multiple aspects were investigated, from which we highlight the solubility of the polonium in the Lead-Bismuth Eutectic and the formation of polonium-containing molecules. The second topic concerns a heterogeneous catalyst (Mn(salen)) for which multi-reference calculations were considered in order to cope with the very small energy differences between the different spin states of this system. Eventually, a proper DFT functional was chosen which describes the correct spin state. This simplification was used in order to be able to treat the full system. The post-Hartree-Fock procedures are too expensive to be used on the extended systems.

6.1 Polonium LBE chemistry

In the Belgian Nuclear Research Centre (SCK-CEN), the construction of a research reactor is planned between 2017 and 2021. This reactor, called MYRRHA[1] (see Figure 6.1), will demonstrate the concept of an accelerator driven system (ADS).[54] In such a system, a sub-critical core is fed by a neutron beam in order to sustain the nuclear reaction. The neutron beam is in its turn created by accelerated high energy protons impacting on a spallation target.

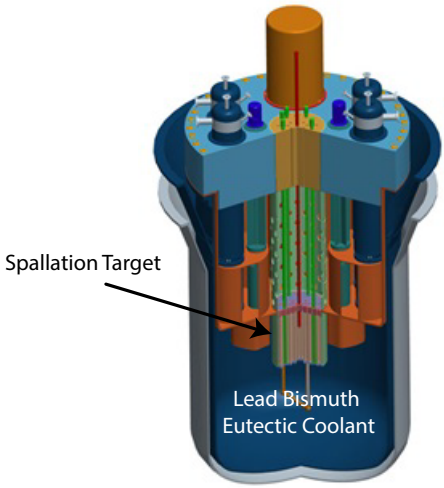

Figure 6.1: An overview of the MYRRHA reactor to be constructed in the SCK-CEN. Figure is used from Ref. [149]

The MYRRHA-project has multiple goals. It will be used in the research of transmutation of nuclear waste and material design for nuclear plants. Secondly, it will contribute to the development of the fourth generation nuclear reactors. This type of reactors uses liquid Lead-Bismuth Eutectic (LBE) as coolant *and* as spallation target.

Within the LBE coolant, collisions of neutrons and protons with ^{209}Bi generate different polonium isotopes (^{209}Po and ^{210}Po after β-decay), all of them being radioactive (α-emitters) and possibly volatile when bound to other atoms. In operating conditions, the LBE will serve as a natural container for these radiotoxic Po nuclei. However, some of the Po atoms will be able to evaporate into the cover gas above the coolant. In MYRRHA, the atmosphere

[1] Multi-purpose hYbrid Research Reactor for High-tech Applications

of the coolant vessel will be continuously filtered to remove these and other toxic elements.

Licensing such a project within the current safety restrictions is a major topic. Therefore, the European SEARCH[2] project aims to investigate the chemistry of the fuel and coolant of the MYRRHA reactor, in order to manage the safety issues both in operation conditions and various accident scenarios. The work described in this Chapter constitutes one (computational) part of an otherwise experimental work package of SEARCH, investigating the interaction of Polonium with LBE. Experiments to investigate the behavior of Po in LBE and in the cover gas are very expensive due to the pollution of equipment and high safety precautions to be taken.

In this regard, *ab initio* calculations are very valuable to get insight in the behavior of Po in and near the LBE. They allow to predict the expected outcome of an experiment and can in that way minimize the number of experiments. These computer simulations are obviously not suffering from the safety drawbacks of physical experiments, described above. In this context multiple research questions can be raised to be of great value for experimental work. Firstly, the solubility of Po in the LBE was investigated (**Paper IX**) and the comparison with Te solubility has shown that such experiments are very valuable to predict the behavior of Polonium. Secondly, the molecules formed after evaporation of Po in the atmosphere was investigated with accurate structure methods, in order to verify the accuracy of DFT approaches. These will be used in further computational research for the construction of filter materials. This work was done in collaboration with PSI (prof. Jürg Neuhausen) and SCK-CEN within the FP7 SEARCH project.

6.1.1 The Solubility of Polonium in LBE

At first instance the solubility of Po in the solid phase of LBE was determined via periodic DFT calculations (see **Paper IX**). Similarly, also the solubility of Te was calculated since it is situated right above Po in the periodic table and can therefore be assumed to have similar properties. If correlations between both sets of data can be found, the experimental conclusions of Te solubility can be re-interpreted to draw conclusions or make predictions for the Po solubility.

In **Paper IX** the Vienna Ab initio Simulation Package (VASP) was used to simulate the solid phase of the LBE. A hcp unit cell was periodically extended once in all directions, resulting in a 2x2x2 supercell. Eight Bi and eight Pb atoms were distributed randomly over the supercell in order to simulate as

[2]Safe ExploitAtion Related CHemistry for HLM reactors

much as possible nearest neighbour configurations for the defect introduced in the calculations. All sixteen atom positions were replaced one by one by the impurity atom (Po or Te).

From these calculations it became clear Po will not spontaneously dissolve in the material and will rather form PbPo complexes. This is consistent with what is found in experiments, where Po is found to migrate to the surface or to grain boundaries. Similar to the Po results, also Te prefers to be in a Pb-rich environment and formation of PbTe is preferred over dissolution of Te in the LBE. In an experimental setup, indeed the PbTe phase is found.

Interestingly, the Te and Po solution enthalpy show a high correlation. This correlation can be used to predict the solution enthalpy for Po, performing only Te experiments.

Also the influence of spin-orbit coupling is examined, showing the absolute enthalpies to be less negative when spin-orbit coupling is included. However, the global trend was similar with and without spin-orbit coupling, and the overall conclusions are not affected. This part of the research was done in collaboration with Kim Rijpstra, PhD candidate at the CMM, which was the main contributor to this work.[150]

6.1.2 Evaporation of Polonium and Formation of Molecules

Po is likely to migrate to the LBE surface. From there it will evaporate and will form different compounds, as experimentally confirmed by thermochromatography experiments.[151] In such experiments, an adsorption surface is placed over a temperature gradient. Different compounds with different adsorption energy on this surface (in practice a quartz surface was used) will be adsorbed at different temperatures and thus at different positions. The distribution of Po compounds is then measured by the radiation emitted by the Po nuclei. This technique can make distinction between different Po compounds, but identification of these compounds is rather speculative.

This is a situation where predictions by *ab initio* calculations could be an valuable alternative to experiments. The aim of **Paper III** is to calculate the dissociation energies (formation energies) D_e of different Po compounds to be expected in the gas atmosphere above the liquid LBE. The focus of this work is on binary and ternary molecules, and are inspired on their light homologues.

The challenges for these calculations are two-fold:

- The heavy elements which need to be considered in these calculations require inclusion of relativistic effects.

method	CO	NO	O_2
exp.	11.142	6.535	5.151
DFT	11.071	6.640	5.395
CASSCF	3.244	0.152	2.388
MRCI	10.340*	6.258	5.277

Table 6.1: Dissociation energy D_e for some light homologues of the calculated molecules. DFT calculations were performed with PBE0 functional. The cc-pVTZ basis set were used for all calculations with exception for * in which a smaller basis set was used. All values are expressed in eV.

- To calculate the dissociation energy, correlation has to be included.

While the gauge-invariance problems of the ZORA Hamiltonian can be solved by including a model potential[75], this model potential is not transferred to single atom calculations. It is therefore preferred to calculate the full dissociation profile when using the ZORA approach with model potential. Due to the incorrect description of bond dissociations of DFT and the necessity of calculating the full dissociation profile with ZORA, this combination can be ruled out. Attempts to use this combination anyway, resulted in the expected errors such as the lack of convergence while dissociating the molecule.

In order to overcome the dissociation problems with DFT, CASSCF calculations were tried, however a benchmark on light equivalent molecules showed the dynamic correlation was essential to find a correct D_e. Subsequent to the CASSCF calculations, MRCI calculations were performed, resulting in corresponding dissociation energies for the same light molecules. The results are summarized in Table 6.1. In this Table, also DFT results are included since the relativistic effects can be neglected and the use of a ZORA Hamiltonian would be exorbitant. This obviously resolves the problems occurring when ZORA and DFT are simultaneously used for the calculation of the dissociation energy.

For the heavy elements, also spin-orbit coupling should be introduced. In this work, it is chosen to use quasi-degenerate perturbation theory to the MRCI calculations (MRCI+SOC).

Also DFT calculations with the PBE0 density functional were used in order to find a method which has significantly lower computational cost. To include relativistic effects, relativistic effective core potentials (RECP) are used in which the core electrons are replaced by a fitted potential.[152] This is relevant for the current topic since the valence electrons are the main con-

tributors to the chemical binding process. As a critical note, this method does not include scalar relativistic effects nor spin-orbit coupling for the valence electron, yielding an approximation which should be validated before the method can be trusted as black box approach.

In **Paper III** it is shown that the latter approach is in relative good agreement with the MRCI+SOC method, also indicated in Figure 6.2. This justifies the use of DFT calculations for the larger complexes with three atoms, which are computationally (nearly) impossible at the high level of theory. In Table 6.2 a list of all studied molecules is given. These molecules are formed from Po, Pb, Bi, Hg, O and H since these elements are present near the LBE surface, while the molecules are inspired by their light homologues (*e.g.* H_2O, O_2, OH, ...).

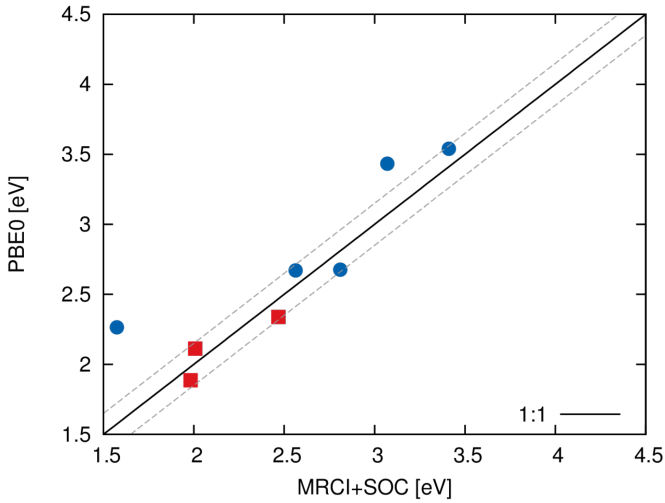

Figure 6.2: Comparison MRCI and PBE0 calculations on diatomic polonium-containing molecules. In blue the ground state spin state energy is given. In red, the other spin state is compared.

Especially when increasing the number of atoms even further in order to simulate the adsorption of these molecules on a surface, a reduction of the number of electrons will be unavoidable. The calculations performed in current work form the basis on which such simplifications can be justified.

Binary	Ternary	
PoH	PoH_2	PoOH
PoO	PoO_2	PoBiO
PoPb	Po_2Pb	PoPbO
PoBi	Po_2Bi	Po_2O
Po_2	Po_3	
PoHg		

Table 6.2: List of polonium containing molecules considered in **Paper III**.

6.1.3 Interaction with Filter Materials

At the last stage, the interaction of atomic Po and the different molecules from **Paper III** with different filter materials were considered. This paper is still under preparation and will be part of the PhD thesis of Kim Rijpstra.[150]

Together with **Paper IX** and **Paper III**, this line of thought illustrates how a combination of modeling tools can have impact on a typical engineering research problem: how to select appropriate filter materials for capturing Po-containing molecules in the MYRRHA reactor. The reason why such an approach is particularly valuable for Polonium, lies in the safety issues that appear when one tries to collect this information experimentally. Modelling will not replace the experimental work, but complement the experimental research and will reduce the number of experimental attempts that are required to obtain the desired information. For difficult experiments as the ones with Polonium, this is surely an advantage.

6.2 Mn(salen) complex

This research is the work of Thomas Bogaerts, PhD candidate at both the COMOC[3] (prof. Pascal Van Der Voort) and the CMM of Ghent University. My input was mainly practical expertise for and interpretation of the calculations for which post-Hartree-Fock electronic structure methods were used.

The salen ligand combined with a metal center form a class of structures with high catalytic activity. However, they get deactivated via formation of dimers, which is to be avoided. In **Paper VIII** this complex was encapsulated in a metal organic framework (MOF), *i.c.* the MIL-101 (see Figure 6.3), in order to avoid dimer species. Theoretical calculations were performed in order to determine what transition states are geometrically possible within this MOF

[3]Center for Ordered Materials, Organometallics & Catalysis

and how the Mn(salen) complex interacts with its host. Due to the small energy separations of the different spin states and the presence of a transition metal, highly accurate post-HF calculations are performed on a model system in literature. [153, 154, 155] However, the size of the full complex is large, as indicated by the dimensions in Figure 6.3, therefore CASSCF calulations were computationally unfeasible. Therefore a density functional was chosen which can reproduce the correct spin state as predicted by CASSCF calculations. Subsequently, this functional was used to calculate free energies for different intermediate steps in the proposed mechanisms. The transition state determining the selectivity fits the pores of the MOF, allowing the same reaction selectivity in the heterogeneous catalyst as in the homogeneous case.

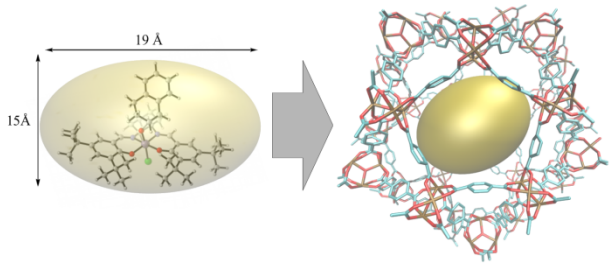

Figure 6.3: The dimensions of the Mn(salen) complex and the encapsulation in the metal-organic-framework MIL-101.

Chapter 7

Conclusions and perspectives

Spectroscopy plays an indispensable role in modern research, such as material science, physical and chemical technology. Its usefulness to gain compositional and structural information of complex molecular systems is inimitable. Key ingredient is the introduction of an external probe, perturbing the vibrational or electronic spectra. Measurements of the absorption or emission of a photon between two energy levels can be done with the help of one of the many spectroscopic techniques available depending on the frequency of the photon. Information obtained using these different techniques must be carefully brought together to gain a thorough understanding of the system at hand.

Computational spectroscopy has grown in importance during the last decade, and has become a ubiquitous tool in the interpretation of experimental spectra. The theoretical predictions have currently attained a high level of accuracy, but there is still room for improvement in the reproduction of specific spectroscopic properties. The main advantage of theoretical simulations lies in their potential to isolate the influence of various effects and hence they are ideally suited to be used in conjunction with experimental information to finally obtain a deep insight into the structure of molecular systems.

The research performed in the framework of this PhD thesis contributed to the development of theoretical tools to determine spectroscopic properties using advanced electronic structure methods. The applications are mostly inspired by collaborations with prominent experimental partners in the field. Existing and new models were applied to investigate defect structures in crystals, vibrational and electronic spectroscopic properties of hydrocarbon compounds and infrared properties of metal-exchanged zeolites. The results nicely show that each application needs its own dedicated computational

approach for which also the choice of the electronic structure method is of utmost importance.

Electron Paramagnetic Resonance The computation of EPR properties of periodic systems, such as crystal structures, has become feasible during the last couple of years. Use of these periodic codes have the advantage over cluster models that they take the molecular environment fully into account, as well as the impact of long range interactions. Despite the higher accuracy that could be achieved using these approaches, it became apparent that the predictions of EPR properties using a periodic approach are in many cases less accurate compared with cluster based approaches. This was explicitly demonstrated by comparing the g-tensor properties of rhodium doped NaCl crystals using both periodic and cluster based approaches. An in-depth benchmark study was also conducted for a set of diatomic molecules, which was chosen to allow comparison to the most accurate methods available in gas-phase codes.

We discovered that this deficiency is mainly due to a wrong DFT implementation of the spin-orbit coupling in the periodic codes. In particular, the spin-other-orbit (SOO) coupling contribution to the g-tensor was incorrectly implemented in the periodic codes. Some of the periodic codes make use of the Pickard and Mauri correction term, which turned out to be too small. In other codes the SOO is simply omitted. In this PhD thesis we deduced a mathematical correlation between the exchange of the SOO and the spin-same-orbit (SSO) term. Within the DFT concept, we could easily implement this relationship in CP2K, removing a first inconsistency. Additionally, also the Coulomb part of the SOO to the g-tensor is systematically neglected in all g-tensor codes. We demonstrated that this term is small for low spin systems, but it can become larger than expected for systems with relatively high spin, often systems containing transition metals.

The new method was validated on a sucrose crystal. The obtained results for the g-tensor are improved compared to previous calculations, especially when taking into account the orientation of the principal axis system.

Further improvement in the accurate determination of the g-tensor using the periodic codes lies within the use of hybrid functionals. Inclusion of exact exchange has become available in periodic codes and only quite recently it is more frequently used. Moreover, the Coulomb contribution to the SOO will be significant for other EPR properties as well. Especially the zero-field splitting (ZFS) could be influenced to a large extent, since it is only present for high spin systems. More importantly, the ZFS has a second order contribu-

tion which depends quadratically on the spin-orbit matrix elements. Further research is necessary in order to quantify this influence.

Molecular Dynamics and spectroscopy In Molecular Dynamics (MD) simulations, the time evolution of the system at an atomic scale is simulated. Experimental conditions are better described in MD as temperature and anharmonic effects form an inherent part of the MD simulations, in contrast to static calculations. The calculation of the electronic excitation on a series of generated snapshots from the MD simulation leads to a averaged dynamical value for this excitation energy. In particular, it was previously shown that the discrepancy between the averaged excitation energy and the excitation energy of the optimized structure can be rather large. Clearly, some specific molecular vibrations are largely responsible for this feature, however, their unique assignment is not evident. Therefore, a new analysis procedure was developed in the frame of this PhD research to assign the dominant vibrational modes influencing the dynamic excitation energy. The method relies on the use of Power Spectra (PS) of the properties of the molecule. As known from vibrational spectroscopy, the so-called vibrational coordinates move with a specific frequency. The PS of this motion shows one peak at this frequency and can therefore act as a fingerprint of this motion. The new method relies on the observation that the PS of the excitation energy exhibits clear distinct peaks at frequencies related to these fingerprints and can thus be linked to individual motions.

Three types of vibrational modes can be distinguished: inactive, linear active and quadratic active modes. The fingerprint of the inactive modes is not present in the ϵPS, as they bear only constant contributions to the electronic excitation energies. Linear active modes, in which the excitation energy depends linearly on the vibrational coordinate, generate peaks in the ϵPS at the same frequencies as in the original VPS. If this mode is sufficiently sampled, the average of the excitation energy over this mode will coincide with the static value. Hence, these modes do not result into a global shift. In this respect, the quadratic active modes are most important. Their fingerprints can be found at twice the original frequency which can be explained by a quadric dependence of the excitation energy on the coordinate. Averaging over such a coordinate results in a shift of the dynamic excitation energy, when compared to the static value.

At different temperatures, the ϵPS can be significantly changed due to the difference in the ensemble when scanning of one (low T) or multiple (high T) minima on the potential energy surface. This also shows the power of the method, compared to static normal mode analysis calculations, in which — by definition — only one minimum is scanned.

Although the developed method is generally applicable, its use becomes complicated for large systems since the definition of vibrational coordinates is not straightforward. It is not trivial to isolate the coordinates exhibiting a perfect fingerprint, *i.e.* with only one frequency with high intensity in its PS. For small systems the mixture between modes is still manageable, for larger systems a more suitable protocol able to properly isolate vibrational modes would be very powerful. It would allow to calculate the overlap of the vibrational fingerprint and the observed power spectrum and quantify the overlap of the PS.

The proposed scheme is not restricted to the excitation energy. The applicability of the method can be very wide and the main concern is the computational cost of an individual calculation of the molecular property of interest. For example, EPR properties could be tracked along the MD trajectory.

The expertise of MD simulations and the link to vibrational spectra was used to investigate a copper holding catalyst material, *i.e.* Cu-SSZ-13, in the selective catalytic reduction (SCR) of NOx. This process is used to reduce the amount of pollution in car exhaust. The vibrational power spectra were computed based on *ab initio* MD simulations and allowed detailed characterization of the catalytically active site and its behavior under NH_3 adsorption. In order to further understand the phenomena occurring at a molecular level and to interpret the high-resolution power diffraction data, adsorption of NO and multiple NH_3 on the copper ion centre was simulated.

Finally, MD was also used to follow the formation of radicals in a rhamnose crystal after it was ionized. Starting from a wide variety of starting geometries, an electron was removed or added, resulting in a paramagnetic system. At first instance the spin is not localized, but after several MD steps radicals were formed. In the case of rhamnose, most of the well-established radicals and several new configurations were retrieved. This method could be applied on similar structures, *e.g.* the irradiated sucrose single crystal. For this system, two observed radicals (T2 and T3) are modeled by identical geometries since there is evidence that they are essentially the same radical with slightly different geometry, due to the influence of the environment. The proposed method could be applied to unravel the differences between the T2 and T3 radical.

Formation of Polonium compounds Expertise concerning relativistic effects and advanced electron structure methods was used to predict the formation of Po-molecules in the cover gas of Lead-Bismuth Eutectic (LBE). This LBE will be used in fourth generation nuclear reactors as a coolant, however, due to neutron or proton capture, radiotoxic Po can be formed, polluting the

system and its environment. The stability of possible formed Po molecules was determined, in order to assist experiments in assigning the different Po compounds on a filter material. The calculations were performed using two very different approaches, one high level (MRCI, ZORA+SOC) and one at lower level (DFT, RECP), which show quite good correspondence. It allowed to predict the stability of several binary and ternary molecules. Due to the good correlation between the high and low level calculations, the low level method could be further used to simulate larger systems, such as the Po-molecules on an filtering surface.

Also the solubility of Po in the solid state was investigated. However, up till now the simulations performed, represent the solid state of LBE and no thermal energy is taken into account. Extension towards calculations on liquid LBE seems the obvious next research step. Such simulations of liquids are typically performed with MD, however due to the high number of electrons treated in this system and the high accuracy, every MD step would require about three hours of computation time (on 8 cpu's). This is a bottleneck for MD simulations since at least 50 ps, preferably longer, would be required. Further approximations would be necessary, for example by reducing the accuracy of these calculations.

Future spectroscopic research in the field of molecular physical chemistry will benefit from new developments at both the theoretical and experimental level. As demonstrated in this PhD work, the required simulation schemes are diverse and highly rely on the studied system: static *vs* dynamic, density based *vs* wavefunction based, gas phase *vs* periodic, ... Increasing computer facilities and algorithm efficiencies enable performance of high-throughput screenings, calculations at much higher level of theory or simulations on systems with increasing size. The recent trends in time-dependent schemes, such as TD-DFT and MD, are in full expansion and increasing computer power will allow simulating on much longer times-scales. Together with the experimental advances focussing on shorter time-steps and higher resolution, the gap between theory and experiments is systematically reduced.

Part II

Papers

Paper I

Accurate spin-orbit and spin-other-orbit contributions to the g-tensor for transition metal containing systems

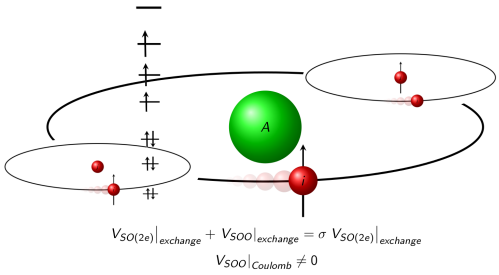

A. Van Yperen-De Deyne, E. Pauwels, V. Van Speybroeck and M. Waroquier
Physical Chemistry Chemical Physics **14**, 10690–10704 (2012)

PCCP

Dynamic Article Links

Cite this: *Phys. Chem. Chem. Phys.*, 2012, **14**, 10690–10704

www.rsc.org/pccp

PAPER

Accurate spin–orbit and spin–other-orbit contributions to the *g*-tensor for transition metal containing systems†

A. Van Yperen-De Deyne, E. Pauwels, V. Van Speybroeck and M. Waroquier*

Received 4th April 2012, Accepted 22nd May 2012
DOI: 10.1039/c2cp41086a

In this paper an overview is presented of several approximations within Density Functional Theory (DFT) to calculate *g*-tensors in transition metal containing systems and a new accurate description of the spin–other-orbit contribution for high spin systems is suggested. Various implementations in a broad variety of software packages (ORCA, ADF, Gaussian, CP2K, GIPAW and BAND) are critically assessed on various aspects including (i) non-relativistic *versus* relativistic Hamiltonians, (ii) spin–orbit coupling contributions and (iii) the gauge. Particular attention is given to the level of accuracy that can be achieved for codes that allow *g*-tensor calculations under periodic boundary conditions, as these are ideally suited to efficiently describe extended condensed-phase systems containing transition metals. In periodic codes like CP2K and GIPAW, the *g*-tensor calculation schemes currently suffer from an incorrect treatment of the exchange spin–orbit interaction and a deficient description of the spin–other-orbit term. In this paper a protocol is proposed, making the predictions of the exchange part to the *g*-tensor shift more plausible. Focus is also put on the influence of the spin–other-orbit interaction which becomes of higher importance for high-spin systems. In a revisited derivation of the various terms arising from the two-electron spin–orbit and spin–other-orbit interaction (SOO), new insight has been obtained revealing amongst other issues new terms for the SOO contribution. The periodic CP2K code has been adapted in view of this new development. One of the objectives of this study is indeed a serious enhancement of the performance of periodic codes in predicting *g*-tensors in transition metal containing systems at the same level of accuracy as the most advanced but time consuming spin–orbit mean-field approach. The methods are first applied on rhodium carbide but afterwards extended to a broad test set of molecules containing transition metals from the fourth, fifth and sixth row of the periodic table. The set contains doublets as well as high-spin molecules.

1 Introduction

Theoretical calculations of magnetic resonance properties can be very useful to assist the interpretation and assignment of electron paramagnetic resonance (EPR) spectra. Several approaches for these calculations have been developed[1–8] which are very successful but often limited to relatively small systems in gas-phase calculations. Much less attention has been given to calculations in extended condensed-phase molecular systems.

Paramagnetic defects in the solid state (such as crystals) are preferentially investigated in periodic codes, where the full environment of the defect is incorporated in the model space in a natural and efficient way. The implementation of the *g*-tensor in periodic codes is rather scarce,[6,8–10] but already demonstrated its usefulness and success in predicting EPR parameters in radiation induced radicals formed in amino acids and proteins.[11–13]

Fully employing the periodicity, one can simulate much larger molecular systems which do not suffer from unphysical borders which are present in cluster-*in-vacuo* simulations. For these extended systems Density Functional Theory (DFT) is the most appropriate method, since the computation time is much smaller compared to other correlated methods, such as post-Hartree–Fock methods.

These periodic programs could be of considerable interest, *e.g.* to investigate transition metal containing materials such as transition metal defects in ionic lattices, transition metal doped zeolites, metal–organic frameworks or even bio-inorganic systems. However, the implementations of the *g*-tensor in programs with periodic boundary conditions such as CPMD,[6] CP2K,[9] GIPAW and BAND have only been scarcely applied to transition metal containing systems.[14,15]

Several studies have calculated EPR properties of transition metal substituted zeolites.[16–18] This spectroscopic technique is very sensitive to the transition metal environment and can be

Center for Molecular Modeling, Ghent University, Technologiepark, 903, B-9052 Zwijnaarde, Belgium. E-mail: michel.waroquier@ugent.be
† Electronic supplementary information (ESI) available: See DOI: 10.1039/c2cp41086a

very successfully used to characterise transition metal centers. However all of the *ab-initio* studies on EPR properties for these systems have used a cluster-*in-vacuo* gas-phase approach to calculate the *g*-tensor. These intrinsically periodic systems require a geometry optimization in periodic codes as the full crystalline structure is taken into account by imposing periodic boundary conditions in the simulation cell.

In these applications it is convenient or even necessary to be able to compute also the *g*-tensor and hyperfine tensors in their true periodic environment. However, a thorough benchmark study on the various implementations for the *g*-tensor in codes with periodic boundaries on systems containing a broad variety of transition metals is prerequisite before the various codes can be reliably applied to more complex and larger applications. The state-of-the-art electronic structure program packages for the computation of spectroscopic EPR parameters and in particular *g*-tensors are ADF,[19–21] ORCA 2.8.0,[22] Gaussian09,[23] Dalton[24] and Mag-ReSpect[25] (see Table 1).

Suitable periodic codes are however rather limited. The pioneering work of Pickard and Mauri[8] resulted in the GIPAW code[26] which is a post-processing module for Quantum ESPRESSO.[27] It uses plane wave functions and a reconstruction scheme for the core electrons. The calculation of EPR parameters, such as the *g*-tensor, has become available recently in CP2K[28–30] but no benchmark calculations with respect to transition metal complexes were performed. This code differs from the GIPAW implementation since it combines plane waves and traditional Gaussian basis sets to perform all-electron calculations. A third periodic code is BAND[31] which differs from most periodic codes since it does not use a plane wave basis set but Slater type orbitals as used in ADF. An overview of available properties and relativistic calculations is presented in Table 1.

Despite all the efforts, predictions of *g*-tensor for transition metal complexes are still more challenging than for organic systems. In this paper we show that one possible cause is the lack of efficient two-electron spin–orbit calculations. Both the direct spin–orbit (SO(2e)) and the spin–other-orbit interaction are revised by reformulating the spin–orbit mean-field approach in second quantization. While the same result is found for spin-$\frac{1}{2}$ systems, a term which was neglected in past studies arises for high spin systems. It originates from the direct spin–other-orbit contribution and can be introduced even in an effective potential method, for which the results are explicitly calculated in this work. Besides this contribution, the exchange contribution of the spin–other-orbit term is discussed in both the spin–orbit mean-field and the effective potential method.

Table 1 Availability of EPR and relativistic modules in several *ab-initio* packages. MAG-ReSpect and Dalton were not used in this work but are given for reference. *A*-tensor: hyperfine tensor, ZFS: Zero-Field-Splitting, DKH: Douglas–Kroll–Hess

	A-tensor	*g*-tensor	ZFS	ZORA	DKH	Periodic
ORCA	✓	✓	✓	✓	✓	
G09	✓	✓			✓	
ADF	✓	✓		✓		
Dalton	✓	✓	✓		✓	
ReSpect	✓	✓	✓		✓	
CP2K	✓	✓			✓	✓
GIPAW	✓	✓				✓
BAND	✓	✓		✓		✓

Before discussing the new approaches concerning the spin–other-orbit contribution, a benchmark is performed using existing methods in both periodic and gas-phase computational schemes to calculate EPR properties for transition metal containing systems. It is complementary to several other studies[7,8,25,32–34] as emphasis is on the impact of the various relativistic and spin–orbit approximations which are implemented in the various codes, with specific focus on the periodic ones. Focus is made on the *g*-tensor calculation, since this property in particular is sensitive to relativistic effects.

As a first test system the transition metal containing rhodium carbide (RhC) is chosen. Experimental data for this molecule are available for the *g*-tensor as well as for the internuclear distance. For this reason the system can very accurately be modeled without extra assumptions with respect to geometry optimization. In addition, the absence of a molecular environment enables a clear assessment of the different methods, without interference of the molecular environment.

This system is typically used as a model system for rhodium in surface chemistry[35,36] and the conclusions made in this study can be used as a validation for extension to more complex molecular structures using Rh or other transition metals.

The EPR spectra for RhC were measured by Brom *et al.*[37] in the gas phase, identifying an orthogonal and parallel component for the *g*-tensor (g_{ortho} = 2.0541 and g_{para} = 2.0039). Configuration interaction methods[36,38] and DFT methods[35] were applied previously to this system. These studies conclude that the wavefunctions predicted in DFT methods are described in a suitable manner.[35]

Subsequently, this benchmark investigation is extended to a set of other diatomic molecules in both doublet and high spin states. We have chosen the same set of molecules as used by Patchkovskii and Ziegler.[33] To allow a one-to-one correspondence, also the internuclear distances, which have been determined computationally in gas phase DFT calculations by these authors, have been used in this work for the computation of the different *g*-tensor contributions.

All the experimental *g*-factors of the diatomic molecules were found by EPR experiments in inert gases.[33,39–59]

Particular attention will be given to the new protocol proposed to treat SO exchange contributions to the *g*-tensor in effective potential models in a more accurate way and to the additional terms in the spin–other-orbit (SOO) contribution for high-spin ($S > 1/2$) molecules.

The structure of the paper is as follows: first the influence of various theoretical approaches and implementations for the *g*-tensor in non-periodic codes are investigated. In particular, special attention is devoted to relativistic corrections (Section 3.1), spin–orbit contributions (Section 3.2) and effects of choosing a suitable gauge (Section 3.3). For the spin–orbit coupling special care is given to the two-electron contributions in density based methods, more specific to how to approximate methods for the exchange integrals and to the derivation of the spin–other-orbit interaction. It is important to assess the importance of each of these models on the results as not all variants are implemented in periodic codes and one can determine the level of accuracy to be expected from these implementations (Section 4.1). Subsequently all conclusions are validated to a broad set of doublet and high spin diatomic

molecules which were also subject of previous theoretical papers[33,60] (Section 4.2 and Section 4.3).

2 Computational details

In order to assess each method for the calculation of the g-tensor on an equal footing, no optimization with respect to the internuclear distance was performed. The experimental value of R = 1.613 Å for RhC was systematically used as well as the same functional (PBE[61]) for all calculations.

For the sets of doublet and high-spin molecules in Sections 4.2 and 4.3, the reported internuclear distances by Belanzoni[60] and Patchkovskii[33] were used.

Several basis sets of increasing size were used to validate the dependence on basis set completeness. Whenever possible (ORCA, Gaussian09, CP2K), the Ahlrichs type basis sets of double-ζ (VDZ) and triple-ζ (TZV) quality were chosen.[62,63] Additional polarization functions (2df, dp, ppp)[64] and diffuse functions (p)[65] were introduced.

In ADF, Slater type basis sets of similar quality were used: a double-ζ (DZ) basis set without polarization functions and a triple-ζ basis set with one (TZP) polarization function. Both are frozen core basis sets up to the 3d and 4p shell.

Since the treatment of core electrons is of great importance for EPR parameters, the Gaussian Augmented Plane Wave (GAPW) method was chosen in the CP2K code.[66] This method does not solely use pseudopotentials, as is usually the case in periodic codes, but treats the core electrons with Gaussian Type Orbitals (GTO's) and valence electrons with a plane wave basis set. In our calculations the Ahlrichs type basis sets were augmented with plane waves up to 300 Rydbergs.

In the QuantumESPRESSO calculations the core region is not explicitly described since Troullier–Martins pseudopotentials[67] were used with a cutoff of 150 Rydbergs. They were generated based on relativistic atomic calculations. The GIPAW post-processing code uses a projector augmented-wave (PAW) like method[68] in which a linear transformation operator T is used to map the valence pseudo-wave functions to the corresponding all-electron wave function. Hence this description treats the core electrons adequately and can be used for accurate calculations of EPR properties.

For the calculation on the gas phase systems in CP2K and GIPAW, convergence with respect to the box size was investigated (see Section 5) and interactions between periodic images of the atoms and charge distribution were switched off. For the latter, the Martyna–Tuckerman Poisson solver[69] was used.

3 Methodological aspects

The g-tensor is defined as a second order property

$$g_{ij} = \frac{2}{\alpha}\frac{\partial^2\langle\Psi|H|\Psi\rangle}{\partial B_i \partial S_j}\bigg|_{\boldsymbol{B}=\boldsymbol{S}=0} \quad (1)$$

in which i and j indicate the Cartesian coordinate indices, α is the fine structure constant, $\boldsymbol{B}$ is the magnetic field and $\boldsymbol{S}$ is the spin operator. Note that in atomic units the Bohr magneton μ_B equals $\frac{\alpha}{2} = \frac{1}{2c}$. All further expressions throughout the paper will be given in atomic units.

The ground state Ψ is an implicit function of the external magnetic field $\boldsymbol{B}$ and double-perturbation theory is applied to evaluate the second order derivative. Eqn (1) yields different contributions arising from different terms in the perturbed Hamiltonian:

$$g_{ij} = g_e\delta_{ij} + \Delta g_{ij}^{ZKE} + \Delta g_{ij}^{SO,para} + \Delta g_{ij}^{SO,dia} + \Delta g_{ij}^{SOO} \quad (2)$$

Terms of the relativistic two particle Hamiltonian which are bilinear in both the spin and magnetic field give rise to the free electron g-factor (g_e = 2.002319304), the Zeeman Kinetic Energy contribution (Δg_{ij}^{ZKE}) and diamagnetic spin–orbit contributions ($\Delta g_{ij}^{SO,dia}$). The paramagnetic spin–orbit ($\Delta g_{ij}^{SO,para}$) and spin–other-orbit (Δg_{ij}^{SOO}) contributions result from terms linear in the electronic spin. The diamagnetic contributions $\Delta g^{SO,dia}$ arise due to the lack of gauge invariance of the magnetic vector potential.

Expressions for all these contributions can be found in the literature, though the formulation can vary.[1,7,9,26,34,70,71] In the further subsections of the methodological part, we only mention those expressions which are relevant to the discussion held in the paper.

Most packages compared in this study use the one-component method first proposed by Schreckenbach and Ziegler[70] in which the spin–orbit coupling is implemented in a perturbative way. For states represented by the $^n\Sigma$ molecular term symbol, such as the ground state of RhC,[36] this method cannot reproduce correctly the parallel component $g_{para} = g_e + \Delta g_{para}$ of the g-tensor since the first order spin–orbit terms vanish. No higher order spin–orbit contributions are taken into account and only small contributions such as the Zeeman kinetic energy and gauge terms are non-vanishing.[1] For this reason, the focus in this paper is on the orthogonal component of the g-tensor, which is substantially influenced depending on the specific spin–orbit or relativistic treatment.

Van Lenthe[3] derived a so-called two-component formalism, in which the Dirac Hamiltonian is appropriately transformed and the spin–orbit coupling is computed during the self-consistent-field iterations. For this non-perturbative calculation of the spin–orbit the g_{para} component is relevant even for $^n\Sigma$ states.

3.1 Relativistic effects

Relativistic effects are not negligible for transition metal containing systems. The most convenient choice is to use the Breit–Pauli Hamiltonian but this perturbation series is not valid near the nucleus. Van Lenthe *et al.* proposed the regular expansion[72] in which unperturbed states are those of the bound electrons. In zeroth order approximation this leads to the ZORA Hamiltonian.[72] Originally it was implemented in the two-component method in ADF, but van Wüllen[73] introduced a model potential which resulted in a computationally less expensive expression, which can be used as a scalar-relativistic method, *e.g.* as implemented in ORCA. Another commonly used relativistic Hamiltonian is the Douglas–Kroll–Hess Hamiltonian.[74] We refer to Table 1 for an overview of various implementations in the different software packages.

In ADF both the (unmodified) ZORA and Breit–Pauli approximations are implemented. Table 2 compares the results

Table 2 Calculated g-tensors ($\Delta g = g - g_e$) in parts per thousand (ppt) for RhC, calculated in ADF using relativistic two-component calculations with various basis sets. For these calculations Gauge Including Atomic Orbitals (GIAO) were used (see Section 3.3)

	Breit–Pauli		ZORA	
Basis set	Δg_{ortho}	Δg_{para}	Δg_{ortho}	Δg_{para}
DZ. 3d	62.92	−0.71	51.00	−0.46
DZ. 4p	58.59	−0.47	—	—
TZP. 3d	51.44	−0.38	52.78	−0.31
TZP. 4p	49.48	−0.32	51.22	−0.29
Exp	51.78	1.58	51.78	1.58

of both methods for the RhC molecule. Both are two-component methods and use the van Lenthe method to calculate g-tensors.[3] This method is not comparable to any method within the other programs used in this work since the spin–orbit operators are not treated perturbatively.

The ZORA results are in general in good agreement with the experimental values. When using the Breit–Pauli Hamiltonian, a good agreement is found when the triple-ζ basis sets are used.

3.2 Spin–orbit coupling

Spin–orbit coupling is the leading correction term in the g-tensor computation. It is relativistic in origin and therefore becomes much more important for heavy elements.

The reduction of the full Dirac equation to two-component equations results in the Breit–Pauli spin–orbit Hamiltonians (H^{BP}), which can be categorised in

(i) the one-electron spin–orbit–nucleus term

$$\hat{H}_{SO(N)} = \sum_i \frac{g'\alpha^2}{4} \sum_A Z_A s_i \cdot \frac{(\boldsymbol{r}_i - \boldsymbol{R}_A) \times \boldsymbol{p}_i}{|\boldsymbol{r}_i - \boldsymbol{R}_A|^3} \tag{3}$$

(ii) the two-electron spin–orbit term

$$\hat{H}_{SO(2e)} = -\sum_i \sum_{j \neq i} \frac{g'\alpha^2}{4} s_i \cdot \frac{(\boldsymbol{r}_i - \boldsymbol{r}_j) \times \boldsymbol{p}_i}{|\boldsymbol{r}_i - \boldsymbol{r}_j|^3} \tag{4}$$

(iii) the spin–other-orbit term

$$\hat{H}_{SOO} = -\sum_i \sum_{j \neq i} \alpha^2 s_i \cdot \frac{(\boldsymbol{r}_j - \boldsymbol{r}_i) \times \boldsymbol{p}_j}{|\boldsymbol{r}_i - \boldsymbol{r}_j|^3} \tag{5}$$

In eqn (3) Z_A represents the nuclear charge and $g' = 2g_e - 2$. The latter will be set to 2 in the remainder of the paper.

The direct calculation of the two-electron Hamiltonian matrix elements requires the evaluation of four-center integrals which are computationally very demanding. Several approximations have therefore been suggested, mainly based on the replacement of the two-body interaction by an effective one-electron operator, although contributions arising from the antisymmetric (or exchange) term are therefore completely neglected, which poses serious problems in the evaluation of the spin–other-orbit term (SOO). A reduction to a single-particle operator is most efficiently accounted for by means of some mean-field approach. As emphasized by Neese[71] a more quantitative accuracy is reached by explicit inclusion of the antisymmetric term. The different approaches, as proposed in the literature, will be tested on their reliability for the g-tensor computation for different isolated paramagnetic molecules with spin varying from 1/2 to 3. In particular the high spin radicals will be the subject of thorough investigation as they pose additional problems due to the presence of multiple singly occupied molecular orbitals.

3.2.1 Spin–orbit mean-field (SOMF). We apply a somewhat different method than proposed by Neese[71] for the derivation of the antisymmetric (direct Coulomb + exchange) two-electron spin–orbit interaction $\hat{H}_{SO(2e)}$ and spin–other-orbit term $\hat{H}_{SOO}$. It relies on second quantization formalism and leads to additional contributions for high-spin molecules. Intermediary key steps are explained in the Appendix.

Completely similar to mean-field approaches, like Hartree–Fock, we define a spin–orbit mean-field $\hat{I}^{SO}$, which takes into account the interaction with all occupied orbitals:

$$\begin{aligned}\langle h|\hat{I}^{SO}|p\rangle &= \sum_{\alpha\in occ} \langle h\alpha|\hat{V}_{12}^{SO}|p\alpha\rangle_{as} \\ &= -\frac{1}{2}\sum_{a\in occ} \langle ha|\hat{L}_{1z}|pa\rangle + \frac{3}{4}\sum_{a\in occ} (\langle ha|\hat{L}_{1z}|ap\rangle + \langle ah|\hat{L}_{1z}|pa\rangle)\end{aligned} \tag{6}$$

with $\hat{V}_{12}^{SO} = \hat{V}_{12}^{SO(2e)} + \hat{V}_{12}^{SOO}$; h stands for the singly occupied orbital in the case of a spin-$\frac{1}{2}$ system and p any virtual orbital. Essential in the evaluation of the mean-field is the antisymmetric nature of the two-body interaction matrix elements including exchange terms besides the direct Coulomb contribution. $\boldsymbol{L}_1$ stands for some pseudo orbital momentum.

$$\boldsymbol{L}_1 = \frac{\alpha^2}{r_{12}^3}(\boldsymbol{r}_{12} \times \boldsymbol{p}_1) \tag{7}$$

which coincides with $-2g^{soc}(1,2)$ used by Neese.[71]

The different steps leading to the final expression of eqn (6) are outlined in the appendix. Use is made of the exact relationship between the exchange of the SOO and the SO(2e)

$$\sum_{\alpha\in occ} \langle h\alpha|V_{12}^{SOO}|\alpha p\rangle = 2\sum_{\alpha\in occ} \langle h\alpha|V_{12}^{SO(2e)}|\alpha p\rangle \tag{8}$$

which remains valid for high-spin systems (see Appendix).

Application of eqn (6) is the so-called spin–orbit mean-field (SOMF) approach, as implemented in ORCA. A similar method is the Atomic Mean-Field Integrals (AMFI) approach, where only one-center integrals are computed to further reduce the computational cost. Even this rather crude approximation performs quite well.[5]

The expression for the spin–orbit mean-field is slightly modified for high-spin complexes. The hp-pair also interacts with the singly occupied orbitals b, leading to some additional contributions in the direct Coulomb term:

$$\begin{aligned}\langle h|I^{SO}|p\rangle = &-\frac{1}{2}\sum_{a\in occ} \langle ha|L_{1z}|pa\rangle - \frac{1}{4}\sum_{b\in occ} \langle hb|L_{1z}|pb\rangle \\ &+\frac{3}{4}\sum_{c=a,b\in occ} (\langle hc|L_{1z}|cp\rangle + \langle ch|L_{1z}|pc\rangle)\end{aligned} \tag{9}$$

In contrast to the spin-$\frac{1}{2}$ systems there is a non-vanishing contribution from the SOO interaction to the direct

Coulomb term

$$-\frac{1}{2}\sum_{b\neq\in\mathrm{occ}}\langle hb|L_{1z}|pb\rangle \tag{10}$$

This term is new and hence not taken into consideration in earlier theoretical works.[71,75] It gives a non-negligible contribution to Δg^{SOO} as discussed in the computational results.

3.2.2 Effective potential within the KS-scheme. Explicit use of a two-body operator in a Kohn–Sham (KS) scheme is in principle inconsistent with the DFT concept. The direct Coulomb term for the two-electron spin–orbit interaction can easily be implemented with DFT, but the exchange contribution cannot be simulated within a one-body scheme. It is not surprising that the method as suggested by G. Schreckenbach and Ziegler[70] where the SO(2e) exchange contribution is modeled as ∇v_{xc} gives rise to arbitrary and thus unreliable results. Similarly it is excluded that the exchange part of the spin–other-orbit contribution can be evaluated within the Kohn–Sham scheme even approximately by using functionals specifically constructed to find an accurate ground state energy.

The effective potential method is based on the fact that the gradient of a Coulombic potential has the same radial dependence (*i.e.* $\boldsymbol{r}/r^3$) as the spin–orbit coupling. This is true for the external potential $v_{\mathrm{ext}}=\sum_A\frac{-Z_A}{|\boldsymbol{r}-\boldsymbol{R}_A|}$ and for the Hartree term $v_{\mathrm{H}}=\int\frac{\rho(\boldsymbol{r})}{|\boldsymbol{r}-\boldsymbol{r}'|}\mathrm{d}\boldsymbol{r}'$

The direct part of the two-body interaction can therefore exactly be reduced to an effective one-body potential

$$\hat{H}^{(1)}_{\mathrm{SO,Coul}}=\sum_i\frac{\alpha^2}{2}\boldsymbol{s}_i\cdot(\nabla v_{\mathrm{H}}(\boldsymbol{r})\times\boldsymbol{p}). \tag{11}$$

Its contribution to the first order-perturbation energy expression, needed for the calculation of the g-matrix (see Appendix) readily becomes

$$\langle\Psi^{(0)}|\hat{H}^{(1)}_{\mathrm{SO,Coul}}|\Psi^{(1)}\rangle=\frac{\alpha^2}{2}\langle m_{s,h}|\boldsymbol{s}|m_{s,p}\rangle\cdot\langle h|\nabla v_{\mathrm{H}}(\boldsymbol{r})\times\boldsymbol{p}|p\rangle \tag{12}$$

$$=-\frac{1}{2}\sum_{a\in\mathrm{occ}}\langle ha|L_{1z}|pa\rangle \tag{13}$$

after inserting the electron density $\rho(\boldsymbol{r}')=\sum_{c\in\mathrm{occ}}\psi^*_c(\boldsymbol{r}')\psi_c(\boldsymbol{r}')$ determined by the Kohn–Sham orbitals ψ_c. $|\Psi^{(1)}\rangle$ represents the first order excitation of the KS ground state $|\Psi^{(0)}\rangle$, where the singly occupied orbital h is replaced by p.

So, the direct Coulomb two-electron distribution of eqn (4) is exactly reproduced by the effective one-body operator (11). On the basis of this exact relationship, this concept has been extended by Schreckenbach and Ziegler[70] and others,[6] to the whole Kohn–Sham potential $v_{\mathrm{KS}}=v_{\mathrm{ext}}+v_{\mathrm{H}}+v_{xc}$. In this way some effective spin–orbit interaction of one-body nature can be introduced:

$$H^{(1)}_{\mathrm{SO,eff}}=\sum_i\frac{\alpha^2}{2}\boldsymbol{s}_i\times(\nabla v_{\mathrm{KS}}(\boldsymbol{r})\times\boldsymbol{p}_i) \tag{14}$$

This effective operator includes the gradient of the exchange correlation functional v_{xc} and one expected that it could mimic the exchange contribution of the two-electron spin–orbit interaction. Unfortunately, as it was already clearly reported by Neese,[71] numerical calculations undoubtedly demonstrate that the corrections arising from the ∇v_{xc} term are more or less of the same magnitude but with opposite sign compared to the exact exchange as calculated in the SOMF. We will come back extensively to this issue later on in the discussion section. Thus far about the two-electron spin–orbit interaction.

Regarding the spin–other-orbit coupling terms, within DFT there is no ready-made solution. Several approximations were suggested:

(i) It can completely be omitted (referred to V_{eff} method), as originally proposed by Schreckenbach and Ziegler.[70] These authors argued that this contribution is very small even if there is more than one unpaired electron. As correctly noticed by Neese[71] this is true for the direct Coulomb contribution in spin-$\frac{1}{2}$ molecules, but certainly not for the exchange term (see eqn (8)).

(ii) Another alternative is the method proposed by Pickard and Mauri[8] for the evaluation of the SOO correction. It is based on the screening of the external field B by the induced electronic currents, as experienced by the unpaired electron ($V_{\mathrm{eff,PM}}$).

$$\Delta g^{\mathrm{SOO}}_{xy}=\frac{1}{S}\int B^{1,x}_y(\boldsymbol{r})[\rho_\alpha-\rho_\beta]\mathrm{d}\boldsymbol{r} \tag{15}$$

in which $B^{1,x}$ is the magnetic field induced by the electronic currents when a magnetic field with unit magnitude is applied in the x direction (referred to as $V_{\mathrm{eff,PM}}$).

(iii) The SOO exchange can be taken into account following its relation with the exchange of SO(2e) as established in eqn (8). This would imply that in the effective potential method the $\hat{H}^{(1)}_{\mathrm{SO},v_{xc}}$ contribution should be multiplied by a factor $+3$ to take into account the spin–other-orbit correction:

$$\Delta g(\mathrm{SO(2e)_{exch}})+\Delta g(\mathrm{SOO_{exch}})=\sigma\Delta g(\nabla v_{xc}) \tag{16}$$

with $\sigma=3$.

However, as already noticed, the $H^{(1)}_{\mathrm{SO},v_{xc}}$ corrections have the wrong sign but roughly the same magnitude (factor 1.3 larger) as the exchange contribution of $V_{12}^{\mathrm{SO(2e)}}$. The scale factor σ switches to a value which can vary between -2 and -2.4. This procedure for computing the SOO exchange following the lines as expressed in eqn (16) with introduction of a scale factor σ is referred to as $V_{\mathrm{eff,SOO}(\sigma)}$. Neese[71] suggested a scale factor $\sigma=-2$ to achieve numerically the best agreement with the SOMF.[71] One of the goals of this work is to investigate the possible transferability of this scale factor to other paramagnetic systems and its dependence on the choice of the exchange correlation functional. Such an investigation has its large merits as it can be further explored to compute spin–orbit corrections to the g-tensor at the same accuracy as the SOMF method, but at a significantly less computational cost, especially for periodic purely density based codes.

(iv) Next to the scaling method, we found for high spin states an extra contribution for the direct SOO part as given by eqn (10). This term can also be written in the form

$$\langle\Psi^{(0)}|\hat{H}_{\mathrm{SOO,eff}}|\Psi^{(1)}\rangle|_{\mathrm{direct}}=\frac{\alpha^2}{2}\langle h|[\nabla v_{\mathrm{H}}[\rho_\uparrow-\rho_\downarrow](r)\times\boldsymbol{p}]_z|p\rangle \tag{17}$$

Table 3 Overview of the various spin–orbit contributions to the $\Delta g_{\mathrm{ortho}}$ shift involved in the different methods. Exchange spin–other-orbit contributions are always evaluated according to the relation $\Delta g(\mathrm{SOO,exchange}) = 2\Delta g(\mathrm{SO(2e),exchange})$. In the effective potential method the exchange contribution of the two-electron spin–orbit interaction is evaluated through $\hat{H}^{(1)}_{\mathrm{SO},Vxc}$, multiplied with a scale factor σ as given in eqn (16). In this convention: $V_{\mathrm{eff}} = V_{\mathrm{eff,SOO}(\sigma=1)}$

			$\mathrm{SO(2e)_{exchange}}$		$\mathrm{SOO_{exchange}}$			
	SO(N)	$\mathrm{SO(2e)_{direct}}$	Two-body	∇V_{xc}	Two-body	∇V_{xc}	PM	$\mathrm{SOO_{direct}}$
Z_{eff}	✓							
V_{eff}	✓	✓		$\sigma = 1$				
$V_{\mathrm{eff,PM}}$	✓	✓		$\sigma = 1$			✓	
$V_{\mathrm{eff,SOO}}$	✓	✓		σ		✓		
$V^{*}_{\mathrm{eff,SOO}}$	✓	✓		σ		✓		✓
SOMF	✓	✓	✓		✓			

with $v_{\mathrm{H}}[\rho_\uparrow - \rho_\downarrow] = \int \frac{\rho_\uparrow(\boldsymbol{r}') - \rho_\downarrow(\boldsymbol{r}')}{|\boldsymbol{r} - \boldsymbol{r}'|} \mathrm{d}\boldsymbol{r}'$, which makes the implementation into CP2K much easier. In Section 4.3 we discuss the results of this new approach. This method, combined with the scaling of the exchange contribution, is referred to as $V^{*}_{\mathrm{eff,SOO}}(\sigma)$.

3.2.3 Effective nuclear charge (Z_{eff}). For completeness we also include a more simple approach which considers the two-electron spin–orbit Hamiltonian terms as screening terms for the one-electron H_{SON} contribution. One could neglect those two-electron contributions and compensate for them using an effective nuclear charge $Z_{A,\mathrm{eff}}$.[7,76–78] Eqn (3) is then rewritten as:

$$\hat{H}_{\mathrm{SO(N)}} = \sum_i \frac{g'}{4c^2} \sum_A Z_{A,\mathrm{eff}} \boldsymbol{s}_i \cdot \frac{(\boldsymbol{r}_i - \boldsymbol{R}_A) \times \boldsymbol{p}_i}{|\boldsymbol{r}_i - \boldsymbol{R}_A|^3} \qquad (18)$$

This simple approximation is available in several packages including Gaussian and ORCA.

For convenience of the reader an overview of the various models discussed in the paper is given in Table 3, including the various ingredients of the method. In Table 4 these are linked to the appropriate *ab initio* programs, including the new implementations.

3.3 Gauge

The vector potential $\boldsymbol{A}$ is defined up to an arbitrary translation. In principle the choice of this gauge should not influence any result, but basis set incompleteness causes a gauge dependency.

When using a common gauge origin (*e.g.* in ORCA) it is of interest to vary its position along the internuclear axis of the RhC molecule. This results in a maximum difference between the calculated g-values of $|g_{\mathrm{ortho}}(-1.2\ \text{Å}) - g_{\mathrm{ortho}}(1.2\ \text{Å})| \leq$ 1ppt which is much smaller than the effect of a relativistic Hamiltonian or the inclusion of the spin–other-orbit term (see below).

Table 4 *Ab-initio* packages–available spin–orbit approximations

	Z_{eff}	V_{eff}	$V_{\mathrm{eff,SOO}}$	$V^{*}_{\mathrm{eff,SOO}}$	$V_{\mathrm{eff,PM}}$	AMFI	SOMF
ORCA	✓	✓	✓				✓
G09	✓						
ADF		✓					
DALTON	✓					✓	
ReSpect	✓					✓	
CP2K		✓	✓	✓	✓		
GIPAW					✓		
BAND		✓					

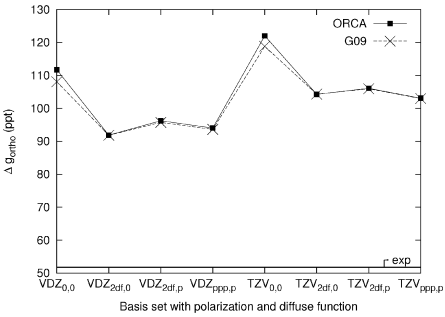

Fig. 1 Non-relativistic Gaussian09 results compared to the ORCA results. In both cases the Z_{eff} spin–orbit approximation was used. Both double (VDZ) and triple (TZV) ξ basis sets are used, to which several types of polarization (2df, ppp) and diffuse functions (p) are added, as indicated on the x-axis.

Another method which is commonly used is to include the gauge dependency into the atomic orbitals (Gauge Including Atomic Orbitals, GIAO[79]) as implemented in the Gaussian program and ADF (see Table 2). In Fig. 1 the Gaussian09 results using the Z_{eff} method (which is the only available option in Gaussian09) are compared with those of ORCA, in which a common gauge at the center of electronic charge was used. We can clearly see the agreement between both approaches. Additionally this figure shows that the gauge dependence is indeed due to a basis set incompleteness, as the differences are smaller for more extended basis sets.

The large discrepancies between experiment ($\Delta g_{\mathrm{ortho}} =$ 51.78 ppt) and computed results are caused by the use of a non-relativistic Hamiltonian and the Z_{eff} method, as will become clear further on.

4 Results and discussion

The focus of the paper is twofold. First we present a complete assessment study for the computation of the g-tensor for a spin 1/2 system containing a transition metal. We choose RhC as test case and discuss the predictions of the various models for the spin–orbit coupling as outlined in the methodology section.

Almost all spin–orbit models are implemented in ORCA. In addition, both relativistic and non-relativistic wave functions can be used, and a large choice of basis sets with polarization and diffuse functions is available in which the wave function can be expanded. For obvious reasons we choose ORCA as the reference non-periodic code for computation of *g*-tensors in gas-phase molecules.

Subsequently the ability of periodic codes to calculate accurately the *g*-tensor of RhC will be investigated. Although periodic codes are not ideally suited to model small isolated molecules, it is useful in this assessment study as the contributions of the different approaches for the *g*-tensor evaluation can easily be compared to their gas phase counterparts. The detailed comparison between the gas phase calculations and the various periodic results can give valuable information on how far the current protocols embedded in periodic codes are suitable to predict accurate *g*-tensors for more extended transition metal containing molecular systems for which standard gas phase calculations cannot be used due to the restrictions imposed on the cluster size.

Next to the preliminary conclusions drawn on the RhC compound, the other objectives of this study can only be accomplished if we extend the validation set to a wider range of molecules. We selected two sets of diatomic radicals used in previous benchmarks.[33,34,60] The first set consists of molecules with one unpaired electron,[34,60] while in the second set only high-spin radicals are taken up.[33] Both sets contain transition metal complexes and thus are relevant for the goal of this paper.

The second focus lies on the prediction of accurate spin–orbit contributions and in particular the exchange part of the two-electron spin–orbit term and the contribution of the spin–other-orbit interaction. In particular for paramagnetic high-spin molecules this discussion has not yet been held in the literature. Focus will also lie on the ability of periodic codes in predicting Δg shifts in close agreement with the spin–orbit mean-field method. The method proposed by Neese to overcome the anomaly present in the effective potential method for the prediction of the exchange contribution has been tested for a whole range of radicals and high-spin molecules.

For all molecules no further optimization has been performed: all geometrical parameters and the spin multiplicity of the energetically most favored configuration (for the high spin radicals) have been taken as reported in the literature.[33,60] When available the experimental values for the internuclear distances were taken for the spin-1/2 molecules. For more details concerning these sets we refer to the ESI.†

Discrepancies between the calculated *g* values and experimental EPR data for this test set can have several reasons: they can be due to the neglect of the molecular environment of the radical in the calculation (typically an inert matrix in the experiment), the internuclear distance might be incorrect (whether calculated or taken from X-ray diffraction experiments), or they indicate an inherent methodological failure of the approach used to calculate the *g*-tensor. In this work we will only concentrate on the last aspect.

To bias the influence of both experimental (internuclear distance, environment) and computational (exchange-correlation functional) errors and focus on the computational accuracy of the method under investigation, we opted to choose computational reference values of high quality calculations.

4.1 RhC as a test case for spin-$\frac{1}{2}$ systems

Rhodium is an element of the second transition row ($Z = 45$) with electronic structure $[Kr]^4d^85s^1$. RhC has a $^2\Sigma^+$ ground state with the unpaired electron in a molecular orbital constructed by the $4d_z^2$ and 5s orbitals of rhodium and the orbital $2p_z$ character of carbon.

The *g*-tensor anisotropy is large: 51.78 ppt for the orthogonal and 1.58 ppt for the parallel component. The prediction for the parallel component of the *g*-tensor is independent of the choice of the spin–orbit approximation and the basis set. A constant value of 0.22 ± 0.01 ppt is found. This is in full agreement with the fact that the Schreckenbach and Ziegler method cannot calculate the g_{para} for molecules with $^n\Sigma$ molecular term symbols.[1] Table 5 collects the various model predictions for the orthogonal Δg_{ortho} contributions in RhC.

4.1.1 Effect of relativistic Kohn–Sham orbitals and basis set dependence. A first survey concerns the impact of a relativistic approach on the g_{ortho} tensor values. Table 5 reveals that relativistic effects give rise to a shift of the *g*-tensor predictions with respect to the non-relativistic results, independently of the spin–orbit coupling method taken into account. The non-relativistic

Table 5 Calculation of the orthogonal component of the *g*-tensor (Δg_{ortho} in ppt) in RhC using the PBE functional in ORCA. Different models and basis sets are considered: non-relativistic *versus* relativistic models and contributions from the various spin–orbit approaches are reported. In $V_{eff,SOO}$ a scale factor of -2 is considered. Relativistic model makes use of the ZORA approach and the common gauge at the center of electron charge. The parallel component g_{para} is not tabulated as the same value (0.22 ± 0.01ppt) is found in all cases

	ORCA								CP2K		
	Relativistic				Nonrelativistic				Nonrelativistic		
	Z_{eff}	V_{eff}	$V_{eff,SOO}$	SOMF	Z_{eff}	V_{eff}	$V_{eff,SOO}$	SOMF	V_{eff}	$V_{eff,PM}$	$V_{eff,SOO}$
VDZ	89.62	62.51	52.27	51.97	111.73	70.72	66.06	65.69	70.80	70.73	67.63
VDZ, 2df	80.02	55.80	46.32	46.05	91.89	57.61	53.66	53.34	58.01	58.00	55.30
VDZ, 2df, p	82.47	56.44	47.83	47.55	96.27	60.45	56.33	56.00	60.63	60.58	57.82
VDZ, ppp, p	81.07	55.33	47.05	46.78	94.03	59.06	55.04	54.71	59.30	59.26	56.56
TZV	98.69	56.26	58.14	57.80	122.04	77.81	72.69	72.27	78.17	78.13	74.52
TZV, 2df	88.56	49.94	51.82	51.50	104.28	66.04	61.59	61.21	66.64	66.61	63.42
TZV, 2df, p	89.56	51.54	52.42	52.10	106.09	67.22	62.68	62.30	67.61	67.59	64.35
TZV, ppp, p	87.81	50.69	51.39	51.08	103.08	65.29	60.88	60.52	65.76	65.75	62.58
Exp	51.78	51.78	51.78	51.78	51.78	51.78	51.78	51.78	51.78	51.78	51.78

predictions are overestimated and strongly affected by the choice of the basis set. Indeed, inclusion of polarization functions leads to significant decrease of the orthogonal component of the g-tensor. The relativistic ZORA-predictions, however, reproduce the experimental value systematically better. The dependence on the presence of polarization functions is less dramatic. When the most advanced spin–orbit approximation, SOMF, is used, both double- and triple-ζ basis sets yield a more pronounced convergence behavior towards experiment with preference to the triple-ζ, which converges towards the experimental g_{ortho}. With a double-ζ basis set, without polarization or diffuse functions, the experimental g_{ortho} is even correctly reproduced, which is most likely a coincidence, but which should be verified in other transition metal doublets.

4.1.2 Spin–orbit approximation. From Table 5, it is clear that the most rudimentary approach (Z_{eff}) performs poorly as it systematically overestimates the experimental data by more than 28 ppt in the relativistic case and even twice this value in the non-relativistic treatment. This method is not appropriate to investigate systems containing transition metals.

The effective potential approximation (V_{eff}) performs much better, despite the unphysical behavior of the $\Delta g(\nabla v_{xc})$ contribution. But as this correction term is small, it does not significantly affect the global Δg shift. Compared to the Z_{eff} results, this approach almost always causes a rise of $\Delta g_{\mathrm{ortho}}$ by about 40 ppt, yielding a much better agreement with experiment.

The agreement further improves if we correct the wrong sign of the effective $\Delta g(\nabla v_{xc})$ contribution ($\sigma = -1$), but it becomes even much better if we consider a scale factor $\sigma = -2$ ($V_{\mathrm{eff,SOO}}$) following the suggestion of Neese, in this way incorporating the spin–other-orbit interaction in the effective potential method, as discussed in the theoretical section. The predictions of the Δg shift with SOMF don't differ much from $V_{\mathrm{eff,SOO}(\sigma=-2)}$, but this is due to the choice of the scale factor. We come back to this issue later in the discussion.

What conclusion can be drawn from Table 5 about the methodology reproducing as best the experimental g-tensor in the case of RhC? In both relativistic and non-relativistic approaches the best performing method is SOMF, followed by the $V_{\mathrm{eff,SOO}(\sigma=-2)}$ method. The former is much more expensive in computation time, while the latter is computationally favorable as no two-body matrix elements have to be evaluated, especially for periodic codes. The remarkable property that the effective exchange contribution scales linearly with SOMF makes this approach the most favorable for larger radicals. It fails when the linear relationship with the SOMF result does no longer hold or when the scale factor is strongly varying throughout the training set. Therefore the accuracy of the $V_{\mathrm{eff,SOO}(\sigma)}$ method will depend on this behavior and will be the subject of study in the remainder of this paper.

Concluding, the two SOMF and $V_{\mathrm{eff,SOO}(\sigma)}$ methods, both including spin–other-orbit interactions perform the best, and in view of the significantly larger computation time for the SOMF method, we could give preference to the $V_{\mathrm{eff,SOO}(\sigma)}$ method, but this should be confirmed by additional calculations on other systems.

4.1.3 Box size dependence on periodic codes. When applying a periodic code on an isolated molecule, the periodic cell should be large enough to prevent unphysical interactions originating from nearby periodic images or boundary conditions. Only under these conditions a reliable comparison with previous results can be made. The CP2K prediction for the orthogonal component of the g-tensor at different box sizes is plotted in Fig. 2. It shows a nice convergence behavior towards the ORCA result, using the same basis set (TZV), functional (PBE) and spin–orbit approximation (V_{eff}). For this small test system with a molecular size of about 1.613 Å, a box size of 12 Å is sufficient to yield an almost completely converged value.

A similar calculation is performed to test the box size dependence of the GIPAW predictions. It is expected that they approach the relativistic ORCA results with ZORA and the V_{eff} method. Due to the inherent usage of plane waves and pseudopotentials in GIPAW a direct comparison to a specific basis set choice in ORCA is not possible. Therefore we consider a range of width 6 ppt, determined by the ORCA–ZORA g_{ortho} values belonging to a TZV basis with various polarization and diffuse functions (see Fig. 2), as a reference for the convergence in GIPAW. Convergence is only reached at very large box sizes (at least 18 Å). This is an undesirable side effect, as large box sizes are computationally very demanding since a huge number of plane waves is required to describe the *vacuo*. This unfavorable aspect with respect to non-periodic codes has no serious consequences for truly periodic systems (*e.g.* defects in salts[15] or zeolites).

BAND on the other hand does not show a typical converging behavior as other periodic codes, but rather exhibits a fluctuating pattern when increasing the box size (Fig. 3). This is probably caused by interactions between periodic images which cannot be turned off in this program.

For the calculation of EPR properties, it is recommended to use an all electron approach. In GIPAW the core electrons are reconstructed, while BAND uses frozen core atoms for heavy elements. In CP2K the g-tensor can be determined from both

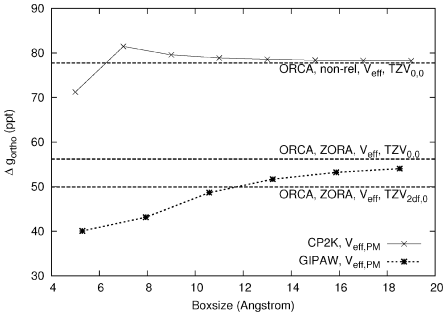

Fig. 2 Box size dependency of the orthogonal component of the g-tensor using the periodic CP2K (non-relativistic, TZV, V_{eff}) and GIPAW code (relativistically corrected pseudopotentials). Reference values are taken from ORCA (TZV basis, V_{eff}) and a range of values generated by ORCA (V_{eff}, ZORA) using a TZV basis set and several diffuse and polarization functions.

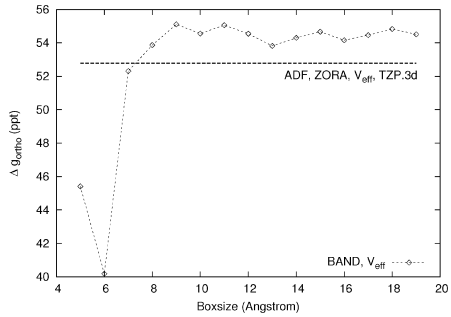

Fig. 3 Box size dependency of the orthogonal component of the *g*-tensor using BAND (TZP.3d basis set). The reference value is an ADF result with the same basis set.

pseudopotential (GPW) and all-electron (GAPW) wavefunction calculations. The GPW method fails to reproduce the experimental data. When 36 core electrons were considered, a Δg of -0.84 ppt was found. Use of a smaller set of core electrons (28) yields no improvement ($\Delta g = -2.22$ ppt). This could be caused by the inaccurate description of the valence electrons in this core region. Therefore, the computationally more expensive all electron GAPW method is highly recommended for *g*-tensor calculations on radicals.

In the current versions of CP2K and GIPAW the $V_{\mathrm{eff,PM}}$ method is the highest level present for the computation of the spin–orbit matrix elements, whereby the spin–other-orbit correction is computed using the Pickard and Mauri (PM) scheme (see theoretical section). From Table 5 it is clear that this spin–other-orbit term is negligible and even shows the wrong sign. As already mentioned the accuracy of the CP2K prediction can seriously be improved by implementing the $V_{\mathrm{eff,SOO}(\sigma)}$ method with $\sigma = -2$ or even a higher value for the scale factor (see further discussion) and inclusion of the direct SOO contribution for high spin systems. In Table 5 both V_{eff} and $V_{\mathrm{eff,SOO}}(\sigma)$ results obtained in ORCA and CP2K are given. They show a nice agreement despite the difference in the choice of gauge.

4.2 Radical doublets (spin 1/2 systems)

The next two subsections will be devoted to the reproduction and the discussion of the various spin–orbit contributions, which lie on the origin of the observed Δg shift from the free electron g_e value. Conclusions drawn for the specific RhC case will be further assessed to a wider range of molecules. The most advanced SOMF method can be taken as reference model, but the performance of the effective $V_{\mathrm{eff,SOO}(\sigma)}$ method will receive special attention due to the significantly less computational cost, the more as in periodic codes as CP2K *g*-tensor calculations are based on the DFT-based effective potential method. In particular the behavior of the scale factor σ will be assessed on its robustness.

First we select a set of diatomic radicals, which already has been used in earlier benchmark studies.[33,34,60] They are listed in Tables 6 and 7 and ordered according to the position of the heaviest element in the periodic table. Experimental Δg shifts are taken from the literature.[60] For all ORCA results a triple-ζ quality basis set with polarization functions (Ahlrichs 2df) was used.

In Table 6 the several contributions to the *g*-tensor are listed to give insight into the importance of each spin–orbit term. Both ORCA and CP2K results are present, however the SO(N) part is only calculated separately using ORCA. The Zeeman Kinetic Energy part (ZKE) is identical for both codes and therefore only reported for ORCA.

The one-electron contribution SO(N) is the trendsetter whether *g* will deviate largely from the free electron value. All species reporting a *g* value significantly different from the free-electron *g*-value report a large SO(N) contribution. In most of the cases the prediction of SO(N) overshoots the observed Δg shift. This is best illustrated with PdH exhibiting the largest deviation from g_e and whose experimental Δg tensor value amounts to 290.88 ppt. From all spin 1/2 molecules

Table 6 Various spin–orbit contributions to the $\Delta g_{\mathrm{ortho}}$ shift(in ppt) for several radical doublets. All calculations were performed with PBE and Ahlrichs TZV, 2df basis set. The scaling factors σ and σ' are defined in eqn(19) and (20) respectively

		ORCA					CP2K			
					SO(2e)$_{\mathrm{exch}}$					
	Exp	ZKE	SO(N)	SO(2e)$_{\mathrm{dir}}$	SOMF	∇v_{xc}	SO(N) + SO(2e)$_{\mathrm{dir}}$	(∇v_{xc})	σ	σ'
RhC	51.78	−0.144	83.680	−18.990	−1.110	1.485	65.869	1.311	−2.24	−2.54
BO	−1.72	−0.095	−2.832	0.790	0.129	−0.174	−1.750	−0.120	−2.22	−2.21
BS	−8.12	−0.107	−11.571	1.822	0.263	−0.362	−9.063	−0.259	−2.18	−3.05
AlO	−1.22	−0.181	−2.861	0.455	0.015	−0.016	−2.545	0.007	−2.85	6.68
GaO	−34.32	−0.234	−37.676	2.360	−0.028	0.006	−35.642	0.030	−14.59	−2.84
ScO	−0.52	−0.070	−1.263	0.912	0.074	−0.091	−0.203	−0.058	−2.45	−3.82
ZnH	−17.12	−0.096	−17.648	1.255	0.154	−0.233	−16.030	−0.162	−1.99	−2.85
ZnF	−6.32	−0.152	−7.309	0.426	0.056	−0.084	−6.878	−0.013	−2.03	−13.45
ZnAg	−11.82	−0.066	−20.200	2.535	0.208	−0.307	−17.124	−0.195	−2.03	−3.20
YO	−0.22	−0.071	−1.778	0.968	0.064	−0.082	−0.695	−0.050	−2.34	−3.80
PdH	290.88	−0.348	344.702	−79.558	−4.664	6.323	250.802	4.765	−2.21	−2.94
CdH	−49.92	−0.098	−55.316	3.102	0.326	−0.481	−51.340	−0.358	−2.03	−2.73
CdF	−17.32	−0.154	−21.812	1.385	0.129	−0.186	−20.211	−0.133	−2.08	−2.91
CdAg	−31.22	−0.072	−60.136	4.696	0.356	−0.579	−54.459	−0.379	−1.85	−2.82
InO	−192.32	−0.247	−110.208	5.635	0.254	−0.396	−104.067	−0.332	−1.93	−2.30

Table 7 Complete $\Delta g_{\mathrm{ortho}}$ in ppt for spin-$\frac{1}{2}$ systems

		ORCA			CP2K	
	Exp	SOMF	V_{eff}	$V_{\mathrm{eff,SOO}}$ ($\sigma = -2$)	V_{eff}	$V_{\mathrm{eff,SOO}}$ ($\sigma' = -2.8$)
RhC	51.78	72.29	77.79	72.69	67.04	61.79
BO	−1.72	−1.75	−2.31	−1.79	−2.29	−1.81
BS	−8.12	−9.07	−10.22	−9.13	−10.25	−9.21
AlO	−1.22	−2.54	−2.60	−2.56	−2.54	−2.56
GaO	−34.32	−35.63	−35.54	−35.56	−35.45	−35.57
ScO	−0.52	−0.20	−0.51	−0.24	−0.46	−0.23
ZnH	−17.12	−16.03	−16.72	−16.02	−16.82	−16.18
ZnF	−6.32	−6.87	−7.12	−6.87	−5.99	−5.94
ZnAg	−11.82	−17.11	−18.04	−17.12	−17.19	−16.41
YO	−0.22	−0.69	−0.96	−0.72	−0.80	−0.60
PdH	290.88	250.80	271.12	252.15	269.63	250.57
CdH	−49.92	−51.33	−52.79	−51.35	−53.27	−51.84
CdF	−17.32	−20.19	−20.77	−20.21	−20.27	−19.74
CdAg	−31.22	−54.44	−56.09	−54.35	−52.56	−51.04
InO	−192.32	−104.06	−105.22	−104.03	−105.50	−104.17

of the training set indeed PdH predicts the largest spin–orbit–nucleus correction, but with 344.70 ppt it overestimates the experimental value with 54 ppt.

The direct Coulomb correction cancels for a part the excess of the SO(N) contribution. It has systematically another sign, and is essential to go closer to the experimental value. We don't see some systematics in its magnitude with respect to the most dominant SO(N) value. Its relative importance with respect to the SO(N) value varies from 5% to more then 50%.

In only one case (InO) the one-electron contribution is largely insufficient for explaining the experimental behavior. With a contribution of −110 ppt it is by far too small to come in the vicinity of the experimental value of −192 ppt. Two-electron spin–orbit contributions are insufficient to compensate this underestimation of the one-electron part.

For the exchange contribution of the SO(2e) part, both the SOMF and the V_{eff} method were used and compared. It is clear from the table that there is a systematic difference of the predictions in both approaches. According to relation (16) discussed in previous section, we report in Table 6 the scale factor σ relating the exchange contribution of the SOMF two-electron term and the effective SO(2e; ∇v_{xc}) prediction. It is determined by

$$\sigma = -\frac{3\Delta g(\mathrm{SO(2e)_{exch,SOMF}})_{\mathrm{ORCA}}}{\Delta g(\nabla v_{xc})_{\mathrm{ORCA}}} \qquad (19)$$

and shows a remarkable tendency to −2 which almost coincides with the suggested value of Neese. This is a highly remarkable behavior and we can make use of it to switch the unrealistic DFT exchange correction SO(2e; ∇v_{xc}) to a reliable value which nicely reproduces the exact exchange obtained from a procedure that needs a much larger computational cost. At the same time the SOO contribution can be taken into account in view of the relation with the two-electron exchange term.

We also include the results obtained with the periodic code CP2K, making use of the effective potential method. Despite the same functional has been employed and the same exchange-correlation functional v_{xc} for the evaluation of the SO(2e; ∇v_{xc}) contribution, we notice some discrepancies in the values predicted by the non-periodic code ORCA. The SO(2e; ∇v_{xc}) contributions are systematically underestimated with respect to their ORCA counterparts. We propose the same procedure as in ORCA in introducing a scale factor σ' relating the CP2K exchange predictions to the exact SO(2e;exch) in SOMF.

$$\sigma' = -\frac{3\Delta g(\mathrm{SO(2e)_{exch,SOMF}})_{\mathrm{ORCA}}}{\Delta g(\nabla v_{xc})_{\mathrm{CP2K}}} \qquad (20)$$

This procedure offers a suitable protocol to overcome the obstacle of unphysical reproduction of exchange values under conditions that the new scale factor σ' also behaves almost constant throughout the training set. The last column in Table 6 indeed confirms that for the radical doublets the scale factor fluctuates between −2.30 and −3.80 with some minor exceptions. The agreement with the computationally more expensive SOMF-ORCA calculations is even largely improved if we apply a scale factor of about −2.80 through the whole set, but this scaling procedure remains some effective approach which requires confirmation in other training sets. The value of −2.80 is in magnitude somewhat larger than the scale factor proposed by Neese, but this is due to the systematic underestimation of the exchange contribution in the periodic CP2K code. There are some exceptions like AlO and ZnF where the scale factor σ' leaps out to +6.68 and −13.45. For these two cases the absolute values of the exchange contributions are particularly small, generating large error bars. Even when applying the effective value of −2.80 for σ' the global spin–orbit Δg shift in these molecules will be hardly affected.

The exchange part has the same sign but is smaller than the direct Coulomb contribution. To estimate its full impact, the numbers of the column $\mathrm{SO(2e)_{exchange}}$ (SOMF) in Table 6 should be multiplied with factor 3 in order to fully take into account the SOO effect. For spin 1/2 systems and in case the g-shift is larger than 5 ppt, the exchange can represent almost 2–8% of the total SO contribution. This is in line with the observations made by Neese. It is by far not the leading term. However, in cases where the deviation of the g-tensor from the free electron value is small, it can even dominate.

Adding up the different individual contributions in Table 6, we get the total $\Delta g_{\mathrm{ortho}}$ values for all diatomic spin-$\frac{1}{2}$ systems (Table 7). In Neese[71] work the different SO operators have been assessed to a training set of small organic molecules with spin 1/2. The $V_{\mathrm{eff,SOO}}(\sigma = -2)$ came out as most accurate, and in fact our results on a completely different training set lead to the same findings.

The overall agreement with experiment is more than satisfactory (see Table 7). The total SOMF predictions succeed in reproducing the experimental fluctuations of the g-tensor from the free electron value taking place in the training set of radical doublets. The two molecules showing the largest deviation have already been discussed: InO and RhC. Use of relativistic wave functions can resolve this discrepancy in the case of RhC. For InO the use of relativistic methods improves the results as well (up to −124.7 ppt) but the relativistic correction does not go far enough.

The conclusion derived for RhC that non-relativistic predictions are overestimating the Δg shift seems to be not valid for most of the transition metal doublets of our test set. In this context it is interesting to mention the case of PdH which has also been investigated in the work of Neyman[80] using a

relativistic density functional Douglas–Kroll method. Despite the relativistic approach the obtained Δg shift of 247 ppt is not better than the non-relativistic SOMF prediction.

For completeness we also investigated the performance of relativistic approaches in predicting the g-tensor shifts in this extended set of radical doublets. We consider both the perturbative treatment (ORCA) and the two-component methods (ADF). The spin–orbit interaction is limited to the effective potential approach in order to compare the results on equal footing. In this approach the SOO is omitted and no scale factor is introduced to correct for the unrealistic exchange part.

Fig. 4 displays the differences in $\Delta g_{\mathrm{ortho}}$ reported by the various relativistic approaches for all diatomic doublet molecules tabulated in Table 6, extended with some heavier elements. The ZORA routine in ADF makes use of the relativistic two-component method of van Lenthe for the evaluation of the spin–orbit matrix elements. A TZP basis set is used. Similar relativistic model is built in BAND. In ORCA the V_{eff} method with ZORA Hamiltonian is considered together with a triple-ζ basis set with 2df polarization functions.

For the light elements, Fig. 4 reveals that the predictions of the different programs are very close to each other, which is not surprising since they only differ in whether the spin–orbit elements were calculated perturbatively or not. For light elements the spin–orbit interaction is indeed supposed to be small. For the heavier elements, however, the deviations become more and more significant, possibly indicating a failure of the perturbative approach.

But despite the same relativistic model the largest deviations from ZORA-ADF are observed for BAND. It was already noted that the g-tensor shows a fluctuating rather than a convergence pattern, caused by interactions between periodic images (see Fig. 3).

A correlation diagram with the experimental data is given in the ESI.†

Conclusion: The set of radical doublets confirms what has been concluded from the particular assessment of RhC: the full treatment in SOMF is always preferable but the proposed modification of the effective potential method makes

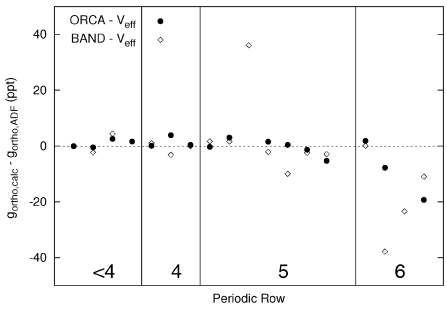

Fig. 4 $\Delta g_{\mathrm{ortho,calc}} - \Delta g_{\mathrm{ortho,ADF}}$ (in ppt) for several doublet molecules, ordered by it's weight. Results of ORCA (with ZORA and V_{eff}) and BAND are compared to the two-component method of ADF. For all calculations a triple-ζ quality basis set with polarization functions (Ahlrichs 2df if possible) was used.

$V_{\mathrm{eff,SOO}}(\sigma = -2)$ an even accurate procedure for predicting g-tensors in transition metal containing doublets due to the robustness of the scale factor σ. A new feature is that this scaling protocol applicable to exchange contributions is also transferable to periodic codes, but with a slightly larger scale factor. We suggest to use $\sigma = -2.8$.

4.3 High spin radicals

For the high spin radicals we select a training set as used by Patchkovskii *et al.*[33] Features observed in the radical doublets will be tested on its transferability to high spin systems with spins varying from 1 to 3.

The results are tabulated in Table 8. The experimental agreement is very good and the largest deviation from experiment is even substantially smaller (less than 50 ppm) than in the training set of radical doublets.

It is clear that the results concerning the exchange contribution formulated for spin-$\frac{1}{2}$ molecules still hold.

The SOMF SO(2e) exchange values are all small but they have to be multiplied with a factor of three to account for the spin–other-orbit corrections before they can be added to the direct Coulomb contribution. The remarkable feature of a quasi constant scale factor relating the exchange contributions between the mean field and the effective potential model still holds. The robustness of the scale factor σ' throughout the whole set of high spin molecules is even better than for the radical doublets. These features have not been assessed and reported before, and therefore very useful to communicate in the recommendation of suitable protocols for g-tensor computations of non-isolated molecules, where periodic codes are obviously more recommended than gas-phase computations.

In Table 8 the direct Coulomb two-electron contribution $(\mathrm{SO(2e)_{direct}})$ does not involve the additional terms arising from the spin–other-orbit (SOO) interaction. In ref. 71 they have been omitted. In the theoretical section we demonstrated the existence of these extra terms, which are only increasing in importance the higher the spin.

In Table 9 results of calculations including and excluding this direct SOO contribution are reported and compared to experimental values. It is clear that this is a non-negligible contribution, which can contribute more than 20% of the total Δg. For molecules with small Δg values, it can even be the dominant contribution. In several cases, the accuracy can be improved quite substantially.

There are, however, some particular cases where the discrepancy with experiment remains large, despite the additional correction terms arising from the direct contribution to the SOO coupling. The origin of these large deviations should be found elsewhere. Changing the internuclear distances does not really improve the experimental agreement. Incorrect KS orbitals could lie at the origin, but this investigation falls outside the scope of this paper. The assumption of isolated molecules in the theoretical calculations might not strike reality when compared to the experimental setup.

5 Conclusion

In this paper an overview is given of all key factors playing a role in the accurate reproduction of the g-tensor of a transition

Table 8 Various spin–orbit contributions to the Δg_{ortho} shift in ppt for several high-spin molecules. Molecules are ranked per spin multiplicity according to the heaviest element. All calculations were performed with PBE and a Ahlrichs TZV 2df. The scaling factors σ and σ' are defined in eqn (19) and (20) respectively

			ORCA					CP2K			
					SO(2e)	SO(2e) exch					
		Spin	ZKE	SO(N)	Direct	SOMF	∇v_{xc}	SO(N) + $SO(2e)_{dir}$	SO(2e) ∇v_{xc}	Scale factor σ	Scale factor σ'
<4	B_2	1	−0.08	0.48	−0.18	−0.03	0.05	0.26	0.03	−1.73	−2.45
<4	*NH*	1	−0.20	2.11	−0.55	−0.09	0.14	1.56	0.11	−1.89	−2.41
<4	*NF*	1	−0.27	2.82	−0.53	−0.10	0.15	2.22	0.12	−2.11	−2.67
<4	*NCl*	1	−0.24	6.84	−0.93	−0.17	0.24	5.84	0.19	−2.08	−2.69
4	*NBr*	1	−0.23	21.59	−1.55	−0.25	0.37	19.91	0.28	−2.06	−2.69
5	*NI*	1	−0.21	−0.47	0.14	0.02	−0.03	−0.22	−0.03	−2.15	−2.41
<4	O_2	1	−0.35	3.98	−0.81	−0.17	0.23	3.11	0.18	−2.23	−2.84
<4	*PH*	1	−0.15	−1.80	6.43	−0.11	0.16	4.60	0.13	−2.03	−2.56
4	*SeO*	1	−0.27	18.32	−1.48	−0.28	0.39	16.48	0.30	−2.15	−2.79
<4	*SO*	1	−0.27	6.58	−1.01	−0.21	0.28	5.45	0.22	−2.24	−2.87
<4	S_2	1	−0.23	16.68	−2.03	−0.32	0.45	14.59	0.35	−2.15	−2.79
<4	*BC*	3/2	−0.11	0.12	−0.04	0.01	0.00	0.07	0.01	7.52	2.67
<4	C_2^+	3/2	−0.15	−0.57	0.15	0.05	−0.05	−0.44	−0.02	−3.24	−6.43
<4	*AlC*	3/2	−0.12	−1.84	0.35	0.06	−0.08	−1.59	−0.05	−2.33	−3.67
<4	*SiB*	3/2	−0.10	−1.42	0.30	0.06	−0.08	−1.19	−0.05	−2.29	−3.60
<4	*SiAl*	3/2	−0.10	−5.14	0.81	0.13	−0.18	−4.40	−0.12	−2.14	−3.02
<4	Si_2^+	3/2	−0.12	−7.98	1.19	0.19	−0.26	−6.74	−0.18	−2.15	−3.04
4	*VO*	3/2	−0.36	−29.98	12.60	1.00	−1.28	−18.02	−0.95	−2.36	−3.15
4	*TiV*	3/2	−0.39	−26.94	11.97	0.90	−1.15	−16.37	−0.89	−2.34	−3.02
4	V_2^+	3/2	−0.35	−18.95	8.12	0.61	−0.78	−12.06	−0.61	−2.34	−2.98
4	*CrN*	3/2	−0.49	−7.18	2.79	0.25	−0.30	−4.54	−0.21	−2.44	−3.53
4	Ge_2^+	3/2	−0.14	−49.65	3.84	0.46	−0.67	−45.63	−0.49	−2.08	−2.83
4	$GaAs^+$	3/2	−0.17	−19.73	1.64	0.19	−0.27	−17.85	−0.19	−2.06	−2.93
5	YB^+	3/2	−0.14	−57.86	17.12	1.01	−1.39	−41.15	−1.01	−2.18	−2.98
5	YAl^+	3/2	−0.15	−100.80	28.53	1.66	−2.30	−73.10	−1.70	−2.17	−2.94
5	*ZrV*	3/2	−0.40	−40.90	15.80	1.11	−1.45	−26.47	−1.09	−2.30	−3.06
5	*MoN*	3/2	−0.36	−6.44	1.46	0.11	−0.14	−5.66	−0.10	−2.37	−3.37
5	*NbO*	3/2	−0.28	−47.61	12.77	0.78	−1.05	−36.05	−0.79	−2.23	−2.97
5	*TiNb*	3/2	−0.34	−43.71	14.50	0.94	−1.25	−31.18	−0.95	−2.27	−2.99
5	*ZrNb*	3/2	−0.32	−63.89	18.16	1.05	−1.43	−47.20	−1.06	−2.21	−2.97
4	*CrF*	5/2	−0.48	−16.49	6.32	0.46	−0.58	−10.66	−0.43	−2.36	−3.20
5	*CrAg*	5/2	−0.51	−0.34	0.58	0.05	−0.07	0.07	−0.04	−2.42	−3.79
4	*MnO*	5/2	−0.57	5.52	−2.35	−0.19	0.27	2.82	0.21	−2.14	−2.83
4	*MnS*	5/2	−0.59	16.89	−5.81	−0.43	0.59	10.40	0.44	−2.18	−2.92
4	*MnH*	3	−0.57	0.08	−0.93	−0.05	0.06	−0.93	0.06	−2.35	−2.52
4	*MnF*	3	−0.58	1.85	−0.94	−0.07	0.10	0.99	0.09	−3.30	−3.54
4	*MnCl*	3	−0.57	3.13	−1.26	−0.09	0.13	2.06	0.11	−2.19	−2.41
4	*MnBr*	3	−0.57	7.93	−1.65	−0.13	0.18	6.69	0.16	−2.15	−2.46
5	*MnAg*	3	−0.58	5.69	−2.19	−0.12	0.17	3.87	0.15	−2.22	−2.50

metal containing system using DFT-based methods: choice of a relativistic Hamiltonian, spin–orbit approximation, gauge corrections of the magnetic vector potential, *etc*. Special attention has been given to the description of the spin–orbit interaction and the contributions of the spin–other-orbit coupling term to the *g*-tensor. A new protocol has been suggested to improve the performance of periodic codes to predict *g*-tensors.

The conclusions of this work can be summarized in two parts:

(i) an effective method has been proposed to correct the unrealistic character of the exchange contribution in periodic codes like CP2K, bringing their *g*-tensor predictions at the same accuracy as those obtained in computationally more expensive spin–orbit mean-field models. A remarkable relationship has been noticed between the two-electron spin–orbit matrix elements and the unrealistic $\Delta g(\nabla v_{xc})$ predictions in the effective potential model within the KS scheme. An almost constant scale factor is found throughout the whole set of radical doublets and high-spin systems relating the wrong V_{eff} exchange contribution to the correct SOMF prediction. In this work a scale factor of about −2.80 is proposed, which is somewhat larger than the factor of −2 proposed by Neese, but bringing the DFT predictions in periodic codes close to those resulting from the computationally more expensive SOMF-ORCA calculations. It opens new perspectives for using periodic codes in the calculation of *g*-tensors in large extended systems containing transition metals.

(ii) for high spin states there appear some extra contributions to the direct Coulomb term belonging to the spin–other-orbit term. This is a direct consequence of the fact that in these systems multiple single occupied molecular orbitals are present. We found that these additional contributions are not negligible and improve the experimental agreement in most of the cases.

Concluding, with the implementation of the scale factor for the exchange contribution and the extra SOO terms for high-spin systems, CP2K has become a viable code for calculating *g*-tensors in periodic systems containing transition elements.

Table 9 The inclusion of the direct contribution of the SOO coupling is compared to previous results. All calculations were performed in CP2K using a TZV 2df basis set and PBE functional. A scaling factor of $\sigma' = -2.8$ is used

	CP2K							CP2K	
	Spin	Exp	$V_{\mathrm{eff,SOO}}$	$V^{*}_{\mathrm{eff,SOO}}$		Spin	Exp	$V_{\mathrm{eff,SOO}}$	$V^{*}_{\mathrm{eff,SOO}}$
B_2	1	−0.8	0.09	0.21	CrN	3/2	−5.6	−4.41	−5.02
NH	1	1.7	1.02	1.24	Ge_2^+	3/2	−63.3	−44.29	−44.66
NF	1	2.0	1.60	1.78	$GaAs^+$	3/2	−4.5	−17.44	−17.55
NCl	1	5.4	5.03	5.28	YB^+	3/2	−42.3	−38.25	−40.20
NBr	1	19.3	18.83	19.18	YAl^+	3/2	−60.3	−68.16	−71.33
NI	1	31.0	−0.34	−0.36	ZrV	3/2	−41.3	−23.60	−27.56
O_2	1	2.9	2.22	2.40	MoN	3/2	−10.9	−5.72	−5.70
PH	1	4.5	4.07	4.24	NbO	3/2	−44.6	−33.97	−35.23
SeO	1	32.7	15.30	15.63	$TiNb$	3/2	−73.8	−28.68	−31.46
SO	1	3.6	4.53	4.74	$ZrNb$	3/2	−98.8	−44.34	−46.22
$S2$	1	14.5	13.31	13.64	CrF	5/2	−1.3	−9.86	−11.56
BC	3/2	−0.3	−0.08	−0.02	$CrAg$	5/2	1.7	−0.32	−0.49
C_2^+	3/2	−0.5	−0.51	−0.48	MnO	5/2	−7.3	1.62	2.36
AlC	3/2	−1.3	−1.50	−1.53	MnS	5/2	6.7	8.47	9.94
SiB	3/2	−1.8	−1.14	−1.17	MnH	3	−1.3	−1.661	−1.35
$SiAl$	3/2	−4.5	−4.13	−4.23	MnF	3	−1.3	0.13	0.47
Si_2^+	3/2	−9.3	−6.31	−6.49	$MnCl$	3	−7.3	1.14	1.54
VO	3/2	−21.9	−15.52	−19.25	$MnBr$	3	−9.3	5.65	6.14
TiV	3/2	−24.3	−14.08	−17.96	$MnAg$	3	−4.3	2.84	3.33
V_2^+	3/2	−46.3	−10.56	−13.20					

6 Appendix: spin–orbit mean field

In this appendix we reformulate the Spin–Orbit Mean-Field (SOMF) method and focus on the contribution of the direct part of the two-body spin–other-orbit contribution which is non-negligible for high-spin complexes.

Two-body interactions can be best treated within second quantization formalism:

$$\frac{1}{2}\sum_{ij}\hat{V}_{ij} \rightarrow \frac{1}{4}\sum_{\alpha\beta\gamma\delta}\langle\alpha\beta|V_{12}|\gamma\delta\rangle_{\mathrm{as}}c_{\alpha}^{\dagger}c_{\beta}^{\dagger}c_{\delta}c_{\gamma} \tag{21}$$

with the antisymmetric matrix element $\langle\alpha\beta|V_{12}|\gamma\delta\rangle_{\mathrm{as}} = \langle\alpha\beta|V_{12}|\gamma\delta\rangle - \langle\alpha\beta|V_{12}|\delta\gamma\rangle$ and α, β, γ and δ as single-electron spin orbitals, represented by creation ($c_{\alpha}^{\dagger}$, $c_{\beta}^{\dagger}$) and annihilation operators (c_{δ}, c_{γ}). The two-body interaction should be first made symmetric with interchange of i and j. The two-body matrix element of the two-electron spin–orbit interaction can then be written as a product in spin and real space:

$$\begin{aligned}\langle\alpha\beta|V_{12}^{\mathrm{SO(2e)}}|\gamma\delta\rangle_{\mathrm{as}} = &-\tfrac{1}{2}\,\delta_{m_{s,b}\,m_{s,d}}\,\langle m_{s,a}|\boldsymbol{s}|m_{s,c}\rangle\cdot\langle ab|\boldsymbol{L}_1|cd\rangle\\ &-\tfrac{1}{2}\,\delta_{m_{s,a}\,m_{s,c}}\,\langle m_{s,b}|\boldsymbol{s}|m_{s,d}\rangle\cdot\langle ab|\boldsymbol{L}_1|dc\rangle\end{aligned} \tag{22}$$

with $\boldsymbol{L}_1 = \frac{\alpha^2}{r_{12}^3}(\boldsymbol{r}_{12}\times\boldsymbol{p}_1)$ which coincides with $-2g^{\mathrm{soc}}(1,2)$ introduced by Neese.[71] In eqn (22) the spin–orbital α is decomposed in the spatial orbital a and spin $m_{s,a}$.

Similar to the spin–other-orbit interaction one gets

$$\begin{aligned}\langle\alpha\beta|V_{12}^{\mathrm{SOO}}|\gamma\delta\rangle_{\mathrm{as}} = &-\tfrac{1}{2}\,\delta_{m_{s,b}\,m_{s,d}}\,\langle m_{s,a}|\boldsymbol{s}|m_{s,c}\rangle\cdot\langle ba|\boldsymbol{L}_1|dc\rangle\\ &-\tfrac{1}{2}\,\delta_{m_{s,a}\,m_{s,c}}\,\langle m_{s,b}|\boldsymbol{s}|m_{s,d}\rangle\cdot\langle ab|\boldsymbol{L}_1|cd\rangle\end{aligned} \tag{23}$$

One easily observes that the two spin–orbit interactions turn out to show a linear relationship only when the spins of all spin orbitals are equal to each other.

In the first order perturbation the most elementary excitation of the ground-state Slater determinant $|\Psi^{(0)}\rangle$ as SCF response to some external perturbation V^{λ} is the substitution of one of the unperturbed occupied orbitals h by its perturbed orbital $h^{(1)}$

$$|h^{(1)}\rangle = \sum_{p\in\mathrm{virt}}\frac{V_{ph}^{\lambda}}{\varepsilon_p-\varepsilon_h}|p\rangle \tag{24}$$

with a sum over all zeroth order virtual orbitals p.

For the further evaluation of the matrix elements it is sufficient to consider a single one-electron particle–one electron hole excitation ($|\Psi^{1}\rangle = c_p^{\dagger}c_h|\Psi^{(0)}\rangle$) where an occupied orbital h is replaced by a virtual orbital p; also called singly substituted determinants.

In the second quantization one gets the standard expression valid for any two-body interaction

$$\begin{aligned}&\left\langle\Psi^{(0)}\middle|\frac{1}{2}\sum_{ij}V_{ij}\middle|\Psi^{(1)}\right\rangle\\ &\quad=\frac{1}{4}\sum_{\alpha\beta\gamma\delta}\langle\alpha\beta|V_{12}|\gamma\delta\rangle_{\mathrm{as}}\langle\Psi^{(0)}|c_{\alpha}^{\dagger}c_{\beta}^{\dagger}c_{\delta}c_{\gamma}c_{p}^{\dagger}c_{h}|\Psi^{(1)}\rangle\end{aligned} \tag{25}$$

$$=\sum_{\alpha\in\mathrm{occ}}\langle h\alpha|V_{12}|p\alpha\rangle_{\mathrm{as}} = \langle h|I^{\mathrm{SO}}|p\rangle \tag{26}$$

determining the spin–orbit mean-field I^{SO}, completely similar as in mean-field approaches appropriate in interacting many-particle problems. For paramagnetic centers with only one singly occupied spin orbital h, the summation runs over all paired occupied molecular orbitals, hence $\sum_{\alpha\in\mathrm{OCC}} = \sum_{a\in\mathrm{OCC}}\sum_{m_{s,a}}$.

For the two-electron spin–orbit interaction the contribution to the spin–orbit mean-field becomes

$$\begin{aligned}&\sum_{\alpha\in\mathrm{occ}}\langle h\alpha|V_{12}^{\mathrm{SO(2e)}}|p\alpha\rangle_{\mathrm{as}}\\ &=-\frac{1}{2}\sum_{a\in\mathrm{occ}}\langle ha|L_{1z}|pa\rangle+\frac{1}{4}\sum_{a\in\mathrm{occ}}\left(\langle ha|L_{1z}|ap\rangle+\langle ah|L_{1z}|pa\rangle\right)\end{aligned} \tag{27}$$

The above expression only holds if the spin of the molecular orbital h is equal to that of the scattered state p: $m_{s,h} = m_{s,p} = \frac{1}{2}$. The first term is the direct Coulomb integral, while the second is the exchange contribution. For the spin–other-orbit interaction, one gets somewhat similar expression:

$$\sum_{a\in\mathrm{occ}} \langle h\alpha|V_{12}^{\mathrm{SOO}}|p\alpha\rangle_{\mathrm{as}} = -\sum_{a\in\mathrm{occ}} \langle ah|L_{1z}|ap\rangle + \frac{1}{2}(\langle ah|L_{1z}|pa\rangle + \langle ha|L_{1z}|ap\rangle) \quad (28)$$

but with the fundamental difference that now the direct Coulomb term is disappearing.

For real spatial wave functions the single-particle matrix elements for the Hermitian momentum operator becomes $\langle a|\boldsymbol{p}|a\rangle = \langle a|p|a\rangle^{*} = \langle a|\boldsymbol{p}^{*}|a\rangle = -\langle a|\boldsymbol{p}|a\rangle = 0$, and hence also the two-body matrix element of the spin–orbit operator $\boldsymbol{L}_1$ will disappear ($\langle ah|\boldsymbol{L}_1|ap\rangle = 0$). Concluding, for spin-$\frac{1}{2}$ complexes the spin–other-orbit interactions only contribute by means of their exchange term. In addition, inspection of eqn (27) and (28) immediately learns that the exchange SOO contribution is exactly twice the exchange contribution of the SO(2e) term:

$$\sum_{\alpha\in\mathrm{occ}} \langle h\alpha|V_{12}^{\mathrm{SOO}}|\alpha p\rangle = 2\sum_{\alpha\in\mathrm{occ}} \langle h\alpha|V_{12}^{\mathrm{SO(2e)}}|\alpha p\rangle \quad (29)$$

This relation is also valid for high spin complexes.

Finally, the spin–orbit mean field I^{SO} is then obtained as

$$\langle h|I^{\mathrm{SO}}|p\rangle = -\frac{1}{2}\sum_{a\in\mathrm{occ}} \langle ha|L_{1z}|pa\rangle + \frac{3}{4}\sum_{a\in\mathrm{occ}} (\langle ha|L_{1z}|ap\rangle + \langle ah|L_{1z}|pa\rangle) \quad (30)$$

The derivation of the expressions, presented in this work, differs slightly from those of Neese[71] and others.[75] However, the final results are equivalent.

Application of eqn (30) to evaluate the Δg^{SO} correction is the so-called spin–orbit mean-field (SOMF) approach, as implemented in ORCA. It is an excellent starting platform to estimate the contribution of the spin–other-orbit (SOO) correction for spin-$\frac{1}{2}$ molecules.

The extension to higher spin states can easily be performed. Instead of one we now consider 2 S singly occupied molecular orbitals β where S represents the total spin of the molecular system. The contribution to the spin–orbit mean-field from the two-electron spin–orbit interaction becomes

$$\sum_{\gamma=\alpha,\beta\mathrm{occ}} \langle h\gamma|V_{12}^{\mathrm{SO(2e)}}|p\gamma\rangle = -\frac{1}{2}\sum_{a\in\mathrm{occ}} \langle ha|L_{1z}|pa\rangle - \frac{1}{4}\sum_{b\in\mathrm{occ}} \langle hb|L_{1z}|pb\rangle + \frac{1}{4}\sum_{c=a,b\in\mathrm{occ}} (\langle hc|L_{1z}|cp\rangle + \langle ch|L_{1z}|pc\rangle) \quad (31)$$

Only in the direct Coulomb term one notices some slight difference in comparison with the spin 1/2 systems. As the b-orbitals are singly occupied they only half contribute to the mean field.

In contrast to the spin 1/2 systems, there is now a non-vanishing contribution from the spin–other-orbit interaction in higher spin molecules to the direct Coulomb term:

$$-\frac{1}{2}\sum_{b=\mathrm{hocc}} \langle hb|L_{1z}|pb\rangle \quad (32)$$

This is not really negligible for high spin systems, *e.g.* diatomic molecules with Mn as element whose ground state configuration generates spin 3 with 6 singly occupied molecular orbitals with parallel spin. In this case of high spin our results apparently differ from those of Neese. On the other hand, the exchange contribution $\mathrm{SOO}_{\mathrm{exch}}$ still obeys relation (8).

Acknowledgements

The authors would like to thank the Fund for Scientific Research (FWO-Flanders, Belgium) and the Research Board of Ghent University for financial support. Part of the computational resources and services used in this work were provided by Ghent University.

References

1 M. Kaupp, M. Bühl and V. G. Malkin, *Calculation of NMR and EPR Parameters*, WILEY-VCH4, 2004.
2 D. A. Case, *J. Chem. Phys.*, 1985, **83**, 5792–5796.
3 E. van Lenthe, P. E. S. Wormer and A. van der Avoird, *J. Chem. Phys.*, 1997, **107**, 2488.
4 K. M. Neyman, D. I. Ganyushin, A. V. Matveev and V. A. Nasluzov, *J. Phys. Chem. A*, 2002, **106**, 5022–5030.
5 O. Vahtras, M. Engström and B. Schimmelpfennig, *Chem. Phys. Lett.*, 2002, **434**, 424–430.
6 R. Declerck, V. Van Speybroeck and M. Waroquier, *Phys. Rev. B: Condens. Matter Mater. Phys.*, 2006, **73**, 115113.
7 F. Neese, *J. Chem. Phys.*, 2001, **115**, 11080–11096.
8 C. J. Pickard and F. Mauri, *Phys. Rev. Lett.*, 2002, **88**, 086403.
9 V. Weber, M. Iannuzzi, S. Giani, J. Hutter, R. Declerck and M. Waroquier, *J. Chem. Phys.*, 2009, **131**, 014106.
10 E. S. Kadantsev and T. Ziegler, *J. Phys. Chem. A*, 2009, **113**, 1327.
11 E. Pauwels, R. Declerck, V. Van Speybroeck and M. Waroquier, *Radiat. Res.*, 2008, **169**, 8.
12 E. Pauwels, R. Declerck, T. Verstraelen, B. De Sterck, C. W. M. Kay, V. Van Speybroeck and M. Waroquier, *J. Phys. Chem. B*, 2010, **113**, 16655.
13 E. Pauwels, H. De Cooman, M. Waroquier, E. O. Hole and E. Sagstuen, *Phys. Chem. Chem. Phys.*, 2010, **12**, 8733.
14 F. Pietrucci, M. Bernasconi, C. Di Valentin, F. Mauri and C. J. Pickard, *Phys. Rev. B: Condens. Matter Mater. Phys.*, 2006, **73**, 134112.
15 N. Sakhabutdinova, A. Van Yperen-De Deyne, V. Van Speybroeck, E. Pauwels, H. Vrielinck, F. Callens and M. Waroquier, *J. Phys. Chem. A*, 2011, **115**, 1721–1733.
16 W. M. Ames and S. C. Larsen, *J. Phys. Chem. A*, 2010, **114**, 589.
17 K. Pierloot, A. Delabie, M. H. Groothaert and R. A. Schoonheydt, *Phys. Chem. Chem. Phys.*, 2001, **3**, 2174–2183.
18 M. Danilczuk and A. Lund, *Chem. Phys. Lett.*, 2010, **490**, 205–209.
19 G. te Velde, F. M. Bickelhaupt, E. J. Baerends, C. F. Guerra, S. J. A. Van Gisbergen, J. G. Snijders and T. Ziegler, *J. Comput. Chem.*, 2001, **22**, 931–967.
20 C. F. Guerra, J. G. Snijders, G. te Velde and E. J. Baerends, *Theor. Chem. Acc.*, 1998, **99**, 391–403.
21 E. Baerends, T. Ziegler, J. Autschbach, D. Bashford, A. Brces, F. Bickelhaupt, C. Bo, P. Boerrigter, L. Cavallo, D. Chong, L. Deng, R. Dickson, D. Ellis, M. van Faassen, L. Fan, T. Fischer, C. F. Guerra, A. Ghysels, A. Giammona, S. van Gisbergen, A. Gtz, J. Groeneveld, O. Gritsenko, M. Grning, S. Gusarov, F. Harris, P. van den Hoek, C. Jacob, H. Jacobsen, L. Jensen, J. Kaminski, G. van Kessel, F. Kootstra, A. Kovalenko, M. Krykunov, E. van Lenthe, D. McCormack, A. Michalak,

M. Mitoraj, J. Neugebauer, V. Nicu, L. Noodleman, V. Osinga, S. Patchkovskii, P. Philipsen, D. Post, C. Pye, W. Ravenek, J. RodrÃguez, P. Ros, P. Schipper, G. Schreckenbach, J. Seldenthuis, M. Seth, J. Snijders, M. Sol, M. Swart, D. Swerhone, G. te Velde, P. Vernooijs, L. Versluis, L. Visscher, O. Visser, F. Wang, T. Wesolowski, E. van Wezenbeek, G. Wiesenekker, S. Wolff, T. Woo and A. Yakovlev, *ADF2009.01, SCM*, http://www.scm.com.
22 http://www.thch.uni-bonn.de/tc/orca/.
23 M. J. Frisch, G. W. Trucks, H. B. Schlegel, G. E. Scuseria, M. A. Robb, J. R. Cheeseman, G. Scalmani, V. Barone, B. Mennucci, G. A. Petersson, H. Nakatsuji, M. Caricato, X. Li, H. P. Hratchian, A. F. Izmaylov, J. Bloino, G. Zheng, J. L. Sonnenberg, M. Hada, M. Ehara, K. Toyota, R. Fukuda, J. Hasegawa, M. Ishida, T. Nakajima, Y. Honda, O. Kitao, H. Nakai, T. Vreven, J. A. Montgomery Jr, J. E. Peralta, F. Ogliaro, M. Bearpark, J. J. Heyd, E. Brothers, K. N. Kudin, V. N. Staroverov, R. Kobayashi, J. Normand, K. Raghavachari, A. Rendell, J. C. Burant, S. S. Iyengar, J. Tomasi, M. Cossi, N. Rega, J. M. Millam, M. Klene, J. E. Knox, J. B. Cross, V. Bakken, C. Adamo, J. Jaramillo, R. Gomperts, R. E. Stratmann, O. Yazyev, A. J. Austin, R. Cammi, C. Pomelli, J. W. Ochterski, R. L. Martin, K. Morokuma, V. G. Zakrzewski, G. A. Voth, P. Salvador, J. J. Dannenberg, S. Dapprich, A. D. Daniels, Farkas, J. B. Foresman, J. V. Ortiz, J. Cioslowski and D. J. Fox, *Gaussian 09 Revision A.1*, Gaussian Inc, Wallingford, CT, 2009.
24 *DALTON, a molecular electronic structure program, Release 2.0*, 2005, http://daltonprogram.org/.
25 O. L. Malkina, J. Vaara, B. Schimmelpfennig, M. Munzarová, V. G. Malkin and M. Kaupp, *J. Am. Chem. Soc.*, 2000, **122**, 9206.
26 C. J. Pickard and F. Mauri, *Phys. Rev. B: Condens. Matter Mater. Phys.*, 2001, **63**, 245101.
27 P. Giannozzi, S. Baroni, N. Bonini, M. Calandra, R. Car, C. Cavazzoni, D. Ceresoli, G. L. Chiarotti, M. Cococcioni, I. Dabo, A. Dal Corso, S. de Gironcoli, S. Fabris, G. Fratesi, R. Gebauer, U. Gerstmann, C. Gougoussis, A. Kokalj, M. Lazzeri, L. Martin-Samos, N. Marzari, F. Mauri, R. Mazzarello, S. Paolini, A. Pasquarello, L. Paulatto, C. Sbraccia, S. Scandolo, G. Sclauzero, A. P. Seitsonen, A. Smogunov, P. Umari and R. M. Wentzcovitch, *J. Phys.: Condens. Matter*, 2009, **21**, 395502(19pp).
28 G. Lippert, J. Hutter and M. Parrinello, *Theor. Chem. Acc.*, 1999, **103**, 124–140.
29 T. Laino, F. Mohamed, A. Laio and M. Parrinello, *J. Chem. Theor. Comput.*, 2005, **1**, 1176–1184.
30 J. VandeVondele, M. Krack, F. Mohamed, M. Parrinello, T. Chassaing and J. Hutter, *Comput. Phys. Commun.*, 2005, **167**, 103–128.
31 P. H. T. Philipsen, G. te Velde, E. J. Baerends, J. A. Berger, P. L. de Boeij, J. A. Groeneveld, E. S. Kadentsev, R. Klooster, K. F. P. Romaniello, D. G. Skachkov, J. G. Snijders, G. Wiesenekker and T. Ziegler, *BAND2010*, http://www.scm.com.
32 A. V. Arbuznikov, M. Kaupp, V. G. Malkin, R. Reviakine and O. L. Malkina, *Phys. Chem. Chem. Phys.*, 2002, **4**, 5467.
33 S. Patchkovskii and T. Ziegler, *J. Phys. Chem. A*, 2001, **105**, 5490.
34 I. Malkin, O. L. Malkina, V. G. Malkin and M. Kaupp, *J. Chem. Phys.*, 2005, **123**, 244103.
35 F. Stevens, V. Van Speybroeck, I. Carmichael, F. Callens and M. Waroquier, *Chem. Phys. Lett.*, 2006, **421**, 281–286.
36 H. Tan, M. Z. Liao and K. Balasubramanian, *Chem. Phys. Lett.*, 1997, **280**, 423–429.
37 J. M. Brom, W. Weltner and W. R. M. Graham, *J. Chem. Phys.*, 1972, **57**, 4116–4124.
38 I. Shim and K. A. Gingerich, *Surf. Sci.*, 1985, **156**, 623.
39 L. B. Knight, B. W. Gregory, S. T. Cobranchi, D. Feller and E. R. Davidson, *J. Am. Chem. Soc.*, 1987, **109**, 3521–3525.
40 M. Tinkham and M. W. P. Strandberg, *Phys. Rev.*, 1955, **97**, 951–966.
41 A. E. Douglas and W. E. Jones, *Can. J. Phys.*, 1966, **44**, 2241–2258.
42 H. Uehara, *Bull. Chem. Soc. Jpn.*, 1969, **42**, 886–889.
43 C. Yamada, Y. Endo and E. Hirota, *J. Chem. Phys.*, 1983, **79**, 4159–4166.
44 L. B. Knight, S. T. Cobranchi, J. T. Petty, E. Earl, D. Feller and E. R. Davidson, *J. Chem. Phys.*, 1989, **90**, 690.
45 L. B. Knight, S. T. Cobranchi and E. Earl, *J. Chem. Phys.*, 1988, **88**, 7348.
46 L. B. Knight, S. T. Cobranchi, J. O. Herlong and C. A. Arrington, *J. Chem. Phys.*, 1990, **92**, 5856.
47 L. B. Knight, R. M. Babb, G. M. King, A. J. McKinley, M. D. Morse and C. A. Arrington, *J. Chem. Phys.*, 1993, **98**, 4404.
48 L. B. Knight, A. J. McKinley, R. M. Babb, M. D. Morse and C. A. Arrington, *J. Chem. Phys.*, 1993, **98**, 6749.
49 Y. M. Hamrick and W. Weltner, *J. Chem. Phys.*, 1991, **94**, 3371.
50 M. Cheeseman, R. J. Van Zee, H. L. Flanagan and W. Weltner, *J. Chem. Phys.*, 1990, **92**, 1553.
51 J. M. Brom, C. H. Durham and W. Weltner, *J. Chem. Phys.*, 1974, **61**, 970–981.
52 L. B. Knight and J. T. Petty, *J. Chem. Phys.*, 1988, **88**, 481.
53 L. B. Knight and J. Steadman, *J. Chem. Phys.*, 1982, **76**, 3378–3384.
54 K. C. Namiki and T. C. Steimle, *J. Chem. Phys.*, 1999, **111**, 6385.
55 R. J. Van Zee, S. Li and W. Weltner, *J. Chem. Phys.*, 1995, **103**, 2762.
56 W. Weltner, *Magnetic Atoms and Molecules*, Dover Publications, 1983.
57 A. Carrington, G. N. Currie, D. H. Levy and T. A. Miller, *Mol. Phys.*, 1969, **17**, 535–542.
58 L. B. Knight, R. Babb, M. Ray, T. J. Banisaukas, L. Russon, R. S. Dailey and E. R. Davidson, *J. Chem. Phys.*, 1996, **105**, 10237.
59 R. J. Van Zee, S. Li and W. J. Weltner, *Chem. Phys. Lett.*, 1994, **217**, 381–386.
60 P. Belanzoni, E. van Lenthe and E. J. Baerends, *J. Chem. Phys.*, 2001, **114**, 4421.
61 J. P. Perdew, K. Burke and M. Ernzerhof, *Phys. Rev. Lett.*, 1996, **77**, 3865–3868.
62 A. Schaefer, H. Horn and R. Ahlrichs, *J. Chem. Phys.*, 1992, **97**, 2571.
63 D. A. Pantazis, X. Y. Chen, C. R. Landis and F. Neese, *J. Chem. Theor.Comput.*, 2008, **4**, 908–919.
64 The Ahlrichs (2df,2pd,2d2fg,3p2df) polarization functions were obtained from the TurboMole basis set library under ftp.chemie.uni-karlsruhe.de/pub/basen.
65 R. Krishnan, J. S. Binkley, R. Seeger and J. A. Pople, *J. Chem. Phys.*, 1980, **72**, 650–654.
66 G. Lippert, J. Hutter and M. Parrinello, *Theor. Chem. Acc.*, 1999, **103**, 124–140.
67 N. Troullier and J. L. Martins, *Phys. Rev. B: Condens. Matter Mater. Phys.*, 1991, **43**, 1993–2006.
68 P. E. Blochl, *Phys. Rev. B: Condens. Matter Mater. Phys.*, 1994, **50**, 17953–17979.
69 G. J. Martyna and M. E. Tuckerman, *J. Chem. Phys.*, 1999, **110**, 2810.
70 G. Schreckenbach and T. Ziegler, *J. Phys. Chem. A*, 1997, **101**, 3388–3399.
71 F. Neese, *J. Chem. Phys.*, 2005, **122**, 034107.
72 E. van Lenthe, E. J. Baerends and J. G. Snijders, *J. Chem. Phys.*, 1993, **99**, 4597–4610.
73 C. van Wullen, *J. Chem. Phys.*, 1998, **109**, 392–399.
74 P. Knappe and N. Rösch, *J. Chem. Phys.*, 1990, **92**, 1153.
75 B. A. Hess, C. M. Marian, U. Wahlgren and O. Gropen, *Chem. Phys. Lett.*, 1996, **251**, 365–371.
76 S. Koseki, M. W. Schmidt and M. S. Gordon, *J. Phys. Chem.*, 1992, **96**, 10768–10772.
77 S. Koseki, M. S. Gordon, M. W. Schmidt and N. Matsunaga, *J. Phys. Chem.*, 1995, **99**, 12764–12772.
78 S. Koseki, M. W. Schmidt and M. S. Gordon, *J. Phys. Chem. A*, 1998, **102**, 10430–10435.
79 R. Ditchfield, *Mol. Phys.*, 1974, **27**, 789–807.
80 K. M. Neyman, D. I. Ganyushin and A. V. Matveev, *J. Phys. Chem. A*, 2002, **106**, 5022–5030.

Supplementary Material for: Accurate spin-orbit and spin-other-orbit contributions to the g-tensor for transition metal containing systems

A. Van Yperen-De Deyne[a], E. Pauwels[a], V. Van Speybroeck[a] and M. Waroquier * [a]

[a] *Center for Molecular Modeling, Ghent University, Technologiepark 903, B-9052 Zwijnaarde, Belgium; E-mail: michel.waroquier@ugent.be*

S.1 RhC test molecule

Table 1 Gaussian 09 calculations of the g-tensor, using several basis sets and the PBE functional. In Gaussian 09 only the Z_{eff} method was used, so they can only be compared to the non-relativistic calculations of ORCA using the same spin-orbit approximation. All values are expressed as $\Delta g = g_{ortho} - g_e$ in ppt.

	ORCA, Z_{eff}		G09, Z_{eff}	
	Δg_{ortho}	Δg_{para}	Δg_{ortho}	Δg_{para}
VDZ	111.73	0.21	108.1	0.21
VDZ, 2df	91.89	0.22	91.85	0.22
VDZ, 2df, p	96.27	0.22	95.76	0.22
VDZ, ppp, p	94.03	0.22	93.62	0.22
TZV	122.04	0.20	118.84	0.20
TZV, 2df	104.28	0.21	104.32	0.21
TZV, 2df, p	106.09	0.22	105.98	0.22
TZV, ppp, p	103.08	0.22	103.00	0.22
exp	51.78	1.58	51.78	1.58

Table 2 GIPAW results of g-tensor calculation in function of the box size (in Bohr). All values are expressed as $\Delta g = g_{ortho} - g_e$ in ppt.

Box Size	V_{eff}, PM	
	Δg_{ortho}	Δg_{para}
5	−8.76	−47.01
10	40.07	−0.23
15	43.15	−0.11
15	43.15	−0.11
20	48.67	−0.10
25	51.68	−0.10
30	53.22	−0.11
35	54.06	−0.11
exp	51.78	1.58

Molecule	d ($\mathring{A}$)	Molecule	d ($\mathring{A}$)
RhC	1.613	ZnAg	2.550
BO	1.204	YO	1.788
BS	1.609	PdH	1.529
AlO	1.618	CdH	1.781
GaO	1.744	CdF	2.014
ScO	1.668	CdAg	2.727
ZnH	1.595	InO	1.875
ZnF	1.799		

Table 3 Internuclear distances d of the diatomic spin-$1/2$ molecules as reported by P. Belanzoni, E. van Lenthe and E. J. Baerends, J. Chem. Phys., 2001, **114**, 4421-4433

S.2 Doublet Molecules

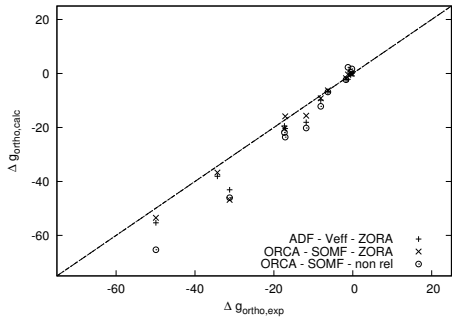

Figure 1 Correlation diagram between $\Delta g_{ortho,exp}$ and $\Delta g_{ortho,calc}$ (y-axis) for several doublet molecules. Results of SOMF (with and without ZORA) and ADF (two-component method) are presented. For all calculations a triple-ζ quality basis set with polarization functions (Ahlrichs 2df if possible) was used.

S.3 High Spin Molecules

Molecule	d ($\mathring{A}$)	Molecule	d ($\mathring{A}$)
B_2	1.618	CrN	1.556
NH	1.053	Ge_2^+	2.461
NF	1.343	$GaAs^+$	2.744
NCl	1.643	YB^+	2.263
NBr	1.808	YAl^+	2.816
NI	2.007	ZrV	2.076
O_2	1.235	MoN	1.659
PH	1.453	NbO	1.714
SeO	1.677	$TiNb$	2.046
SO	1.518	$ZrNb$	2.245
$S2$	1.931	CrF	1.784
BC	1.496	$CrAg$	2.554
C_2^+	1.418	MnO	1.629
AlC	1.986	MnS	2.043
SiB	1.935	MnH	1.710
$SiAl$	2.459	MnF	1.833
Si_2^+	2.327	$MnCl$	2.241
VO	1.597	$MnBr$	2.395
TiV	1.835	$MnAg$	2.539
V_2^+	1.741		

Table 4 Internuclear distances d of the diatomic high spin molecules as used by S. Pathkovskii and T. Ziegler, J. Phys. Chem. A, 2001, **105**, 5490-5497

Paper II

Exploring the vibrational fingerprint of the electronic excitation energy via molecular dynamics

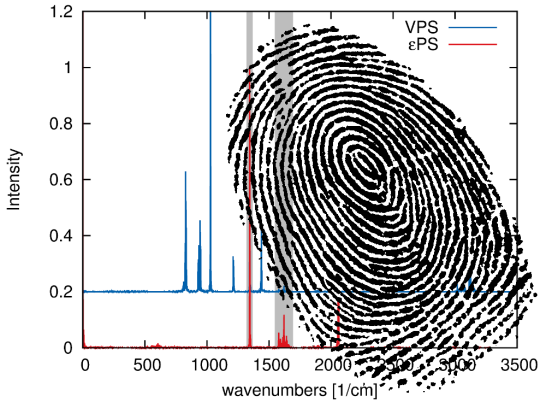

A. Van Yperen-De Deyne, T. De Meyer, E. Pauwels, A. Ghysels, K. De Clerck, M. Waroquier, V. Van Speybroeck and K. Hemelsoet *The Journal of Chemical Physics* **140**, 134105 (2014)

THE JOURNAL OF CHEMICAL PHYSICS **140**, 134105 (2014)

Exploring the vibrational fingerprint of the electronic excitation energy via molecular dynamics

Andy Van Yperen-De Deyne,[1] Thierry De Meyer,[1,2] Ewald Pauwels,[1,a)] An Ghysels,[1] Karen De Clerck,[2] Michel Waroquier,[1] Veronique Van Speybroeck,[1] and Karen Hemelsoet[1,b)]

[1]*Center for Molecular Modeling (CMM), Ghent University, Technologiepark 903, 9052 Zwijnaarde, Belgium*
[2]*Department of Textiles, Ghent University, Technologiepark 907, 9052 Zwijnaarde, Belgium*

(Received 24 November 2013; accepted 19 March 2014; published online 4 April 2014)

A Fourier-based method is presented to relate changes of the molecular structure during a molecular dynamics simulation with fluctuations in the electronic excitation energy. The method implies sampling of the ground state potential energy surface. Subsequently, the power spectrum of the velocities is compared with the power spectrum of the excitation energy computed using time-dependent density functional theory. Peaks in both spectra are compared, and motions exhibiting a linear or quadratic behavior can be distinguished. The quadratically active motions are mainly responsible for the changes in the excitation energy and hence cause shifts between the dynamic and static values of the spectral property. Moreover, information about the potential energy surface of various excited states can be obtained. The procedure is illustrated with three case studies. The first electronic excitation is explored in detail and dominant vibrational motions responsible for changes in the excitation energy are identified for ethylene, biphenyl, and hexamethylbenzene. The proposed method is also extended to other low-energy excitations. Finally, the vibrational fingerprint of the excitation energy of a more complex molecule, in particular the azo dye ethyl orange in a water environment, is analyzed. © *2014 AIP Publishing LLC*. [http://dx.doi.org/10.1063/1.4869937]

I. INTRODUCTION

Computational modeling of spectroscopic observables is of fundamental importance to gather information on the stability and reactivity of a molecular system since spectroscopy provides unique fingerprints of molecular properties. If the spectroscopic transition is fast compared to the time-scale of the dynamical phenomenon, averaging over different configurations – generated during a dynamical simulation – is often considered the best technique to obtain theoretical results which can complement measured data. Both classical and *ab initio* Molecular Dynamics (MD) have been used for this purpose, as reviewed for the simulation of UV/Vis spectra of large molecules in solution in Ref. 1. The resulting averages are an estimate of the electronic transition energy and line-width. The obtained transition energy is often shifted compared to the result from a single static simulation.[2–4] At present, there is no simple recipe to gain insight in the molecular motions contributing to this shift. In general, it is very hard to link changes in electronic spectra with particular conformational features. We recently reported that MD simulations are indispensable for obtaining good agreement between experimental and theoretical UV/Vis spectra of large dyes and aromatic hydrocarbons.[3,4] It was observed that some particular motions caused a strong distortion of the π system contributing the shift between a static and a dynamic approach. In this paper, we present a systematic method to correlate changes observed in a spectral property to changes in the molecular geometry. In principle, the method may be used on any spectral property, but here we apply it on vertical excitation energies. The group of Barone *et al.*[5–8] developed in a number of seminal contributions a general and robust computational tool for simulating vibrationally resolved electronic spectra. Their method is based on a harmonic approximation, and a single-state approach is used throughout. In addition to an adiabatic description, also a vertical gradient approach is implemented avoiding the geometry optimization and frequency calculation in the excited state.[6] The latter approximation enables to compute the Franck-Condon and Herzberg-Teller contributions even for extended systems with a large number of normal modes. In general, the normal coordinates of the ground and excited states are not the same; they can be distorted, displaced, and rotated. Such a normal mode rotation (or mixing) is called the Duschinsky effect and can lead to significant broadening of the absorption spectra for π–π^* transitions, as studied in detail for ethylene and allene.[9,10] Our goal is to complement these studies by providing insight into the geometrical motions responsible for the unique spectral fingerprints.

We propose a Fourier transform based method to identify the internal motions that govern changes in computed electronic spectra. In particular, we mainly focus on the lowest electronic excitation energy which is observed in absorption of UV and visible light, although excitations to higher excited states are also examined. In recent years, time-dependent density functional theory (TD-DFT)[11,12] has proven very

a)Current address: UGent HPC, Ghent University, Krijgslaan 281, S9, B-9000 Gent, Belgium.
b)Electronic mail: karen.hemelsoet@ugent.be

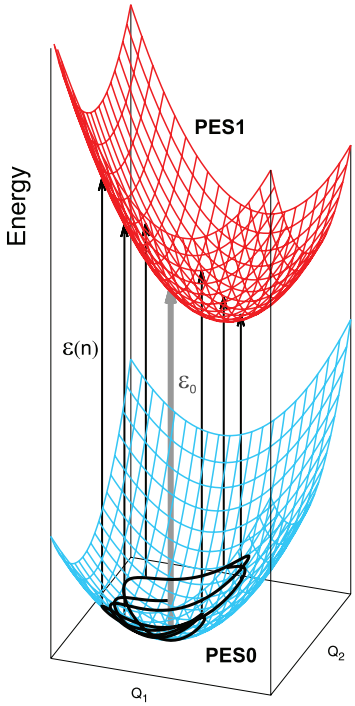

FIG. 1. Pictorial view of the static versus the dynamic approach for the simulation of the excitation energy ϵ, leading to ϵ_0 (in light grey) and $\langle\epsilon\rangle$ (obtained from averaging over the various $\epsilon(n)$ generated during the MD of the PES 0, in black), respectively. Overall, a vertical approach is applied, reflecting the short-time dynamics of the molecular system.

valuable for the fairly accurate and yet efficient calculation of excitation properties of medium- to large-size molecules.[13–16] In Figure 1, the static and dynamic approach are schematically depicted on an energy diagram. The most simple approximation to the excitation energy corresponds with a vertical static computation (ϵ_0), only involving the optimized ground state geometry and representing a temperature of 0 K. Temperature effects can be added from a normal mode analysis; however, this is not straightforward for large systems due to the huge number of internal degrees of freedom and the occurrence of anharmonic motions. MD provides an interesting alternative to capture these effects, because calculation of different values $\epsilon(n)$ on a series of generated snapshots leads to a dynamical averaged property $\langle\epsilon\rangle$ (Figure 1). Additionally, MD allows scanning of multiple minima if they are accessible at the given temperature. The goal of the method is to find relationships between electronic transitions and vibrational coordinates, or more specifically, the identification of vibrational coordinates which directly influence ϵ. Importantly, our analysis is entirely based on MD simulations on the ground state potential energy surface (PES 0) and subsequent vertical TD-DFT simulations on extracted snapshots. Previously, a regression analysis[17,18] or scans along a limited set of coordinates[19,20] have been used. The latter method is, however, not systematic and might neglect coordinates which are less obvious, such as delocalized motions.

Power spectra, defined as the Fourier transform of a dynamical property, have been introduced and applied successfully to the calculation of vibrational spectra.[21–23] In particular, inelastic neutron scattering (INS), infrared (IR), and Raman spectra can be simulated, with the atomic velocities, the dipole moment, and the polarizability as the dynamical property under consideration, respectively. Recent developments focus on decoding these vibrational spectra.[24–26] Champagne *et al.*[27,28] previously developed methods to determine the derivatives of the frequency-dependent polarizability with respect to nuclear coordinates, responsible for the Raman intensities, and computed the zero point vibrational average (ZPVA) correction to the polarizability. However, such a procedure has not yet been examined for the excitation energy.

In Sec. II, we provide the theoretical background of the proposed method, as well as the particular computational details applied hereafter. To test the proposed method and to show its possibilities and limitations, the vibrational fingerprints of the first vertical excitation of three case studies – ethylene, biphenyl, and hexamethylbenzene – are discussed in Sec. III A. The analysis is extended to multiple excited states in Sec. III B. In Sec. III C, a more complex molecule is investigated, demonstrating the possibilities of the method to real-life systems. We then conclude in Sec. IV.

II. THEORY AND METHODS

A. Identification of active internal modes influencing the electronic excitation using power spectra

This section outlines our method to identify active internal vibrational modes influencing the electronic excitation energy. A velocity power spectrum (VPS) generated by a MD simulation contains all information about the internal vibrational modes (associated with vibrational coordinates Q_i) with frequencies ω_i (see below).[29,30] Assume the vibrational coordinate Q_i fluctuates about its reference value Q_i^0 with an amplitude A_i and frequency ω_i

$$Q_i(t) = Q_i^0 + A_i \cos \omega_i t. \tag{1}$$

The VPS contains information regarding the change of the molecular structure during the MD run. At each snapshot during the MD simulation the geometry of the molecular system is characterized by the set of vibrational coordinates $\{Q_1, Q_2, \ldots, Q_{3N-6}\}$. Sampling of the ground state PES 0 and subsequent computation of the vertical excitation energy creates a time series of $\epsilon(n)$ values (see Figure 1). The excitation energy ϵ hence becomes an implicit function of time through the vibrational coordinates: $\epsilon(t) = \epsilon(Q_1, Q_2, \ldots, Q_{3N-6})$. It can be

expressed as a power series of the vibrational coordinates

$$\begin{aligned}\epsilon(Q_1, Q_2, \dots Q_{3N-6}) &= \epsilon\left(Q_1^0, Q_2^0, \dots Q_{3N-6}^0\right) \\ &+ \sum_i \delta Q_i \left.\frac{\partial \epsilon}{\partial Q_i}\right|_0 + \frac{1}{2}\sum_i \delta Q_i^2 \left.\frac{\partial^2 \epsilon}{\partial Q_i^2}\right|_0 \\ &+ \frac{1}{2}\sum_{i\neq j} \delta Q_i \delta Q_j \left.\frac{\partial^2 \epsilon}{\partial Q_i \partial Q_j}\right|_0 + \cdots \qquad (2)\end{aligned}$$

$$= \epsilon_0 + \sum_i \epsilon(Q_i) + \frac{1}{2}\sum_{i\neq j} \epsilon(Q_i, Q_j) + \cdots \qquad (3)$$

with $\delta Q_i = Q_i(t) - Q_i^0$ and ϵ_0 the value of the vertical excitation energy computed for the optimized ground state. $\epsilon(Q_i)$ is a shorthand notation for $\epsilon(Q_1^0, \dots Q_i, \dots Q_{3N-6}^0)$ and represents the shift of the excitation energy due to the change of only one vibrational coordinate Q_i, while all other coordinates remain fixed at their reference value. Using Eq. (1), the power series (2) can be written as

$$\epsilon(t) = \epsilon_0 + \sum_i \left(A_i \left.\frac{\partial \epsilon}{\partial Q_i}\right|_0 \cos \omega_i t + \frac{1}{2} \left.\frac{\partial^2 \epsilon}{\partial Q_i^2}\right|_0 A_i^2 \cos^2 \omega_i t \right) + \frac{1}{2}\sum_{i\neq j} A_i A_j \left.\frac{\partial^2 \epsilon}{\partial Q_i \partial Q_j}\right|_0 \cos \omega_i t \cos \omega_j t + \cdots . \qquad (4)$$

Not all variations δQ_i of the vibrational coordinates affect the electronic excitation energy. For some Q_i, the partial derivatives are zero and hence, different types of vibrational coordinates and corresponding modes are obtained as will be discussed hereafter.

To identify the vibrational coordinates Q_i that significantly influence the changes in ϵ, we investigate their correlation using Fourier transforms. First, we determine the VPS, defined as[30]

$$I_{VPS}(\omega) = \sum_{\alpha=x,y,z} \sum_{l=1}^{N} \left| \int v_{l,\alpha}(t) \exp(-i\omega t) \mathrm{d}t \right|^2 , \qquad (5)$$

for a system with N nuclei and where $v_{l,\alpha}$ is the αth Cartesian component of the velocity of the lth nucleus. The VPS shows high intensities at frequencies corresponding to the vibrational energy levels. It contains all information about the internal motions of the studied systems. Similarly, the corresponding power spectrum of the excitation energy (ϵPS) can be calculated as

$$I_{\epsilon PS}(\omega) = \left| \int \epsilon(t) \exp(-i\omega t) \mathrm{d}t \right|^2 . \qquad (6)$$

The ϵPS is characteristic for fluctuations in ϵ. To detect correlations between internal motions and the electronic spectrum generated by the property ϵ, one needs to examine the overlap between $I_{\epsilon PS}$ and I_{VPS}.

We now investigate which terms in (4) give peaks in ϵPS and whether the corresponding coordinate causes a shift of the dynamic average $\langle\epsilon\rangle$, computed as $\langle\epsilon\rangle = \frac{1}{n_{tot}} \sum_{n=1}^{n_{tot}} \epsilon(n)$ (with n_{tot} the number of snapshots):

- Inactive coordinate: $\left.\frac{\partial \epsilon}{\partial Q_i}\right|_0 = 0$ and $\left.\frac{\partial^2 \epsilon}{\partial Q_i \partial Q_j}\right|_0 = 0$, $\forall j$. There is no peak in ϵPS. The coordinate Q_i does not shift the dynamic average (in Eq. (3))
$$\langle \epsilon(Q_i) \rangle = \langle \epsilon(Q_i, Q_j) \rangle = 0. \qquad (7)$$
- Linearly active coordinate: $\left.\frac{\partial \epsilon}{\partial Q_i}\right|_0 \neq 0$.
The term $A_i \left.\frac{\partial \epsilon}{\partial Q_i}\right|_0 \cos \omega_i t$ gives a peak at ω_i in ϵPS. This coordinate does not shift the excitation energy, because averaging over a period τ, with $\tau = \frac{2\pi}{\omega_i}$ results in
$$\langle \epsilon(Q_i) \rangle = A_i \left.\frac{\partial \epsilon}{\partial Q_i}\right|_0 \frac{1}{\tau} \int_0^\tau \cos \omega_i t \, dt = 0. \qquad (8)$$
- Quadratically active coordinate: $\left.\frac{\partial^2 \epsilon}{\partial Q_i^2}\right|_0 \neq 0$.
The term $\frac{1}{2} \left.\frac{\partial^2 \epsilon}{\partial Q_i^2}\right|_0 A_i^2 \cos^2 \omega_i t = \frac{1}{4} \left.\frac{\partial^2 \epsilon}{\partial Q_i^2}\right|_0 A_i^2 (\cos 2\omega_i t + 1)$ gives a peak at $2\omega_i$ in ϵPS. The frequency axis of the ϵPS should be scaled by a factor 1/2, while the VPS is unchanged, in order to map the corresponding modes for these quadratical dependencies. Importantly, averaging over a period τ, with $\tau = \frac{2\pi}{\omega_i}$ results in a non-vanishing term and hence contributes to the shift between the static and dynamic values
$$\begin{aligned}\langle \epsilon(Q_i) \rangle &= \frac{1}{2} A_i^2 \left.\frac{\partial^2 \epsilon}{\partial Q_i^2}\right|_0 \frac{1}{\tau} \int_0^\tau \cos^2 \omega_i t \, dt \\ &= \frac{1}{4} A_i^2 \left.\frac{\partial^2 \epsilon}{\partial Q_i^2}\right|_0 . \qquad (9)\end{aligned}$$
- Mixed coordinates: $\left.\frac{\partial^2 \epsilon}{\partial Q_i \partial Q_j}\right|_0 \neq 0$.
The term $\frac{1}{2} A_i A_j \left.\frac{\partial^2 \epsilon}{\partial Q_i \partial Q_j}\right|_0 \cos \omega_i t \cos \omega_j t = \frac{1}{2} A_i A_j \left.\frac{\partial^2 \epsilon}{\partial Q_i \partial Q_j}\right|_0 \left(\cos(\omega_i + \omega_j)t + \cos(\omega_i - \omega_j)t\right)$ and gives peaks at $\omega_i + \omega_j$ and $\omega_i - \omega_j$ in the ϵPS.

For (large) molecular systems, it is not straightforward to decompose the MD-based vibrational VPS spectra into molecular motions. Several methods have been proposed in literature for assigning vibrational bands to atomic motions.[24–26] The coordinates Q_i used in this work are determined with Principal Component Analysis (PCA) which relies on an equipartition assumption.[24] PS spectra corresponding with one particular coordinate (Q_iPS) are introduced. The Q_iPS is constructed by first projecting the atomic velocities on the Q_i coordinate and then computing its spectrum as in Eq. (5). The PCA coordinates are linear combinations of atomic displacements and are constructed such that the Q_iPS are as localized as possible in frequency.[24] Figure 2 illustrates the decomposition of the VPS in its various Q_iPS parts. Typically, modes at low wavenumbers can be properly disentangled (illustrated by Q_1PS in Figure 2), whereas this is in general no longer the case for modes at higher wavenumbers (see Q_iPS and Q_jPS in Figure 2). If multiple minima are present in the PES 0, the PCA does not represent good vibrational coordinates and the projection of the structure on the new coordinates can lead to unphysical geometries – as will be

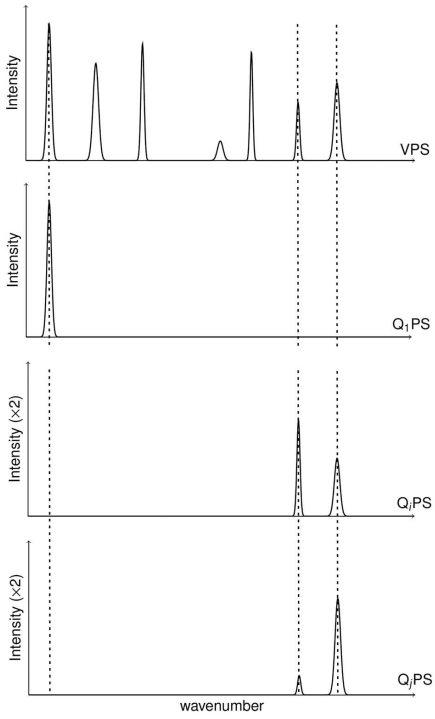

FIG. 2. Schematical representation of the decomposition of a VPS in Q_iPS. Typically, modes at low wavenumbers can be properly disentangled (e.g., Q_1PS), whereas this is in general no longer the case for modes at higher wavenumbers (e.g., Q_iPS and Q_jPS).

demonstrated for biphenyl. Nevertheless, PCA allows assigning motions to frequencies which is sufficient for the current goal.

Figure 3 summarizes the proposed methodology, clearly stating that the aim of this analysis is to link fluctuations in the electronic excitation energy (characterized by ϵPS) with vibrational motions (characterized by Q_iPS). In summary, different types of coordinates are obtained: (i) inactive coordinate, with ϵ invariant under change of this coordinate, (ii) linearly active coordinate, with ϵ linearly dependent on the change of the coordinate, (iii) quadratically active coordinate, with ϵ quadratically dependent on the change of the coordinate, and (iv) mixed coordinate. The shift of the dynamic averaged value $\langle\epsilon\rangle$ with respect to the static value ϵ_0 is mainly caused by quadratically active coordinates.

B. Computational details

The Born-Oppenheimer MD simulations are performed on the gas phase molecules using CP2K[31,32] with a *NVT* Nosé-Hoover thermostat.[33,34] MD simulations are performed at various temperatures. For the case studies ethylene, biphenyl, and hexamethylbenzene, MD runs are done at 300

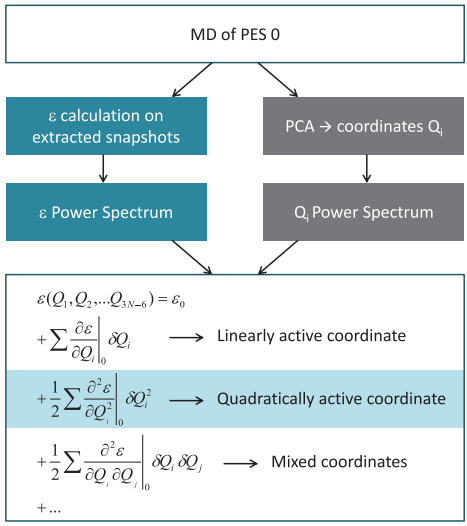

FIG. 3. Flow scheme for identifying the dominant – in particular quadratically active – internal modes responsible for changes in excitation properties.

and 600 K, and for ethylene the situation at 100 K is also included. For the energy and the force evaluation, the BLYP functional[35,36] with Grimme D3 dispersion corrections[37,38] is used, combined with a Molopt TZVP basis set[39] – optimized for the Goedecker-Tetter-Hutter pseudopotentials[40] – and a cutoff of 280 Ry. The simulation length is 50 ps after equilibration and a sampling rate of $\Delta t = 5$ fs is used, resulting in 10^4 snapshots. The Fourier transform is calculated using FFT modules in MD-tracks.[29] Gaussian09[41] is used with TD-DFT,[11,12] together with the B3LYP[36,42] functional and a DGTZVP basis set to evaluate the vertical electronic energies. Details of the QM/MM MD simulations of the azo dye ethyl orange can be found in Ref. 3. The gas phase MD simulations on this system were consistently performed with the same QM parameters. In line with that work, TD-DFT calculations are done using the B3LYP functional and 6-31+G(d,p) basis set, in combination with the PCM method modeling a continuum water solvent.[43–46] Again a total simulation time of 50 ps has been applied with a sampling rate of $\Delta t = 5$ fs.

The vibrational coordinates Q_i are the principal components obtained from the standard PCA[24] as implemented in GROMACS,[47] i.e., the Q_i are the eigenvectors of the covariance matrix of the atomic coordinates $r_j, (j = 1, \ldots, 3N)$. The scan along a vibrational coordinate Q_i (e.g., Figure 5(b)) is performed by creating a series of geometries and evaluating the electronic excitation energy in each geometry. These geometries are created by interpolating the atomic coordinates between the two geometries where Q_i is extreme, i.e., the geometry with minimum and maximum Q_i value during the MD run. The geometry averaged over the MD run is chosen as reference geometry ($Q_i = 0$) by the atomic coordinates $r_j^0 (j = 1, \ldots, 3N)$. Note that the optimized ground state

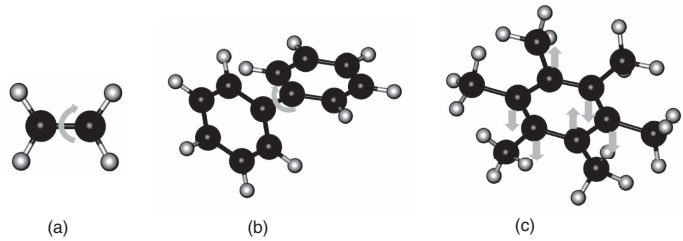

FIG. 4. Optimized ground state geometries of ethylene (a), biphenyl (b), and hexamethylbenzene (c). The dominant vibrational mode responsible for changes in the electronic spectrum are also indicated.

geometry with excitation energy ϵ_0 not necessarily belongs to this set of geometries. The vibrational coordinate Q_i is measured in Angström and is associated to the geometry change, defined by $\sqrt{\sum_{j=1}^{3N}(r_j - r_j^0)}$, with respect to the average geometry r_j^0. In the case of biphenyl, the principal component related to the torsion between both phenyl planes leads to large deformations, and in this particular situation a fix scan along the corresponding angle is used (see discussion in Sec. III A).

It is important to note that overall, there is no restriction on the type of MD (BOMD,[3] CPMD,[48] Classical MD,[18] etc.), choice of ensemble (*NVE*, *NVT*, *NPT*, etc.), nor on the level of theory to calculate the electronic excitations (single-excitation configuration interaction (CIS), TD-DFT, coupled-cluster with single, double and triple excitations (CCSD(T)), ...). The length of the MD simulation is not essential; however, it should be long enough to have a good sampling of the phase-space and an acceptable resolution for the VPS. The method is here presented for vertical excitation energies, but is in principle extendable to other properties such as magnetic resonance properties (NMR, EPR), hyperpolarizability,[27,28] etc.

III. RESULTS AND DISCUSSION

A. General approach

To show the possibilities and limitations of the proposed method, three case studies are discussed in detail. In particular, ethylene, biphenyl, and hexamethylbenzene (see Figure 4) are investigated, and the first vertical excitation energies and corresponding oscillator strengths are summarized in Table I. Various temperatures were tested for the MD simulations (see Table I). Overall, it is found that $\langle\epsilon\rangle$ decreases with increasing temperature, see hereafter.

The first excitation energy of ethylene is analyzed first. The vibrational behavior of this molecule is experimentally and theoretically well-known and the calculated peak positions of the VPS (Figure 5(a)) are in very good agreement with the experimental values (see Table II). As seen in Figure 5(a), the VPS is sufficiently resolved allowing identification of the various vibrational frequencies and corresponding coordinates Q_i without a PCA analysis.

The high-temperature simulation at 600 K is used for detailed analysis. To gain more insight in the motions responsible for the shift between the static and dynamic result (7.72 eV versus 7.45 eV, see Table I), the ϵPS and VPS are plotted in Figure 5. The ϵPS shows three main peaks around $\nu = 1344, 1625$, and $2058\ \mathrm{cm}^{-1}$ (see Figure 5(a)). The first two peaks show clear overlap with mode 6 (CH_2 scissors) and mode 8 (CC stretch) of the VPS (see Table II), indicating a linear variation of ϵ along these modes. This is illustrated for mode 6 in Figure 5(b), where both the ground state (PES 0) and first excited state (PES 1) potential energy surface are plotted along this mode. The surfaces represent displaced parabolic surfaces; they have the same curvature with their minima at different values for Q_6. This results in a

TABLE I. Calculated vertical excitation energy (ϵ_0, $\langle\epsilon\rangle$) (eV) and corresponding oscillator strength (f_0, $\langle f\rangle$) of the first excitation at various temperatures T (K). Identification of dominant internal motions responsible for the shift between the static and dynamic value.

	Excitation	ϵ_0[a]	f_0[a]	T	$\langle\epsilon\rangle$[b]	$\langle f\rangle$[b]	Dominant motions
Ethylene	$S_0 \rightarrow S_1$			100	7.61	0.336	
		7.72	0.360	300	7.49	0.286	CH_2 torsion
				600	7.45	0.256	
Biphenyl	$S_0 \rightarrow T_1$	3.26	0.000[c]	300	3.16	0.000[c]	Inter-ring torsion
				600	3.09	0.000[c]	
Hexamethylbenzene	$S_0 \rightarrow S_1$	4.91	0.000	300	4.81	0.002	Butterfly motion
				600	4.69	0.006	

[a]The static values correspond to B3LYP/DGTZVP TD-DFT computations on optimized BLYP/TZVP geometries (see Sec. II B).
[b]The dynamic values result from B3LYP/DGTZVP TD-DFT computations on 10^4 snapshots generated during a MD simulation using BLYP-D3 (see Sec. II B).
[c]Calculated oscillator strengths of singlet-triplet transitions are zero due to spin-symmetry.

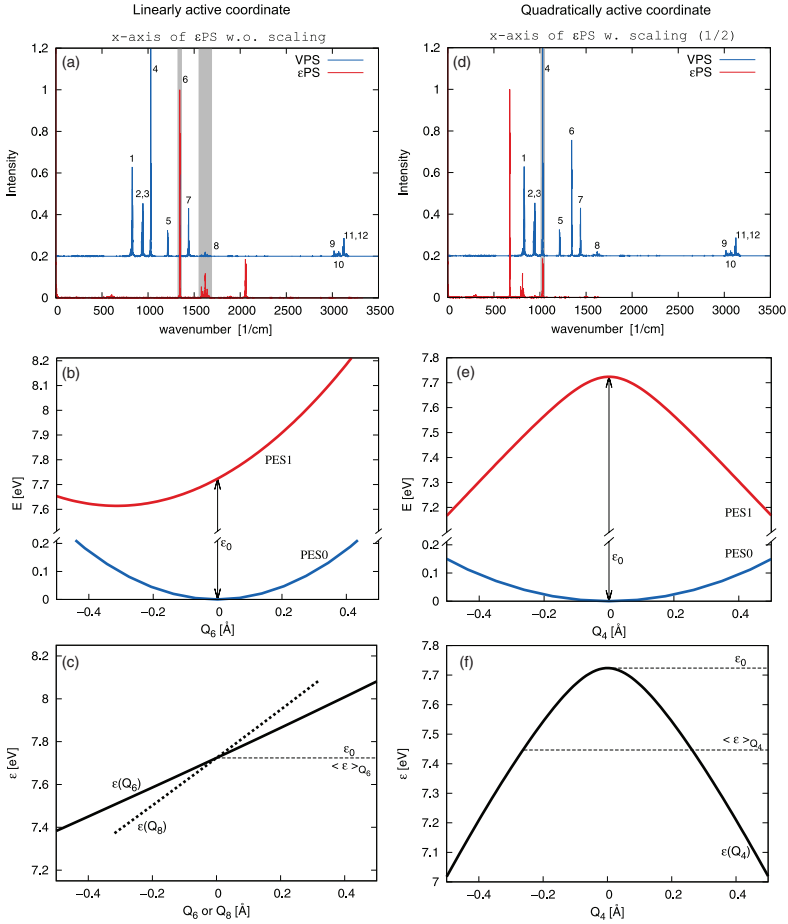

FIG. 5. Power spectra and scanning plots of ethylene sampled at 600 K. (a) Calculated VPS (blue, shifted upwards) and ϵPS (red). (b) PES 0 (blue) and PES 1 (red) along vibrational mode 6. (c) ϵ as a function of coordinate Q_6 (full line) and Q_8 (dotted line). (d) The same VPS (blue) as in (a) is displayed with the scaled ϵPS (red). (e) PES 0 (blue) and PES 1 (red) along vibrational mode 4. (f) ϵ as a function of coordinate Q_4.

TABLE II. Experimental[49] (Exp.) and calculated (Calc.) vibrational frequencies (Freq.) of ethylene, accompanied by the motion type and irreducible representation representing the vibrational mode (Irrep.).

	Freq. (cm^{-1})					Freq. (cm^{-1})			
	Exp.	Calc.	Type	Irrep.		Exp.	Calc.	Type	Irrep.
1	826	829	CH_2 rock	B_{2u}	7	1444	1440	CH_2 scissors	B_{1u}
2	940	936	CH_2 wag	B_{2g}	8	1625	1621	CC stretch	A_g
3	949	944	CH_2 wag	B_{3u}	9	2989	3017	CH_2 s-stretch	B_{1u}
4	1026	1029	CH_2 torsion	A_u	10	3022	3067	CH_2 s-stretch	A_g
5	1222	1211	CH_2 rock	B_{3g}	11	3083	3115	CH_2 a-stretch	B_{3g}
6	1344	1344	CH_2 scissors	A_g	12	3105	3125	CH_2 a-stretch	B_{2u}

linear dependence of ϵ along this coordinate (Figure 5(c)). If the sampling along this mode is symmetrical around the equilibrium geometry and if the corresponding surface is harmonic, the average transition energy $\langle\epsilon\rangle_{Q_6}$ along the variation of this motion coincides with the energy ϵ_0 corresponding with the equilibrium geometry. Hence, we notice no global shift for ϵ. The same results hold for mode 8 (Figure 5(c)).

The original peak at 2058 cm^{-1} in the ϵPS (see Figure 5(a)) cannot be explained with a linear dependence since no vibration with this frequency is present in the VPS. However, the peak is explained based on a quadratic dependency of the electron transition energy on the coordinate, since then a frequency twice as large as for the vibrations is found (see Sec. II A). The frequency axis of ϵPS is now scaled with 1/2 (see Figure 5(d)). It hence becomes clear that vibrational mode 4 (ν = 1026 cm^{-1}, CH_2 twist) has a significant influence on ϵ. The excitation energy ϵ depends quadratically on this coordinate (Q_4) and therefore, averaging over samples which contain this CH_2 twist will cause a global shift of the excitation energy. The reason that this mode is quadratically active is that the curvature of the PES 0 and PES 1 are different, but due to symmetry reasons there is no linear component: the PES 1 has a maximum at the equilibrium geometry (see Figure 5(e)). Therefore, a quadratic-like dependence for ϵ is found for mode 4 (Figure 5(f)). This conclusion is clearly in line with the well-known fact that in the excited state, ethylene is twisted over 90°.[9,10] This torsion dominates the changes in the excitation energy (see Table I) and hence if this motion is prohibited, then the ϵPS spectrum will no longer display this quadratic dependency and hence the computed excitation energy will be almost independent of geometrical distortions.

The occurrence of mixing modes – representative of the Duschinsky effect – should correspond to peaks at $\omega_i + \omega_j$ and $|\omega_i - \omega_j|$. Mebel *et al.*[9] reported the Duschinsky matrix of ethylene and discussed in particular the mixing of the four modes of *A* symmetry (i.e., modes 4, 6, 8, and 10 in Table II). Mixing of modes 4 (torsion) and 10 (CC stretch) implies frequency peaks at 4096 and 2038 cm^{-1}. Due to the complication of possible overlap with other peaks in the region slightly above 2000 cm^{-1} (see discussion of the quadratic behavior), we concentrate on the high frequency peak at 4096 cm^{-1}. This peak is indeed observable in the spectrum (see Figure S1 in the supplementary material[54]). Most importantly, all peaks in the region above 2100 cm^{-1} have very low intensities compared to the discussed features in Figures 5(a) and 5(d). For example, the intensity of the peak at 4096 cm^{-1} is only 0.1% of those in Figure 5. Due to this low intensity, we are confident that the assignment at 2058 cm^{-1} to the quadratically active torsional mode is still valid.

Simulations at lower temperatures lead to the same assignment of vibrational modes. The maximum amplitude of the oscillations obviously decreases with lower temperatures, implying that the PES 0 is sampled in a smaller range. In case of Q_4 (see Figure 5(f)), this results in a higher $\langle\epsilon\rangle$ as listed in Table I.

A second example is biphenyl. The equilibrium ground state conformation is non-planar (see Figure 4(b)) and a dihedral angle of 39.8° between the phenyl ring planes – hereafter referred to as the torsional angle – is found. Due to symmetry reasons, the PES 0 has an equivalent minimum at a torsional angle of −39.8°. The inter-ring torsion of biphenyl has been studied before and both the lowest triplet – which is favored in energy – and singlet excited states have minima corresponding with a planar geometry since the relatively minor steric interaction can be overcome in the excited state.[50] Due to the energetic preference (see Ref. 50 and Table IV considered hereafter) we investigate in detail the $S_0 \rightarrow T_1$ excitation, whereas other excitations are discussed in Sec. III B. A value of 3.26 eV is found for ϵ_0, and the dynamic averages $\langle\epsilon\rangle$ are 3.16 and 3.09 eV for MD temperatures of 300 and 600 K, respectively (see Table I). For the simulation of the VPS, the hydrogen atoms are neglected since their contribution to the VPS is dominant, while their influence on the π system is very small. The total VPS and ϵPS are given in the supplementary material (Figure S2).[54] Their comparison is however complicated due to the complexity of the VPS, and hence Q_iPS (with i = 1, …, 30, only taking into account the vibrational motions of the 12 carbon atoms) are introduced. As pointed out in the Introduction (see Figure 2) the decomposition of the VPS and localization of Q_iPS is not straightforward: it is seen that most Q_iPS contain more than one peak (see the supplementary material[54]).

In the ϵPS spectrum at 600 K, 6 peaks can be distinguished, as listed in Table III. Detailed comparison between the ϵPS and Q_iPS result in an assignment of 5 linearly active and 2 quadratically active PCA coordinates. For the linear motions, both ring deformations and the inter-ring

TABLE III. Assignment table of biphenyl at 600 K. Characteristic peaks of the ϵPS (corresponding with the $S_0 \rightarrow T_1$) are given for the linearly (unscaled) and quadratically (scaled with 1/2) active modes. Peaks of separate Q_iPS are also listed. All data are given in cm^{-1}.

	Linear						Quadratic		
	ϵPS (ω_i)	Q_{20}PS	Q_{26}PS	Q_{28}PS	Q_{29}PS	Q_{30}PS	ϵPS[a] (ω_i/2)	Q_1PS	Q_{10}PS
1	53						26	30	
2	728	729					364		
3	985	987		983			492		
4	1241	1241	1246	1241			620		620
5a	1540				1540		770		
5b	1554					1550	777		

[a]Scaled values.

C–C stretch are found to be active. The double peak around 1550 cm^{-1} corresponds with two similar ring deformations involving the two aromatic rings: the lowest peak (1540 cm^{-1}) corresponds with a symmetrical motion, while the antisymmetric vibration of the two ring deformations is assigned to the highest peak (1554 cm^{-1}). The fact that ϵPS is able to discriminate these two modes illustrates the efficiency of the method. For the quadratic motions, the Q_1 coordinate (30 cm^{-1}) mainly corresponds with the torsional angle, whereas Q_{10} corresponds with ring deformations. These vibrational modes are mainly responsible for the change between the static and dynamic excitation energy. All peaks in the ϵPS can be assigned to vibrational modes, indicating that the power series up to second-order (see Eq. (4)) is sufficient to capture the fluctuating behavior of the first vertical excitation energy. From Table III it is clear that some peaks in the ϵPS are present in various Q_iPS, e.g., the coordinates Q_{20}, Q_{26}, and Q_{28} all contain a peak at 1241 cm^{-1}.

At 600 K, ϵPS is dominated by a peak at 53 cm^{-1} which is characteristic for the inter-ring torsion. The obtained value is in reasonable agreement with the experimental value of 70 cm^{-1}.[51,52] For this well-known vibration, correspondence is found between ϵPS and Q_1PS (as shown in Figure 6(a) and Table III) as a quadratically active mode.

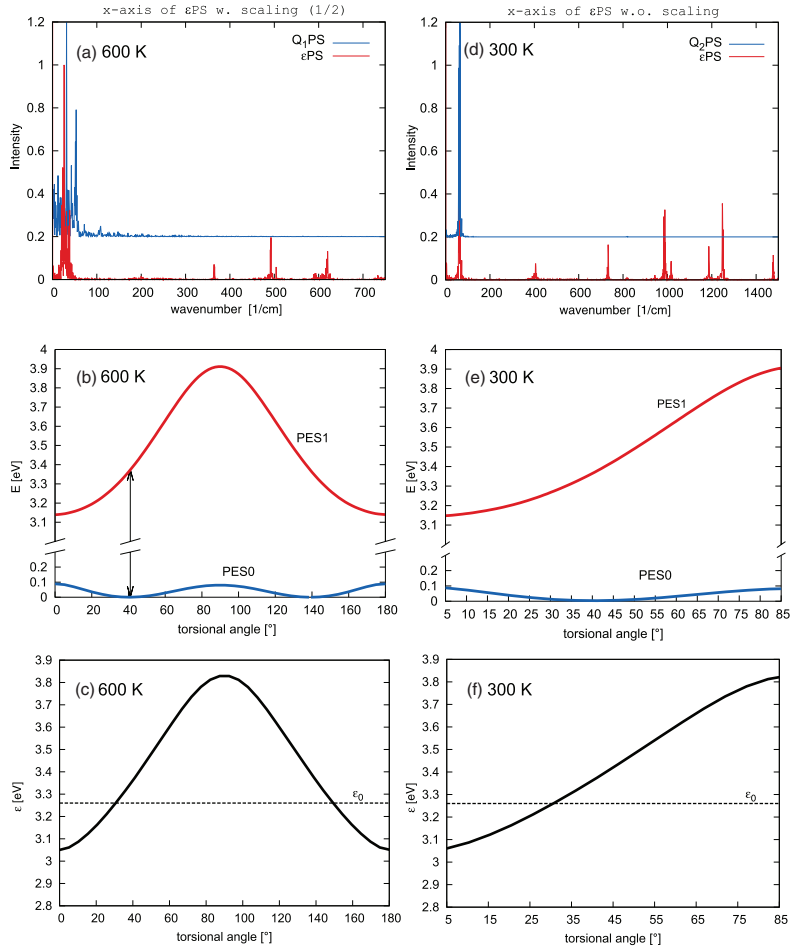

FIG. 6. Power spectra and PES surfaces of biphenyl in case of MD sampling at 600 K (a)–(c) and 300 K (d)–(f). (a) Calculated Q_1PS (blue, shifted upwards) and ϵPS (red) with the scaled frequency axis at 600 K. (b) PES 0 (blue) and PES 1 (red) in function of the torsional angle (ranging between 0° and 180°). (c) ϵ over the available range of the torsional angle at 600 K. (d) Calculated Q_2PS (blue, shifted upwards) and ϵPS (red) at 300 K. (e) PES 0 (blue) and PES 1 (red) in function of the torsional angle (ranging between 5° and 81°). (f) ϵ over the available range of the torsional angle at 300 K.

The high-temperature simulation enables full rotation of both phenyl rings about the central C–C axis, corresponding with variation of the torsional angle between 0° and 360°. This event occurs several times during the MD run. Both minima of the PES 0 of biphenyl are hence sampled in this MD run (see Figure 6(b)). As a result, projected PCA coordinates are ill defined and an explicit scan along these PCA coordinates is unphysical. It is nevertheless instructive to investigate the PES 0 and PES 1 in function of the torsional angle (varying between 0° and 180°, as seen in the MD run at 600 K). The resulting explicit scan is depicted in Figure 6(b), and Figure 6(c) displays the first electronic excitation energy as a function of the torsional angle, clearly showing a quadratic dependence. This explicit scan also shows that depending on the MD sampling, averaging the excitation energy over this torsional angle can result in a smaller or larger $\langle\epsilon\rangle$, most likely depending on the temperature of the system. In the simulation at 600 K, sufficient sampling over this torsional angle will lead to a rise of the average value. However, the other quadratic mode (Q_{10}) has only one minimum and contributes substantially to the shift between the static and dynamic result.

The vibrational torsion is also investigated at 300 K. Lowering the MD temperature has the advantage that the sampling is now restricted to one minimum of the PES 0. In Figure 6(d), the situation at 300 K is shown, for which the torsional angle ranges between 5° and 81°. Indeed, only one minimum of the PES 0 is sampled and the PCA coordinates are better defined. Figure 6(d) depicts the ϵPS and Q_2PS and makes clear that the ϵPS is dominated by a peak at 65 cm^{-1}, characterized by the inter-ring torsion of PCA coordinate Q_2.[53] This coordinate is linearly active. To allow clear comparison with the high-temperature situation, the PES surfaces and excitation energy are plotted in function of the torsional angle (which now varies between 5° and 80° to represent the MD run at 300 K) in Figures 6(e) and 6(f).

The final case study is hexamethylbenzene (depicted in Figure 4(c)); the computed vertical excitation energies using a static and dynamic approach again deviate substantially as listed in Table I. The MD simulation at 600 K is used for further analysis. In Figure 7(a), the VPS (again without taking into account the hydrogen atoms) is plotted with the ϵPS without scaling of the frequency axis and hence this figure is used to identify the linearly active motions. Figure 7(a) indicates a perfect overlap for ϵPS and VPS for the modes at $\nu = 515$ cm^{-1} – corresponding with a simultaneous CC stretch of all methyl groups and their closest benzene carbon – and a mode at $\nu = 1219$ cm^{-1} – corresponding with the deformation of the aromatic ring. These modes indeed influence the π structure of the system and therefore the excitation energy. However, these linearly active motions again do not influence the average dynamic excitation energy $\langle\epsilon\rangle$. The quadratically active modes can be identified from inspecting Figure 7(b), where the frequency axis of ϵPS is scaled with a factor of 1/2. Clearly, the peak at $\nu = 165$ cm^{-1} corresponds with a quadratically active motion, in particular this is a skeletal motion with two methyl groups in anti-phase with the four others, often referred to as a butterfly motion. Averaging over this motion causes a shift of 0.29 eV (see Table I, 600 K) and hence confirms its dominant behavior.

B. Extension to other low-lying excited states

Thus far, the first vertical excitation has been discussed. However, the proposed analysis method is not restricted to first excitation energies and can easily be extended to multiple vertical excitations. Figure 8 displays ϵPS spectra of the first five electronic excitations for the investigated molecules ethylene, biphenyl, and hexamethylbenzene from MD runs at 600 K. In the case of biphenyl, transitions to both singlets and triplets are shown (Figure 8(b)). Also the first excitation ($S_0 \rightarrow S_1$ for ethylene and hexamethylbenzene and $S_0 \rightarrow T_1$ for biphenyl) as discussed in Sec. III A is included in the figure (in grey). An overview of the calculated excitation energies and corresponding oscillator strengths is given in Table IV.

Comparison of the ϵPS of ethylene reveals that the three peaks as originally observed in the ϵPS of the first excitation ($S_0 \rightarrow S_1$) are not necessarily maintained for higher excitations. From Figure 8(a), it is clear that compared to the first excitation ($S_0 \rightarrow S_1$) the large peak at 1344 cm^{-1} disappears for the excitations $S_0 \rightarrow S_4$ and $S_0 \rightarrow S_5$, whereas the peak located at 1625 cm^{-1} dominates the ϵPS of these

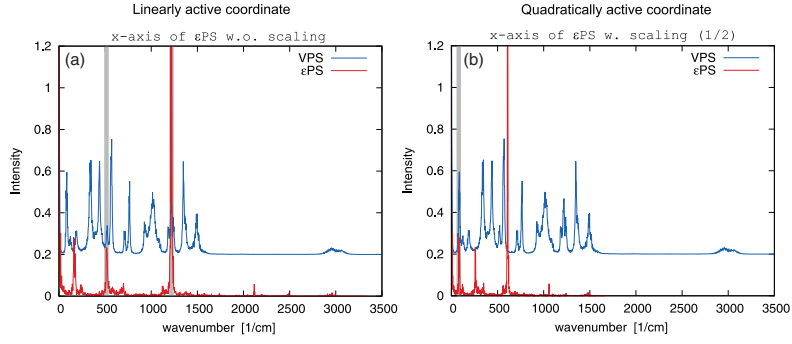

FIG. 7. Power spectra of hexamethylbenzene corresponding with the MD simulation at 600 K. (a) Calculated VPS (blue, shifted upwards) and ϵPS (red), without scaling of the frequency axis for ϵPS. (b) Calculated VPS (blue, shifted upwards) and ϵPS (red), with scaling of the frequency axis for ϵPS by 1/2.

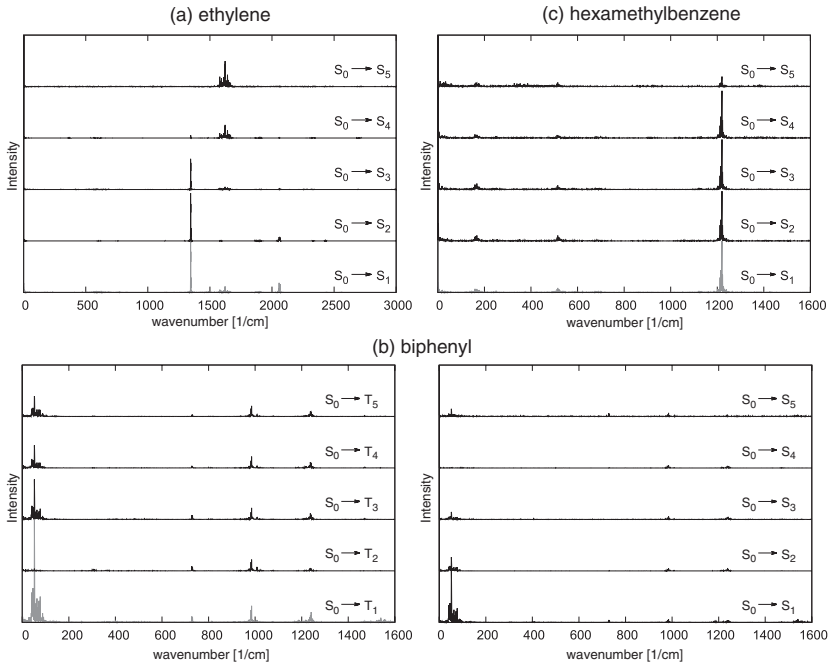

FIG. 8. Power spectra (ϵPS) at 600 K of multiple electronic excitations for ethylene (a), biphenyl (b), and hexamethylbenzene (c). The lowest five excitations are displayed; the first excitation is displayed at the bottom of each subfigure (in grey).

excitations. Importantly, the quadratically active peak (located at 2058 cm^{-1} in the ϵPS and hence corresponding with the CH_2 torsion at 1026 cm^{-1}) is significantly smaller in the ϵPS spectra of the higher vertical excitations from S_0. For these excitations, very small additional peaks appear in the ϵPS spectra, suggesting the importance of other vibrational modes.

In the case of biphenyl, electronic singlet-triplet excitations are found to be lower in energy compared to singlet-singlet excitations (see Table IV). The first important

TABLE IV. Calculated vertical excitation energies and corresponding oscillator strengths of multiple excited states (MD at 600 K).

	Ethylene					Hexamethylbenzene			
Transition	ϵ_0	f_0	$\langle\epsilon\rangle$	$\langle f\rangle$	Transition	ϵ_0	f_0	$\langle\epsilon\rangle$	$\langle f\rangle$
$S_0 \rightarrow S_1$	7.72	0.362	7.45	0.256	$S_0 \rightarrow S_1$	4.91	0.000	4.69	0.006
$S_0 \rightarrow S_2$	8.07	0.000	7.95	0.094	$S_0 \rightarrow S_2$	5.50	0.004	5.22	0.051
$S_0 \rightarrow S_3$	9.08	0.000	8.93	0.004	$S_0 \rightarrow S_3$	6.27	0.660	5.95	0.531
$S_0 \rightarrow S_4$	9.48	0.007	9.30	0.007	$S_0 \rightarrow S_4$	7.12	0.009	6.06	0.508
$S_0 \rightarrow S_5$	9.68	0.000	9.51	0.004	$S_0 \rightarrow S_5$	7.14	0.000	6.74	0.016
	Biphenyl								
Transition	ϵ_0	f_0	$\langle\epsilon\rangle$	$\langle f\rangle$	Transition	ϵ_0	f_0	$\langle\epsilon\rangle$	$\langle f\rangle$
$S_0 \rightarrow T_1$	3.26	0.0	3.09	0.0	$S_0 \rightarrow S_1$	4.86	0.444	4.78	0.225
$S_0 \rightarrow T_2$	3.86	0.0	3.60	0.0	$S_0 \rightarrow S_2$	4.88	0.000	4.73	0.018
$S_0 \rightarrow T_3$	4.33	0.0	4.14	0.0	$S_0 \rightarrow S_3$	4.91	0.000	5.07	0.020
$S_0 \rightarrow T_4$	4.36	0.0	4.26	0.0	$S_0 \rightarrow S_4$	5.59	0.016	5.41	0.029
$S_0 \rightarrow T_5$	4.39	0.0	4.38	0.0	$S_0 \rightarrow S_5$	5.69	0.109	5.23	0.103

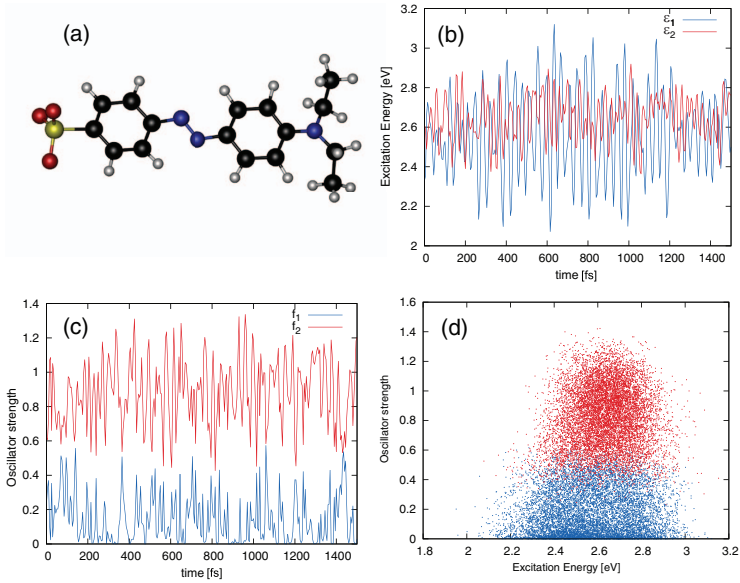

FIG. 9. (a) Optimized geometry of ethyl orange (gas phase). (b) Excitation energy trajectories. (c) Trajectories of oscillator strength. (d) Correlation plot between the oscillator strength and excitation energy for the 10 000 snapshots.

observation is that some of the higher excited state surfaces are close to each other, and crossing of surfaces might occur. This is, e.g., the case for the excitations from S_0 to higher triplet surfaces T_3, T_4, and T_5, corresponding with vertical excitation energies of 4.33, 4.36, and 4.39 eV, respectively (see Table IV). A similar feature holds for the excitations to the singlet excited states, since S_1, S_2, and S_3 are also found to be close (4.86, 4.88, and 4.91 eV) as well as excitations to S_4 and S_5. For the series of $S_0 \rightarrow S_i$ transition, the excited states are ordered based on their oscillator strengths to avoid crossing between states which are close in energy. This ordering is necessary to obtain reliable values of the dynamic averages. The important inter-ring torsion, located at 53 cm^{-1}, dominates the $S_0 \rightarrow T_1$ and $S_0 \rightarrow S_1$ ϵPS. However, as can be seen in Table IV, the shift between the static and dynamic excitation energy is larger for the second excitation $S_0 \rightarrow T_2$ than for $S_0 \rightarrow T_1$. This seems at first instance surprising, since the dominant quadratic peak at 53 cm^{-1} is not present in the ϵPS of the $S_0 \rightarrow T_2$ transition (shown in Figure 8(b)). However, in Sec. III A, we concluded that sampling of multiple minima in the PES 0 might raise or lower the averaged value, and other quadratic modes (e.g., Q_{10}, see Table III) are responsible for the energy shift. Since the torsional angle Q_1 is neither linear nor quadratic for the second excitation energy, a combination of other quadratic modes will cause the larger shift.

For hexamethylbenzene, the five ϵPS spectra look very similar, suggesting that the PES surfaces of the singlet excited states 1 to 5 are very similar.

C. Application to an azo dye in a water environment

As a final example, a more complex molecule is selected to illustrate the possibilities of the proposed method. In particular, ethyl orange is chosen (see Figure 9(a)). This molecule is an azo dye used as pH-indicator and its halochromic behavior was previously studied by some of the presenting authors.[3] First, the PES 1 and PES 2 surfaces – corresponding with the first and second vertical excitation – are investigated after a MD sampling of ethyl orange in the gas phase. Second, a more realistic QM/MM MD simulation has been performed on this azo dye surrounded by water molecules, as the experimental UV/Vis spectrum of the dye solvated in water is available. It was shown that this experimental spectrum could be reproduced with great accuracy using a dynamic approach.[3]

Ethyl orange requires the consideration of both first and second vertical excitation energies, since these are very close in energy. As a starting point, the optimized structure is considered and the static predictions of the excitation energies are taken as reference values. The first excitation energy (hereafter referred to as ϵ_1) corresponds with the HOMO−1 to LUMO transition (ϵ_1 = 2.70 eV) and has an oscillator strength of 0.008. The second excitation energy (hereafter referred to as ϵ_2) has a higher oscillator strength (1.203) and corresponds with the HOMO to LUMO transition (ϵ_2 = 2.75 eV). These two transitions are largely fluctuating during the MD simulation and are constantly crossing, as visualized in Figure 9(b). They are well separated from the higher excitations, and hence the discussion can be restricted to the

$\epsilon_1(t)$ and $\epsilon_2(t)$ trajectories. The HOMO−1 to LUMO transitions are almost forbidden and lead to very small oscillator strengths in the MD run, and this observation clearly separates the two trajectories $\epsilon_1(t)$ and $\epsilon_2(t)$ (see Figure 9(c)). Hence, both signals are ordered according to the computed oscillator strength. Using all 10^4 snapshots taken during the total simulation (see Sec. II B) a correlation plot between the excitation energy and oscillator strength for the two signals can be easily constructed (Figure 9(d)): the ϵ_1 signals vary over a larger range than their ϵ_2 counterparts, and both categories are well separated although there is some narrow overlap region.

In Figure 10(a), the ϵPS spectra of the $\epsilon_1(t)$ and $\epsilon_2(t)$ trajectories are displayed. We note that these spectra exhibit relatively low noise, as a result from sorting both states according to their computed oscillator strength. The two ϵPS spectra differ in many aspects. ϵ_1PS reveals more prominent peaks, due to the larger fluctuations as can be seen in Figures 9(b) and 9(d). However, ϵ_1PS is less relevant for our purposes since the ϵ_1 transitions show a much lower average oscillator strength compared to ϵ_2 and hence contribute less to the maximum of a UV/Vis spectrum. Therefore, investigation of ϵ_2PS is more relevant. Naturally, there are common

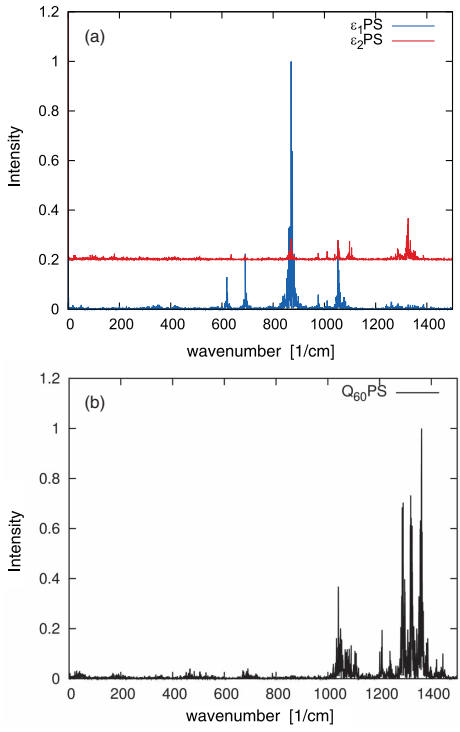

FIG. 10. (a) ϵPS for both trajectories $\epsilon_1(t)$ and $\epsilon_2(t)$. (b) Q_{60}PS with emphasis on the three peaks around 1300 cm^{-1}.

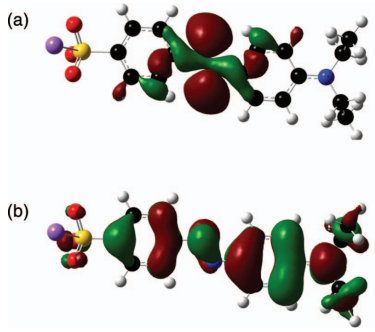

FIG. 11. The (a) HOMO−1 and (b) HOMO orbitals of ethyl orange (isosurfaces of 0.02 are shown).

peaks in both spectra (in particular, at 869 and 1052 cm^{-1}), however ϵ_1PS shows additional peaks at 620 and 690 cm^{-1}, whereas in ϵ_2PS peaks are observed at 1100 and 1330 cm^{-1}. The association of vibrations to the prominent peaks is done by PCA (without taking into account the hydrogen atoms) and the corresponding Q_iPS are compared to the two ϵPS (see the supplementary material[54]). The peak at 869 cm^{-1}, occurring in both ϵPS, can be assigned to a clear N–N stretch and related C–N–N bending (i.e., corresponding with PCA coordinate Q_{47}). The C–N stretches near the azo-bond correspond with the 1052 cm^{-1} peak. We now concentrate on the cluster of peaks around 1300 cm^{-1}, which only appears in the ϵ_2PS and is much less prominent in ϵ_1PS. The power spectrum of the Q_{60} coordinate of the PCA analysis reproduces the three peaks around 1300 cm^{-1} very well (see Figure 10). They arise from some ring vibrations leaving intact the azo bond and only affecting the HOMO orbital. These conclusions are supported by examining the HOMO−1 and HOMO orbitals in Figure 11. For the HOMO−1 to LUMO transition, we determined that the N–N bond plays a key role for the behavior of ϵ_1. Indeed, the HOMO−1 orbital is mainly located at this N–N azo bond, while the HOMO orbital is more spread out over both phenyl rings. The latter is again in correspondence with high intensities for the ϵ_2PS for the ring vibration frequencies. This could partly explain why the peaks are missing in the ϵ_1PS. Other PCA coordinates that could assign vibrations with other peaks in ϵ_2PS are taken up in the supplementary material.[54] Possible quadratic peaks in both ϵPS are of low intensity and not easy to identify due to quite broad Q_iPS in the corresponding region at low wavenumbers.

As a final aspect, we examined the influence of water molecules in the MD simulation on the proposed analysis. The experimental UV/Vis spectrum can be compared with the dynamic spectrum resulting from averaging over 10^4 snapshots (see Figure S7 in the supplementary material[54]). The correspondence with experiment is very good, as already reported in Ref. 3, and manifestly better than the two static predictions. Overall, using the MD run with the water molecules leads to a very similar analysis as the gas phase situation. Similar ϵPS spectra are obtained apart from more noise; they are

also displayed in the supplementary material (Figure S8).[54] In this case, a PCA analysis is found to be less straightforward: the generated Q_iPS spectra provide little detailed information since large delocalization of the peaks is observed. The disentanglement of these spectra can be tackled by splitting the molecule into separate fragments or by using filters; this is, however, outside the scope of this work. Nevertheless, the ϵPS spectra can be generated for a complex molecule embedded in a water environment.

IV. CONCLUSIONS

In this paper, we proposed a Fourier based analysis method allowing to identify the dominant vibrational motion(s) responsible for changes in spectroscopic properties. The method was here developed for vertical electronic excitation energies, although it is generally applicable to other spectroscopic characteristics. Earlier studies showed that molecular dynamics simulations give rise to non-negligible shifts in the UV/V is spectra due to the account for temperature and molecular anharmonic vibrations. The presented methodology allows for a thorough analysis of the data provided by a molecular dynamics run of the ground state PES and subsequent simulations of the excitation energies using TD-DFT. As such, information about the PES of the excited state is provided, without the cost of extra calculations. According to the presented method, peaks in the power spectrum of the excitation energy are compared with peaks in the velocity power spectrum. For peaks at the same frequency in both power spectra, no correction term to the average excitation energy is expected, whereas higher order terms (in particular quadratic terms) give rise to shifts comparing the dynamic and static values.

The method is illustrated with three small gas phase molecules. For these examples, the shift between the static excitation energy of the optimized geometry and the averaged excitation energy using a dynamic approach is between 0.1 and 0.3 eV. This shift can predominantly be assigned to a CC and inter-ring torsion in case of ethylene and biphenyl, respectively. Whereas for hexamethylbenzene a butterfly motion is found to dominate the changes in the first excitation energy. When increasing the temperature, the ground state PES is sampled over a larger range, leading to larger deviations in the averaged excitation energy. In the case of biphenyl, a second minimum in the PES 0 is sampled at 600 K, a situation beyond the possibilities of a standard harmonic approximation approach. The proposed method is also extended to other low-lying excited states and differences between the various PES are deduced.

Overall, computational techniques are essential for gaining a better understanding of the fundamentals of spectroscopy. In this light, molecular dynamics is of vital use in the future development of new and more complete analysis methods. The proposed proof-of-concept is applied on a larger system, i.e., the azo dye ethyl orange, both in the gas phase and solvated in water. Based on the MD trajectories and the generated signals of the excitation energies, power spectra are computed and the vibrational fingerprint of the electronic excitation is explored. It is found that the excitation with low intensity is mainly dominated by the azo bond present in this dye, while the HOMO to LUMO transition is mainly influenced by ring vibrations in the phenyl rings. Overall, identification of the dominant vibrational modes responsible for changes in spectroscopic properties can assist and guide further detailed research.

ACKNOWLEDGMENTS

The computational resources and services used in this work were provided by Ghent University (Stevin), the Hercules Foundation (Tier-1 Flemish Supercomputer Infrastructure), and the Flemish Government – Department of EWI. Funding was received from the Research Board of Ghent University (BOF), the Foundation of Scientific Research – Flanders (FWO), and BELSPO in the frame of IAP/7/05. A.G. and K.H. are post-doctoral researchers with the FWO.

[1] V. Barone and A. Polimeno, Chem. Soc. Rev. **36**, 1724 (2007).
[2] V. Barone, J. Bloino, S. Monti, A. Pedone, and G. Prampolini, Phys. Chem. Chem. Phys. **12**, 10550 (2010).
[3] T. De Meyer, K. Hemelsoet, L. Van der Schueren, E. Pauwels, K. De Clerck, and V. Van Speybroeck, Chem. - A Eur. J. **18**, 8120 (2012).
[4] K. Hemelsoet, Q. Qian, T. De Meyer, K. De Wispelaere, B. De Sterck, B. M. Weckhuysen, M. Waroquier, and V. Van Speybroeck, Chem. - A Eur. J. **19**, 16595 (2013).
[5] V. Barone, J. Bloino, M. Biczysko, and F. Santoro, J. Chem. Theory Comput. **5**, 540 (2009).
[6] J. Bloino, M. Biczysko, F. Santoro, and V. Barone, J. Chem. Theory Comput. **6**, 1256 (2010).
[7] F. Santoro, C. Cappelli, and V. Barone, J. Chem. Theory Comput. **7**, 1824 (2011).
[8] A. Baiardi, J. Bloino, and V. Barone, J. Chem. Theory Comput. **9**, 4097 (2013).
[9] A. M. Mebel, Y. T. Chen, and S. H. Lin, Chem. Phys. Lett. **258**, 53 (1996).
[10] A. M. Mebel, M. Hayashi, K. K. Liang, and S. H. Lin, J. Phys. Chem. A **103**, 10674 (1999).
[11] E. Runge and E. Gross, Phys. Rev. Lett. **52**, 997 (1984).
[12] *Time-Dependent Density Functional Theory*, edited by M. A. L. Marques, C. A. Ullrich, F. Nogueira, A. Rubio, K. Burke, and E. K. U. Gross (Springer, 2006).
[13] D. J. Tozer and N. C. Handy, Phys. Chem. Chem. Phys. **2**, 2117 (2000).
[14] D. Jacquemin, V. Wathelet, E. A. Perpète, and C. Adamo, J. Chem. Theory Comput. **5**, 2420 (2009).
[15] D. Jacquemin, A. Planchat, C. Adamo, and B. Mennucci, J. Chem. Theory Comput. **8**, 2359 (2012).
[16] C. Adamo and D. Jacquemin, Chem. Soc. Rev. **42**, 845 (2013).
[17] E. Pauwels, T. Verstraelen, H. De Cooman, V. Van Speybroeck, and M. Waroquier, J. Phys. Chem. B **112**, 7618 (2008).
[18] J. Přecechtělovaá, P. Novaák, M. L. Munzarová, M. Kaupp, and V. Sklenář, J. Am. Chem. Soc. **132**, 17139 (2010).
[19] G. Brancato, N. Rega, and V. Barone, J. Am. Chem. Soc. **129**, 15380 (2007).
[20] N. Rega, M. Cossi, and V. Barone, J. Am. Chem. Soc. **119**, 12962 (1997).
[21] D. McQuarrie, *Statistical Mechanics* (Harper and Row, 1976).
[22] D. W. Noid, M. L. Koszykowski, and R. A. Marcus, J. Chem. Phys. **67**, 404 (1977).
[23] M. Brehm and B. Kirchner, J. Chem. Inf. Model. **51**, 2007 (2011).
[24] M. Martinez, M.-P. Gaigeot, D. Borgis, and R. Vuilleumier, J. Chem. Phys. **125**, 144106 (2006).
[25] G. Mathias and M. D. Baer, J. Chem. Theory Comput. **7**, 2028 (2011).
[26] G. Mathias, S. D. Ivanov, A. Witt, M. D. Baer, and D. Marx, J. Chem. Theory Comput. **8**, 224 (2012).
[27] O. Quinet, B. Champagne, and B. Kirtman, J. Comput. Chem. **22**, 1920 (2001).
[28] O. Quinet, B. Champagne, and B. Kirtman, J. Comput. Chem. **23**, 1495 (2002).
[29] T. Verstraelen, M. Van Houteghem, V. Van Speybroeck, and M. Waroquier, J. Chem. Inf. Model. **48**, 2414 (2008).

[30]M. Van Houteghem, T. Verstraelen, D. Van Neck, C. Kirschhock, J. A. Martens, M. Waroquier, and V. Van Speybroeck, J. Chem. Theory Comput. **7**, 1045 (2011).
[31]G. Lippert, J. Hutter, and M. Parrinello, Mol. Phys. **92**, 477 (1997).
[32]J. VandeVondele, M. Krack, F. Mohamed, M. Parrinello, T. Chassaing, and J. Hutter, Comput. Phys. Commun. **167**, 103 (2005).
[33]S. Nosé, Mol. Phys. **52**, 255 (1984).
[34]S. Nosé, J. Chem. Phys. **81**, 511 (1984).
[35]A. D. Becke, Phys. Rev. A **38**, 3098 (1988).
[36]C. Lee, W. Yang, and R. G. Parr, Phys. Rev. B **37**, 785 (1988).
[37]S. Grimme, J. Antony, S. Ehrlich, and H. Krieg, J. Chem. Phys. **132**, 154104 (2010).
[38]S. Grimme, S. Ehrlich, and L. Goerigk, J. Comput. Chem. **32**, 1456 (2011).
[39]J. VandeVondele and J. Hutter, J. Chem. Phys. **127**, 114105 (2007).
[40]S. Goedecker, M. Teter, and J. Hutter, Phys. Rev. B **54**, 1703 (1996).
[41]M. J. Frisch, G. W. Trucks, and H. B. Schlegel *et al.*, Gaussian 09, Revision A.1, Gaussian, Inc., Wallingford, CT, 2009.
[42]A. D. Becke, J. Chem. Phys. **98**, 1372 (1993).
[43]M. Orozco and F. L. Luque, Chem. Rev. **100**, 4187 (2000).
[44]J. Tomasi and M. Persico, Chem. Rev. **94**, 2027 (1994).
[45]J. Tomasi, B. Mennucci, and R. Cammi, Chem. Rev. **105**, 2999 (2005).
[46]A. V. Marenich, C. J. Cramer, and D. G. Truhlar, J. Phys. Chem. B **113**, 6378 (2009).
[47]E. Lindahl, B. Hess, and D. van der Spoel, J. Mol. Model. **7**, 306 (2001).
[48]J. R. Asher and M. Kaupp, Theor. Chem. Acc. **119**, 477 (2008).
[49]R. J. Sension and B. S. Hudson, J. Chem. Phys. **90**, 1377 (1989).
[50]A. Imamuram and R. Hoffmann, J. Am. Chem. Soc. **90**, 5379 (1968).
[51]G. Zerbi and S. Samdroni, Spectrochim. Acta A **24**, 483 (1968).
[52]S. Y. Lee, Bull. Korean Chem. Soc. **19**, 93 (1998).
[53]We note that for the simulation at 300 K, the vibrational torsion is found to correspond with Q_2, meaning that this vibration is indeed less principle compared to the simulation at 600 K.
[54]See supplementary material at http://dx.doi.org/10.1063/1.4869937 for additional VPS of ethylene in the region above 2100 cm^{-1}, detailed discussion of the various Q_iPS spectra of biphenyl and ethyl orange, and the ϵPS of the solvated ethyl orange. Also the influence of neglecting crossings of the excited state PES is discussed.

Exploring the Vibrational Fingerprint of the Electronic Excitation Energy via Molecular Dynamics — Supplementary Material

Andy Van Yperen-De Deyne,[1] Thierry De Meyer,[1] Ewald Pauwels,[1, a)] An Ghysels,[1] Karen De Clerck,[2] Michel Waroquier,[1] Veronique Van Speybroeck,[1] and Karen Hemelsoet[1, b)]

[1)] *Center for Molecular Modeling (CMM), Ghent University, Technologiepark 903, 9052 Zwijnaarde, Belgium*

[2)] *Department of Textiles, Ghent University, Technologiepark 907, 9052 Zwijnaarde, Belgium*

(Dated: 7 March 2014)

[a)]Current address: UGent HPC, Ghent University, Krijgslaan 281, S9, B-9000 Gent

[b)]Electronic mail: karen.hemelsoet@ugent.be

a. Ethylene The occurrence of mixing modes - representative of the Duschinsky effect - should correspond to peaks at $\omega_i + \omega_j$ and $|\omega_i - \omega_j|$.[1]. Mixing of modes 4 (torsion) and 10 (CC stretch) implies frequency peaks at 4096 and 2038 cm^{-1}. Due to the complication of possible overlap with other peaks in the region slightly above 2000 cm^{-1}, we concentrate on the high frequency peak at 4096 cm^{-1}. This peak is indeed observable in Figure S1. All peaks in the region above 2100 cm^{-1} have very low intensities. For example, the intensity of the peak at 4096 cm^{-1} is only 0.1 % of those in Figure 5a.

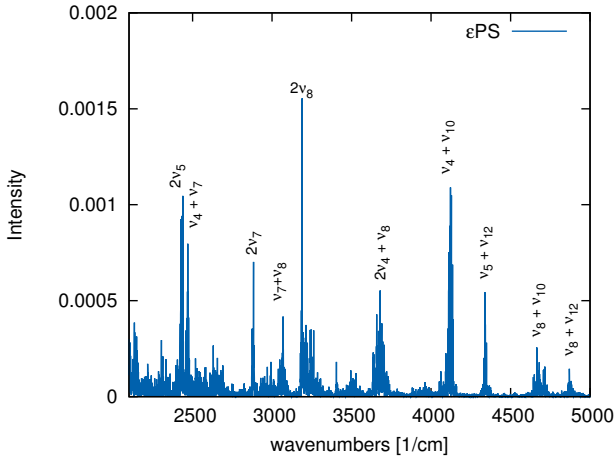

FIG. S1: The high frequency range of the ϵPS of ethylene. The peaks are labeled by the combinations at the appropriate position. In order of increasing frequency the following assignments can be made: $2\nu_5$ =2422 cm^{-1}, $\nu_4 + \nu_7 = 2469$ cm^{-1}, $2\nu_7 = 2882$ cm^{-1}, $\nu_{10} = 3067$ cm^{-1}, $2\nu_8 = 3187 - 3336$ cm^{-1}, $2\nu_4 + \nu_8 = 3680$ cm^{-1}, $\nu_4 + \nu_{10}$ =4096 cm^{-1}, $\nu_5 + \nu_{12}$ =4336 cm−1, $\nu_8 + \nu_{10}$ =4667 cm^{-1}, $\nu_8 + \nu_{12} = 4872$ cm^{-1}.

b. Biphenyl Detailed overview of the results for the $S_0 \rightarrow T_1$ transition of biphenyl (MD at 600 K) are given. Figure S2 displays the ϵPS compared with the overall VPS. Due to the complexity of the VPS, it is difficult to determine linearly or quadratically active peaks and therefore Q_iPS are used instead.

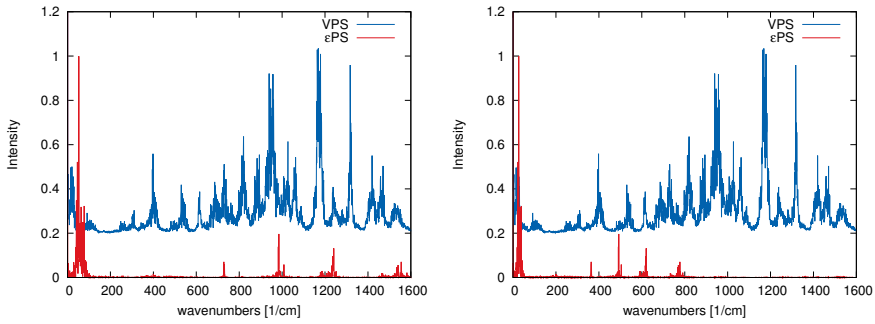

(a) (b)

FIG. S2: (a) Calculated VPS (blue, shifted upwards) and ϵPS (red) for biphenyl. (b) The VPS (blue, shifted upwards) and scaled ϵPS (red) for biphenyl.

Overall, 7 Q_iPS spectra were found that exhibit peaks that coincide with characteristic peaks in the ϵPS: 5 linearly active (see Figure S3) and 2 quadratically active (see Figure S4).

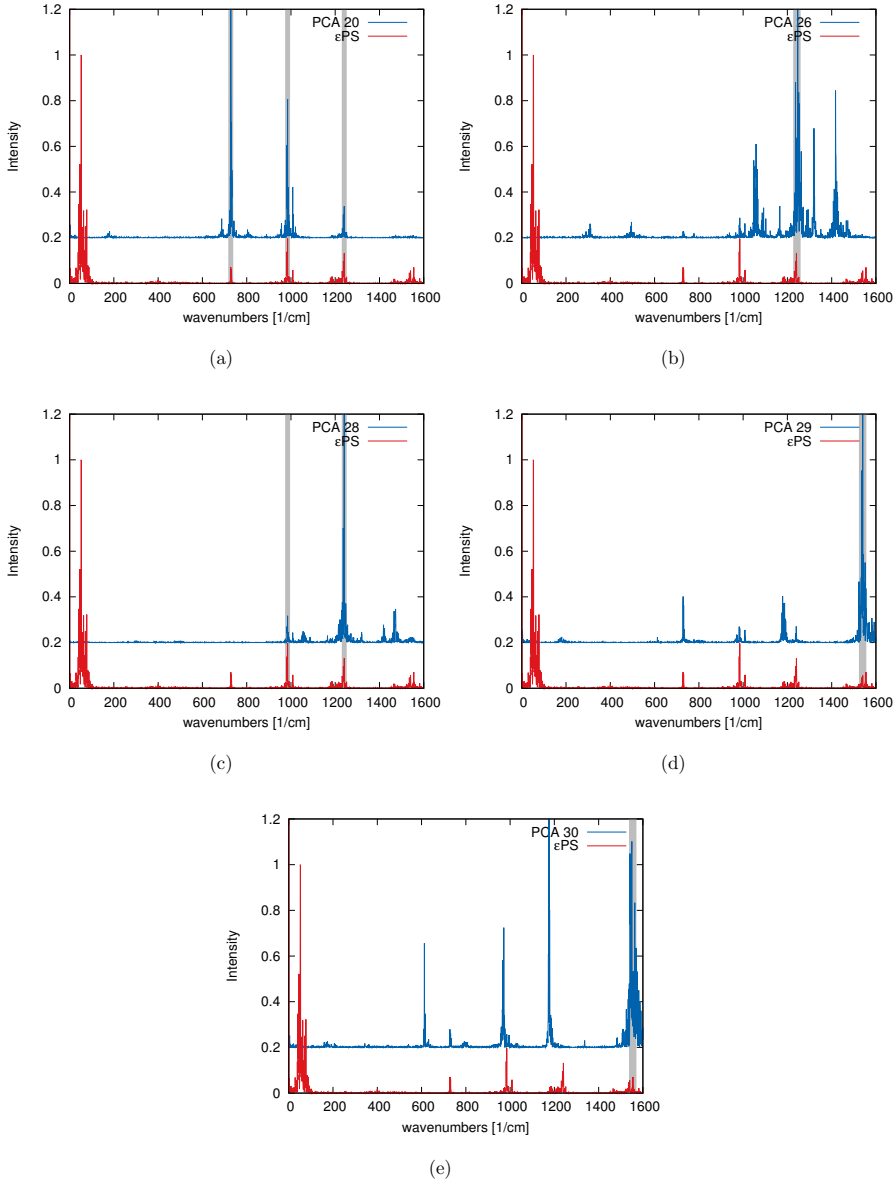

FIG. S3: Calculated Q_iPS (blue, shifted upwards) and ϵPS (red) for biphenyl. Five linearly active modes can be distinguished: Q_{20}, Q_{26}, Q_{28}, Q_{29} and Q_{30}.

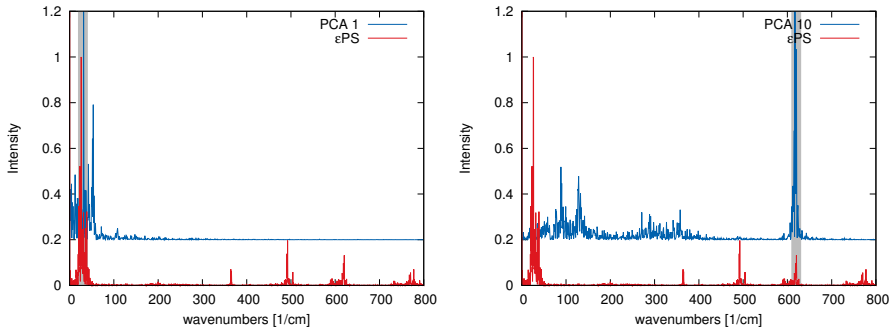

(a) (b)

FIG. S4: Calculated Q_iPS (blue, shifted upwards) and scaled ϵPS (red) for biphenyl. Two quadratically active modes can be distinguished: Q_1 and Q_{10}.

c. Ethyl orange in gas phase A more detailed assignment of the peaks of ϵ_1PS and ϵ_2PS is given in Figures S5 and S6. In both ϵPS spectra, four peaks can be distinguished; two are observed (at 860 and 1051 cm^{-1}) in both power spectra. In the case of ethyl orange, no clear quadratic mode is identified; although they might be present but with much lower intensities.

Figure S5 shows that the first excitation energy (ϵ_1 in the main text) changes mostly with C-N-N scissors (mode Q_{33}), azo N-N stretch (mode Q_{40} and Q_{47}) and related C-N stretches (mode Q_{47} and Q_{51}). It is no surprise these are influencing the HOMO-1 orbital (see Figure 10a in the main manuscript), since it is located at the azo bond. Note that both Q_{47} and Q_{33} do not perfectly correspond to isolated peaks in their power spectrum. Comparing with other power spectra of principal components resulted in a very plausible assignment.

In contrast to the HOMO-1, the HOMO orbital is a π-like orbital spread over both phenyl groups and therefore ring vibrations are dominating the ϵ_2PS (Figure S6). These are located at 1052 cm^{-1} (Q_{54}) and three peaks at 1330 cm^{-1} (Q_{60}), both corresponding to in plane ring vibrations. Surprisingly, the out-of-plane motions as well as global motions (such as a phenyl-azo-phenyl bending motion) are not or less pronounced in the ϵ_2PS. The N-N stretch is again present in the ϵ_2PS but much less dominant compared to the ϵ_1PS. Both Q_{47} and Q_{51} can be correlated to this power spectrum.

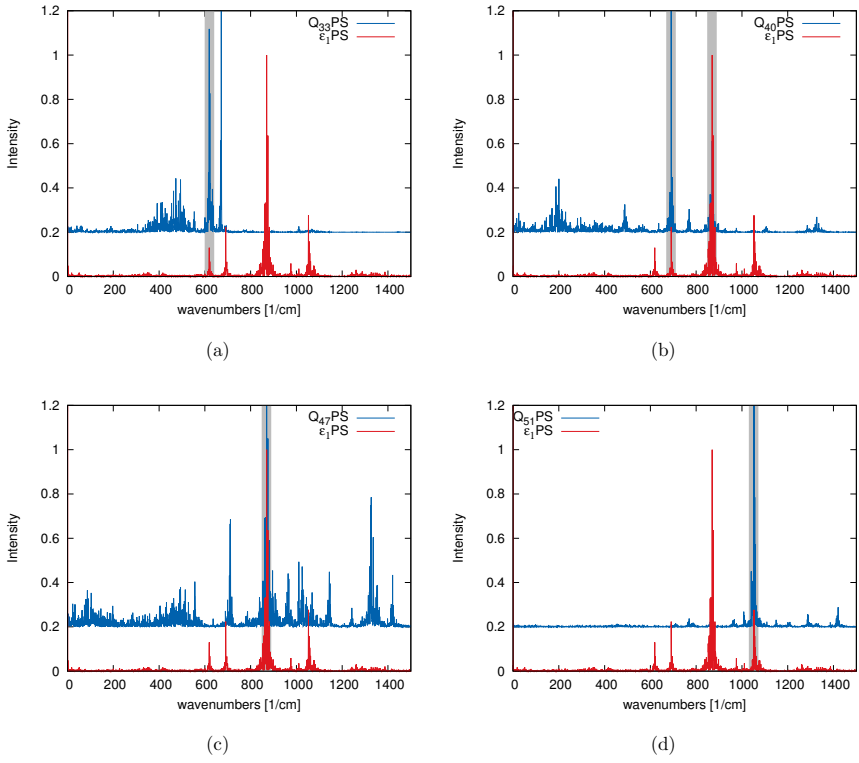

FIG. S5: Assignment of peaks in the ϵ_1PS to principal components Q_i via the Q_iPS. (a) Q_{33} with peak position at 620 cm^{-1}, corresponding with a C-N-N scissor motion (b) Q_{40} with peak positions at both 690 cm^{-1} and 869 cm^{-1} and (c) Q_{47} located at mainly 869 cm^{-1} both corresponding to N-N stretching motions, (d) Q_{51} with peak position at 1052 cm^{-1} corresponding with C-N stretches.

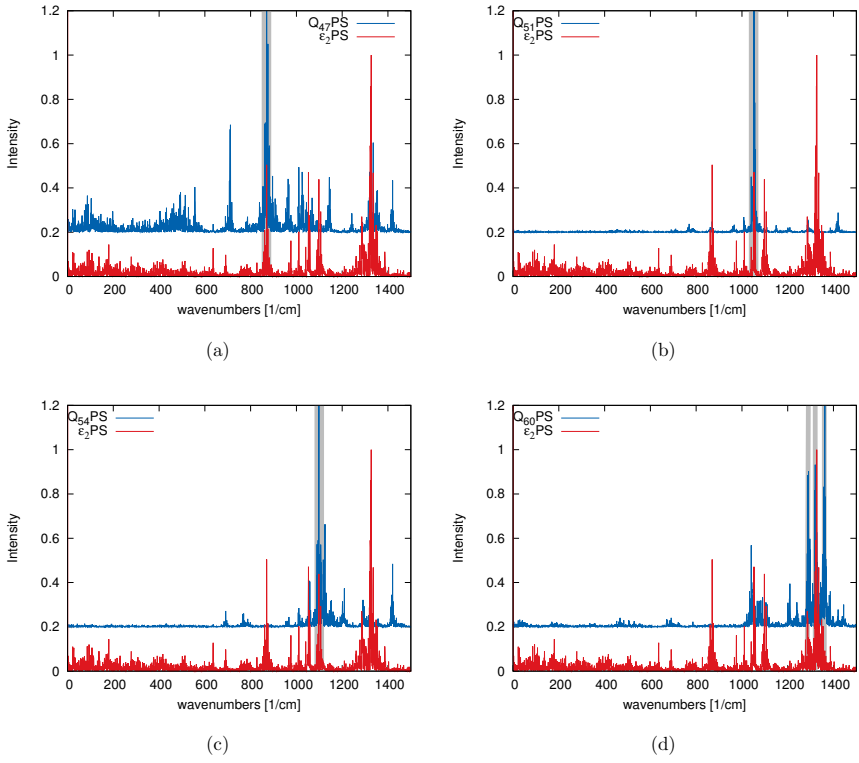

FIG. S6: Assignment of peaks in the ϵ_2PS to principal components Q_i via the Q_iPS. (a) Q_{47} corresponding to a N-N stretch at 869 cm^{-1}, (b) Q_{51} at 1052 cm^{-1} related to the C-N stretch in azo-benzene, (c) Q_{54} located at 1100 cm^{-1} and (d) Q_{60} located at 1330 cm^{-1}, both corresponding to in-plane ring vibrations.

d. Influence of water on ethyl orange When an explicit solvent, treated at the MM level, is added during the MD simulation, a dynamic spectrum (using snapshots from the QM/MM MD run followed by TD-DFT simulations on the isolated dye) can be computed which is in excellent agreement with an experimentally measured UV/Vis spectrum of the solvated dye as shown in Figure S7.

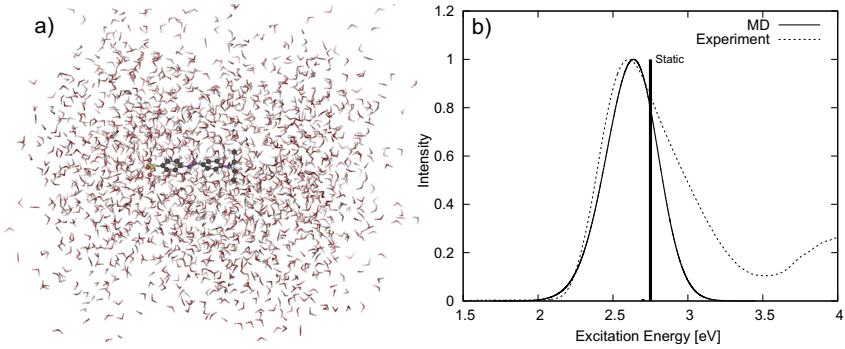

FIG. S7: (a) Ethyl orange surrounded by a water box containing 1830 water molecules used for the QM/MM MD simulation. (b) Experimental and computed MD UV/Vis spectra. The static vertical excitation energies (both the first and second excitation) - corresponding with the optimized structure of ethyl orange in a PCM surrounding - are also given.

However, the power spectra resulting from the original QM/MM MD simulation are much more noisier and interpretation is less convenient. Additional peaks in the power spectra are clearly present (see Figure S8), e.g. below 500 cm^{-1} several peaks are present for ϵ_2PS in the case of the solvated molecule. A clear assignment of these new peaks is not feasible with PCA and therefore other methods should be used. This lies beyond the scope of this work.

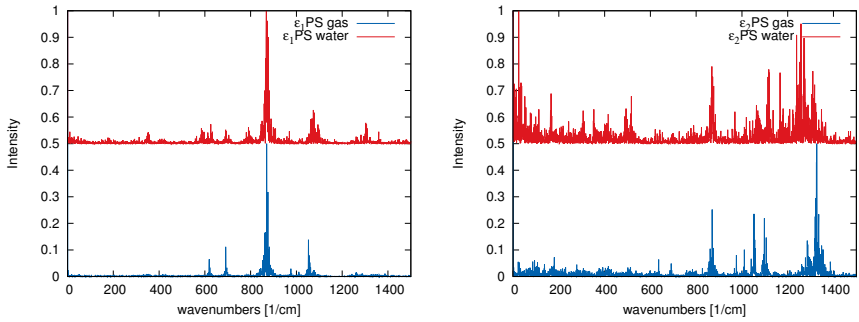

(a) (b)

FIG. S8: The ϵ_1PS and ϵ_2PS for gas phase case (blue) and the solvated case (red).

e. Ethyl orange for $\epsilon_1 < \epsilon_2$ at each time step When for each time step the smallest excitation energy is considered to be ϵ_1 and the second ϵ_2, different excitations are monitored within the same signal. This can clearly be seen in Figures S9a,b: the oscillator strength is crossing at almost each sampled step. The resulting ϵPS contains more noise and peaks at positions related to this level crossing rather then the actual change of a particular situation (see Figure S9c). The main characteristics are preserved (e.g. high intensity at 869 cm^{-1}), but new peaks are introduced in the ϵ_1PS which correspond to phenyl ring vibrations, proven not to be as dominant for the HOMO-1 to LUMO transition.

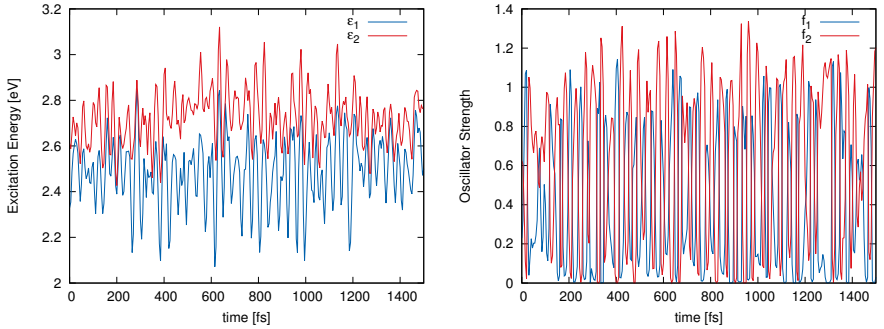

(a) (b)

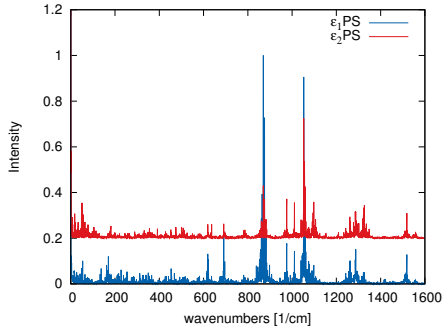

(c)

FIG. S9: (a) Excitation trajectory for the first 1.5 ps, (b) Trajectory of the oscillator strength, (c) The resulting ϵ_1PS and ϵ_2PS when level crossing is not taken into account.

REFERENCES

[1]A. M. Mebel, Y. T. Chen, and S. H. Lin, Chem. Phys. Lett. **258**, 53 (1996).

Paper III

Binary and Ternary Po-containing Molecules Relevant for LBE-coolant in Reactors

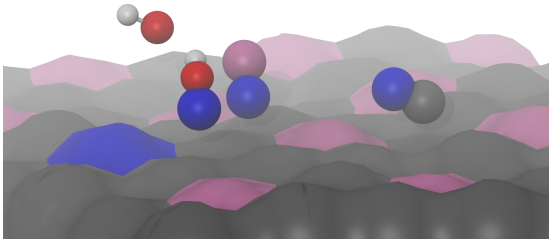

A. Van Yperen-De Deyne, K. Rijpstra, M. Waroquier, S. Cottenier, V. Van Speybroeck *Journal of Nuclear Materials*, *to be submitted*

Binary and Ternary Po-containing Molecules Relevant for LBE-coolant Reactors

Andy Van Yperen-De Deyne, Kim Rijpstra, Michel Waroquier, Veronique Van Speybroeck, Stefaan Cottenier*

Center for Molecular Modeling (CMM), Ghent University, Technologiepark 903, 9052 Ghent, Belgium

Abstract

Quantum-chemical calculations at several levels of theory were used to assess the stability of a set of 13 binary and ternary Po-containing molecules that could possibly be formed in an environd with Lead, Bismuth, oxygen and water. These are conditions that are relevant for a heavy liquid metal cooled fission reactor. The conclusions are that especially PoPb, PbPoO and PoOH are very stable and that Po_2, PoO and PoO_2 stable compared to atomic fragments. They are likely to be found near the LBE. In contrast Po_3, PoBi and PoHg are unlikely to be present under the assumed conditions since they have small dissociation energies. Additionally, the results of a medium level of theory (Density Functional Theory, PBE0 with Relativistic Effective Core Potentials) show good correspondence with calculations performed with much higher level of theory (Multi Reference Configuration Interaction, with spin-orbit coupling and scalar relativistic Hamiltonian). This allows to use the medium level of theory for much larger systems, unfeasible for the high level calculation method.

Keywords: MYRRHA, LBE, Polonium, evaporation

*Corresponding author
Email address: stefaan.cottenier@ugent.be (Stefaan Cottenier)

1. Introduction

Lead-Bismuth eutectic (LBE) is under consideration as coolant for generation IV fission reactors[1]. Neutron capture of ^{209}Bi present in the LBE results in a notable amount of radiotoxic ^{210}Po dispersed throughout the LBE volume. For safety reasons, it is important to know how this Po-contaminated LBE behaves, in operating conditions and accident scenarios.

For a reactor in operation, the liquid LBE serves as a natural container for the radiotoxic Po nuclei. Most of them will decay before they ever leave the coolant, especially at low temperatures. Some Po atoms, however, will eventually escape from the liquid, and will be present in the gas atmosphere above the coolant. The exact amount will depend to a large extent on the chemical properties of Po: if Po can form volatile molecules with elements commonly found in this environment, then more Po will make it to the gas atmosphere. The kind of molecules that can be formed will also determine which kind of filters is needed to capture them, in order to prevent release of Po outside the reactor system. For these reasons, we will examine in this work the stability of small molecules formed by Po at one hand and Pb, Bi, O and H at the other hand.

The aim of this paper is twofold: Firstly, we want to assess computationally the stability of a class of binary and ternary Po-containing molecules. Secondly, we want to examine which level of theory is sufficient to obtain reliable results. If one can resort to lower levels of theory and therefore to less demanding calculations, it will be possible to study molecules that are too complex to address with the high-level methods used in this work.

Various experimental studies on Po-containing LBE have lead to postulating the existence of PoO, PoPb, PoBi, H_2Po and PoO_2.[2, 3, 4, 5, 6] These molecules, among others, will be examined from a theoretical point of view in this work. Most theoretical studies on heavy elements focus on fundamental aspects, using a variety of computational methods[7, 8, 9]. The challenges in this regard are twofold. Firstly the introduction of relativity is expected to have large effects.

Secondly, sufficient correlations should be incorporated in the applied method to predict accurate dissociation energies.

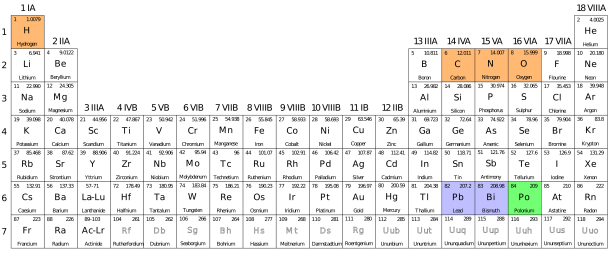

$OH \rightarrow PoH$	$H_2O \rightarrow PoH_2$
$CO \rightarrow PoBi$	$CO_2 \rightarrow Po_2Pb$, $PoPbO$
$NO \rightarrow PoPb$	$NO_2 \rightarrow Po_2Bi$, $PoBiO$
$O_2 \rightarrow PoO$	$O_3 \rightarrow Po_3$, Po_2O, PoO_2
$O_2 \rightarrow Po_2$	

Figure 1: (left) Periodic table of elements with the considered atoms marked in green (Po), blue (heavy elements) and their homologues in the first rows of the periodic table (orange); (right) A set of 13 Po-containing molecules that can be formed by analogy to familiar molecules formed by light chemical elements from the same group.

2. Theoretical framework and computational details

2.1. Literature review

The most simple approach to describe relativistic effects in molecules with heavy elements is to use a set of pre-constructed relativistic effective core potentials (RECP). This approach reduces the all-electron quantum chemical problem to only the valence electrons and replaces the presence of the core electrons by an effective potential, in which the major relativistic effects are implicitly involved. This constitutes a serious approximation, but it has been used frequently for handling similar complexes[10, 11] and is unavoidable when considering extended systems. Several variants have been proposed [12] and in some of them spin-orbit effects have been neglected[13].

A more accurate approach is to include scalar relativistic effects variationally with a Douglas-Kroll-Hess (DKH)[14, 15] or Zeroth Order Regular Approximation (ZORA) Hamiltonian[16, 17, 18]. Originally the ZORA approach was

developed in a two-component approach, but a spin-free adaption is more frequently used[17]. In Ref. [18] the two-component ZORA approach is compared with the full four component Dirac solution with discrepancies acceptable for the current purpose (*i.e.*, $< \mathrm{O}(0.05)\mathring{A}$ for the internuclear distance and $< \mathrm{O}(0.3)eV$ for the dissociation energy). It can be concluded that the ZORA is sufficient to describe valence properties even for superheavy elements - *i.e.*, 7p atoms. In the present work, we will only consider atoms containing up to 6p electrons for which relativistic effects are even smaller, affirming the ZORA Hamiltonian to be valid in this situation.

Next to the scalar relativistic effects, the spin-orbit coupling is expected to be non-negligible. Different approaches are available to include this interaction. The fully variational treatment assumes a two-component solution for which the spin-orbit operator is solved iteratively and is therefore part of the Fock operator acting on a two-component spinor. Most papers use a perturbative treatment however, in which the spin-orbit operator expectation value is calculated for the ground state or the spin-orbit operator is diagonalized in a basis set constructed by the ground state and several excited states (quasi degenerate perturbation theory, QDPT). Those expectation values and matrix elements can themselves be calculated in multiple ways, *e.g.* using nuclear screening[19], using an effective potential[20], the atomic-mean-field (AMFI)[21] or the related spin-orbit mean field (SOMF) methods[22].

The four component method, used as a reference to benchmark the ZORA approach in Ref. [18], is the most complete description since it starts from the Dirac equation. The method also treats positrons, but is complex and computationally quite expensive, - especially when a high level wavefunction approach is also envisaged. Recently, several papers have used these methods[7, 23]: Pershina et al.[7, 24, 25] applies an in-house relativistic Density Functional Theory (DFT) method within the noncolinear spin-polarized formalism[26]. Their objective is to calculate systems including atoms which are situated one row lower in the periodic table, or even beyond[27]. Comparison of dissociation energies and bond distances of M_2 molecules, where M are elements up to the 7th row,

revealed a different trend for the 7th row elements compared to their lighter homologues, caused by a dominant spin-orbit coupling. Since Polonium is a 6th row element, spin-orbit effects are important but probably not dominant. In our study we will not go beyond the 6th row and a perturbative treatment of spin-orbit coupling seems allowed.

2.2. Computational Details

Two types of calculations were performed in this work: one at a medium level and one at a high level of theory. The medium level calculations are based on the DFT method treating the relativistic effects with RECP[28] (see Sec. 2.1). This method is compared to accurate high level calculations. This high level all-electron calculations rely on scalar relativistic effects through the ZORA Hamiltonian and using MRCI as the solver. Spin-orbit coupling was treated perturbatively in the latter method. Both methods will be described hereafter in more detail.

In the medium-level RECP method, only valence electrons are treated quantum-mechanically. This method parameterizes the most important relativistic effects into an effective core potential and enables the use of available non-relativistic quantum chemistry methods. This valence-only approximation can be justified since the core electrons are unlikely to participate in the chemical bond and the reduced complexity allows a more accurate treatment of the valence electrons. Also from a computational point of view, this approach will be unavoidable for follow-up studies that examine, for instance, the interaction between Po-containing molecules and filter surfaces. The calculations are performed at the Density Functional Theory (DFT) level using the PBE0[29, 30] functional and a cc-pVTZ[31, 32, 33] basis set for the valence electrons of Pb, Bi and Po. The same basis set was used for all electrons of O and H. All molecules were optimized at this level of theory. This single reference method is inadequate to derive a full dissociation profile. Therefore the dissociation energy D_e was calculated as the difference between the energy of the optimized structure and the sum of the energies of their fragments. In fact, this approach eliminates

the possibility of using a ZORA Hamiltonian as an approach to include scalar relativistic effects: the original formulation does not yield gauge invariance[16], an artefact which is solved by including a model potential. This solution causes the ZORA Hamiltonian to be not size-extensive[17]. These problems do not occur for the non-relativistic Hamiltonian in combination with the RECP.

Secondly, all-electron calculations are performed now using the zeroth-order regular approximation (ZORA) Hamiltonian[16, 17] to take into account the scalar relativistic effects. For these calculations the ZORA-adapted TZVP[34, 35] basis set was used. The calculations were performed with Multireference Configuration Interaction (MRCI) following a Complete Active Space Self Consistent Field (CASSCF) calculation. The CAS consists of all 6p orbitals for Pb, Bi and Po, 2p orbitals for O and 1s, 2s and 2p orbitals for H. This high level of theory allows to accurately determine the dissociation energy curve for binary molecules and thus the use of a model-potential based ZORA Hamiltonian poses no problem. From the energy curve, the dissociation energy D_e and bond distance R_e can be fitted to a Morse potential.

$$M(R) = D_e \left(1 - \exp(-a(R - R_e))\right)^2 \tag{1}$$

To reduce the computational cost, the ternary molecules were not optimized at this high level of theory but their DFT geometries were used. Due to the lack of size-extensibility in a CI approach, the energy of the dissociated molecule is calculated for the three fragments at sufficiently large distance (≈ 10 $\mathring{A}$).

The spin-orbit and spin-spin interactions were treated at the quasi-degenerate perturbation theory (QDPT) level [36], both for the equilibrium geometry and the dissociated molecule. The spin-spin interaction will not be reported in what follows, since its contribution is negligibly small.

3. Results and Discussion

In order to select a plausible set of binary and ternary molecules for Po in an environment with LBE, air and water, we take advantage of the fact that

molecule	n_{el}	n_{orb}	2S+1 (n_{roots})
PoH	5	8	2(2)
PoO	8	6	1(3),3(3)
PoPb	6	6	1(1),3(9)
PoBi	7	6	2(4),4(5)
Po_2	8	6	1(3),3(3)

Table 1: Active space of binary molecules, defined through the number of active electrons and active orbitals. The second column gives information about the considered spin-multiplicity and the number of roots for this spin-state is given between brackets.

Pb, Bi and Po are isoelectronic to the lighter elements C, N and O. We consider all known binary and ternary molecules where at least one oxygen atom (to be replaced by Po) combines with carbon or nitrogen (to be replaced by Pb or Bi) and hydrogen or other oxygen atoms. This leads to the set of 5 binary and 8 ternary Po-containing molecules that is listed in Figure 1. This set includes all molecules that have been proposed based on experimental work (see Section 1).

Firstly we have focused on binary molecules for which the dissociation energy was calculated at both a medium level of theory (DFT with RECP) and high level of theory (CASSCF with subsequently MRCI and spin-orbit corrections with all-electron ZORA basis set). This allows to benchmark the medium level of theory which then will be subsequently used for the ternary species, for which the high level is very soon too expensive.

3.1. Binary Molecules

The calculated dissociation energies D_e and corresponding bond distances R_e for the binary molecules are given in Table 2. For completeness all investigated spin states are reported for DFT, CASSCF and MRCI calculations, while the spin-orbit corrections were only performed on the ground state. Due to the limited availability of experimental reference data, also computational results from literature are included.

Table 2 lists first the DFT results with RECP (some correlation, indirect effective spin-orbit coupling), secondly the CASSCF calculations (static correlation, no spin-orbit interaction) and finally the MRCI calculations (static plus dynamic correlation, done with and without spin-orbit interaction). The spin-spin contribution was calculated with MRCI and turned out to be negligible.

	2S+1	DFT		CASSCF		MRCI		MRCI+SOC	Literature	
		R_e [Å]	D_e [eV]	R_e [Å]	D_e [eV]	R_e [Å]	D_e [eV]	D_e [eV]	D_e [eV] (exp.)	D_e [eV] (calc.)
PoH	2	1.7480	2.6760	1.7572	2.3327	1.7531	2.5213	2.8098		$2.25^{(2)}$,$2.428^{(3)}$
PoO	1	1.9220	2.3382	1.9806	2.1388	1.9729	2.4681			
	3	1.9208	3.4328	2.0079	1.6748	1.9470	3.0609	3.0704	$2.88^{(1)}$	$2.92^{(2)}$
PoPb	1	2.6720	3.5395	2.9690	1.5985	2.6989	3.4050	3.4112		
	3	2.9312	2.1120	3.0025	1.2358	2.9311	2.0074			
PoBi	2	2.6950	2.2638	3.0305	0.6304	2.7227	2.0647	1.5742		
	4	2.8593	0.2534	2.7607	1.3989	2.9536	1.1676			
Po_2	1	2.7171	1.8855	2.7511	1.8514	2.7590	1.9820			$2.15^{(4)}$,$1.938^{(1)}$
	3	2.7210	2.6702	2.8299	1.1763	2.7329	2.3680	2.5635		
PoHg	1	2.6372	0.0337	-	-0.3734					
	3	2.9634	0.2609	-	0.0000					

Table 2: Equilibrium energy and dissociation energy for the binary molecules with different spin multiplicity.

(1) Reference [37] (exp.)

(2) Reference [38] at mixed DFT/CCSD(T) level of theory (calc.)

(3) Reference [12] using MCQDPT (calc.)

(4) Reference [7] using 4-component DFT (calc.)

Overall, the distances are little influenced by the computational method, in complete agreement with other theoretical work. For the dissociation energy D_e, the inclusion of dynamic correlation is essential as clearly demonstated by the comparison between CASSCF and MRCI calculations. On the other hand, the effect due to the inclusion of spin-orbit coupling is rather unpredictable: in most cases it causes a more tight binding, with widely varying size. In contrast,

for PoBi, the spin-orbit interaction leads to less binding which is exceptional within this small set of molecules. A much larger dataset would however be needed to draw more decisive conclusions. Fortunately, the use of relativistic effective core potentials performs quite well, according to the good correlation in Figure 2. The computational cost can therefore drastically be reduced.

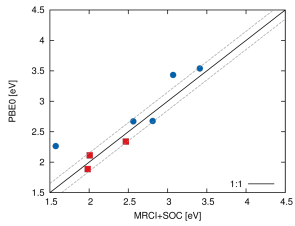

Figure 2: Correlation between MRCI and DFT results for the testset of binary molecules. The blue points indicate the most stable states, the red points are excited states with different spin.

PoPb, PoO and PoH are the most stable molecules, although Po_2 is also quite well bound. In realistic reactor conditions, however, the abundance of Po is that low that molecules with more than one Po are unlikely to appear. From this series PoBi turns out to be the least bound and hence more unlikely to be found near the LBE. This corresponds with the identification of PoPb as a stable molecule which evaporates from both LBE and Pb-Li eutectic[2, 3, 4] and with the recent hypothesis of PoO being formed near the LBE [5]. In literature, PoH was not yet considered to be present near the LBE. This candidate is however as stable as other binary molecules, confirmed by both DFT and literature data. Filter design for LBE-cooled reactors should therefore focus on capturing PoPb, PoO and PoH (as well as elemental Po). A test molecule that is expected not to show a stable bond, PoHg, does indeed provide a nearly zero value for the formation energy.

In general, DFT appears to overbind the binary molecules slightly compared

Reaction			D_e [eV]
PoPb	→	$\frac{1}{2}$ Po_2 + Pb	2.2044
PoBi	→	$\frac{1}{2}$ Po_2 + Bi	0.9287
PoO	→	$\frac{1}{2}$ Po_2 + $\frac{1}{2}$ O_2	-0.5512
PoH	→	$\frac{1}{2}$ Po_2 + $\frac{1}{2}$ H_2	-0.6001

Table 3: Possible dissociation reactions within our subset of binary Po-containing molecules (supplemented with the elemental atoms and O_2 and H_2). All values rely on DFT results which allows to use the difference in energy $D_e = E(products) - E(reactants)$

to the high-level reference calculations. The strength of all bonds is, however, of the same order of magnitude for the medium and the high-level method (see Figure 2).

A different approach to discuss the stability of the diatomic molecules, is to consider dissociation reactions of the Po-molecules to elemental atoms and molecules present in the LBE cover gas (i.e. O_2 and H_2). The results are listed in Table 3. From these energy differences, again PoPb is found to be by far the most stable structure. The formation of PoO and PoH is energetically unfavorable, according to this interpretation. The energy difference is however not extremely high and combined with the previous analysis, the presence of PoO and PoH cannot be ruled out.

Below the results are discussed in more detail for every binary molecule in particular.

3.1.1. PoH

Polonium hydride has a double degenerate ground state and has one unpaired electron. All studied methods predict the atoms to bound with this spin multiplicity (*i.e.* 2S+1 = 2). It is clear from comparison between the CASSCF and MRCI calculations that inclusion of correlation coupling and spin-orbit coupling causes the bond to be stronger. With a dissociation energy D_e of 2.8 eV, the most accurate method (MRCI+SOC) gives a result that is larger than the ones of all other methods. The dissociation energy calculated from DFT lies

somewhere in between both, not too distant from the most accurate method considered here.

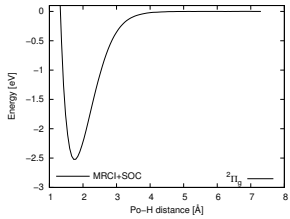

Figure 3: Dissociation curve of polonium hydride with MRCI for the lowest doublet.

3.1.2. PoO

For polonium monoxide, multiple spin states are considered. The MRCI calculations show the ground state to be non-degenerate and can be labeled by the $^3\Sigma$ molecular term symbol in absence of SOC. The first excited state is the double degenerate $^1\Delta$ state (see Figure 4), followed by $^1\Sigma$ and $^3\Pi$ states, all forming stable bonds. In this work the main interest goes to the ground state, which has a dissociation energy of 3.07 eV, rather close agreement with experimental and references [37, 38].MRCI slightly overestimates the dissociation energy, with respect to experiment and literature. The influence of spin-orbit coupling is minor, which is remarkable for this high spin system. CASSCF goes completely wrong, predicting a dissociation energy for the triplet which is more the 1 eV less bound and putting the singlet state forward as the most stable. DFT is more reliable: it predicts the correct ground state at the right position, but overestimates the binding energy (3.43 eV).

3.1.3. PoPb

The most stable binary molecule is the polonium-lead complex with a binding energy of approximately 3.4 eV (MRCI) or 3.53 eV (DFT). The ground state is the singlet $^1\Sigma$ state. Spin-orbit coupling again has little influence on the

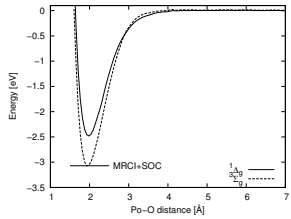

Figure 4: Dissociation curve of polonium monoxide with MRCI for the lowest singlet (full line) and triplet (dashed line) state.

stability of the ground state. Due to the high abundance of Pb in the system, this is a very likely candidate to form near the LBE surface.

For PoPb we can draw the same conclusion as for PoO with respect to the spin-orbit coupling: it makes the ground state (here a singlet) a little bit more bound, while DFT slightly overestimates and CASSCF completely fails in reproducing the correct binding profile.

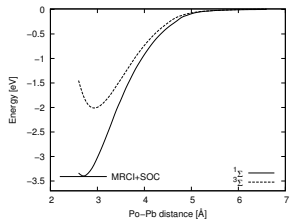

Figure 5: Dissociation curve of polonium lead with MRCI for the lowest singlet (full line) and triplet (dashed line) state.

3.1.4. PoBi

Both DFT and MRCI calculations predict a doublet spin character for the Polonium-bismuth ground state. In contrast to all other molecules, the disso-

ciation energy is lowered by the introduction of spin-orbit couping (see Figure 6). The DFT dissociation energy follows this trend with slightly tighter bound molecules compared to the MRCI results, in correspondence with the spin-orbit corrected MRCI results for all other molecules. Therefore, the lowering of dissociation energy due to spin-orbit interaction is not found with DFT, probably because this effect was not anticipated in the construction of the RECP used for these calculations.

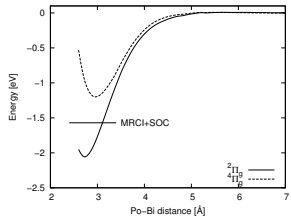

Figure 6: Dissociation curve of polonium bismuth with MRCI for the lowest singlet (full line) and triplet (dashed line) state.

3.1.5. Po_2

With the same number of valence electrons as oxygen, it is not surprising that dipolonium is found in a triplet ground state $^3\Sigma$ as predicted by DFT and MRCI methods. In literature only the dissociation energy for the singlet state is reported, in very close agreement with the MRCI result obtained in this work. We found however that the triplet state is more bound.

3.2. Ternary molecules

Secondly, ternary molecules were considered. In contrast to their light-element homologues, there is no a priori knowledge about their geometry. Since high energy barriers between different conformers might not be overcome during a geometry optimization, multiple starting geometries were considered. We

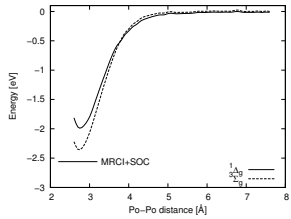

Figure 7: Dissociation curve of dipolonium with MRCI for the lowest singlet (full line) and triplet (dashed line) state.

even considered geometries beyond the principle of equivalence with light homologues. Below, the results are presented for the most stable configurations. In Table 4 two internuclear distances (A–B and B–C) and the angle (AB̂C) are listed for all ternary molecules. The sequence of atoms (A–B–C) is chosen in such a way that the A–B and B–C distances are the smallest ones and the angle AB̂C is the largest.

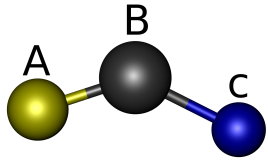

Figure 8: A dummy ternary molecule to illustrate the values in table 4. In cases where two equivalent atoms are present in the system, the two outer elements A and C are chosen identical. For all others, the labeling of the atoms is chosen such that A–B and B–C represent the smallest internuclear distances (with A–B the smallest of the two) and θ_{ABC} represents the largest angle.

When describing the stability of these molecules, multiple reference states can be considered. First, the free atoms can be chosen as a reference, similar to the binary molecules described above. Secondly, all possible reactions can

A – B – C	R_{AB} [Å]	R_{BC} [Å]	θ_{ABC} [degree]
H – Po – H	1.7459	1.7459	89.47
O – Po – O	1.8933	1.8937	107.11
Po – O – H	2.0644	0.9610	106.89
Po – Bi – Po	2.8948	2.8970	60.92
Po – Bi – O	2.8975	1.9101	99.87
Po – Pb – Po	2.8944	2.8938	61.68
Po – O – Pb	2.1689	2.1012	82.93
Po – Po – O	2.7272	1.9109	109.51
Po – Po – Po (1)	2.8133	2.8126	82.57
Po – Po – Po (2)	2.7549	2.7549	113.39

Table 4: Structural information of ternary molecules, optimized by RECP with DFT. For Po_3 the values for both triplet (1) and singlet (2) states are given because both dissociation energies are very close to each other while the geometrical parameters show significant differences.

be considered that dissociate the ternary molecule into a sum of unary and/or binary molecules (*e.g.* 2BiPoO ↔ 2Bi + Po_2 + O_2). We limit ourselves to reactions that have at their right-hand side any of the binary Po-containing molecules in Figure 1, extended with the free atoms and O_2 and H_2. Depending on whether the left-hand side or right-hand side of the reaction has the lowest energy, the ternary molecule is either stable or unstable in the thermodynamic limit. However, in typical reactor conditions of Po evaporating from the LBE, some of these reactions are statistically unlikely to happen due to the small amount of Po in the atmosphere. Therefore, a third stability criterion is considered: the dissociation energy with respect to the fragments of a single ternary molecule, *i.e.* one binary molecule and one atom.

3.2.1. Stability with respect to free atoms

Regarding the dissociation energy with respect to the free atoms, the available results are listed in Table 5. Only few systems could be verified using the demanding MRCI+SOC calculations, due to computational limitations or

	2S+1	DFT	CASSCF	MRCI	MRCI+SOC
		D_e [eV]	D_e [eV]	D_e [eV]	D_e [eV]
PoH_2	1	5.5259	3.9267	5.2736	4.7846
PoO_2	1	6.3159	3.9485	5.5158	5.0456
PoOH	2	7.1322			
PbPoO	1	6.5430	4.4129	6.1493	
$PbPo_2$	1	5.7948			
BiPoO	2	5.1798	3.2400	4.3351	
$BiPo_2$	2	4.7382			
Po_3	1	4.0231			
Po_3	3	4.0347			

Table 5: Dissociation energy of ternary molecules with respect to the free atoms at the DFT, CASSCF, MRCI and MRCI+SOC levels of theory.

convergence issues. From those limited cases, the discrepancy between the MRCI+SOC and DFT results is larger than for the binary cases, with the MRCI+SOC dissociation energy being smaller than the DFT dissociation energy. One plausible explanation is that for MRCI+SOC no geometry optimization was performed, which does not rule out the existence of small geometry changes with possible large energy differences. Allowing full geometry optimizations at a MRCI+SOC level would necessarily reduce the discrepancy with DFT. There is no indication in Table 5 that DFT leads to qualitatively wrong results, but actual values of the dissociation energies from DFT should be used with some care. From the size of all binding energies, it can safely be concluded that for all considered molecules there is an energy gain when the corresponding free atoms meet and bind. As far as this stability criterion is concerned, these molecules will be present near the LBE.

Reaction			D_e [eV]
2 PbPoO	↔	2 Pb + Po_2 + O_2	2.51 eV
2 PoOH	↔	Po_2 + 2OH	1.25 eV
2 BiPoO	↔	Po_2 + 2Bi + O_2	1.15 eV
2 Po_2Pb	↔	2PoPb + 2 Po_2	0.92 eV
Po_2Bi	↔	Po_2 + Bi	0.08 eV
2 Po_3	↔	Po_2 + Po	0.03 eV
2 Po_2O	↔	2Po_2 + O_2	-0.34 eV
2 PoH_2	↔	Po_2 + 2H_2	-0.38 eV
2 PoO_2	↔	Po_2 + 2O_2	-1.69 eV

Table 6: Possible reactions considered for the formation or dissociation of the ternary Po molecules. For positive reaction energy (last column), the reactants are most stable, for negative reaction energy the products are formed in the thermodynamical limit. $D_e = E(products) - E(reactants)$

3.2.2. Stability in the thermodynamical limit

As it is impossible to examine all reactions that involve these ternary molecules, we have limited ourselves to the subset of dissociation reactions that result into any of the binary molecules from Section 3.1, and/or the free Pb, Bi or Po atoms, O_2 and H_2. The molecules PbPoO, PoOH, BiPoO, Po_2Pb, Po_2Bi and Po_3 turn out to be stable against all examined dissociation reactions. Po_2O, PoH_2 and PoO_2, on the other hand, decay at thermodynamical equilibrium into smaller fragments. It must be stressed that this does not mean that a molecule as PoO_2 cannot exist in typical reactor conditions: as Po is rare anyway, the chance that two PoO_2 molecules meet and react to form Po_2 and 2 O_2 is small. There are indeed experimental claims for the existence of PoO_2 in similar conditions.[5]

3.2.3. Stability with respect to fragments

In Table 7, the dissociation energy of an isolated ternary Po-containing molecule with respect to a binary molecule and a free atom is listed. Several reaction paths have been examined, all listed in Table 7. In each case, we

Reaction			D_e [eV]	Reaction			D_e [eV]
PoH_2	$\leftrightarrow$	PoH; H	2.8499	PoH_2	$\leftrightarrow$	Po; H_2	0.9572
PoO_2	$\leftrightarrow$	PoO; O	2.8831	PoO_2	$\leftrightarrow$	Po; O_2	0.9200
PoOH	$\leftrightarrow$	PoO; H	3.6994	PoOH	$\leftrightarrow$	Po; OH	2.5844
PbPoO	$\leftrightarrow$	PbPo; O	3.0035	PbPoO	$\leftrightarrow$	PoO; Pb	3.1101
$PbPo_2$	$\leftrightarrow$	PbPo; Po	2.2553	$PbPo_2$	$\leftrightarrow$	Po_2; Pb	3.1247
BiPoO	$\leftrightarrow$	PoO; Bi	1.7470	BiPoO	$\leftrightarrow$	PoBi; O	2.9160
$BiPo_2$	$\leftrightarrow$	BiPo; Po	2.4744	$BiPo_2$	$\leftrightarrow$	Po_2; Bi	2.0681
Po_3	$\leftrightarrow$	Po_2; Po	1.3021	Po_3^*	$\leftrightarrow$	Po_2; Po	1.3137

Table 7: Dissociation energy of ternary molecules with respect to the fragments. Calculations performed with RECP at a DFT level of theory. * the dissociation energy for the triplet state. $D_e = E(products) - E(reactants)$.

considered the most stable Po-containing binary and an atom, as indicated. All these dissociation energies are quite large, most of them far beyond 1 eV (to be compared with positive reaction energies that can be below 0.1 eV in Table 6) and few around this value (e.g. PoH_2, PoO_2 and Po_3). This implies that an isolated Po-containing ternary molecule that does not meet another (rare) ternary molecule, is unlikely to decay into a Po-containing binary. In typical reactor conditions with very small Po-concentrations, these ternaries are therefore stable with respect to binaries.

4. Conclusion

In this work we calculated the dissociation energy of small Polonium-containing molecules to investigate their possible formation in a generation IV fission reactor, for which LBE will be used as a coolant. These dissociation energies were calculated at a high level of theory - MRCI with inclusion of scalar relativistic effects and SOC - as well as at a more approximative medium level of theory - DFT with RECP. In particular a hybrid functional (PBE0) was used for the DFT calculations. Although some disagreement between both levels of theory is

found – indicating the crucial role of relativistic effects in these systems – rather similar trends are observed. Therefore we can conclude that a DFT approach in which only the valence electrons are variationally treated due to the use of RECPs, is sufficient a level of theory to study the behaviour of Po-containing molecules.

From all the molecules examined in this work, especially PoPb, PbPoO and PoOH are found to be stable in all considered stability criteria, while PoO and PoO_2 are found to be more than averaged stable compared to their atomic elements. Dipolonium can also be considered as a stable molecule. In contrast, Po_3, PoBi and PoHg have small dissociation energies. Despite the prediction of molecules with only Po and light elements being unstable in the thermodynamic limit, the considered reactions require presence of multiple Po atoms very near to each other, a situation which is unlikely under operation conditions of LBE.

5. Acknowledgments

This work is supported by the European Commission through the FP7 project SEARCH (Safe ExploitAtion Related CHemistry for HLM reactors, project nr. 295736) and by the Research Board of Ghent University. The authors acknowledge helpful discussions with Alexander Aerts (SCK-CEN, Mol), Jörg Neuhasen, Emilio Andrea Maugeri and Matthias Rizzi (all PSI, Villigen). Stefaan Cottenier acknowledges financial support from OCAS NV by an OCAS-endowed chair at Ghent University. Calculations were carried out using the Stevin Supercomputer Infrastructure at Ghent University, funded by Ghent University, the Hercules Foundation, and the Flemish Government (EWI Department).

References

[1] H. A. Abderrahim, P. Baeten, D. De Bruyn, J. Heyse, P. Schuurmans, J. Wagemans, Myrrha, a multipurpose hybrid research reactor for high-

end applications, Nuclear Physics News 20 (1) (2010) 24–28. arXiv:http://dx.doi.org/10.1080/10506890903178913.

[2] W. G. Witteman, A. L. Giorgi, D. Vier, The preparation and identification of some intermetallic compounds of polonium, Journal of Physical Chemistry 64 (1960) 434–440.

[3] H. Feuerstein, J. Oschinski, S. Horn, Behavior of po-210 in molten pb-17li, Journal of Nuclear Materials 91 (1992) 288–291.

[4] L. O. Amaya, J. Braet, Purification of lead-bismuth eutectic used in accelerator driven systems, in: WM2009 Conference, 2009.

[5] E. A. Maugeri, J. Neuhausen, R. Eichler, D. Piguet, T. M. Mendona, T. Stora, D. Schumann, Thermochromatography study of volatile polonium species in various gas atmospheres, Journal of Nuclear Materials submitted.

[6] J. Buongiorno, C. Larson, K. R. Czerwinski, Speciation of polonium released from molten lead bismuth, Radiochim. Acta 91 (2003) 153–159.

[7] V. Pershina, A. Borschevsky, J. Anton, T. Jacob, Theoretical predictions of trends in spectroscopic properties of homonuclear dimers and volatility of the 7p elements, Journal of Chemical Physics 132 (2010) 194314.

[8] A. Türler, V. Pershina, Advances in the production and chemistry of the heaviest elements, Chemical Reviews 113 (2013) 1237–1312.

[9] K. G. Dyall, An exact separation of the spinfree and spindependent terms of the diraccoulombbreit hamiltonian, Journal of Chemical Physics 100 (1994) 2118.

[10] R. Ayala, J. M. Martinez, R. R. Pappalardo, A. M. noz Paez, E. S. Marcos, Po(iv) hydration: A quantum chemical study, Journal of Physical Chemistry B 112 (2008) 5416–5422.

[11] K. Balasubramanian, D. Dai, Group vi trimers (se_3, te_3 and po_3). electronic states and potential energy surfaces, Journal of Chemical Physics 90 (1993) 5239–5250.

[12] Zeng, Fedorov, Klobukowski, Multireference study of spin-orbit coupling in the hydrides of the 6p-block elements using the model core potential method (calculated value), Journal of Chemical Physics 132 (2010) 074102.

[13] L. Mahé, S. F. Boughdiri, J. C. Barthelat, Electronic structures and energetics in the cux and cu_2x series (x= o, s, se, te, po), Journal of Physical Chemistry A 101 (1997) 4224–4230.

[14] M. Reiher, A. Wolf, Exact decoupling of the dirac hamiltonian. i. general theory, The Journal of Chemical Physics 121 (5) (2004) 2037–2047.

[15] M. Reiher, A. Wolf, Exact decoupling of the dirac hamiltonian. ii. the generalized douglaskrollhess transformation up to arbitrary order, The Journal of Chemical Physics 121 (22) (2004) 10945–10956.

[16] E. van Lenthe, E. J. Baerends, J. G. Snijders, Relativistic regular two-component hamiltonians, Journal of Chemical Physics 99 (1993) 4597.

[17] C. van Wüllen, Molecular density functional calculations in the regular relativistic approximation. method, application to coinage metal diatomics, hydrides, fluorides and chlorides, and comparison with first-order relativistic calculations, Journal of Chemical Physics 109 (1998) 392–399.

[18] W. Liu, C. van W$^{\tilde{}}$ullen, Spectroscopic constants of mh and m_2 (m= tl, e113, bi, e115): Direct comparison of four-and two-component apapproach in the framework of relativistic density functional theory, Journal of Chemical Physics 116 (9) (2001) 3626.

[19] S. Koseki, M. W. Schmidt, M. S. Gordon, Mcscf/6-31g(d,p) calculations of one-electron spin-orbit-coupling constants in diatomic-molecules, Journal of Physical Chemistry 96 (26) (1992) 10768–10772.

[20] G. Schreckenbach, T. Ziegler, Calculation of the G-tensor of electron paramagnetic resonance spectroscopy using gauge-including atomic orbitals and density functional theory, Journal of Physical Chemistry A 101 (18) (1997) 3388–3399.

[21] B. A. Hess, C. M. Marian, U. Wahlgren, O. Gropen, A mean-field spin-orbit method applicable to correlated wavefunctions, Chemical Physics Letters 251 (5-6) (1996) 365–371.

[22] F. Neese, Efficient and accurate approximations to the molecular spin-orbit coupling operator and their use in molecular g-tensor calculations, Journal of Chemical Physics 122 (2005) 034107.

[23] S. Höfener, R. Ahlrichs, S. Knecht, L. Visscher, Relativistic and non-relativistic electronic molecular structure calculations for dimers of 4p-, 5p- and 6p-block elements, ChemPhysChem 13 (2012) 3952–3957.

[24] V. Pershina, J. Anton, Theoretical predictions of properties and gas-phase chromatography behaviour of carbonyl complexes of group-6 elements cr, mo, w, and element 106, sg, The Journal of Chemical Physics 138 (17) (2013) –.

[25] A. Borschevsky, V. Pershina, E. Eliav, U. Kaldor, Ab initio studies of atomic properties and experimental behavior of element 119 and its lighter homologs, The Journal of Chemical Physics 138 (12) (2013) –.

[26] J. Anton, B. Fricke, E. Engel, Noncollinear and collinear relativistic density-functional program for electric and magnetic properties of molecules, Physical Review A 69 (2004) 012505.

[27] V. Pershina, Theoretical Chemistry of the Heaviest Elements, Springer US, 2003, Ch. 2, pp. 31–94.

[28] M. Dolg, Relativistic Electronic Structure Theory, Part 1: Fundamentals, Elsevier Science B. V., 2002, Ch. 14, p. 793.

[29] J. P. Perdew, K. Burke, M. Ernzerhof, Genegeneral gradient approximation made simple, Physical Review Letters 77 (1996) 3865–3868.

[30] C. Adamo, V. Barone, Tosimpl reliable density functional mmethod witwith adjustable parameters: The pbe0 model, Journal of Chemical Physics 110 (1999) 6158–6169.

[31] K. A. Peterson, Journal of Chemical Physics 119 (2003) 11099.

[32] K. A. Peterson, D. Figgen, E. Goll, H. Stoll, M. Dolg, Journal of Chemical Physics 119 (2003) 11113.

[33] K. A. Peterson, C. Puzzarini, Theoretical Chemistry Accounts 114 (2005) 283.

[34] C. R. L. D. A. Pantazis, X. Y. Chen, F. Neese, J. Chem. Theory Comput. 4 (2008) 908.

[35] D. A. Pantazis, F. Neese, Theor. Chem. Acc. 131 (2012) 1292.

[36] M. Roemelt, F. Neese, Excited states of large open-shell molecules: An efficient, general and spin-adapted approach based on restricted open-shell ground state weave function, Journal of Physical Chemistry A 117 (2013) 3069–3083.

[37] K. P. Huber, G. Herzberg, Molecular Spectra and Molecular Structure, IV. Constants of Diatomic Molecules, Van Nostrand Reinhold, New York, 1979.

[38] M. L. Laury, A. K. Wilson, Examining the heavy p-block with a pseudopotential-based composite method: Atomic and molecular applications of rp-ccca. (calculated value), Journal of Chemical Physics 137 (2012) 214111.

Paper IV

Assessment of Periodic and Cluster-in-Vacuo Models for First Principles Calculations of EPR Parameters of Paramagnetic Defects in Crystals: Rh^{2+} Defects in NaCl as Case Study

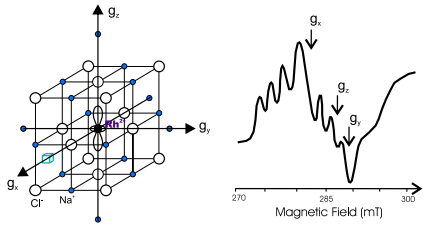

N. Sakhabutdinova, A. Van Yperen-De Deyne, E. Pauwels, V. Van Speybroeck, H. Vrielinck, F. Callens and M. Waroquier *The Journal of Physical Chemistry A* **114**, 1721–1733 (2011)

THE JOURNAL OF PHYSICAL CHEMISTRY A

ARTICLE

pubs.acs.org/JPCA

Assessment of Periodic and Cluster-in-Vacuo Models for First Principles Calculation of EPR Parameters of Paramagnetic Defects in Crystals: Rh^{2+} Defects in NaCl as Case Study

N. Sakhabutdinova,[†] A. Van Yperen-De Deyne,[†] E. Pauwels,[†] V. Van Speybroeck,[†] H. Vrielinck,[‡] F. Callens,[‡] and M. Waroquier*,[†]

[†]Center for Molecular Modeling, Ghent University, Technologiepark, 903, B-9052 Zwijnaarde, Belgium, and QCMM-alliance Ghent-Brussels, Belgium

[‡]Department of Solid State Sciences, Ghent University, Krijgslaan 281-S1, B-9000 Gent, Belgium

Supporting Information

ABSTRACT: In order to find a reliable and efficient calculation scheme for electron paramagnetic resonance (EPR) spectroscopic parameters for transition metal complexes in ionic solids from first principles, periodic and finite cluster-in-vacuo density functional theory (DFT) simulations are performed for **g** tensors, ligand hyperfine tensors (**A**), and quadrupole tensors (**Q**) for Rh^{2+}-related centers in NaCl. EPR experiments on NaCl:Rh single crystals identified three Rh^{2+} monomer centers, only differing in the number of charge compensating vacancies in their local environment, and one dimer center. Periodic and cluster calculations, both based on periodically optimized structures, are able to reproduce experimentally observed trends in the ligand **A** and **Q** tensors and render very satisfactory numerical agreement with experiment. Taking also computation time into account as a criterion, a full periodic approach emerges as most appropriate for these parameters.The **g** tensor calculations, on the other hand, prove to be insufficiently accurate for model assessment. The calculations also reveal parameters of the complexes which are not directly accessible through experiments, in particular related to their geometry.

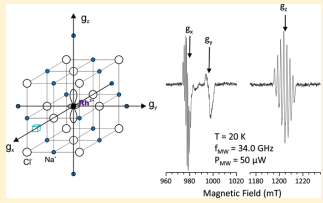

I. INTRODUCTION

Transition metal ions are very often doped into insulating hosts (halides, oxides) in order to change/control their optical, magnetic, and catalytic properties, etc. The specific way in which these ions are incorporated in the crystalline matrix, in particular their lattice position, association with other defects or impurities, and charge compensation mechanism, may to a large extent determine their functionality. Experimental information concerning these issues comes from spectroscopic investigations, e.g., optical absorption and luminescence, electron magnetic resonance (EMR), and extended X-ray absorption fine structure. Among these, the EMR techniques—electron paramagnetic resonance (EPR) and electron nuclear double resonance (ENDOR)—have a special place.[1−3] Although these techniques are only applicable to the study of paramagnetic ions, they yield very detailed information on the lattice surroundings of the transition metal ions through the observation of hyperfine interactions between unpaired electrons and neighboring nuclei. However, even EMR spectroscopy very often only provides indirect information on the defect structure, e.g., with respect to the presence of nonmagnetic impurity nuclei or vacancies in the vicinity of the transition metal ions. For this, ab initio quantum chemical calculations of defect structures can present an important added value, establishing a relation between the microscopic structure of the defect and its spectroscopic properties.[4−6]

This paper focuses on the calculation of spin Hamiltonian parameters extracted from EPR and ENDOR experiments: **g** tensors for paramagnetic transition metal centers and hyperfine **A** and quadrupole **Q** tensors for the central and neighboring nuclei in the Hamiltonian:[7]

$$\hat{H}_S = \mu_B \vec{B} \cdot \overleftrightarrow{g} \cdot \hat{\vec{S}} + \sum_i \left(\hat{\vec{S}} \cdot \overleftrightarrow{A}_i \cdot \hat{\vec{I}}_i - g_{N,i} \vec{B} \cdot \hat{\vec{I}}_i + \hat{\vec{I}}_i \cdot \overleftrightarrow{Q}_i \cdot \hat{\vec{I}}_i \right) \quad (1)$$

Many program packages are nowadays available offering modules for the ab initio computation of these EPR parameters. However, their adequacy and reliability to unravel fine details in the spectroscopic data has not been systematically assessed for transition metal ions, and therefore a thorough investigation of this issue remains a challenge. The objective of this work is to offer a computational protocol for achieving maximal reliability, by testing various available packages which differ in their description of the crystalline environment of the paramagnetic ion.

Most of the present-day ab initio EPR program packages are based on cluster-in-vacuo calculations in gas phase, and hence are subject to restrictions due to the finite cluster size to keep the computation feasible. For defects in crystals, with long-range

Received: October 4, 2010
Revised: January 4, 2011
Published: February 07, 2011

The Journal of Physical Chemistry A ARTICLE

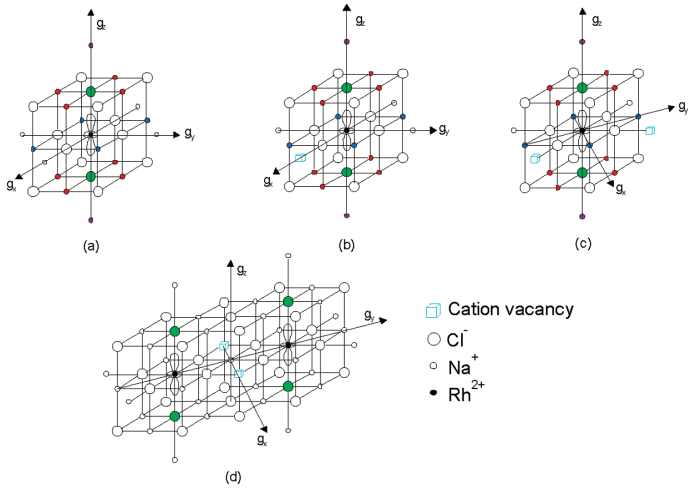

Figure 1. Structural model for Rh-related centers identified in NaCl. (a) $[RhCl_6]^{4-}$.0Vac. (b) $[RhCl_6]^{4-}$.1Vac. (c) $[RhCl_6]^{4-}$.2Vac. (d) Rh dimer. For the ions indicated in color, the interactions have been determined from ENDOR analyses: green, first shell axial Cl ions in (0,0,1) positions; purple, fourth shell axial cations in (0,0,2) positions; blue, second shell equatorial cations in (1,1,0) positions; red, second shell nonequatorial cations in (1,0,1) and (0,1,1) positions.

interactions between ions, this is a serious constraint. Periodic codes are more appropriate as they fully take into account the crystalline structure by imposing periodic boundary conditions (PBCs) on the simulation cell. Only recently models for an accurate computation of EPR **g** tensors and hyperfine coupling tensors have become available in periodic codes.[8−10] Specifically, we refer to the recent work of Weber et al.[11] where the calculation of EPR parameters is implemented in CP2K.[9,10] They form by construction the most plausible method for a theoretical investigation of the electronic structure affected by incorporating point defects in lattices. However, they also show limitations in their applicability, feasibility, and numerical accuracy. In this paper, their performance will be tested in comparison with cluster-in-vacuo models for which a rich variety of methods is available. Such a thorough comparative study between periodic and gas-phase models for the reproduction of EPR parameters for paramagnetic defects in lattices has never been done before, and it will represent a benchmark investigation in which the most appropriate, numerically accurate, computationally feasible, and efficient protocol for this type of system is proposed. The validation of the periodic codes with respect to cluster-in-vacuo models will be carried out by the electronic structure program packages ADF[12] and ORCA,[13] which are generally recognized as being among the best for the computation of spectroscopic EPR parameters and in particular the **g** tensors. Both programs contain state-of-the-art relativistic methods (ZORA and spin−orbit coupling) to treat heavy nuclei. For gas-phase complexes extensive benchmarking was performed by Neese,[14] and this justifies the use of ORCA for comparative study in the search for the most plausible method for the computation of the **g** tensor for paramagnetic defects in ionic lattices. This work does not aim to assess all existing periodic codes. In a very recent review of Ziegler[15] on first principles calculation of EPR parameters in solids, the "full potential" program BAND[16] has been tested for its adequacy to reproduce hyperfine parameters of hydrogen defects in some important IIIA−VA semiconductors in zinc-blende phase and the **g** tensor of S_2^- in KCl crystal lattice. Their scheme succeeded in doing better than the cluster model,[17] but the overall agreement with experiment is still not satisfactory.

We have chosen divalent rhodium (Rh^{2+}, $4d^7$ ($t_2^6e^1$) electron configuration) complexes in sodium chloride (NaCl) as test systems for this case study, as much experimental data are available for these systems. These centers were first studied in the 1970s[18] and 1980s,[19] but there was a renewed interest in the 1990s when NaCl:Rh turned out to be an interesting model system for studying similar complexes in AgCl microcrystals of photographic emulsions. A thorough EPR and ENDOR study of melt- and solution-grown crystals[20−25] led to the identification of three paramagnetic Rh^{2+} monomer centers, one Rh^{2+} dimer center,[23,26] and a Rh^+ center.[27] The occurrence and stability of the centers was demonstrated to depend on the crystal growth conditions. In solution-grown crystals Rh is incorporated in its diamagnetic trivalent state (Rh^{3+}) and may trap one or two electrons upon X-irradiation to form paramagnetic Rh^{2+} and Rh^+ ions. Via melt growth, Rh directly enters the NaCl lattice in its divalent (Rh^{2+}) state. In this study we study divalent Rh^{2+} centers and fully characterize their properties. This paper comprises a complete investigation of geometric aspects, energetic considerations, and spectroscopic properties, aiming at a full assessment of the available relevant computer codes, and offering a comparative study with theoretical studies already performed in the literature with respect to Rh^{2+} defects in NaCl. In the remainder of this section, the geometric aspects and electronic ground state of these defects, as established from the experimental EPR and ENDOR studies, are briefly introduced.

Both in melt-grown and in solution-grown NaCl crystals, Rh ions are always found to occupy substitutional cation positions.

They are octahedrally coordinated by six anions to form $[RhCl_6]^{4-}$ complexes. Cation vacancies play an important role in the charge compensation of these transition metal ions embedded in ionic solids. Their number and position may affect the depth and efficiency of the electron trap caused by the dopant ion. Furthermore, diffusion of the vacancies may stabilize the trapped electron center. Such charge compensating cation vacancies cannot be directly observed with EPR and ENDOR, but they change the symmetry of the complex. This is reflected in the center's **g** tensor and **A** and **Q** tensors for neighboring nuclei. In NaCl hexachloro centers associated with 0, 1, or 2 cation vacancies in next nearest neighbor (nnn) positions with respect to the Rh ion have been discovered. We refer to them with the $[RhCl_6]^{4-}$.*n*Vac (n = 0, 1, 2) notation. Their structural models are well established and are displayed in Figure 1.

In perfect cubic surroundings, the two 4d orbitals of Rh^{2+} with e symmetry (d_{z^2} and $d_{x^2-y^2}$) are degenerate. The complexes undergo a Jahn−Teller elongation (elongation axis labeled as z), lifting this degeneracy and leaving the unpaired electron in a d_{z^2} orbital. Hence, the center without cation vacancies in its near surroundings, $[RhCl_6]^{4-}$.0Vac, exhibits tetragonal D_{4h} symmetry. It was shown to be the most stable Rh^{2+} center produced by X-ray irradiation at room temperature in solution-grown crystals.[25] Its symmetry is reflected in the **g** tensor with $g_z \approx g_e < g_x = g_y$. The unpaired electron exhibits a much stronger hyperfine interaction with the two Cl^- ligands along the elongation axis, characterized by an axial hyperfine tensor, than with the four equatorial ligands, although the latter are at shorter distance. A lot of theoretical DFT-based studies have been performed on this center by the group of Moreno.[28−30] They mainly concentrated on structural, magnetic, and optical properties of the center and also presented detailed theoretical insight into the Jahn−Teller effect occurring for these ions. As will be discussed further, there is good qualitative agreement between their results and those presented in this paper. The validity of their approach will be assessed through comparison with periodic calculations.

As already mentioned, charge compensating defects around these complexes have only been found in nnn positions, i.e., at one lattice constant distance from the Rh^{2+} ion in a ⟨100⟩ direction (see Figure 1b−d). Furthermore, they were only found in the plane perpendicular to the Jahn−Teller elongation z-axis. The $[RhCl_6]^{4-}$.1Vac center, presented in Figure 1b, has orthorhombic symmetry with principal axes along the cubic ⟨100⟩ crystal axes. It has been shown to be the most stable center in melt-grown crystals.[21,23,24] The presence of the vacancy produces an inequivalence between the x and y directions of the center, reflected in the principal **g** values (g_x slightly larger than g_y). The position of the vacancy on the center's x-axis was deduced from the observed motional averaging of EPR spectra at elevated temperatures, when the Jahn−Teller elongation hops between the equivalent y and z directions, producing a center with, on average, axial symmetry.[21] In addition, at low temperature a small but measurable tilting angle was observed for the principal **A** and **Q** tensor axes of the Cl^- ions along the z-axis in the zx mirror plane of the complex.[2]

The $[RhCl_6]^{4-}$.2Vac complex (Figure 1c) is the only Rh^{2+} center produced in solution-grown NaCl upon X-ray irradiation at 77 K and also appears as secondary species in melt-grown crystals. The vacancies are arranged in a cis configuration, and as a result the center has C_{2v} symmetry with the principal axes in the xy plane along ⟨110⟩ directions. This particular arrangement leads to a nearly axial **g** tensor,[1] whose rhombicity could nonetheless clearly be resolved at W-band microwave frequencies (95 GHz)[1,24] ($g_x > g_y$). In Q-band ENDOR measurements[1] a tilting of the **A** and **Q** tensors for the axial Cl^- in the xz plane of the center was observed, identifying this as the mirror plane of the complex and the g_x axis as its 2-fold rotation axis.

Finally, a Rh^{2+} dimer center with total spin S = 1 has also been identified as a secondary species in melt-grown crystals.[23,26] The model in Figure 1d was derived from W-band EPR[26] and Q-band ENDOR measurements.[3] In particular, the two Rh^{2+} ions were established to occupy next nearest neighbor positions on a ⟨110⟩ axis, corresponding to the g_y axis of the center. The presence of the vacancies was deduced from the striking resemblance in **g** tensors between this center and the $[RhCl_6]^{4-}$.2Vac complex.

For the last three centers no theoretical calculations have been performed up to now, and the rich experimental data on spectroscopic properties for these defects give an ideal perspective for a thorough assessment of the theoretical models.

II. COMPUTATIONAL METHODS

CP2K[31] is a freely available periodic code under the GNU General Public License (GPL) general program to perform atomistic and molecular simulations of solid state, liquid, molecular, and biological systems. It is ideally suited by its construction to handle periodic electronic systems, such as the ionic lattices under study in this work. CP2K has been selected as the authors have collaborated with the developers of CP2K in implementing the calculation of EPR parameters.[11,32] One particularly attractive feature is that it uses a dual basis of atom centered Gaussian orbitals and plane waves to perform the periodic calculations.[33]

All geometry optimizations were performed with CP2K using the PBE gradient-corrected exchange-correlation functional[34] and the GPW approach.[33] A Gaussian basis set of double-ζ quality[35] was applied in combination with Goedecker−Teter−Hutter pseudopotentials.[36] We used a 700 Ry cutoff for the auxiliary plane wave grid. This high value was required to ensure sufficient convergence in the Rh−ligand distances (see Section III.A).

To prevent interaction of the defect with neighboring periodic images, the simulation cell comprised several crystallographic unit cells. Three such supercell sizes were tested: 6 × 6 × 6, 8 × 8 × 8, and 10 × 10 × 10, consisting of 216, 512, and 1000 atoms, respectively.

The most plausible method for the calculation of EPR **g** tensors and hyperfine coupling tensors for defects in ionic lattices is the use of periodic codes where periodic boundary conditions (PBCs) are imposed on a simulation cell, in this way perfectly describing the periodic structure of the solid. Recently, these modules have become available in CP2K[11,37] making use of the Gaussian and augmented-plane-wave (GAPW)[38−40] formalism in its all-electron (AE) version. The Gaussian basis sets used for these AE calculations were taken from the Environmental Molecular Sciences Laboratory (EMSL) basis set exchange library.[41] The approach is based on density function perturbation theory (DFPT).[42] The all-electron description of the system permits the evaluation of the **g** tensor for all elements. However, the implementation of the required theoretical methods in PBC simulations was far from trivial: due to methodological and/or practical limitations some approximations have to be incorporated (e.g., the treatment of the two-electron spin−other-orbit coupling), and in addition an AE calculation on a large simulation cell containing 512 atoms demands a huge computational effort. The performance of periodic codes on such large simulation cells has not yet been assessed, and a comparative study with

state-of-the-art cluster-in-vacuo calculations could be very instructive to make conclusions on the most appropriate way to compute EPR parameters for paramagnetic defects in solids.

The main drawback of cluster calculations is the lack of a full description of the molecular environment due to cluster size limitations. We have therefore cut out a cluster from the optimized geometry obtained in CP2K and have consistently used it in the assessment with cluster-in-vacuo models. As such we could fully validate the effect on the magnetic response properties starting from the same geometry. We selected two program packages, ADF and ORCA, containing different DFT-based implementations for the **g** tensor. ADF contains both the one-component method of Schreckenbach and Ziegler[43] and the two-component model of Van Lenthe.[44] In the first an effective potential is introduced to approximate the spin−orbit operators. This makes the comparison with the CP2K result highly instructive as the **g** tensor computation is based on the same model. In the current version of ORCA several variants of spin−orbit coupling operators are implemented. They are based on effective potential and mean-field approaches. They vary from the more elementary so-called scaled spin−orbit approximation[45] to the more complex spin−orbit mean-field (SOMF) method developed by Hess et al.[46] and further investigated by Neese.[14] We systematically applied the SOMF(1X) approximation, which is believed to be the most accurate method available in ORCA. The influence of relativistic effects has also been tested with ZORA,[47] but these calculations do not deviate much from those without relativistic corrections, and will not be taken up in the further discussion.

This large variety of methods makes a comparative study highly challenging, as a **g** tensor calculation of a transition metal defect in an ionic lattice is not evident in a periodic code nor in a sufficiently large cluster approach.

In ADF a triple-ζ basis set with polarization function (TZP) was selected for the six chlorine ligands and the two axial sodium cations nearest the Rh defect, while for the other atoms of the cluster a frozen core approximation was applied for the inner atomic shells and a triple-ζ basis set was used for the valence orbitals. The gradient corrected BP86 functional[48,49] was used in all calculations unless otherwise specified.

The relativistic atomic potentials were calculated using the auxiliary program DIRAC,[50] as is comprised in the ADF program package. In ORCA the B3LYP functional[51,52] was employed along with the triple-ζ basis set for all atoms.

III. RESULTS AND DISCUSSION

III.A. Geometric Structure. *III.A.1. Optimization of the Methodology.* Geometry optimizations could be performed using (embedded) cluster models based on DFT methods, but these results are seriously affected by the absence of the full periodic environment.[53,54] This could be circumvented by imposing constraints on the border atoms, but this approach is not recommended as experience learns that convergence problems often occur in such methodology. Periodic calculations offer a more natural way of dealing with periodic lattices, as they are not triggered by any constraints. In all calculations performed in this study we used cubic supercells. Only supercells with a side containing an even number of ions are suitable, in view of the PBCs to be imposed on them. However, in these cells the substitutional Rh defects studied here, which are centered on cation positions, cannot be placed such that the doped cell has the symmetry expected for the defect in the lattice. Optimization of the periodically extended structure should in principle result in the correct symmetry, provided that appropriate convergence criteria (size of the supercell, plane wave energy cutoff, see below) are imposed. Inspection of the symmetry of the Rh-defect geometries, hence, serves as a first test for the reliability of the periodic optimizations.

Table 1. Rh−Cl Distances (in Å) along the Principal Axes for a $[RhCl_6]^{4-}$.1Vac Complex[a]

	R		
	−	+	Δ
		6 × 6 × 6 cell	
unit cell			
axial *z*	2.749 238	2.749 236	0.000 002
equatorial *x*	2.449 128	2.358 231	−0.090 897
equatorial *y*	2.449 127	2.424 798	0.024 330
		8 × 8 × 8 cell	
unit cell			
axial *z*	2.741 713	2.741 716	0.000 003
equatorial *x*	2.425 911	2.356 719	−0.069 192
equatorial *y*	2.449 263	2.449 257	−0.000 006
		10 × 10 × 10 cell	
unit cell			
axial *z*	2.740 407	2.740 395	−0.000 012
equatorial *x*	2.434 996	2.352 521	−0.082 475
equatorial *y*	2.454 049	2.454 048	−0.000 001

[a] A value of 700 Ry was used for the kinetic energy cutoff.

Table 2. Asymmetry in the Optimized Rh−Cl Distances (8 × 8 × 8 Supercell) along the Principal Axes for Different Values of the Cutoff in the Case of a $[RhCl_6]^{4-}$.1Vac Complex[a]

	Δ		
	300 Ry	700 Ry	1200 Ry
axial *z*	0.6126	0.0003	0.0003
equatorial *x*	−4.8353	−6.9192	−6.9192
equatorial *y*	0.1625	−0.0006	−0.0006

[a] Distances in picometers (pm).

In searching for an optimal simulation cell size, we optimized the geometry for the $[RhCl_6]^{4-}$.1Vac center in CP2K using periodic supercells of different sizes. The unpaired electron density is expected to be localized nearly completely within the $[RhCl_6]^{4-}$ complex, and the spectroscopic properties we intend to calculate should to a large extent be determined by the positions within this complex. Therefore, the Rh−Cl distances and the reproduction of the correct symmetry were used as criteria in the choice of the supercell. Sufficiently large sizes of the cell and accurate description of the electron orbitals should result in the correct orthorhombic C_{2v} symmetry for the $[RhCl_6]^{4-}$.1Vac complex.

Table 1 summarizes the relevant Rh−Cl distances optimized in the 6 × 6 × 6, 8 × 8 × 8, and 10 × 10 × 10 supercells. The plus and minus signs indicate the two Cl^- ions in either direction of the three principal ⟨100⟩ axes (see Figure 1). The Δ parameter represents the asymmetry in the calculated distances along

The Journal of Physical Chemistry A ARTICLE

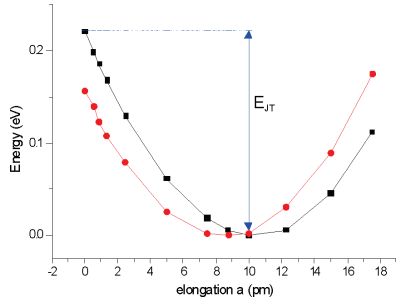

Figure 2. Total binding energy (in eV) as a function of the elongation parameter a for the $8 \times 8 \times 8$ unit cell in the periodic CP2K code (solid black curve) and for the finite $RhCl_6Na_{12}Cl_8Na_6Cl_6$ cluster (solid red curve) as obtained in ref 29. All energies are relative with respect to the absolute energy minimum at $a = 10.3$ pm for the periodic calculation and $a = 8.75$ pm for the finite cluster calculation.

the principal ⟨100⟩ axes. Only in the x direction, along which the cation vacancy is located, this parameter is expected to be nonzero. Indeed, in Table 1 the asymmetry in the z and y directions does not exceed 0.001 pm and the difference in the x direction displays the lattice strain due to the vacancy presence. The asymmetry in the y direction for the $6 \times 6 \times 6$ cluster indicates that for this cell size the geometry is not yet fully reliable. The $10 \times 10 \times 10$ unit cell generates essentially the same results as the $8 \times 8 \times 8$ unit cell, both producing accurately symmetric results along the z and y directions. Because of its lower computational cost, the $8 \times 8 \times 8$ unit cell was chosen for the remainder of the paper. Only for determining the energetically most favorable position of the vacancy will the $10 \times 10 \times 10$ results also be taken into consideration (see Section III.B). Comparing the results of the calculations with the three cells, we may safely state that the Rh−Cl distances are calculated to an accuracy better than 1 pm.

Throughout this work a value of 700 Ry for the kinetic energy cutoff has been consistently used. This high value turned out to be required for obtaining the correct symmetry of the defect. This becomes clear after inspecting Table 2, where the asymmetry in the various Rh−Cl distances is reported for various values of the energy cutoff.

The value of 300 Ry is manifestly too small. Cutoff values of 700 and 1200 Ry yield the same accuracy; hence the former is selected to be the most appropriate because of computational feasibility. However, it should be mentioned that also these calculations require extensive computing times.

III.A.2. Results for the [RhCl$_6$].0Vac Defect. As already mentioned in the Introduction, the symmetry of this center decreases from $O_h \rightarrow D_{4h}$ as a result of a Jahn−Teller distortion together with, or induced by, molecular binding with the two equivalent chlorine ions along the elongation axis. Detailed theoretical insight into the Jahn−Teller distortion in this center has already been given by Barriuso et al.[29] in 2001. We summarize here their main conclusions. Calculations on clusters of relatively small sizes were performed to optimize the geometry and to compute the Jahn−Teller elongation and energy. When O_h symmetry was imposed, an equilibrium distance $R_0 = 2.532$ Å was obtained for the Rh^{2+} ligand distances in the ground state configuration,

Table 3. Rh−Cl Distances (in Å) of the $[RhCl_6]^{4-}$ Complex along the Crystal Axes after Separate Geometry Optimizations of the Rh^{2+} Centers in CP2K[a]

	R						
		1 vacancy		2 vacancies		Rh dimer	
	0 vacancy	−	+	−	+	−	+
equatorial x	2.423	2.426	2.357	2.451	2.371	2.445	2.378
equatorial y	2.423	2.449	2.449	2.451	2.371	2.445	2.378
axial z	2.732	2.742	2.742	2.783	2.783	2.775	2.775

[a] Use of $8 \times 8 \times 8$ unit cell and a cutoff value of 700 Ry. Vacancies in nnn position according to Figure 1. Distances in angstroms. The corresponding optimized Rh−Cl distances in the dimer for two Rh ions are the same for the two defects at positions $(-a,-a,0)$ and $(a,a,0)$.

implying an inward relaxation of 10% with respect to the Na^+-Cl^- distance in the host lattice (2.825 Å). Allowing a decrease in symmetry to tetragonal, an elongation parameter a was introduced distinguishing the equatorial and axial Rh−Cl ligand distances, following

$$R_{ax} = R_0 + 2a; \qquad R_{eq} = R_0 - a \tag{2}$$

A clear energy minimum was obtained at $a = 8.75$ pm involving a Jahn−Teller energy of $E_{JT} = 0.15$ eV (1200 cm^{-1}) as displayed in Figure 2 (solid red curve).

We have investigated how the cluster-in-vacuo calculations made by Barriuso et al., which were at that time very advanced calculations, can be compared to our results using a periodic approach. The CP2K predictions for the equilibrium Rh^{2+} ligand distances are given in Table 3, from which the Jahn−Teller parameters are easily derived: an average distance R_0 of 2.526 Å is found, in very close agreement with the cluster value (2.532 Å) obtained in ref 29 and the elongation parameter $a = 10.3$ pm turns out to be somewhat larger. Figure 2 displays the calculated total energy (in electronvolts) relative to the global ground state configuration (squares, solid black curve). The energetic behavior is less symmetric around the equilibrium value of a, compared with the finite cluster calculation.[29] The Jahn−Teller energy E_{JT} of 0.22 eV predicted by the periodic calculation is higher than that for the cluster result. This is not completely surprising as a finite cluster computation will systematically underestimate the binding of the most stable configuration, exactly due to the finiteness of the cluster. In addition, the more pronounced the tetragonal character of the structure, the larger the boundary effects of the cluster. The size of the cluster used in ref 29 is restricted to only 39 atoms, and it is clear that the environment is not fully taken into account in it, as is manifestly shown in Figure 1 of ref 29. As regards recent articles on Jahn−Teller impurities, it should be noted that Garcia-Fernandez et al.[55] also have calculated the Jahn−Teller energy using clusters and the CASPT2 method. For the defect center under study in this work they found 0.227 eV, which is completely coincident with our results.

Note that for the computation of the curve in Figure 2 no geometry optimization has been performed for values of a different from the equilibrium prediction. The Cl^- ligands in the $[RhCl_6]^{4-}$ complex are displaced according to the above expressions for R_{ax} and R_{eq}, but the remainder of the ions, not belonging to the complex, are kept fixed. This approach seems justified since a complete relaxation of the unit cell imposing

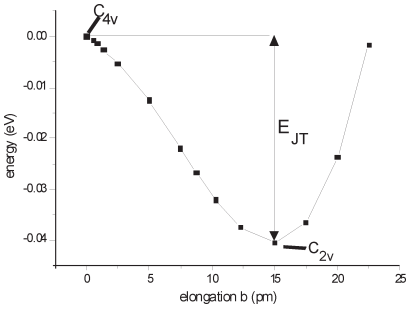

Figure 3. Total binding energy (in eV) for the $[RhCl_6].1Vac$ complex as a function of the elongation parameter b for the $8 \times 8 \times 8$ unit cell in the periodic CP2K code. All energies are relative with respect to the C_{4v} symmetric ground state at $b = 0$.

cubic symmetry ($a = 0$) alters only very slightly the Jahn−Teller energy (0.21 eV instead of 0.22 eV). Furthermore, we expect the periodic calculations to predict more reliable values for a and E_{JT} than the finite cluster computations, but a definite answer around this discrepancy can only be given indirectly by investigating the behavior of the superhyperfine interactions as a function of the elongation and will be discussed in the appropriate section.

III.A.3. Results for the [RhCl$_6$].nVac Complexes (n = 1, 2) and the Rh Dimer. The presence of one cation vacancy in an nnn position reduces the initial symmetry of the complex from $O_h \rightarrow C_{4v}$. This vacancy represents an effective negative charge in NaCl. Considering only its Coulomb interaction, it is expected to repel the first few neighboring shells of anions and to attract cations. This results in a compression of the $[RhCl_6]^{4-}$ octahedron along the Rh−Vac axis (x axis) which lifts the degeneracy for its unpaired electron, now expected to occupy a b_1 type ($d_{y^2-z^2}$) orbital. The EPR results below 80 K, however, unambiguously demonstrated that this complex has orthorhombic (C_{2v}) symmetry with the unpaired electron in a d_{z^2} orbital, with z perpendicular to the Rh−Vac axis.[2,23,24] This indicates that a configuration resulting from an elongation along a ⟨100⟩ axis in the plane perpendicular to the Rh−Vac axis has even lower energy and a Jahn−Teller-like distortion occurs, although not required by orbital degeneracy. This is confirmed by our calculations, which indicate that the C_{4v} symmetric state (I) is 0.04 eV higher in energy than the C_{2v} ground state (II). To estimate the magnitude of this Jahn−Teller-like distortion, we start from the cubic O_h geometry of the lattice, create a vacancy in an nnn position (x-axis) and perform a geometry optimization with the constraint that the unit cell keeps the C_{4v} symmetry. It yields a local energy minimum (I) giving predictions for R_z, R_y, R_{x+}, and R_{x-} (see Figure 1b) with R_{x+} the length of the Rh^{2+}−Cl^- bond closest to the vacancy (cf. Table 1). Due to the C_{4v} symmetry $R_z = R_y$, whose equilibrium value we define as R'_0. We then gradually apply a Jahn−Teller distortion following $R_y = R'_0 - b$ and $R_z = R'_0 + b$ while keeping the lattice positions of the other ions unaltered. The symmetry is reduced to C_{2v} symmetry once $b \neq 0$. Figure 3 plots the total binding energy as a function of the distortion parameter b. A minimum is observed at $b = 15$ pm, predicting a Jahn−Teller energy E_{JT} of 0.04 eV. Note that this minimum (III) does not really represent the absolute C_{2v} minimum (II), but it turns out that the difference is particularly small (on the order of 0.0001 eV) and also the geometries of II and III are practically coincident.

Table 4. Total Energy Differences $\Delta = E_{nnn} - E_{nn}$ for the Rh^{2+} Center with One Cation Vacancy in the Next Nearest Neighbor (nnn) and Nearest Neighbor (nn) Positions[a]

method	code	functional	size	Δ (eV)
		Rh^{2+} Center		
periodic	CP2K	PBE	$6 \times 6 \times 6$	−0.0326
		PBE	$8 \times 8 \times 8$	−0.0148
		PBE	$10 \times 10 \times 10$	−0.008
		BLYP	$8 \times 8 \times 8$	−0.0147
		BLYP	$8 \times 8 \times 8$[b]	0.3294
cluster in vacuo	ADF	BP86	125 atoms	−0.0286
cluster in vacuo	ORCA	B3LYP	125 atoms	0.0284
			179 atoms	−0.0466
			185 atoms	−0.2644
	ORCA	BP86	125 atoms	−0.0015
			179 atoms	−0.0353
			185 atoms	−0.2642
	ORCA	PBE	125 atoms	−0.0249
			179 atoms	0.0291
			185 atoms	−0.2668
		Mn^{2+} Center		
periodic	CP2K	PBE	$8 \times 8 \times 8$	0.0103
	expt[c]			0.034
	expt[d]			0.043
		Ir^{2+} Center		
periodic	CP2K	PBE	$8 \times 8 \times 8$	−0.0089

[a] For the periodic calculation a cutoff value of 700 Ry is used. Geometry optimizations in a CP2K ($8 \times 8 \times 8$) run with PBE functional and GPW basis set unless separately indicated. Energy differences are given in eV. Also predictions for the Mn^{2+} and Ir^{2+} centers are given. [b] Use of the geometry optimized in $8 \times 8 \times 8$ supercell with BLYP as functional. [c] Experimental results from ref 59. [d] Experimental results from ref 60.

From the lattice positions of the ions in the optimized supercell containing $[RhCl_6].1Vac$ (given in the Supporting Information), we derive an important relaxation of the first shell of Cl^- ions around the vacancy away from it, as very clearly seen in the Rh−Cl distance along the positive x-axis in Table 3. The second anion shell around the vacancy also undergoes an appreciable outward relaxation (with respect to the vacancy), reflected in an increase of the Rh−Cl distance along the z-axis (see Table 3). Very similar observations are made for $[RhCl_6].2Vac$ and the dimer, exhibiting an even stronger increase of the elongation of the axial Rh−Cl bond. Barriuso et al.[28] predicted this behavior (without calculations) and considered it as a possible explanation for the experimentally observed trends in the ^{103}Rh self hyperfine interactions in these complexes. A wide discussion on this pseudo Jahn−Teller effect is given in a book by Bersuker.[56]

The effect on the neighboring cation shells is less straightforward to predict: the relaxation expected from Coulomb considerations might be partially canceled by the displacements of the anions. The first shell undergoes a relaxation toward the vacancy (displacement = 0.22 pm (see the Supporting Information). On the contrary, the second shell, to which the Rh^{2+} ion belongs, has an increased distance to the vacancy (displacement of 4.52 pm

for the Rh^{2+} center), being pushed away from it by the first shell Cl^- ions. As a result of this combination of cation and anion displacements, the Rh−Cl bonds along the elongation axis are no longer exactly parallel to the ⟨001⟩ axis. This leads to very small but experimentally observed tilting of the **A** and **Q** tensor axes for these axial Cl^- ions, as is discussed in more detail in section III.D. A final point worth noting in Table 3 is the striking resemblance in geometry between the $[RhCl_6]$.2Vac complex and the environments around the individual Rh^{2+} ions in the dimer. The Rh−Cl distances are indeed identical within 1 pm. This is also reflected in the EPR and ENDOR parameters for these centers (see below).

III.B. Position of the Vacancies. The experimental results demonstrate that cation vacancies locally compensating the $[RhCl_6]^{4-}$ complexes are always found in nnn positions. From purely electrostatic considerations, one would expect complexes with nearest neighbor (nn) vacancies to be more stable, as the distance between the central ion with an extra positive charge and the vacancies with an effective negative charge is smaller. Up to now no theoretical calculations have been performed which explicitly support these experimental findings. We performed periodic calculations for defects with the two possible vacancy positions to unravel this apparent contradiction. The results are summarized in Table 4. They reveal that for Rh^{2+} complexes the nnn cation vacancy is energetically slightly favored over the nn position. This agrees with the experimental findings, although the calculated differences are very small. In addition, the energy difference between the two possible vacancy positions appears to decrease as the supercell size increases. Use of another density functional does not alter the final conformational preference, provided the same functional is used for the geometry optimization. BLYP results are also taken up in Table 4, predicting the same quantitative preference for the nnn cation vacancy. If, however, the same functional is not consistently used in both geometry and energetic computation, BLYP predicts the wrong nn position as most favorable by 0.33 eV.

It is clear that this issue deserves special attention as the energetically most favored configuration is very sensitive to the model taken into consideration. We therefore performed additional finite cluster calculations using the geometries as obtained in the CP2K applications with PBE (see section II). The results are also taken up in Table 4. As ORCA posed fewer convergence problems in performing single-point calculations than ADF, we preferred the former for a more profound investigation of the influence of the functional on the energetics. We applied three functionals to allow cross reference. When choosing the cluster size too small, there is no consistency in the energy difference $\Delta = E_{nnn} - E_{nn}$. The B3LYP result predicts the nn cation vacancy position as most favorable, as seen for the cluster containing 125 atoms (total charge is equal to +1). A cluster in vacuo containing 179 atoms appears to be sufficiently large to take into account all relevant environmental aspects to produce the correct ground state vacancy configuration. Now the nnn position for the vacancy is favored in two of the three DFT methods, but the cluster has a rather high total charge (−5). Including six Na^+ cations on the ⟨100⟩ axes might resolve this inconvenience. We performed these 185 atom cluster calculations, and remarkably we now obtained an energy difference of −0.26 eV consistently predicted by the three functionals, favoring the nnn position for the vacancy as in CP2K/PBE. For completeness we also included an ADF calculation on the 125 atom cluster with BP86 as functional. The result is not in contradiction to ORCA. It is interesting to note that in the 125 ion cluster the vacancy is situated on the border of the cluster, whereas in the 179 or 185 ion cluster, it is fully quantum mechanically embedded. As such these results are more reliable and indeed predict the correct vacancy position. This result is completely in agreement with conclusions obtained in our previous studies on chalcogen defects (O^-, S^-) in alkali metal halide lattices.[53] The relatively large inward relaxation around the Rh^{2+} ion is also compatible with finding the nnn position as energetically most favorable for the charge compensating vacancy: indeed, Bannon et al.[57,58] for closed shell divalent cations and Stevens et al.[53] for X^- anions (X = O, S) found that the nnn (nn) vacancy position is preferred when substituting a lattice ion by a smaller (larger) ion.

The theory also demonstrates that the favorable nnn position is not trivial: Mn^{2+} defects give the opposite results in agreement with experiment. The ionic radius of Mn^{2+} is considerably larger than that for Rh^{2+}, and this favors a vacancy in the nearest neighbor position.

For completeness we also include the case with an Ir^{2+} defect (ionic radius = 87.5 pm) and which favors the nnn position for the vacancy.

III.C. Hyperfine and Quadrupole Interactions. In many transition metal ion complexes where the transition metal has nuclear spin, the self hyperfine interaction with this nucleus is much larger than that with neighboring nuclei. ^{103}Rh has nuclear spin $I = 1/2$ at full natural abundance, and its hyperfine interaction has been observed in certain Rh^{2+} complexes (see, e.g., refs 61 and 62). The EPR and ENDOR spectra of $[RhCl_6]^{4-}$ complexes in NaCl, however, demonstrated that the self hyperfine interaction is much smaller than that with the Cl^- ions along the elongation axis. For the $[RhCl_6]^{4-}$.0Vac center, the ^{103}Rh hyperfine interaction could not be identified in the spectra, and for the $[RhCl_6]^{4-}$.*n*Vac centers principal values on the order of 10 MHz were found, much smaller than the isotropic value expected from core polarization. Barriuso et al.[28] presented a semiquantitative explanation for this: using plausible values for geometric and electronic parameters for the $[RhCl_6]^{4-}$.0Vac complex, they showed that the contributions from core polarization, spin−orbit coupling, and 4d−5s hybridization may cancel each other almost exactly out. These contributions are, however, very difficult to calculate from first principles and are also strongly dependent on the details of calculations (basis sets, functional). Our CP2K, ORCA, and ADF calculations lead to strongly varying results, with typical isotropic and anisotropic values on the order of a couple of tens of megahertz, much larger than experimentally observed. We prefer not to present them here and concentrate on hyperfine interactions with neighboring nuclei. In particular, we focus on the nearest ^{35}Cl (75% $I = 3/2$) and ^{23}Na (100% $I = 3/2$) nuclei on the elongation *z*-axis, for which **A** and **Q** tensors could be determined very accurately. The hyperfine tensors are presented in Table 5.

III.C.1. $[RhCl_6]$.0Vac Defect: Comparison with Earlier Theoretical Results. EPR and ENDOR spectra clearly show the existence of a strong hyperfine interaction[24,25] of the unpaired electron with the two axial Cl^- ligands, much larger than the interaction with the four equatorial anions, although the axial Rh−Cl distance R_{ax} is notably larger than the equatorial distance R_{eq} (Table 5, zero vacancies). This is perfectly reproduced in all periodic and cluster (179 atoms) calculations.

In ref 29 average principal values for the axial and equatorial Cl^- ligands, A_{ax} and A_{eq}, were computed as a function of the elongation parameter *a* using an optimized cluster consisting of

Table 5. Hyperfine Tensors for Neighboring Nuclei of $[RhCl_6]^{4-}$.*n*Vac and the Rh-Dimer Centers in NaCl[a]

complex	code	unit cell or cluster size	ion position	A_x	A_y	A_z	A_{iso}	θ
0 vacancy			Na(0,0,2)					
	CP2K	8 × 8 × 8		4.34	4.34	5.36	4.68	
	CP2K	8 × 8 × 8*[b]		3.29	3.30	4.81	3.80	
	ORCA	179 atoms		2.96	2.96	4.32	3.41	
	ADF	125 atoms		5.34	5.34	7.31	6.00	
	expt[c]			2.88	2.88	4.29	3.35	
			Cl(0,0,1)					
	CP2K	8 × 8 × 8		28.31	28.31	71.97	42.86	0.0
	CP2K	8 × 8 × 8*[b]		30.45	30.45	75.68	45.53	
	ORCA	179 atoms		31.21	31.21	72.23	44.88	
	ADF	125 atoms		29.34	29.34	82.45	47.04	
	expt[c]			33.90	33.90	75.50	47.77	0.0
			Cl(1,0,0)					
	CP2K	8 × 8 × 8		10.00	5.73	5.71	7.15	
	CP2K	8 × 8 × 8*[b]		11.13	6.27	5.72	7.71	
	ORCA	179 atoms		9.40	6.00	5.94	7.11	
	ADF	125 atoms		10.19	4.61	6.34	7.05	
			Na(1,1,0)					
	CP2K	8 × 8 × 8		−0.47	−0.45	0.35	−0.19	
	ORCA	179 atoms		−0.45	−0.43	0.40	−0.16	
			Na(1,0,1)					
	CP2K	8 × 8 × 8		−0.66	−0.48	0.24	−0.30	
	ORCA	179 atoms		−0.66	−0.53	0.26	−0.31	
1 vacancy			Na(0,0,2)					
	CP2K	8 × 8 × 8		4.61	4.61	5.62	4.95	
	CP2K	8 × 8 × 8*[b]		3.52	3.52	5.02	4.02	
	ORCA	179 atoms		3.18	3.18	4.53	3.63	
	ADF	125 atoms		5.60	5.60	7.56	6.25	
	expt[d]			3.15	3.17	4.59	3.64	
			Cl(0,0,1)					
	CP2K	8 × 8 × 8		29.13	29.14	70.13	42.80	0.3
	CP2K	8 × 8 × 8*[b]		31.30	31.29	73.71	45.43	
	ORCA	179 atoms		31.75	31.75	69.73	44.41	
	ADF	125 atoms		30.02	30.54	80.59	48.24	
	expt[c]			34.00	34.10	74.50	47.53	0.9
2 vacancies			Na(0,0,2)					
	CP2K	8 × 8 × 8		5.17	5.17	6.22	5.52	
	CP2K	8 × 8 × 8*[b]		3.99	3.99	5.55	4.51	
	ORCA	179 atoms		3.68	3.68	5.09	4.15	
	ADF	125 atoms		6.11	6.12	8.15	6.79	
	expt[c]			3.31	3.31	4.76	3.79	
			Cl(0,0,1)					
	CP2K	8 × 8 × 8		29.67	29.67	69.90	43.08	0.6
	CP2K	8 × 8 × 8*[b]		31.94	31.94	73.46	45.78	
	ORCA	179 atoms		32.35	32.35	68.80	44.50	
	ADF	125 atoms		30.81	30.81	80.20	47.27	
	expt[c]			33.90	33.90	72.70	46.83	0.2
dimer			Na(0,0,2)					
	CP2K	8 × 8 × 8		2.51	2.53	3.05	2.70	0.3
	CP2K	8 × 8 × 8*[b]		1.93	1.95	2.72	2.20	
	ORCA	179 atoms		1.40	1.42	2.11	1.65	
	expt			–	–	–	–	
			Cl(0,0,1)					
	CP2K	8 × 8 × 8		14.78	14.80	35.22	21.60	
	CP2K	8 × 8 × 8*[b]		15.86	15.86	36.93	22.83	

dx.doi.org/10.1021/jp109517g |*J. Phys. Chem. A* 2011, 115, 1721–1733

Table 5. Continued

complex	code	unit cell or cluster size	ion position	A_x	A_y	A_z	A_{iso}	θ
	ORCA	179 atoms		15.18	15.19	34.62	21.66	
	ADF	125 atoms		14.63	14.61	40.01	23.08	
	expt[c]			17.00	17.00	37.00	23.67	1.0

[a] Values are given in megahertz. The interactions with the Na and Cl ions on the elongation axis are given for all centers, and for the $[RhCl_6]^{4-}$.0Vac complex interactions with the nearest equatorial Cl^- and Na^+ ions are given as well. The tilting angles θ for the axial Cl^- ions are expressed in degrees. Functionals for the various codes are those as specified in section II. [b] Basis set TZV for the $[RhCl_6]^{4-}$ complex. [c] Experimental results from ref 25. [d] Experimental results from ref 2. [e] Experimental results from ref 3.

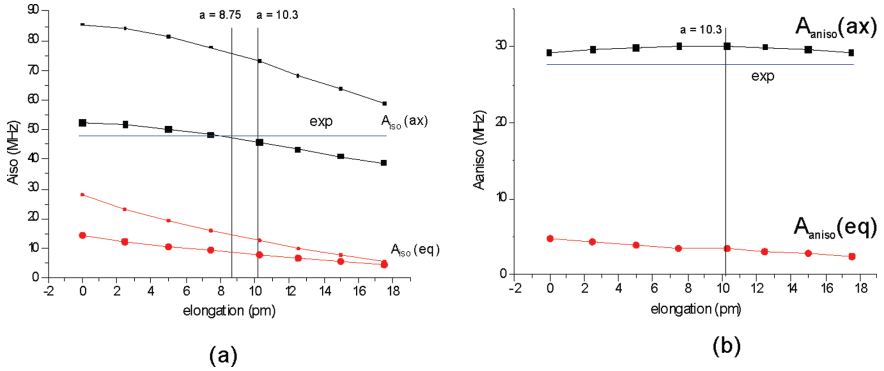

Figure 4. Calculated values for the isotropic (a) and anisotropic (b) superhyperfine interactions with the axial and equatorial Cl^- ligands as a function of the elongation parameter a. Results from CP2K calculations with the use of TZV basis set and an $8 \times 8 \times 8$ unit cell are displayed with large black squares for the axial values and large red circles for the equatorial values. Lines connecting small symbols indicate cluster calculations of ref 29. In (b) the largest anisotropic component for the axial and equatorial ligands is plotted.

39 atoms. Their results are displayed in Figure 4. As the axial Rh−Cl distance becomes larger, the hyperfine interaction with the axial Cl^- anions decreases as one might expect. At the same time the equatorial distance goes down, and one might expect an increase of the A_{eq} value, but on the contrary it drops, albeit less than A_{ax}. Barriuso et al.[29] successfully explained these features based on a molecular orbital model allowing 5s admixtures in the axial ($4d_{3z^2-r^2}$) orbital. On the quantitative level, however, the calculations by Barriuso et al. overestimated the A_{ax} values considerably, not only at the equilibrium elongation of a = 8.75 pm but for the whole range. This is probably a result of an overestimation of the delocalization of the spin density onto the Cl^- ligands in the small cluster. They found 12% delocalization on each of the axial Cl^- ligands and 2.25% on each of the equatorial ligands, which is substantially higher than the 7% and 1% delocalization resulting from the periodic calculations respectively. In Figure 4 the CP2K results of the isotropic A_{ax} and A_{eq} values as a function of the elongation parameter a are also presented. Both A_{ax} and A_{eq} are calculated to be much smaller than in ref 29, but exhibit the same trend: they decrease as a increases. On the other hand, the anisotropic part (defined as $A_{aniso}(ax) = A_z - A_{iso}$) of the tensor for the axial ligands hardly changes upon varying the elongation and goes through a maximum at the equilibrium geometry. This is illustrated in Figure 4b, where the largest anisotropic contribution for the equatorial Cl^- ligands is also plotted. At values of the elongation parameter close to the equilibrium value (a = 10.3 pm, see section III.A.2), the CP2K result for A_{ax} practically coincides with the experimental value and A_{eq} is about 6 times smaller. Although lower values for a would yield A_{ax} predictions slightly closer to experiment, the obtained agreement is an indication that the periodic calculations give an almost perfect reflection of the geometry of the $[RhCl_6]^{4-}$ complex in an ionic lattice. The A_{eq} at equilibrium cannot be verified experimentally as this interaction could not be identified in the EPR and ENDOR spectra. The fact that it is much smaller than A_{ax} is in qualitative agreement with experiment, though. Also the anisotropic values for the axial Cl^- ions are fairly well reproduced by the periodic and cluster calculations.

The choice of the basis set when using the periodic CP2K code for the computation of EPR properties requires a special note. For the geometry optimizations a double-ζ basis set for the atom centered Gaussian orbitals is largely sufficient, but for the all-electron calculation of both superhyperfine and quadrupole tensors, a higher level of basis sets is required to acquire the requested accuracy with regard to the experimental values. This comment is (obviously) equally valid for the other defect models. In general, a double-ζ Gaussian basis set fails in predicting correctly the isotropic part of the coupling. Enhancing the basis set to a triple-ζ for the atoms of the central $[RhCl_6]^{4-}$ complex (TZV, indicated as $8 \times 8 \times 8^*$ in Tables 5 and 6) affects considerably the isotropic predictions, giving for many nuclei an even better agreement with experimental A_z values than the cluster-in-vacuo results. The anisotropy is less affected by the basis set choice. The ADF results produced with the 125 atom cluster do not reach the same accuracy obtained with the periodic

Table 6. Quadrupole Interactions for $[RhCl_6]^{4-}$.*n*Vac Centers in NaCl[a]

complex	code	unit cell or cluster size	nucleus	Q_x	Q_y	Q_z	θ
0 vacancy			Na(0,0,2)				
	CP2K	8 × 8 × 8		−0.03	−0.03	0.06	
	CP2K	8 × 8 × 8*[b]		−0.03	−0.03	0.06	
	ORCA	179 atoms		−0.05	−0.05	0.09	
	expt[c]			−0.04	−0.04	0.08	
			Cl(0,0,1)				
	CP2K	8 × 8 × 8		1.21	1.21	−2.41	
	CP2K	8 × 8 × 8*[b]		0.94	0.95	−1.89	
	ORCA	179 atoms		0.76	0.76	−1.52	0.0
	expt[c]			0.72	0.72	−1.44	0.0
1 vacancy			Na(0,0,2)				
	CP2K	8 × 8 × 8		−0.05	−0.01	0.06	
	CP2K	8 × 8 × 8*[b]		−0.05	−0.01	0.06	
	ORCA	179 atoms		−0.07	−0.02	0.10	
	expt[d]			−0.06	−0.02	0.08	
			Cl(0,0,1)				
	CP2K	8 × 8 × 8		1.22	1.16	−2.38	1.4
	CP2K	8 × 8 × 8*[b]		0.95	0.91	−1.86	
	ORCA	179 atoms		0.76	0.71	−1.47	1.9
	expt[e]			0.70	0.70	−1.40	1.7
2 vacancies			Na(0,0,2)				
	CP2K	8 × 8 × 8		−0.02	−0.0.02	0.05	
	CP2K	8 × 8 × 8*[b]		−0.02	−0.02	0.05	
	ORCA	179 atoms		−0.04	−0.04	0.07	
	expt[f]			−0.03	−0.03	0.06	
			Cl(0,0,1)				
	CP2K	8 × 8 × 8		1.08	1.09	−2.16	3.3
	CP2K	8 × 8 × 8*[b]		0.84	0.85	−1.69	
	ORCA	179 atoms		0.63	0.64	−1.27	4.6
	expt[e]			0.64	0.69	−1.33	2.0
dimer			Na(0,0,2)				
	CP2K	8 × 8 × 8		−0.02	−0.02	0.05	
	CP2K	8 × 8 × 8*[b]		−0.02	−0.02	0.05	
	ORCA	179 atoms		0.00	−0.06	0.06	
	expt			-	-	-	
			Cl(0,0,1)				
	CP2K	8 × 8 × 8		1.07	1.12	−2.19	2.5
		8 × 8 × 8*[b]		0.84	0.88	−1.72	
	ORCA	179 atoms		0.65	0.67	−1.31	5.5
	expt[g]			0.63	0.66	−1.29	2.0

[a] Values are given in megahertz. The tilting angle θ is given in degrees. Only the interactions with the Na and Cl ions on the axial axis are given. [b] With basis set TZV. [c] Experimental results from ref 25. [d] Experimental results from ref 21. [e] Experimental results from ref 1. [f] Experimental results from ref 20. [g] Experimental results from ref 3.

code and larger clusters. This is probably due to a too small cluster size. Analogous calculations with the 179 atom cluster were not possible within the current computational resources.

The hyperfine interactions of the unpaired electron of the Rh defect with the surrounding cations were measured to be much weaker than that with the axial Cl^- ions. All our ab initio calculations succeed in reproducing this trend. Nevertheless it is instructive to examine which cations yield the largest interaction, in view of the many papers published in the literature on this item. They predict a stronger interaction with the fourth shell axial cations in (0,0,2) positions than with the second shell of equatorial cations in (1,1,0) or (1,0,1) positions, which are much nearer the central Rh^{2+} ion. This has been explained by a transfer of unpaired spin density onto the fourth shell axial cations via overlap with the axial Cl^- ions.[19] The theoretical predictions of this work confirm this behavior. To illustrate: a Mulliken spin population analysis for the $[RhCl_6]^{4-}$.0Vac defect reports a spin density of 0.80 for the Rh^{2+} center, and 0.07 and 0.01 for the axial Cl^- and Na^+ ions. The equatorial Cl^- ligands show values ranging from 0.01 to 0.02.

III.C.2. $[RhCl_6]$.nVac Defects and Dimer: Reproduction of Trends and Numerical Values. In the experimental principal superhyperfine and quadrupole interaction parameters, definite trends are observed as a function of the number of cation vacancies. The reproduction of these trends presents a stringent test for the validity of computational approaches. For the first shell of axial ^{35}Cl nuclei, the A_z and Q_z components slightly but clearly decrease as the number of vacancies increases. Both periodic and cluster calculations succeed in reproducing this trend, and even lead to a fairly satisfactory numerical agreement with experiment. Periodic calculations tend to perform slightly better for the A_z parameter, while for Q_z the cluster calculations are in closer agreement with experiment. Cluster and periodic calculations predict very small tilting angles away from ⟨001⟩ orientations for the principal A_z and Q_z directions, which also very closely match the experimentally observed tilting. The cluster calculations consistently overestimate these tilting angles, which is obviously related to their finite size.

The principal hyperfine values of the fourth shell of axial ^{23}Na nuclei increase with the number of vacancies. Also this trend is perfectly reproduced by all our calculations. The numerical agreement with experiment is manifestly better in the cluster approach. CP2K tends to overestimate the isotropic hyperfine constants rather systematically. In the reproduction of the quadrupole parameters for these nuclei, cluster and periodic calculations perform approximately equally well. In particular, the qualitative feature is that for the centers with zero and two vacancies the **Q** tensor is (nearly) exactly axial, whereas for the defect with one vacancy it has a large rhombic component, and is reproduced in all calculations. Finally, we note that the axial ^{35}Cl and ^{23}Na hyperfine parameters for the dimer center are roughly half the typical values for the Rh^{2+} monomer defects. This is a result of the strong interaction picture $(S = 1)^3$ in which both the experimental and the theoretical spin Hamiltonian parameters are represented. This relation between the parameters for monomer and dimer centers implies that the environment around the individual Rh^{2+} ions in the dimer very strongly resembles the situation encountered in a monomer ($[RhCl_6]^{4-}$.2Vac).

The ability of quantum chemical calculations to reproduce the subtle effects of nnn cation vacancies on hyperfine and quadrupole tensors of neighboring nuclei, such as trends in magnitude of parameters, small tilting angles, and degrees of rhombicity, on the one hand lends additional support to the vacancy models proposed for these defects and on the other hand strongly indicates that these types of quantum chemical calculations are sufficiently reliable for testing defect models for yet unidentified defects. It should be noted, though, that for such identification both high-level quantum chemical calculations and highly accurate experimental data are required.

The Journal of Physical Chemistry A ARTICLE

Table 7. g Tensors for $[RhCl_6]^{4-}$.*n*Vac Centers[a]

complex	code	unit cell or cluster size	g_x	g_y	g_z
0 vacancy	CP2K	8 × 8 × 8	2.3369	2.3568	2.0017
	ORCA	179 atoms	2.4029	2.4027	2.0288
		125 atoms	2.4023	2.4020	2.0288
		125 atoms[b]	2.4062	2.4062	2.0287
	ORCA/ZORA	125 atoms	2.4051	2.4049	2.0259
	ADF	125 atoms	2.2293	2.2278	2.0150
	expt[c]		2.4510	2.4510	2.0190
1 vacancy	CP2K	8 × 8 × 8	2.4211	2.2837	1.9833
	ORCA	179 atoms	2.4759	2.3538	2.0377
		125 atoms	2.4766	2.3528	2.0381
		125 atoms[b]	2.4793	2.3586	2.0377
	ORCA/ZORA	125 atoms	2.4783	2.3568	2.0346
	ADF	125 atoms	2.2654	2.2049	2.0166
	expt[d]		2.4779	2.4301	2.0154
2 vacancies	CP2K	8 × 8 × 8	2.4037	2.3740	2.0571
	ORCA	179 atoms	2.4431	2.4414	2.0288
		125 atoms	2.4432	2.4414	2.0289
		125 atoms[b]	2.4417	2.4400	2.0288
	ORCA/ZORA	125 atoms	2.4471	2.4453	2.0262
	ADF	125 atoms	2.2527	2.2515	2.0094
	expt[e]		2.4797	2.4712	2.0118
dimer	ORCA	179 atoms	2.4178	2.4269	2.0291
	expt[f]		2.4609	2.4599	2.0080

[a] For the computation in cluster-in-vacuo models (ORCA and ADF) clusters are cut out from the optimized geometry obtained in an 8 × 8 × 8 unit cell by use of CP2K. [b] Cluster from optimized geometry obtained in 6 × 6 × 6 supercell in CP2K. [c] Experimental results from ref 25. [d] Experimental results from ref 20. [e] Experimental results from refs 20 and 24. [f] Experimental results from ref 26.

Returning to the objective of this paper to propose an adequate computational protocol for transition metal ion centers, the calculations of **A** and **Q** parameters of neighboring nuclei demonstrate once more that our periodic calculations provide accurate defect geometries at low computational cost. However, for the actual calculation of these parameters, taking into account an overall numerical agreement with experiment as a criterion, we would tend to give slight preference to cluster calculations (on clusters cut out from geometries optimized in a periodic code). In view of the computational benefit of a factor of 10 with respect to ORCA (CP2K scales much better with the number of CPUs), and in view of the required geometry optimization which preferentially should be performed with the periodic code, we may conclude that CP2K is highly appropriate for the computation of **A** and **Q** EPR parameters.

III.D. g Tensors. EPR experiments up to W-band frequencies demonstrate that all defects are characterized by a nearly axial **g** tensor with g_z only slightly larger than the free electron value and $g_{x,y} > g_z$. In view of its symmetry the $[RhCl_6]^{4-}$.0Vac complex has a perfectly axial **g** tensor ($g_x = g_z$). One vacancy in the $g_x - g_y$ plane produces an appreciable rhombic component in the **g** tensor, while adding the second vacancy in a cis configuration almost completely restores the axial symmetry. The **g** tensor for the dimer is also very close to axial. For the $[RhCl_6]^{4-}$.*n*Vac complexes one experimentally observes that g_z closely approaches the free electron value while $(g_x + g_y)/2$ rises as the number of vacancies increases. In the following we will check how far computational results are reliable enough to reproduce these trends.

We performed periodic CP2K runs for the **g** tensor calculation for the first three defect models, but they demanded an exorbitantly high computation time and hence they cannot be recommended as a standard routine for common use in such extended systems. One run used approximately 665 GB of memory and took 53 h of computer time on 512 cores. For the cluster calculations with ORCA the computational cost is much lower and the large cluster size of 179 atoms does not constitute large obstacles. On the other hand, a full electron calculation with ADF poses additional insurmountable problems when the cluster size exceeds 125 atoms. The large difference in numerical results between cluster and periodic calculations is immediately noticed. Considering their better reproduction of g_x and their prediction of a positive shift for g_z, one might be tempted to consider the cluster calculations more reliable. However, they also are unable to reproduce all experimental trends among others in g_z, as a function of the number of vacancies. An important experimental finding reproduced by all calculations is the strongly reduced rhombicity for the $[RhCl_6]^{4-}$.2Vac complex in comparison to that with only one vacancy. The slight inequivalence between the equatorial **g** components for the $[RhCl_6]^{4-}$.2Vac complex was attributed to the fact that the angle between the two Rh−Vac axes is slightly larger than 90°.[1,20] The CP2K geometry predicts a value of 90.05°. This is explained by repulsion between the two cation vacancies which both represent an effective negative charge in the lattice.

Although certain qualitative features are successfully predicted by the calculations, it seems that both cluster and periodic approaches fail in accurately describing the experimental data, especially if one aims at defect identification. For the periodic calculations, this may be attributed to a shortcoming of the description of the spin−orbit and spin−other-orbit contributions in the implementation of the **g** tensor in CP2K, as mentioned in section II. We conclude that computation of **g** tensors for defects in ionic lattices by means of the method implemented in CP2K is not recommendable, particularly when also considering the immensely high computational cost. For the cluster calculations, the finite size might be regarded as an obvious cause of inaccuracy. However, it is striking that the size of the cluster is not of great importance, as the changes in principal **g** values of clusters of different size are only minor. It is also very improbable that inaccuracies in the geometry lie at the origin of the discrepancies with experiment: only very small changes in the **g** values are noticed when using the 125 atom cluster, cut out from the geometry optimized in a smaller periodic unit cell (6 × 6 × 6).

For completeness of the study we also included the **g** tensor predictions for the various defect models taking into account relativistic effects (ORCA/ZORA in Table 7), but their influence does not affect the above-made conclusions. The current observations on the **g** tensor calculations are a good test case for future model developments.

IV. CONCLUSIONS

In this work $[RhCl_6]^{4-}$.*n*Vac centers, with $n = 0$, 1, and 2, and a Rh^{2+} dimer in a NaCl ionic lattice have been studied theoretically using DFT methods, both through gas-phase finite cluster simulations and in periodic codes. The defect models proposed from experiment have all been correctly modeled by the calculations. We have shown that periodic supercell calculations provide

very accurate geometries for the complexes, giving the right symmetry features at low computational cost, on which spectroscopic parameters can be reliably evaluated. For the transition metal complexes, as studied here, it must be noted that a sufficiently large plane wave cutoff value is chosen (here 700 Ry). The calculations also reveal features which are not directly accessible by experiment, e.g., regarding the magnitude of Jahn−Teller (like) distortions for the $n = 0$ ($n = 1$) monomer complex and lattice relaxations around vacancies. Theoretical calculations also provide evidence that the geometry and electronic ground state of the individual Rh^{2+} ions in the dimer strongly resemble those in the $[RhCl_6]^{4-}$.2Vac center.

Next, periodic and finite cluster calculations of EPR parameters have been evaluated for their ability to reproduce observed trends, for their overall numerical agreement with experiment, and computational efficiency. For cluster-in-vacuo calculations a finite cluster with the defect in its center was cut out from the periodically optimized structure. Both periodic and gas-phase calculations reproduce all experimental trends in the **A** and **Q** tensors of neighboring ions and even provide very satisfactory numerical agreement. Our results indicate that the calculations of ligand **A** and **Q** parameters are sufficiently reliable to identify the effect of subtle changes in the environment of transition metal complexes in ionic lattices, also when their origin is not clear from experiment. However, highly accurate experimental results and sufficiently large basis sets (TZP for cluster calculations and at least a triple-ζ localized Gaussian basis set in CP2K) are prerequisite. Although the overall quantitative agreement is slightly better using finite cluster calculations (especially in ORCA), taking also the computing time as a criterion, the periodic approach (CP2K) must be preferred.

In contrast, the results for the **g** tensor calculations are rather disappointing. None of the examined approaches is able to reproduce all experimental trends for these parameters, and the numerical accuracy is also rather poor. In addition, the CP2K calculations take an excessive computational cost and ADF calculations on sufficiently large clusters are simply not feasible. ORCA calculations seem the only reasonable option for transition metal complexes in ionic crystals. The current system may be used as an inspiration for future theoretical developments of **g** tensor values, as these quantities seem to be very difficult to reproduce. Therefore, it is not recommended to assign defect models solely based on comparing the calculated **g** values with experimental data.

■ ASSOCIATED CONTENT

Supporting Information. Table S.I, coordinates of atoms in the *xy* plane for Rh^{2+} centers after geometry optimization in an $8 \times 8 \times 8$ supercell with CP2K and 700 Rydberg cutoff; Table S.II, atom displacement in the geometry optimization for Rh centers in an $8 \times 8 \times 8$ supercell with CP2K and 700 Rydberg cutoff; Table S.III, cluster-in-vacuo predictions for spectroscopic properties of a $[RhCl_6]^{4-}$.2Vac complex in NaCl after geometry optimization of a relaxed 124 atom cluster using ADF and the Bp86 functional in combination with a TZ2P basis set; Figure S1, snapshot in the *xy* plane containing Rh ion. This material is available free of charge via the Internet at http://pubs.acs.org.

■ AUTHOR INFORMATION

Corresponding Author
*E-mail: michel.waroquier@Ugent.be.

■ ACKNOWLEDGMENT

The authors would like to thank the Fund for Scientific Research (FWO-Flanders, Belgium) and the Research Board of Ghent University for financial support. Part of the computational resources and services used in this work were provided by Ghent University.

■ REFERENCES

(1) Vrielinck, H.; Callens, F.; Matthys, P. *Phys. Rev. B* **2001**, *64*, 6.
(2) Vrielinck, H.; Sabbe, K.; Callens, F.; Matthys, P. *Phys. Chem. Chem. Phys.* **2001**, *3*, 1709.
(3) Vrielinck, H.; Sabbe, K.; Callens, F.; Matthys, P. *Radiat. Eff. Defects Solids* **2003**, *158*, 221.
(4) Stevens, F.; Van Speybroeck, V.; Pauwels, E.; Vrielinck, H.; Callens, F.; Waroquier, M. *Phys. Chem. Chem. Phys.* **2005**, *7*, 240.
(5) Stevens, F.; Vrielinck, H.; Callens, F.; Pauwels, E.; Waroquier, M. *Phys. Rev. B* **2002**, *66*, 12.
(6) Stevens, F.; Vrielinck, H.; Callens, F.; Pauwels, E.; Waroquier, M. *Phys. Rev. B* **2003**, *67*, 7.
(7) Abragam, A.; Bleaney, B. *Electron Paramagnetic Resonance of Transition Ions*; Clarendon Press: Oxford, 1970.
(8) Kadantsev, E. S.; Ziegler, T. *J. Phys. Chem. A* **2008**, *112*, 4521.
(9) Kadantsev, E. S.; Ziegler, T. *J. Phys. Chem. A* **2009**, *113*, 1327.
(10) Pickard, C. J.; Mauri, F. *Phys. Rev. Lett.* **2002**, *88*, 4.
(11) Weber, V.; Iannuzzi, M.; Giani, S.; Hutter, J.; Declerck, R.; Waroquier, M. *J. Chem. Phys.* **2009**, *131*, No. 014106.
(12) ADF. SCM, Department of Theoretical Chemistry, Vrije Universiteit, Amsterdam, The Nederlands .
(13) Neese, F. *ORCA*; University of Bonn: Bonn, Germany, 2008.
(14) Neese, F. *J. Chem. Phys.* **2005**, *122*, No. 034107.
(15) Kadantsev, E. S.; Ziegler, T. *Magn. Reson. Chem.* **2010**, *48* (S1), S2.
(16) te Velde, G.; Baerends, E. J.; Philipsen, P. H. T.; Wiesenekker, G.; Groeneveld, J. A.; Berger, J. A.; de Boeij, P. L.; Klooster, R.; Kootstra, F.; Romaniello, P.; Snijders, J. G.; Kadantsev, E. S.; Ziegler, T. *BAND*; SCM, Department of Theoretical Chemistry, Vrije Universiteit: Amsterdam, The Nederlands.
(17) Stevens, F.; Vrielinck, H.; Callens, F.; Waroquier, M. *Solid State Commun.* **2004**, *132*, 787.
(18) Shock, J. R.; Rogers, M. T. *J. Chem. Phys.* **1975**, *62*, 2640.
(19) Pinhal, N. M.; Vugman, N. V. *J. Phys. C: Solid State Phys.* **1985**, *18*, 6273.
(20) Callens, F.; Vrielinck, H.; Matthys, P.; Zdravkova, M.; Vercammen, H.; Schoemaker, D. *J. Appl. Phys.* **1998**, *84*, 422.
(21) Sabbe, K.; Callens, F.; Boesman, E. *Appl. Magn. Reson.* **1998**, *15*, 539.
(22) Sabbe, K.; Vrielinck, H.; Callens, F.; Boesman, E.; Vercammen, H.; Kass, H.; Goovaerts, E.; Bouwen, A.; Schoemaker, D. *J. Chem. Soc., Faraday Trans.* **1998**, *94*, 2993.
(23) Schweizer, S.; Spaeth, J. M. *J. Phys. Chem. Solids* **1997**, *58*, 859.
(24) Vercammen, H.; Schoemaker, D.; Kass, H.; Goovaerts, E.; Bouwen, A.; Vrielinck, H.; Callens, F. *J. Appl. Phys.* **1998**, *84*, 428.
(25) Zdravkova, M.; Vrielinck, H.; Callens, F.; Boesman, E.; Vercammen, H.; Schoemaker, D. *J. Appl. Phys.* **1997**, *82*, 2476.
(26) Vercammen, H.; Goovaerts, E.; Kass, H.; Bouwen, A.; Schoemaker, D. *J. Chem. Soc., Faraday Trans.* **1998**, *94*, 3003.
(27) Vrielinck, H.; Callens, F.; Zdravkova, M.; Matthys, P. *J. Chem. Soc., Faraday Trans.* **1998**, *94*, 2999.
(28) Barriuso, M. T.; Aramburu, J. A.; Moreno, M. *J. Phys.: Condens. Matter* **2002**, *14*, 6521.
(29) Barriuso, M. T.; Garcia-Fernandez, P.; Aramburu, J. A.; Moreno, M. *Solid State Commun.* **2001**, *120*, 1.
(30) Garcia-Fernandez, P.; Bersuker, I. B.; Aramburu, J. A.; Barriuso, M. T.; Moreno, M. *Phys. Rev. B* **2005**, *71*, 10.
(31) http:/cp2k.berlios.de.
(32) Declerck, R.; Van Speybroeck, V.; Waroquier, M. *Phys. Rev. B* **2006**, *73*, No. 115113.

(33) Lippert, G.; Hutter, J.; Parrinello, M. *Mol. Phys.* **1997**, *92*, 477.
(34) Perdew, J. P.; Burke, K.; Ernzerhof, M. *Phys. Rev. Lett.* **1996**, *77*, 3865.
(35) VandeVondele, J.; Hutter, J. *J. Chem. Phys.* **2007**, *127*, No. 114105.
(36) Goedecker, S.; Teter, M.; Hutter, J. *Phys. Rev. B* **1996**, *54*, 1703.
(37) Declerck, R.; Pauwels, E.; Van Speybroeck, V.; Waroquier, M. *Phys. Rev. B* **2006**, *74*, 8.
(38) Iannuzzi, M.; Chassaing, T.; Wallman, T.; Hutter, J. *Chimia* **2005**, *59*, 499.
(39) Krack, M.; Parrinello, M. *Phys. Chem. Chem. Phys.* **2000**, *2*, 2105.
(40) Lippert, G.; Hutter, J.; Parrinello, M. *Theor. Chem. Acc.* **1999**, *103*, 124.
(41) Schuchardt, K. L.; Didier, B. T.; Elsethagen, T.; Sun, L. S.; Gurumoorthi, V.; Chase, J.; Li, J.; Windus, T. L. *J. Chem. Inf. Model.* **2007**, *47*, 1045.
(42) Putrino, A.; Sebastiani, D.; Parrinello, M. *J. Chem. Phys.* **2000**, *113*, 7102.
(43) Schreckenbach, G.; Ziegler, T. *J. Phys. Chem. A* **1997**, *101*, 3388.
(44) vanLenthe, E.; Wormer, P. E. S.; vanderAvoird, A. *J. Chem. Phys.* **1997**, *107*, 2488.
(45) Neese, F. *J. Chem. Phys.* **2001**, *115*, 11080.
(46) Hess, B. A.; Marian, C. M.; Wahlgren, U.; Gropen, O. *Chem. Phys. Lett.* **1996**, *251*, 365.
(47) vanLenthe, E.; Snijders, J. G.; Baerends, E. J. *J. Chem. Phys.* **1996**, *105*, 6505.
(48) Becke, A. D. *Phys. Rev. A* **1988**, *38*, 3098.
(49) Perdew, J. P. *Phys. Rev. B* **1986**, *33*, 8822.
(50) Herman, F.; Skillman, F. *Atomic Structure Calculations*; Prentice-Hall: Engelwood Cliffs, NJ, 1963.
(51) Becke, A. D. *J. Chem. Phys.* **1993**, *98*, 5648.
(52) Lee, C. T.; Yang, W. T.; Parr, R. G. *Phys. Rev. B* **1988**, *37*, 785.
(53) Stevens, F.; Vrielinck, H.; Van Speybroeck, V.; Pauwels, E.; Callens, F.; Waroquier, M. *J. Phys. Chem. B* **2006**, *110*, 8204.
(54) Van Speybroeck, V.; Stevens, F.; Pauwels, E.; Vrielinck, H.; Callens, F.; Waroquier, M. *J. Phys. Chem. B* **2006**, *110*, 8213.
(55) Garcia-Fernandez, P.; Trueba, A.; Barriuso, M. T.; Aramburu, J. A.; Moreno, M. *Phys. Rev. Lett.* **2010**, *104*, 4.
(56) Bersuker, I. B. *The Jahn-Teller Effect*; Cambridge: Cambridge, U.K., 2006.
(57) Bannon, N. M.; Corish, J.; Jacobs, P. W. M. *Philos. Mag. A: Phys. Condens. Matter: Struct., Defects Mech. Prop.* **1985**, *51*, 797.
(58) Bannon, N. M.; Corish, J.; Jacobs, P. W. M. *Philos. Mag. A: Phys. Condens. Matter: Struct., Defects Mech. Prop.* **1985**, *52*, 61.
(59) Watkins, G. D. *Phys. Rev.* **1958**, *113*, 79.
(60) Lopez, F. J.; Jaque, F. *J. Phys. Soc. Jpn.* **1974**, *37*, 1466.
(61) Muniz, R. P. A.; Vugman, N. V.; Danon, J. *J. Chem. Phys.* **1971**, *54*, 1284.
(62) Suss, J. T.; Raizman, A.; Szapiro, S.; Low, W. *J. Magn. Reson.* **1972**, *6*, 439.

■ NOTE ADDED AFTER ASAP PUBLICATION

This article was published ASAP on February 7, 2011, with an error in the abstract graphic. The correct version was reposted on February 14, 2011.

Paper V

Dominant Stable Radicals in Irradiated Sucrose: g Tensors and Contribution to the Powder Electron Paramagnetic Resonance Spectrum

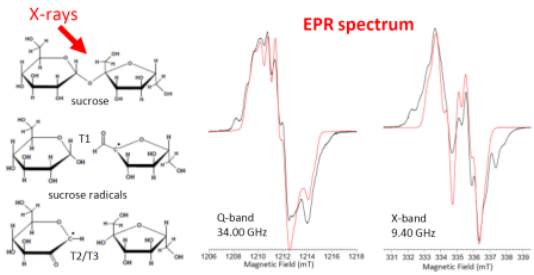

H. De Cooman, J. Keysabyl, J. Kusakovskii, A. Van Yperen-De Deyne, M. Waroquier, F. Callens and H. Vrielinck *The Journal of Physical Chemistry B* **117**, 7169–7178 (2013)

THE JOURNAL OF PHYSICAL CHEMISTRY B

Article

pubs.acs.org/JPCB

Dominant Stable Radicals in Irradiated Sucrose: g Tensors and Contribution to the Powder Electron Paramagnetic Resonance Spectrum

Hendrik De Cooman,[†,‡] Joke Keysabyl,[†] Jevgenij Kusakovskij,[†,§] Andy Van Yperen-De Deyne,[‡] Michel Waroquier,[‡] Freddy Callens,[†] and Henk Vrielinck[†,*]

[†]Ghent University, Department of Solid State Sciences, Electron Magnetic Resonance Research Group, Krijgslaan 281-S1, B-9000 Ghent, Belgium

[‡]Ghent University, Center for Molecular Modeling, Technologiepark 903, B-9052 Zwijnaarde, Belgium

[§]Vilnius University, Institute of Applied Research, Sauletekio av. 9-III, LT-10222 Vilnius, Lithuania

Supporting Information

ABSTRACT: Ionizing radiation induces a composite, multiline electron paramagnetic resonance (EPR) spectrum in sucrose, that is stable at room temperature and whose intensity is indicative of the radiation dose. Recently, the three radicals which dominate this spectrum were identified and their proton hyperfine tensors were accurately determined. Understanding the powder EPR spectrum of irradiated sucrose, however, also requires an accurate knowledge of the **g** tensors of these radicals. We extracted these tensors from angular dependent electron nuclear double resonance-induced EPR measurements at 110 K and 34 GHz. Powder spectrum simulations using this completed set of spin Hamiltonian parameters are in good agreement with experimentally recorded spectra in a wide temperature and frequency range. However, as-yet nonidentified radicals also contribute to the EPR spectra of irradiated sucrose in a non-negligible way.

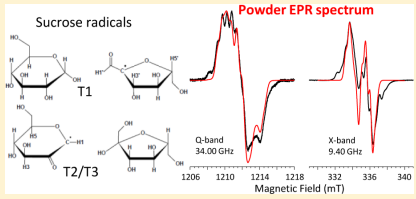

1. INTRODUCTION

The structure of radiation-induced radicals in solid state sucrose has been studied with electron magnetic resonance (EMR) techniques, electron paramagnetic resonance (EPR) in particular, since the early sixties of the 20th century.[1−6] However, only recently has the identity of three radicals (T1−T3), which appear to have a dominant contribution to the room temperature (RT) stable EPR spectrum of irradiated sucrose, been convincingly established via comparison of proton hyperfine (HF) interactions, determined from single crystal electron nuclear double resonance (ENDOR) experiments, with the results of high-level density functional theory (DFT) calculations.[7−9] Figure 1 shows the intact sucrose molecule along with the models for these dominant radicals. T1 has the unpaired electron mainly localized at carbon atom C2′ in the fructose unit. The EMR properties of T2 and T3 are very similar, and hence, they are believed to have basically the same radical structure, in slightly different conformations. They have their main unpaired electron density at C1 in the glucose unit. The formation of all three radicals involves scission of the glycosidic bond between the rings. Moreover, the carbon atom bearing the main unpaired electron density is located next to the ring oxygen and has a carbonyl group at a β-carbon position. These radical structures differ strongly from the intact sucrose molecule and most probably have a complex multistep formation mechanism. In contrast, the (at RT) highly unstable radicals produced by irradiation at 10 K are formed by simple H-abstraction at C or O atoms.[10]

There are two main motivations for studying these radicals. The first is mostly fundamental: elucidating the complex radiation chemistry of carbohydrates, and more specifically understanding the role of sugar radicals in the radiation damage to complex biomolecules such as DNA. In this context, the glycosidic bond scission in the stable radicals in sucrose, also observed for the dominant metastable radical in glucose 1-phosphate,[11,12] is remarkable and supports the idea that sugar radicals are precursors for strand breaks in DNA.[13]

A second motivation springs from the fact that ionizing radiation induces stable radicals in sugars, whose EPR signal intensity may be applied to determine the radiation dose. Since the beginning of the 1980s, the potential of sucrose in radiation dosimetry has been recognized,[14,15] and it has been the subject of many EPR studies since then.[16−22] When samples are properly stored, the EPR spectrum of irradiated sucrose has long-term stability, and after a short initial period of strong changes[20,23] it shows only limited fading. Sucrose exhibits a radiation sensitivity similar to that of alanine but a smaller linear dose range. Table sugar consists of over 90% sucrose. The

Received: January 3, 2013
Revised: May 23, 2013
Published: May 24, 2013

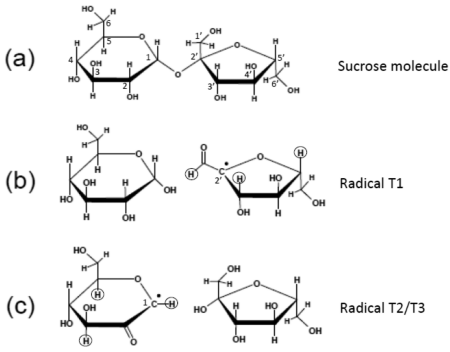

Figure 1. Intact sucrose molecule with IUPAC atomic labeling (a) and models for the RT stable radicals T1 (b) and T2/T3 (c), as determined from comparison with DFT calculated ^{1}H HF tensors.[8,9] The carbon positions bearing the main spin density, C2′ in the fructose unit for T1, and C1 in the glucose unit for T2−T3, are indicated in the radical structures with •. The ^{1}H nuclei whose HF interaction is resolved in the EPR and/or ENDOR spectra in the two radical models are circled.

radiation-induced EPR spectra of these materials resemble each other very closely. For this reason, table sugar seems particularly interesting for accident and emergency dosimetry. The composite nature of the stable EPR spectrum of irradiated sucrose, as a result of the formation of various types of radicals,[21] along with the complex transformations of this spectrum a short time after irradiation,[20,23] are issues of concern. In the same context, one can apply EPR spectrometry for detection and control of irradiated sugar-containing foodstuffs.[24−27] An additional complication arises here: in foodstuffs, usually a mixture of sugars is present, all giving rise to different radiation-induced EPR spectra. In this respect, a detailed understanding of the shape of the powder EPR spectrum of various irradiated common sugars is very relevant, and this study aims to contribute to understanding the spectrum of irradiated sucrose.

Following the recent thorough characterization and identification of three dominant, RT stable radicals in sucrose,[7−9] one may easily presume that the powder EPR spectrum of irradiated table sugar is understood to a large extent. Reliable powder pattern simulations, however, also require knowledge of the **g** tensors for the radicals, whose anisotropy is expected to be considerable because of delocalization of the unpaired electron onto the β-carbonyl and ring oxygen.[4,8,9] Attempts have been made to determine these tensors experimentally from the angular dependence of the Q-band EPR spectra on single crystals recorded at RT, but due to the compositeness of the spectra, this allowed determination of the **g** tensor for only one of the radicals.[4] In a later study,[6] the **g** tensors of the radicals were extracted via simulation of the powder EPR spectra in four microwave frequency bands (9.7−285 GHz), using the HF tensors determined in a low-temperature (55 K) ENDOR study.[5] A more recent ENDOR study[7] of our group at 110 K demonstrated that the HF tensors determined by Vanhaelewyn et al.[5] needed substantial correction, casting also doubt on the analysis of the high-frequency powder EPR spectra. In the present study we determine the **g** tensors of the three dominant RT stable radicals using ENDOR-induced EPR (EIE)[28] for separating the EPR spectra of different types of radicals. The methodology is similar to that in the pioneering EIE work of Kang et al. on determining the **g** tensors for radicals in malonic acid and guanine hydrochloride dehydrate.[29] The obtained **g** tensors are compared to those from the previous studies and to results of periodic DFT calculations on the known models for these radicals (Figure 1). Afterward, having the **g** tensors at hand, powder EPR simulations at X- and Q-band frequencies (9.5 and 34 GHz, respectively) are compared with experimental spectra. Interestingly, the statistical decomposition of the EPR spectrum of irradiated sucrose yielded up to six distinct components, three of which were clearly dominant.[5] In support of this finding, we show that certain features of the powder EPR spectra are not covered by the simulations of the known radicals.

2. EXPERIMENTAL AND COMPUTATIONAL METHODS

A. Experimental Details. Sucrose single crystals were grown from saturated aqueous solutions in our laboratory.[7] Powders were either obtained directly (Sigma Aldrich) or obtained by crushing single crystals. Sucrose crystals are monoclinic with space group $P2_1$ and two symmetry related molecules (= sites) in the unit cell, transformed into one another by a 2-fold screw-rotation around the $\langle b\rangle$ axis.[30] The lattice parameters are a = 1.0868 nm, b = 0.8710 nm, c = 0.7761 nm, and β = 102.97°, with β the angle between the $\langle a\rangle$- and $\langle c\rangle$-axes. Sucrose powders and single crystals were X-ray irradiated at RT to a dose in the range 10−100 kGy using a Philips tungsten anticathode X-ray tube operated at 60 kV and 40 mA. The crystals were subsequently oriented by X-ray diffraction (pole figures) with a Bruker D8 diffractometer, transferred and glued to quartz sample rods to allow sample rotation in the magnetic field around the $\langle a^*\rangle$ (perpendicular to $\langle b\rangle$ and $\langle c\rangle$), $\langle b\rangle$, and $\langle c\rangle$ axes.

Q-band EPR, ENDOR, and EIE spectra were recorded using a continuous wave Bruker ElexSys E500 spectrometer, equipped with an Oxford CF935 He-flow cryostat (2−300 K), a Pendulum CNT-90XL frequency counter, and a Bruker ER 035 NMR Gaussmeter. The magnetic fields were calibrated against the $g_\perp$ component of a CO_3^{3-} radical in irradiated calcite powder ($g_\perp$ = 2.0031).[31] X-band powder EPR spectra were recorded using a Bruker ESP300E setup, fitted to an Oxford ESR-900 cryostat, equipped with a HP-5350 frequency counter and a Bruker ER 035 NMR Gaussmeter. For field calibration in X-band, the spectrum of diphenyl picryl hydrazyl (DPPH, g = 2.0036) was measured. All presented X- and Q-band EPR spectra have been normalized to 9.40 and 34.00 GHz, respectively, and were recorded at low microwave power (<100 μW) and low modulation frequency (1−3 kHz), in order to avoid distortion of the spectra.

The spectra were interpreted using the standard spin Hamiltonian[28] for a paramagnetic center with $S = {}^1/_2$ interacting with nuclei with $I = {}^1/_2$ (protons, ^{1}H)

$$\hat{H}_S = \mu_B \vec{B}\cdot\vec{g}\cdot\hat{\vec{S}} + \sum_k (\hat{\vec{S}}\cdot\vec{A}^k\cdot\hat{\vec{I}}^k - g_N\vec{B}\cdot\hat{\vec{I}}^k) \quad (1)$$

in which the symbols have their usual meaning, with g_N referring to the proton nuclear g factor. In agreement with our previous studies on sucrose, $\langle a^*\rangle$, $\langle b\rangle$, and $\langle c\rangle$ are chosen as orthogonal reference system for representation of the **g** and HF tensors. The actual rotation planes in the angular

dependent EIE study (see caption of Figure 2) were accurately determined by simultaneously fitting the angular variations of

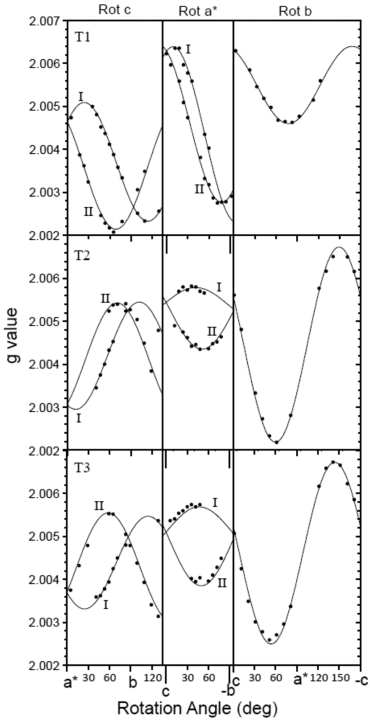

Figure 2. EIE angular variation of the stable radicals T1, T2, and T3 in X-irradiated sucrose, recorded at Q-band and 110 K (symbols), and simulations using the **g** tensor presented in Table 1 (I) and the symmetry-related tensor (II) by applying a 180° rotation around the ⟨*b*⟩ axis (full lines). In the (ca*) rotation plane (rot b), the spectra of the two symmetry related sites coincide. The rotation planes were slightly misaligned. The polar angles of the actual rotation planes, determined by fitting the ENDOR angular dependence, for the rot ⟨*c*⟩, rot ⟨*a**⟩, and rot ⟨*b*⟩ data were $\theta = -6°$, $\phi = -48°$; $\theta = 92°$, $\phi = 7°$; and $\theta = 91°$, $\phi = 94°$, respectively.

the ENDOR spectra for the largest HF coupling for each radical ($H_{\beta 1}$(T1), H_α(T2), and H_α(T3)), using the previously determined HF tensors for the stable radicals in sucrose[7,9] (see Table S1 in the Supporting Information). All single crystal and powder EPR and ENDOR spectra were simulated by full diagonalization of the spin Hamiltonian (1) using the EasySpin libraries[32] in Matlab.

B. Computational Details. All calculations were made with the CP2K program package[33] in a periodic approach using a super cell, consisting of two sucrose crystallographic unit cells along the *c* axis (four sucrose molecules, one of which having the radical structure, 179 atoms in total) as the periodic unit. Geometry optimizations were first made using the Gaussian and plane-waves (GPW) method[34] with a plane-wave cutoff of 320 Ry, TZV2P GTH basis sets, and GTH pseudopotentials.[35,36] Subsequently, geometries were further optimized in an all-electron approach using the Gaussian-augmented plane-wave (GAPW) method[37] with a plane-wave cutoff of 250 Ry and TZV2P basis sets.[38] The **g** tensor calculations[39] were also performed using the GAPW method, with the same basis set and plane-wave cutoff, while the theoretical HFC tensors[40] were calculated in previous work.[9] A BLYP functional[41,42] was employed for all calculations. This method has been validated for ^{1}H HF tensor calculations in similar work on sucrose and has the advantage of including the environment in a more natural way compared to cluster calculations.[43] However, for **g** tensor calculations it has been shown by Neese et al.[44] and by Van Yperen-De Deyne et al.[45] that effective potential (V_{eff}) methods[46] fail in describing the exchange contribution of the two-electron spin−orbit interaction. The effective spin−orbit interaction includes the gradient of the exchange correlation functional v_{xc}, and it has first been demonstrated by Neese that this ∇v_{xc} term yields a contribution of approximately the same magnitude but with opposite sign compared to the exact exchange as calculated in the spin−orbit mean field (SOMF) approach, as implemented in ORCA. This shortcoming is circumvented by introducing a scaling approximation, where the small underestimated spin-other-orbit corrections were also taken into consideration. This issue has also been intensively investigated by Van Yperen-De Deyne et al., and the periodic CP2K code has been adapted in view of this scaling method (with a scaling factor $\sigma' = -2.8$), bringing the periodic DFT predictions close to SOMF and similar methods, available in nonperiodic codes.[44,47,48]

3. RESULTS AND DISCUSSION

A. Single Crystal EIE Study at 110 K. In order to extract the **g** tensors of the radicals T1, T2, and T3, we followed a procedure similar to that in ref 29, as outlined in Figures 2 and 3 of ref 49. EIE spectra were recorded at 110 K, the temperature at which our earlier ENDOR studies were conducted, monitoring the intensity of the $H_{\beta 1}$ proton coupling for T1 and the H_α coupling for T2 and T3 as a function of magnetic field strength in three rotation planes, where possible for the two symmetry related sites. Q-band ENDOR spectra at RT exhibited too low signal-to-noise ratio for recording EIE spectra. For EIE spectra that exhibited an approximately symmetric HF structure, the center of the pattern was used as data point. The combined error of determining this center and of possible differences between HF patterns recorded with EIE and EPR, due to the strongly different conditions of saturation in the two types of experiments, is estimated to be smaller than 0.15 mT (~2×10^{-4} in *g* value). The **g** tensors were then determined by least-squares error fitting of calculated resonance field positions from the first term in the spin Hamiltonian (1) to the experimental data. The best-fit principal *g* values and directions are listed in Table 1. The results of experiments and fittings are summarized in Figure 2: the final simulations match experiments very well, with root-mean-square errors of 6×10^{-5}, 7×10^{-5}, and 1×10^{-4} for T1, T2, and T3, respectively. For all three radicals, one principal *g* value is very close to g_e while the other two exhibit considerable positive shifts, as expected for carbon-centered radicals with delocalization of the unpaired electron onto (carbonyl and ring) oxygen. Similar shifts have been observed and reproduced by DFT calculations for semiquinone and tyrosyl radicals, whereas glycyl radicals,

The Journal of Physical Chemistry B Article

Table 1. g Tensors Determined from EIE Experiments at 110 K for T1−T3 in Irradiated Sucrose, Compared with Literature and DFT Results, Represented in the ⟨a*⟩, ⟨b⟩, ⟨c⟩ Crystal Reference Frame and All Related to the Same Site (I)[a]

		g	δg		δg*	⟨a*⟩	⟨b⟩	⟨c⟩	Δ
					Radical T1				
exp[b]	1	2.0021	−0.2	Iso.	2.23	0.3619	−0.9232	−0.1295	
	2	2.0049	2.6	Ax.	2.43	0.8781	0.2909	0.3798	
	3	2.0066	4.3	Rh.	0.70	−0.3130	−0.2512	0.9160	
exp[c] not analyzed									
exp[d]	1	2.00197	−0.33	Iso.	2.10				
	2	2.00466	2.36	Ax.	2.43				
	3	2.00658	4.28	Rh.	0.79				
DFT[b]	1	2.00232	0.002	Iso.	2.02	0.4612	−0.8855	−0.0560	7.4
	2	2.00458	2.260	Ax.	2.02	0.8244	0.4043	0.3962	7.3
	3	2.00612	3.802	Rh.	0.76	−0.3282	−0.2289	0.9165	1.4
					Radical T2				
exp[b]	1	2.0020	−0.3	Iso.	2.40	0.8367	−0.2505	0.4871	
	2	2.0054	3.1	Ax.	2.70	0.3042	0.9521	−0.0328	
	3	2.0067	4.4	Rh.	0.48	−0.4555	0.1756	0.8728	
exp[c]	1	2.0027	0.4	Iso.	2.47	0.882	0.187	0.435	25
	2	2.0049	2.6	Ax.	2.07	0.022	0.902	−0.432	28
	3	2.0067	4.4	Rh.	0.87	−0.472	0.391	0.790	13
exp[d]	1	2.00180	−0.50	Iso.	1.90				
	2	2.00400	1.70	Ax.	2.40				
	3	2.00680	4.50	Rh.	1.17				
DFT[b]	1	2.00212	−0.192	Iso.	2.08	0.8024	−0.2174	0.5557	4.8
	2	2.00498	2.659	Ax.	2.27	0.2645	0.9644	−0.0047	2.8
	3	2.00609	3.774	Rh.	0.49	−0.5349	0.1508	0.8313	5.3
					Radical T3				
exp[b]	1	2.0020	−0.3	Iso.	2.43	0.7428	−0.3772	0.5532	
	2	2.0055	3.2	Ax.	2.73	0.3363	0.9246	0.1790	
	3	2.0067	4.4	Rh.	0.44	−0.5790	0.0531	0.8136	
exp[c]	1	2.0027	0.4	Iso.	2.47	0.882	0.187	0.435	34
	2	2.0049	2.6	Ax.	2.07	0.022	0.902	−0.432	40
	3	2.0067	4.4	Rh.	0.87	−0.472	0.391	0.790	20
exp[d]	1	2.00200	−0.30	Iso.	2.12				
	2	2.00524	2.94	Ax.	2.42				
	3	2.00603	3.73	Rh.	0.33				
DFT[b]	1	2.00212	−0.192	Iso.	2.08	0.8024	−0.2174	0.5557	9.8
	2	2.00498	2.659	Ax.	2.27	0.2645	0.9644	−0.0047	11.5
	3	2.00609	3.774	Rh.	0.49	−0.5349	0.1508	0.8313	6.2

[a]Errors on the experimental principal values are estimated at ±0.0002 and ±0.0100 for the direction cosines. δg values are given in parts per thousand and angles between principal directions, Δ, in degrees, relative to our experimental results. [b]This study. [c]Reference 4. [d]Reference 6.

where delocalization onto neighboring oxygen is absent, do not exhibit such shifts.[50−53]

It is worth noting that the procedure followed here implicitly eliminates Schonland ambiguity,[54,55] which refers to the fact the **g** or **A** tensor fitting result of angular dependent EPR and ENDOR data, respectively, in three rotation planes may not be unique. In many cases, two tensors with distinct principal values and directions fit the data in these planes equally well, but only one of them—the actual tensor to be determined—also reproduces the angular variation outside these three planes. The origin of this ambiguity is an ambiguity in the crystal rotation sense. For crystals exhibiting monoclinic or orthorhombic symmetry, this is related to the site assignation in the rotation planes. In our previous studies of these centers, we solved the Schonland ambiguity for the HF tensors by measurements in additional rotation planes.[7,9] Hence, simulations allow assigning each branch of ENDOR transitions in each rotation plane unambiguously to one of the two sites, leaving no ambiguity in the assignation of the corresponding branches in the EIE angular dependences. The **g** and HF tensors corresponding to the largest coupling for each of these radicals are thus unambiguously related and refer to the same site. A site ambiguity remains for the smaller couplings, as will be discussed further on.

Figure 3 shows the experimental EIE spectra recorded for magnetic field orientations close to the ⟨a*⟩, ⟨b⟩, and ⟨c⟩ directions, along with simulated EPR HF patterns for the three radicals, using the **g** tensor data in Table 1 and the HF tensors in Table S1 of the Supporting Information. The overall agreement is very good, especially for the peak positions. It is not so surprising that EIE spectra do not perfectly reproduce the relative EPR line intensities of the simulations, as possible nonlinear effects of the magnetic field strength on the ENDOR frequencies are not considered in this technique. In addition, EPR and ENDOR signal intensities are governed by strongly different relaxation mechanisms, which may produce differences in line shapes as well.

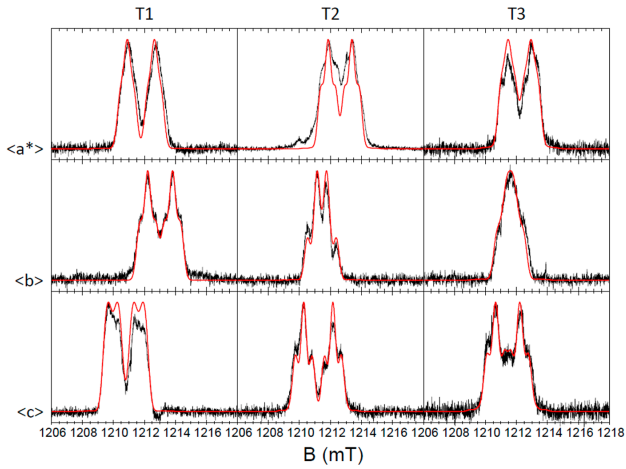

Figure 3. Comparison between experimental (black) and simulated (red) Q-band (34.00 GHz) single crystal EIE spectra in the ⟨*a**⟩, ⟨*b*⟩, and ⟨*c*⟩ crystal orientations. Simulations were performed using the **g** tensor data in Table 1 and the HF tensor data for three ^{1}H nuclei of each radical in Table S1. An isotropic residual line width of 0.48 mT has been used for the simulations.

Simulations for other orientations in the three rotation planes, displayed in Figure S1 of the Supporting Information, also lead to very convincing agreement, proving the validity of our **g** tensor analysis. Because also the smaller HF couplings are resolved, it is important for the simulations of these angular dependent spectra—and for simulations of powder spectra further on—that the **g** and all HF tensors refer to the same site. This connection between the tensors may in principle be established experimentally via EIE measurements on ENDOR lines of the smaller couplings or via General Triple spectroscopy,[28] but we have not systematically performed such experiments. We made the connection here via comparison with DFT calculations for the radicals,[8,9] which directly yield tensors related to the same site. The agreement between DFT calculated (see refs 8 and 9) and experimental HF tensors in Table S1 is so good that this can be done unambiguously. On some of the tensors published in refs 7 and 9, a symmetry transformation corresponding to a rotation over 180° around the ⟨*b*⟩ axis has been applied in order to match the DFT calculated direction cosines. We also verified that the combinations of tensors in Table S1 produce the best agreement between experimental EIE and simulated EPR spectra (see Figure S1).

In the EIE angular dependence of radical T2, for certain orientations in the (*bc*) plane (site II around 50°, e.g.), a fourth HF splitting appears to be resolved, which could not be extracted from the ENDOR analysis.[7] Very probably, this splitting corresponds to a smaller ^{1}H interaction of a more distant proton. DFT calculations (results not shown) indicate that the coupling with one of the protons hydrogen-bound to the radical may have the right order of magnitude. The presence of this extra splitting has little influence on determining the HF pattern centers, which are very well reproduced by the simulations.

B. Comparison with Earlier Literature Results and DFT Calculations of the g Tensors. In Table 1 our results for the **g** tensors are compared with those reported in the literature. Sagstuen et al. determined the **g** tensor for one of the radicals, deduced from Q-band EPR measurements on single crystals at RT.[4] Georgieva et al. determined **g** tensors for all three dominant radicals from multifrequency powder EPR measurements at variable temperature.[6] Principal directions are compared by calculating the angles Δ between corresponding direction cosines (always referred to our present experimental results). More than on absolute principal values, we focus on the deviations (δg, expressed in parts per thousand) from the free electron *g* value (g_e = 2.0023) and properties derived from these: the isotropic shift $\delta g_{iso} = (\delta g_1 + \delta g_2 + \delta g_3)/3$, the axial parameter $\delta g_{ax} = (\delta g_2 + \delta g_3)/3 - 2\delta g_1/3$, and the relative rhombicity $(\delta g_3 - \delta g_2)/\delta g_{ax}$, as for the three **g** tensors we determined $g_e \approx g_1 \ll g_2 < g_3$.

The comparison with the results of Sagstuen et al.[4] is most straightforward. As explained in ref 7, the radical for which the **g** tensor is determined in that paper most probably corresponds to T3, and certainly not to T1. Hence, we compare it here with T2 and T3. As in ref 8, a correction in the sign of certain principal direction cosines of the **g** tensor is applied before comparison with our present results. There is an obvious good agreement between the principal values of the tensors in the two studies, although the tensor we determined appears to be slightly more axial and considerably less rhombic than that earlier reported. The difference in the principal directions is more substantial. The agreement seems best with T2, but this may be fortuitous. The most plausible reason for this discrepancy is that determining the **g** tensor, especially its principal directions, from angular dependent composite EPR spectra is obviously more subject to errors than using EIE, where contributions of distinct radicals are isolated. A second source of discrepancy may be a previously reported slight temperature dependence of the spin Hamiltonian parameters of these radicals.[7] However, neither the single crystal spectra in the ⟨*a**⟩, ⟨*b*⟩, and ⟨*c*⟩ directions (see section 3.C and Figure 4)

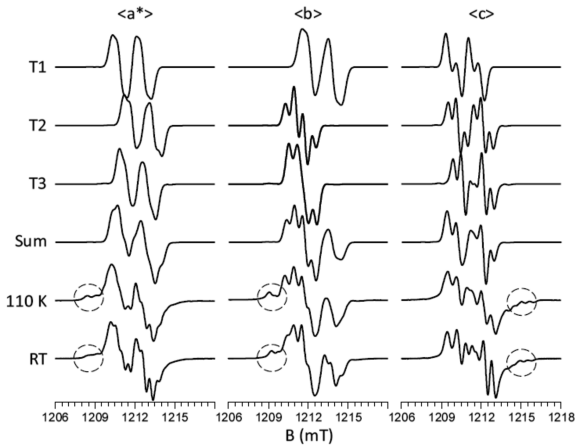

Figure 4. Comparison between experimental (recorded at 110 K and RT, modulation frequency 3 kHz, microwave power 9 μW at 110 K and 90 μW at RT) and simulated Q-band (34.00 GHz) single crystal EPR spectra in the ⟨a^*⟩, ⟨b⟩, and ⟨c⟩ crystal orientations. Simulations were performed using the **g** tensor data in Table 1 and HF tensor data for three ^{1}H nuclei of each radical in Table S1. The individual radical contributions are given anisotropic line widths with principal directions along the ⟨a^*⟩, ⟨b⟩, and ⟨c⟩ axes and principal values for T1: [17, 20, 15] MHz, and T2 and T3: [17, 16, 15] MHz. In the sum spectra T1:T2:T3 intensity ratios of 1:0.72:0.48 have been used. These values were determined via optimization of the agreement between simulated and experimental spectra by visual inspection.

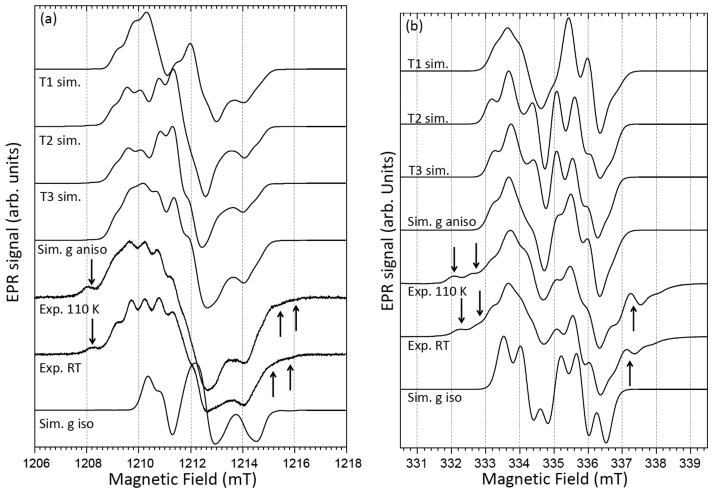

Figure 5. Q-band (a) and X-band (b) experimental powder EPR spectra at 110 K and RT, and simulations. In the sum spectra the three radicals have been attributed a weight ratio (T1:T2:T3) of 1:0.72:0.48, like in the single crystal. Wing lines not covered by the simulations are marked with arrows. All experimental spectra were recorded at a modulation frequency of 3 kHz. (a) Q-band spectra were normalized to 34.00 GHz and recorded at a low microwave power of 9 μW (110 K) and 90 μW (RT). For simulations, a line width tensor proportional (×0.9, close to 1) to that derived from the single crystal simulations was used. (b) X-band spectra were normalized to 9.40 GHz and recorded at low microwave powers of 20 μW (110 K) and 200 μW (RT). For the simulations a line width proportionality factor of 0.7 was used.

nor the powder spectra (see section 3D and Figure 5) exhibit significant changes in spectral line positions in the magnetic field region of the T1−T3 contribution. This strongly suggests that the temperature dependence of the **g** tensor of these radicals is very limited in the temperature range between 110 K and RT.

For the comparison with the results of Georgieva et al., we first note that the principal directions of the **g** tensors in that study are only given indirectly, via the Euler angles of the proton HF tensors of ref 5 in the **g** tensor reference frame of each radical. As the relative Euler angles of the HF tensors corresponding to a single radical are not consistent between refs 6 and 5, we cannot compute a single set of principal directions for these **g** tensors. Moreover, the principal HF tensor directions in ref 5 were later on shown to need substantial correction. For these reasons, only a comparison for the principal g values seems meaningful. Despite the aforementioned inconsistencies, for radical T1 the comparison is quite favorable: the isotropic value, axiality, and rhombicity are quite similar. For T2 and T3, when only comparing absolute principal values, one might at first glance also consider the agreement fair. Closer inspection of the g shifts and derived parameters, however, shows that for T2 the rhombicity reported in ref 6 is much larger than that for our results, whereas for T3 exactly the opposite is observed. Comparing the literature tensors[6] for T2 and T3, one observes that their largest g values and rhombicities differ quite substantially from each other. One would not expect this for radicals otherwise exhibiting very similar properties and sharing the same basic structure. Indeed, the **g** tensors we determined for T2 and T3 have practically the same principal values, but slightly different principal directions, like for their three ^{1}H HF tensors. This is consistent with the viewpoint that these are two slightly different conformations of the same radical structure. This already indicates that the **g** tensors determined in this work are more reliable, although the accuracy of their principal values may be further improved by experiments at higher microwave frequencies. The use of inaccurate HF tensors and the large number of fitting parameters used in the powder EPR simulations are obvious sources of errors in ref 6.

Finally, also reported in Table 1 are the results of periodic **g** tensor calculations for the two radical models valid for radicals T1 and T2/T3, respectively.[9,8] Very few accurate **g** tensors are available in the literature for carbon-centered radicals in sugars, for which also the radical model is well-established. One might thus consider the stable radicals in sucrose as benchmark systems for DFT calculations of **g** tensors on this class of substances. The overall agreement of the calculated **g** tensors with those we experimentally determined is remarkably good. Considering first the principal values, the DFT results underestimate the absolute values of δg by about 15%, resulting in a computed isotropic shift and axiality smaller than the experimental values found in this work. The rhombicity and principal directions of the experimental tensors, on the other hand, are very well reproduced by the calculations.

C. Single Crystal EPR Spectrum Simulations. In Figure 4 the EPR spectra in the $\langle a^* \rangle$, $\langle b \rangle$, and $\langle c \rangle$ orientations, recorded at 110 K, low microwave power (<10 μW), and low modulation frequencies (3 kHz) are compared to simulations including contributions of the three radicals. Although the EIE spectra can be reproduced very well by simulations (see Figures 3 and S1), the agreement for the EPR spectra is less good. The positions of resolved lines in the simulated spectra still correspond well with features in the experimental spectra, but the relative line intensities are not reproduced and certain lines in the experimental spectra have no counterpart in the simulations. A limited trial and error search for optimization indicated that the EPR line widths exhibit a weak anisotropy (best result line widths are given in the caption of Figure 4). It seems, however, doubtful that more extensive fitting of these parameters would considerably reduce the mismatch, which also prevents an accurate estimate of the relative contributions of the three radicals. Visual inspection of agreement between simulated and experimental spectra allowed us to determine that the (T2 + T3)/T1 intensity ratio ranges between 0.9 and 1.7 and the T2/T3 ratio between 1 and 3. Simulations using optimum ratios of (T2 + T3)/T1 = 1.2 and T2/T3 = 1.5 are shown in Figure 4, along with the calculated individual contributions of the three radical species in each orientation.

In view of the good reproduction of the EIE spectra, the discrepancies between simulated and experimental single crystal spectra EPR are rather unexpected. Although it is hard to exclude that the observed deviations are not in part instrumental or due to (small) crystal misalignments, it is clear that certain parts of the spectra (indicated with circles in Figure 4) cannot be covered by simulations with the radicals analyzed till now. This shows that still other radicals contribute to the EPR spectrum in a non-negligible way, in agreement with the results of earlier statistical decomposition studies of the EPR spectra of irradiated sucrose powder.[5]

In order to assess the temperature dependence of the spectra and the validity of the spin Hamiltonian parameters here determined for simulation of powder spectra at RT, the single crystal EPR spectra in the $\langle a^* \rangle$, $\langle b \rangle$, and $\langle c \rangle$ orientations (3 kHz modulation frequency and 90 μW power) have also been recorded at RT and are shown in the bottom line of Figure 4. The positions of the most prominent transitions (in the 1210−1215 mT range) hardly exhibit any shift, whereas the HF interactions seem to be slightly better resolved at RT. This suggests that neither the **g** nor the HF tensors of T1−T3 exhibit strong temperature dependence in this range.

D. Powder EPR Spectrum Simulations. In the following we concentrate on powder EPR spectra of irradiated sucrose, as these are the most relevant for applications in dosimetry and irradiation of sugar-containing foodstuffs. As the single crystal analysis was performed at Q-band microwave frequencies, we will first focus on this frequency band. Next, the X-band spectrum will be dealt with, because for applications the EPR spectra are most often recorded in this band. In these two bands, both the 110 K and the RT spectra are recorded and compared with the simulations. In view of the above-mentioned limited temperature dependence of the single-crystal EPR spectra, one may expect that knowledge of the spin Hamiltonian parameters of T1−T3 at 110 K also allows understanding the powder EPR spectrum at RT, which is most relevant for applications. We have also simulated the powder spectra in higher microwave frequency bands, in which spectra have previously been recorded.[6] As we have no direct access to these spectra, the latter simulations are given in the Supporting Information (Figure S2).

The **g** and HF tensors determined in our single crystal studies (section 3A) are used as fixed input parameters for the simulations. A large number of parameters ($\sim$ 20) could in principle still be varied in order to fit the simulated spectra to experiment: principal values and directions of an anisotropic line width tensor—resulting from natural line broadening, unresolved HF interactions, and/or strain in the g and HF parameters—line shapes for each radical, and the relative contributions of the three radicals. We have explicitly chosen not to fit these parameters. All simulations presented in this section have been performed assuming the same radical intensity ratios as for the single crystal simulations. Variations

of the relative radical concentrations, that were not attempted here, may lead to slight further improvement of the agreement between experimental and simulated spectra and could result from differences in the crystal size, the radiation dose (rate), and postradiation history. The anisotropic line width parameters in the Q- and X-band simulations have been chosen to be proportional to those in the single crystal simulations, with the single proportionality factor (the same for the three radicals) being the only free parameter in the simulations, determined by visual inspection of the agreement between experimental and simulated spectra. For the Q-band simulation, the line width proportionality factor is found to be close to 1. The smaller factor necessary for the X-band simulations very probably indicates that part of the residual EPR line width is due to strain in the g values.

Parts a and b of Figure 5 show the Q-band and X-band spectra, respectively. They are organized in the same way: the top three spectra represent the simulations for the individual radical components, taking the anisotropy of their **g** tensors into account, and the fourth spectrum shows the weighed sum of these spectra. The fifth and sixth traces from the top display the experimental spectra at 110 K and RT, respectively. These spectra were recorded at low microwave power and low modulation frequency (see caption). Finally, the bottom traces show simulations ignoring the g anisotropy of the radicals, i.e. by taking the average g value of each radical as the isotropic g value in the simulations.

From the comparison of 110 K, RT, and simulated powder spectra, we conclude the following:

(1) Similarly as in the single crystal spectra, the main changes in the central part of the spectra between 110 K and RT appear to be that the HF structure is better resolved at RT.

(2) The simulations including g anisotropy reproduce the experimental spectra, both at 110 K and at RT, quite well, especially considering that only one parameter has been optimized. Hence, knowledge of the spin Hamiltonian parameters of the dominant stable radicals in irradiated sucrose does allow understanding the essential characteristics of its powder EPR spectra.

(3) Knowledge of the **g** tensor for these radicals, with delocalization of spin density onto (carbonyl and ring) oxygen atoms, is essential in the powder EPR simulations. Ignoring the g anisotropy leads to an obvious mismatch at Q-band but, perhaps more surprisingly, even at X-band microwave frequencies, important for dosimetry applications. Simulations at higher frequencies (see Supporting Information, Figure S2) show that the basic characteristics of the stable high-field EPR spectra of irradiated sucrose may also be understood using the **g** tensors deduced in this work, keeping, of course, in mind the limited accuracy of their principal values, determined at 34 GHz.

(4) In the wings of the X- and Q-band EPR spectra, clear evidence is seen of as-yet unidentified radical components. These, most probably, also have a non-negligible contribution to the central part of the EPR spectra. A deeper understanding of these extra components should allow a considerably better reproduction of the complete EPR spectrum of irradiated sucrose and an accurate quantification of the relative radical contributions. This presents a strong motivation for characterizing and structurally identifying these components, combining ENDOR and EIE spectroscopy with DFT calculations. The study of these radicals falls outside the scope of the present paper, however.

4. CONCLUSIONS

We determined the **g** tensors for the three stable radical species that dominate the EPR spectrum of irradiated sucrose, from angular dependent EIE measurements at 110 K on single crystals. On the basis of the very good reproduction of the single crystal EIE spectra, we are confident that the principal values and directions, axiality and rhombicity of these tensors are more reliable than those published earlier. The accuracy of the principal values is, of course, limited by the microwave frequency at which the study was performed and single crystals studies at higher frequencies may further improve these. DFT calculated **g** tensors for the previously established models for these radicals are in the best agreement one may expect (principal g values within roughly 15%) with the tensors we determined here, the agreement in principal directions even being excellent. Simulations at X- and Q-band frequencies reproduce the experimental powder EPR spectra recorded at 110 K and RT fairly well, especially considering the fact that only one line width parameter was optimized and that non-negligible radical contributions, clearly evident in the wings of the spectra, but also influencing the shape of the central part, are not taken into account. Knowledge of the spin Hamiltonian parameters of the radicals T1−T3 does allow understanding of the main characteristics of the dosimetric sucrose EPR spectrum. This motivates a thorough spectroscopic and DFT study of the still unidentified components in order to understand this dosimetric spectrum fully. The present study has shown that the **g** tensor information is crucial for obtaining reliable powder EPR simulations of these radicals, even at the low X-band microwave frequencies. From a more general perspective, we also demonstrated that when using literature spin Hamiltonian data for simulating angular dependent single crystal and powder EPR spectra of radicals in similar systems, it is important to bear Schonland and radical site ambiguities in mind.

■ ASSOCIATED CONTENT

Ⓢ Supporting Information

g and hyperfine tensors, all referring to the same radical site, for T1−T3, used in the single crystal EPR simulations in Figures 3−7 and S1. Experimental EIE and simulated EPR spectra for radicals T1−T3 as a function of rotation angle in three rotation planes. Simulation of the powder EPR spectrum of irradiated sucrose at 94, 190, and 285 GHz. This material is available free of charge via the Internet at http://pubs.acs.org.

■ AUTHOR INFORMATION

Corresponding Author

*E-mail: Henk.Vrielinck@UGent.be. Telephone: +32 9 264 4356. Fax: +32 0 264 4996.

Notes

The authors declare no competing financial interest.

■ ACKNOWLEDGMENTS

The authors thank the Research Foundation Flanders (FWO-Vlaanderen) for financial support. H.D.C. acknowledges a Postdoctoral Fellowship with the same organization. A.V.Y.-

D.D. acknowledges a Ph.D. scholarship of the Research Board of Ghent University. The computational resources and services used were provided by Ghent University (Stevin Supercomputer Infrastructure).

REFERENCES

(1) Shields, H.; Hamrick, P. X-Irradiation Damage of Sucrose Single Crystal. *J. Chem. Phys.* **1962**, *37*, 202−203.

(2) Lomaglio, G. Résonance Paramagnétique Electronique et Susceptibilité Paramagnétique d'un Monocristal de Saccharose Irradié. *C. R. Seances Acad. Sci., Ser. B* **1967**, *264*, 1637.

(3) Gräslund, A.; Löfroth, G. Free-Radicals in Gamma-Irradiated Single-Crystals of Trehalose Dihydrate and Sucrose Studied by Eelectron-Paramagnetic Resonance. *Acta Chem. Scand., Ser. B* **1975**, *29*, 475−482.

(4) Sagstuen, E.; Lund, A.; Awadelkarim, O.; Lindgren, M.; Westerling, J. Free-Radicals in X-Irradiated Single-Crystals of Sucrose—A Reexamination. *J. Phys. Chem.* **1986**, *90*, 5584−5588.

(5) Vanhaelewyn, G.; Sadlo, J.; Callens, F.; Mondelaers, W.; De Frenne, D.; Matthys, P. A Decomposition Study of the EPR Spectrum of Irradiated Sucrose. *Appl. Radiat. Isot.* **2000**, *52*, 1221−1227.

(6) Georgieva, E. R.; Pardi, L.; Jeschke, G.; Gatteschi, D.; Sorace, L.; Yordanov, N. D. High-Field/High-Frequency EPR Study on Stable Free Radicals Formed in Sucrose by Gamma-Irradiation. *Free Radical Res.* **2006**, *40*, 553−563.

(7) De Cooman, H.; Pauwels, E.; Vrielinck, H.; Dimitrova, A.; Yordanov, N. D.; Sagstuen, E.; Waroquier, M.; Callens, F. Radiation-Induced Defects in Sucrose Single Crystals, Revisited: A Combined Electron Magnetic Resonance and Density Functional Theory Study. *Spectrochim. Acta A* **2008**, *69*, 1372−1383.

(8) De Cooman, H.; Pauwels, E.; Vrielinck, H.; Sagstuen, E.; Callens, F.; Waroquier, M. Identification and Conformational Study of Stable Radiation-Induced Defects in Sucrose Single Crystals Using Density Functional Theory Calculations of Electron Magnetic Resonance Parameters. *J. Phys. Chem. B* **2008**, *112*, 7298−7307.

(9) De Cooman, H.; Pauwels, E.; Vrielinck, H.; Sagstuen, E.; Van Doorslaer, S.; Callens, F.; Waroquier, M. ENDOR and HYSCORE Analysis and DFT-Assisted Identification of the Third Major Stable Radical in Sucrose Single Crystals X-Irradiated at Room Temperature. *Phys. Chem. Chem. Phys.* **2009**, *11*, 1105−1114.

(10) De Cooman, H.; Pauwels, E.; Vrielinck, H.; Sagstuen, E.; Waroquier, M.; Callens, F. Oxidation and Reduction Products of X Irradiation at 10 K in Sucrose Single Crystals: Radical Identification by EPR, ENDOR, and DFT. *J. Phys. Chem. B* **2010**, *114*, 666−674.

(11) De Cooman, H.; Vanhaelewyn, G.; Pauwels, E.; Sagstuen, E.; Waroquier, M.; Callens, F. Radiation-Induced Radicals in Glucose-1-phosphate. I. Electron Paramagnetic Resonance and Electron Nuclear Double Resonance Analysis of in situ X-Irradiated Single Crystals at 77 K. *J. Phys. Chem. B* **2009**, *112*, 15045−15053.

(12) Pauwels, E.; De Cooman, H.; Vanhaelewyn, G.; Sagstuen, E.; Callens, F.; Waroquier, M. Radiation-Induced Radicals in Glucose-1-phosphate. II. DFT Analysis of Structures and Possible Formation Mechanisms. *J. Phys. Chem. B* **2009**, *112*, 15054−15063.

(13) Von Sonntag, C. *Free-radical-induced DNA damage and its repair—A chemical perspective*; Springer-Verlag: Berlin, 2006.

(14) Nakajima, T. Sugar as an Emergency Populace Dosimeter for Radiation Accidents. *Health Phys.* **1988**, *55*, 951−955.

(15) Nakajima, T. Possibility of Retrospective Dosimetry for Persons Accidentally Exposed to Ionizing-Radiation Using Electron-Spin Resonance of Sugar and Mother-of-Pearl. *Br. J. Radiol.* **1989**, *62*, 148−153.

(16) Silveira, F. A. M.; Baffa, O. Lyoluminescence and ESR Measurements on Alanine and Sucrose Dosimeters. *Appl. Radiat. Isot.* **1995**, *46*, 827−830.

(17) Son, P. K.; Ok, C. I.; Kim, J. W. EPR Study of Sugar Irradiated with X-Rays. *J. Korean Phys. Soc.* **2001**, *38*, 315−317.

(18) Yordanov, N. D.; Gancheva, V.; Georgieva, E. EPR and UV Spectroscopic Study of Table Sugar as a High-Dose Dosimeter. *Radiat. Phys. Chem.* **2002**, *65*, 269−276.

(19) Yordanov, N. D.; Georgieva, E. EPR and UV Spectral Study of Gamma-Irradiated White and Burned Sugar, Fructose and Glucose. *Spectrochim. Acta A* **2004**, *60*, 1307−1314.

(20) Desrosiers, M.; Wadley, S. Time Dependence of the Radiation-Induced EPR Signal in Sucrose. *Radiat. Prot. Dosim.* **2006**, *118*, 479−481.

(21) Trompier, F.; Bassinet, C.; Wieser, A.; De Angelis, C.; Viscomi, D.; Fattibene, P. Radiation-Induced Signals Analysed by EPR Spectrometry Applied to Fortuitous Dosimetry. *Ann. Ist. Super. Sanita* **2009**, *45*, 287−296.

(22) Karakirova, Y.; Yordanov, N. D.; De Cooman, H.; Vrielinck, H.; Callens, F. Dosimetric Characteristics of Different Types of Saccharides: An EPR and UV Spectrometric Study. *Radiat. Phys. Chem.* **2010**, *79*, 654−659.

(23) Vrielinck, H.; De Cooman, H.; Karakirova, Y.; Yordanov, N. D.; Callens, F. Early-Stage Evolution of the EPR Spectrum of Crystalline Sucrose at Room Temperature after High-Dose X Irradiation. *Radiat. Res.* **2009**, *172*, 226−233.

(24) Helle, N.; Linke, B.; Magern, M.; Schreiber, G.; Bogl, K. W. Evaluation of the Electron-Spin-Resonance Technique for the Detection of Irradiated Foofstuffs. *Z. Ernaehrungswiss.* **1992**, *31*, 205−218.

(25) Raffi, J.; Stevenson, M. H.; Kent, M.; Thiery, J. M.; Belliardo, J.-J. European Intercomparison on Electron-Spin-Resonance Identification of Irradiated Foodstuffs. *Int. J. Food Sci. Technol.* **1992**, *27*, 111−124.

(26) Desrosiers, M. F. Current Status of the EPR Method to Detect Irradiated Food. *Appl. Radiat. Isot.* **1996**, *47*, 1621−1628.

(27) Yordanov, N. D.; Pachova, Z. Gamma-Irradiated Dry Fruits—An Example of a Wide Variety of Long-Time Dependent EPR Spectra. *Spectrochim. Acta A* **2006**, *63*, 891−895.

(28) Spaeth, J.-M.; Niklas, J. R.; Bartram, R. H. *Structural analysis of point defects in solids—An introduction to multiple magnetic resonance spectroscopy*; Springer-Verlag: Berlin-Heidelberg, 1992.

(29) Kang, J.; Tokdemir, S.; Shao, J.; Nelson, W. H. Electronic g-Factor Measurement from ENDOR-Induced EPR Patterns: Malonic Acid and Guanine Hydrochloride Dehydrate. *J. Magn. Reson.* **2003**, *165*, 128−136.

(30) Brown, G. M.; Levy, H. A. Further Refinement of Structure of Sucrose Based on Neutron-Diffraction Data. *Acta Crystallogr., Sect. B: Struct. Sci.* **1973**, *29*, 790−797.

(31) Serway, R. A.; Marshall, S. A. Electron Spin Resonance Absorption Spectra of CO_3^- and CO_3^{3-} Molecule-Ions in Irradiated Single-Crystal Calcite. *J. Chem. Phys.* **1967**, *46*, 1949−1952.

(32) Stoll, S.; Schweiger, A. EasySpin, a Comprehensive Software Package for Spectral Simulation and Analysis in EPR. *J. Magn. Reson.* **2006**, *178*, 42−55.

(33) Lippert, G.; Hutter, J.; Parrinello, M. A Hybrid Gaussian and Plane Wave Density Functional Scheme. *Mol. Phys.* **1997**, *92*, 477−487.

(34) VandeVondele, J.; Krack, M.; Mohamed, F.; Parinello, M.; Chassaing, T.; Hutter, J. QUICKSTEP: Fast and Accurate Density Functional Calculations Using a Mixed Gaussian and Plane Waves Approach. *Comput. Phys. Commun.* **2005**, *167*, 103−128.

(35) Goedecker, S.; Teter, M.; Hutter, J. Separable Dual-Space Gaussian Pseudopotentials. *Phys. Rev. B* **1996**, *54*, 1703−1710.

(36) Hartwigsen, C.; Goedecker, S.; Hutter, J. Relativistic Separable Dual-Space Gaussian Pseudopotentials from H to Rn. *J. Phys. Rev. B* **1998**, *58*, 3641−3662.

(37) Lippert, G.; Hutter, J.; Parrinello, M. The Gaussian and Augmented-Plane-Wave Density Functional Method for Ab Initio Molecular Dynamics Simulations. *Theor. Chem. Acc.* **1999**, *103*, 124−140.

(38) Krishnan, R.; Binkley, J. S.; Seeger, R.; Pople, J. A. Self-Consistent Molecular-Orbital Methods 0.20. Basis Set for Correlated Wave-Functions. *J. Chem. Phys.* **1980**, *72*, 650−654.

(39) Weber, V.; Iannuzzi, M.; Giani, S.; Hutter, J.; Declerck, R.; Waroquier, M. Magnetic Linear Response Properties Calculations with the Gaussian and Augmented-Plane-Wave Method. *J. Chem. Phys.* **2009**, *131*, No. 014106.
(40) Declerck, R.; Van Speybroeck, V.; Waroquier, M. First-Principles Calculations of Hyperfine Parameters with the Gaussian and Augmented-Plane-Wave Method: Application to Radicals Embedded in a Crystalline Environment. *Phys. Rev. B* **2006**, *74*, No. 245103.
(41) Becke, A. D. Density-Functional Exchange-Energy Approximation with Correct Asymptotic-Behavior. *Phys. Rev. A* **1988**, *38*, 3098−3100.
(42) Lee, C.; Yang, W.; Parr, R. Development of the Colle-Salvetti Correlation-Energy Formula into a Functional of the Electron-Density. *Phys. Rev. B* **1988**, *37*, 785−789.
(43) Pauwels, E.; Asher, J.; Kaupp, M.; Waroquier, M. Cluster or Periodic, Static or Dynamic-the Challenge of Calculating the g Tensor of the Solid-State Glycine Radical. *Phys. Chem. Chem. Phys.* **2011**, *13*, 18638−18646.
(44) Neese, F. Efficient and Accurate Approximations to the Molecular Spin-Orbit Coupling Operator and their Use in Molecular g-Tensor Calculations. *J. Chem. Phys.* **2005**, *122*, No. 034107.
(45) Van Yperen-De Deyne, A.; Pauwels, E.; Van Speybroeck, V.; Waroquier, M. Accurate Spin-Orbit and Spin-Other-Orbit Contributions to the g-Tensor for Transition Metal Containing Systems. *Phys. Chem. Chem. Phys.* **2012**, *14*, 10690−10704.
(46) Schreckenbach, G.; Ziegler, T. Calculation of the g-Tensor of Electron Paramagnetic Resonance Spectroscopy using Gauge-Including Atomic Orbitals and Density Functional Theory. *J. Phys. Chem. A* **1997**, *101*, 3388−3399.
(47) Kaupp, M.; Reviakine, R.; Malkina, O. L.; Arbuznikov, A.; Schimmelpfennig, B.; Malkin, V. G. Calculation of Electronic g-Tensors for Transition Metal Complexes Using Hybrid Density Functionals and Atomic Meanfield Spin-Orbit Operators. *J. Comput. Chem.* **2002**, *23*, 794−803.
(48) Malkin, V. G.; Malkina, O. L.; Reviakine, R.; Arbouznikov, A. V.; Kaupp, M.; Schimmelpfennig, B.; Malkin, I.; Helgaker, T.; Ruud, K. MAG-Respect, Version 1.2 (2003).
(49) Tarpan, M. A.; Vrielinck, H.; De Cooman, H.; Callens, F. Determination of the g Tensors for the Dominant Stable Radicals in X-Irradiated beta-D-Fructose Single Crystals. *J. Phys. Chem. A* **2009**, *113*, 7994−8000.
(50) Kaupp, M.; Remenyi, C.; Vaara, J.; Malkina, O. L.; Malkin, V. G. Density Functional Calculations of Electronic g-Tensors for Semiquinone Radical Anions. The Role of Hydrogen Bonding and Substituent Effects. *J. Am. Chem. Soc.* **2002**, *124*, 2709−2722.
(51) Jeschke, G. EPR Techniques for Studying Radical Enzymes. *Biochim. Biophys. Acta* **2005**, *1707*, 91−102.
(52) Un, S. The g-Values and Hyperfine Coupling of Amino Acid Radicals in Proteins: Comparison of Experimental Measurements with Ab Initio Calculations. *Magn. Reson. Chem.* **2005**, *43*, S229−S236.
(53) Svistunenko, D. A.; Jones, G. A. Tyrosyl Radicals in Proteins: A Comparison of Empirical and Density Functional Calculated EPR Parameters. *Phys. Chem. Chem. Phys.* **2009**, *11*, 6600−6613.
(54) Schonland, D. S. On the Determination of the Principal g-Values in Electron Spin Resonance. *Proc. Phys. Soc. London* **1959**, *73*, 788−792.
(55) Vrielinck, H.; De Cooman, H.; Tarpan, M. A.; Sagstuen, E.; Waroquier, M.; Callens, F. Schonland Ambiguity in the Electron Nuclear Double Resonance Analysis of Hyperfine Interactions: Principles and Practice. *J. Magn. Reson.* **2008**, *195*, 196−205.

		g	δg		δg*	$\langle a* \rangle$	$\langle b \rangle$	$\langle c \rangle$	Δ
Exp.	1	2.0021	-0.2	Iso.	2.23	0.3619	-0.9232	-0.1295	
	2	2.0049	2.6	Ax.	2.43	0.8781	0.2909	0.3798	
	3	2.0066	4.3	Rh.	0.7	-0.313	-0.2512	0.916	
DFT	1	2.00246	0.16	Iso.	2.82	0.4597	-0.8861	-0.0595	7
	2	2.00542	3.12	Ax.	2.66	0.8307	0.4054	0.3815	7
	3	2.00749	5.19	Rh.	0.78	-0.3139	-0.2248	0.9225	2
DFT	1	2.00232	0.002	Iso.	2.02	0.4612	0.8855	-0.056	7.4
σ=-2.8	2	2.00458	2.26	Ax.	2.02	0.8244	-0.4043	0.3962	7.3
	3	2.00612	3.802	Rh.	0.76	-0.3282	0.2289	0.9165	1.4

Table V.1: Experimental and computational determined g-tensor for the T1 radical

		g	δg		δg*	$\langle a* \rangle$	$\langle b \rangle$	$\langle c \rangle$	Δ
Exp.	1	2.002	-0.3	Iso.	2.4	0.8367	-0.2505	0.4871	
	2	2.0054	3.1	Ax.	2.7	0.3042	0.9521	-0.0328	
	3	2.0067	4.4	Rh.	0.48	-0.4555	0.1756	0.8728	
DFT	1	2.0022	-0.1	Iso.	2.89	0.8032	-0.2221	0.5528	5
	2	2.00597	3.67	Ax.	2.99	0.2476	0.9684	0.0295	5
	3	2.00739	5.09	Rh.	0.48	-0.5419	0.1132	0.8328	7
DFT	1	2.00212	-0.192	Iso.	2.08	0.8024	-0.2174	0.5557	4.8
σ=-2.8	2	2.00498	2.659	Ax.	2.27	0.2645	0.9644	-0.0047	2.8
	3	2.00609	3.774	Rh.	0.49	-0.5349	0.1508	0.8313	5.3

Table V.2: Experimental and computational determined g-tensor for the T2 radical

		g	δg		δg*	$\langle a* \rangle$	$\langle b \rangle$	$\langle c \rangle$	Δ
Exp.	1	2.002	-0.3	Iso.	2.43	0.7428	-0.3772	0.5532	
	2	2.0055	3.2	Ax.	2.73	0.3363	0.9246	0.179	
	3	2.0067	4.4	Rh.	0.44	-0.579	0.0531	0.8136	
DFT	1	2.0022	-0.1	Iso.	2.89	0.8032	-0.2221	0.5528	10
	2	2.00597	3.67	Ax.	2.99	0.2476	0.9684	0.0295	10
	3	2.00739	5.09	Rh.	0.48	-0.5419	0.1132	0.8328	4
DFT	1	2.00212	-0.192	Iso.	2.08	0.8024	-0.2174	0.5557	9.8
σ=-2.8	2	2.00498	2.659	Ax.	2.27	0.2645	0.9644	-0.0047	11.5
	3	2.00609	3.774	Rh.	0.49	-0.5349	0.1508	0.8313	6.2

Table V.3: Experimental and computational determined g-tensor for the T3 radical

Paper VI

Automated generation of radical species in crystalline carbohydrate using ab initio MD simulations

S. G. Aalbergsjø, E. Pauwels, A. Van Yperen-De Deyne, V. Van Speybroeck and E. Sagstuen *Physical Chemistry Chemical Physics*, **16**, 17196–17205 (2014)

PCCP

PAPER

Automated generation of radical species in crystalline carbohydrate using *ab initio* MD simulations†

Cite this: *Phys. Chem. Chem. Phys.*, 2014, **16**, 17196

Siv G. Aalbergsjø,*[a] Ewald Pauwels,[b] Andy Van Yperen-De Deyne,[c] Veronique Van Speybroeck[c] and Einar Sagstuen[a]

Received 19th May 2014,
Accepted 26th June 2014

DOI: 10.1039/c4cp02179g

www.rsc.org/pccp

As the chemical structures of radiation damaged molecules may differ greatly from their undamaged counterparts, investigation and description of radiation damaged structures is commonly biased by the researcher. Radical formation from ionizing radiation in crystalline α-L-rhamnose monohydrate has been investigated using a new method where the selection of radical structures is unbiased by the researcher. The method is based on using *ab initio* molecular dynamics (MD) studies to investigate how ionization damage can form, change and move. Diversity in the radical production is gained by using different points on the potential energy surface of the intact crystal as starting points for the ionizations and letting the initial velocities of the nuclei after ionization be generated randomly. 160 *ab initio* MD runs produced 12 unique radical structures for investigation. Out of these, 7 of the potential products have never previously been discussed, and 3 products are found to match with radicals previously observed by electron magnetic resonance experiments.

1. Introduction

A procedure for automatic generation of radical products using *ab initio* molecular dynamics (MD) simulations has been applied to carbohydrates in the solid state. The necessity for such a procedure originates in the need for describing and understanding radical formation in molecular systems as a consequence of exposure to ionizing radiation. Ionizing radiation yields mainly one-electron reduction and oxidation products, usually in the form of charged primary radical species. These interact with molecules in their environment and will then participate in chemical reactions, forming new, more stable and often electrically neutral radical species. In spite of the large number of different radicals potentially formed upon exposure to ionizing radiation, only a handful of stable radicals are observed.[1] This selectivity is of interest since it allows better understanding and therefore prediction of the effect ionizing radiation will have on bio molecular systems.

An important experimental technique for obtaining knowledge about radiation induced damage is the use of electron magnetic resonance (EMR) measurements as they enable studies of the radical species without the disturbance from the undamaged surrounding molecular structures. But although there are sturdy methods for determining radical structures based on the magnetic properties of the radicals, sometimes experimental data do not clearly fit in these types of models.[2–5] At this point the use of quantum mechanical calculations such as density functional theory (DFT) has proved to be an essential tool for exploring and evaluating different radical structures.[6]

Irradiating a single molecular substance may lead to a plethora of radical structures. These radicals are often descendent from different electronically excited states as the irradiation delivers large amounts of energy locally. The radicals formed may also be largely influenced by their environment. A simple geometry optimization with DFT starting with the doublet ground state is not able to access different minima of the potential energy surface which are well separated. Manual input by manipulating the geometrical structures is required in order to describe different radicals. This is most often done by (re)moving hydrogen atoms or breaking bonds manually, but even then the theoretician is sometimes at a loss to describe all of the radicals formed.[3–5] In this respect, a bias of experimentalists or theoretician's view of what radicals are most likely can lead to incomplete investigations. Therefore an unbiased procedure is desirable in order to be open to all suggestions.

Previously, Tachikawa and co-workers have used femtosecond *ab initio* molecular dynamics simulations to investigate

[a] *Department of Physics, University of Oslo, P. O. Box 1048 Blindern, N-0316, Oslo, Norway. E-mail: s.g.aalbergsjo@fys.uio.no*
[b] *UGent HPC, Ghent University, Krijgslaan 281 S9, B-9000 Gent, Belgium*
[c] *Center for Molecular Modeling, Ghent University, Technologiepark 903, B-9052 Zwijnaarde, Belgium*

† Electronic supplementary information (ESI) available. See DOI: 10.1039/c4cp02179g

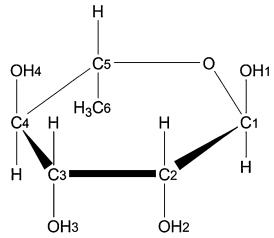

Fig. 1 Chemical structure and atomic numbering scheme of α-L-rhamnose.

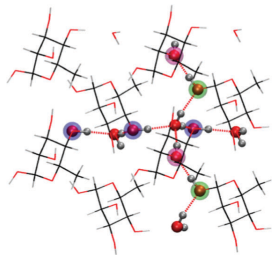

Fig. 2 Illustration of hydrogen bond scheme in α-L-rhamnose monohydrate single crystals. Two chains of hydrogen bonds are marked in dotted red. O4 positions are marked in blue, O1 positions are marked in green and O2 positions are marked in magenta. The two hydrogen bond chains intersect at a water molecule.

radiation induced radical production for small biomolecules and water clusters in the gas phase.[7,8] The formation of radical structures is initiated by adding or removing an electron to the neutral structure, thus mimicking the ionization by *e.g.* X-rays. In the present work, the method of Tachikawa *et al.* has been further developed in order to generate large numbers of different radical structures in solid state systems. Using different geometrical conformations and velocity distributions for the atomic nuclei as starting points for the ionization, several kinds of radical structures were modeled. The staring points were collected from an MD simulation of the neutral crystal structure.

The system studied is the α-L-rhamnose carbohydrate crystal, simulated using DFT and periodic boundary conditions (PBC). α-L-Rhamnose (Fig. 1) is known to have a rich radiation chemistry which has been studied previously by EMR spectroscopy[9–12] and DFT simulations both in a cluster approach and using PBC.[13–16] Four different EMR-characterized radical molecular species are reported in the literature, one alkoxy radical[10,11] and three hydroxy alkyl radicals.[9,12] But so far all exploration of possible radical structures has been performed by the researcher's bias in suggesting radical structures with rather small geometrical changes, focusing on deprotonation or H-atom abstraction at different positions. In particular no structures containing a broken ring have been studied.

2. Model system and computational details

The crystallographic unit cell of α-L-rhamnose monohydrate is monoclinic with dimensions a = 7.901 Å, b = 7.922 Å, c = 6.670 Å and β = 95.521°.[17] There are two asymmetric units per crystallographic unit cell, each consisting of one rhamnose molecule and one water molecule. The crystalline water molecules contribute to form two infinite hydrogen bond chains through the crystal structure along with hydroxyl groups of the rhamnose molecules, see Fig. 2. One chain is along the b-direction of the crystal $[O4–H–Ow–H–]_\infty$ and the other is along the c-direction $[O1–H–O2–H–Ow–H–]_\infty$. These two chains are intersecting at the water molecules, and are consequently connected. They have previously been found to play an important role for the selectivity of oxidative radical formation in this crystal.[13] To properly include this important feature and to separate radical fragments from their images in the periodic calculations, the crystallographic unit cell was doubled in all directions, yielding a $\langle 2a2b2c \rangle$ supercell containing 416 atoms.

All calculations were performed with the CP2K program[18] and periodic boundary conditions, using the BLYP functional.[19,20] Geometry optimizations and MD runs were performed using the Gaussian and plane wave (GPW) method[21,22] in which only valence electrons are treated explicitly and the atomic nuclei and core electrons are modeled by GTH pseudo-potentials.[23–25] The DZVP-GTH basis was used and the plane wave cutoff was set to 400 Ry. All MD calculations were performed within an NVT ensemble, relying on a canonical sampling through velocity rescaling (CSVR) thermostat[26] with a time constant of 10 fs to ensure fast thermal equilibration. Throughout all MD simulations, Mulliken population analysis was used to determine and follow shifts in the spin distribution in each system.

A diagram of the computational sequence is shown in Fig. 3. The neutral crystallographic $\langle 2a2b2c \rangle$ supercell of rhamnose was optimized and then subject to MD simulations: the structure was first equilibrated to 300 K for 4.4 ps, the run was continued for another 0.5 ps from which 10 geometries were extracted, one every 0.05 ps. These were used as starting points for further MD simulations on charged/damaged systems. For each of the 10 geometries, 16 2-ps MD simulations (Δt = 0.5 fs) were performed: 8 with a cationic (charge +1, spin 1/2) configuration and 8 with an anionic (charge −1, spin 1/2) configuration, equilibrating half of them to 100 K and the other half to 200 K. Altogether 160 *ab initio* MD runs were performed on charged systems. Variety between the MD runs that started from the same initial geometry was introduced by randomly assigning velocities to the nuclei in the first step of the MD run.

The radicals formed in these MD runs were classified according to initial charge, location of the radical center and chemical structure. For each of the resulting radical type one representative structure was chosen for geometry optimization followed by computation of hyperfine coupling (hfc) tensors. To calculate these EMR properties, the augmented plane wave method[27,28] (GAPW) was used in combination with the all electron TZVP basis[29] and a plane wave cutoff of 400 Ry. In the instances where radical

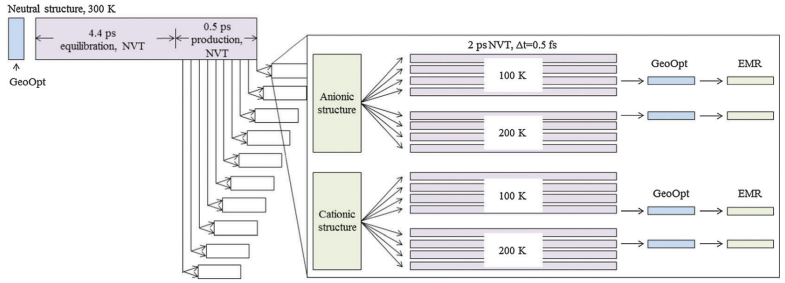

Fig. 3 Diagram of computational sequence. From the last 0.5 ps of an MD run on the neutral ⟨2a2b2c⟩ crystallographic supercell, 10 geometries were selected. For each of these, 16 further MD runs were performed where charge (and spin) was introduced in the system: 8 cationic and 8 anionic, each time with 4 runs at 100 K and 4 runs at 200 K. For each radical type obtained, a representative structure was chosen for further geometry optimization and calculation of EMR properties.

production in the MD simulation also resulted in the formation of a hydrogen molecule, the final geometry was additionally optimized in the absence of this molecule and EMR properties recalculated. This was motivated by experimental evidence that H_2 molecules are able to escape the crystal structures of carbohydrates.[30,31]

3. Radical formation processes

Radicals were produced in 67 out of the 160 MD simulations performed, in the other instances no spin localization was attained during the 2 ps investigated. In all cases the MD run started out with a spin density distributed over the entire supercell. This density clearly does not describe a radical structure but seemingly the DFT ground state of the chemically intact structures. After a number of MD steps the calculations resulted in a geometrical configuration for the molecules for which the spread out density no longer described the ground state and a conical intersection was crossed. As DFT is not a multi reference method, crossing a conical intersection will not be a smooth process. During the period of crossing the conical intersection, not surprisingly, the temperature of the system increased dramatically due to DFTs lack of ability to produce a physical density for this time period. And during this short time interval, structural changes such as proton transfers and dehydroxylations occurred readily. This, though not a physical process but rather an artifact of DFT, aided the production of radical structures that either stabilized or continued to take part in chemical reactions after a physical density and temperature for the system had been re-established.

Common for the MD runs was that protons were easily transferred along the hydrogen bond chains in the crystal structure. These hydrogen bond chains acted as effective transport paths for both positive and negative charge by creating a ''current'' of positive protons. The readiness of these proton transfers seemed to effect the radical stabilization, and it was observed that the protons were more readily transported in the cationic structures. Also increased temperature contributed to the ease of the proton transfers.

All together 12 different radical species were observed in this study, 7 reduction products and 5 oxidation products. For each initial crystal geometry four different sets of initial velocities were used and different radicals were produced as the initial velocities of the nuclei varied. The initial velocities therefore seem to influence radical production more than the initial geometrical structure itself.

3.1. Reduction products

Seven different reduction products were generated by the MD procedures and these can be divided in to 3 different categories: dehydroxylation, ring-opening and H-atom abstraction. Table 1 lists the different species formed and their frequency of occurrence. Fig. 4 illustrates their chemical structures. In general more reduction product radicals were formed in the higher temperature (200 K) simulations.

The dehydroxylation products (structures (a)–(c) in Fig. 4) were formed when spin localized on a carbon atom which

Table 1 Radical reduction products and their frequency of occurrence

	Occurrences	Specification	Structure
Reduction products 100 K			
Dehydroxylation	6	2 × from C1	(a)
		3 × from C2	(b)
		1 × form C4	(c)
Ring-opening and protonation of ring oxygen	1	1 × scission between C5 and ring oxygen	(d)
H-atom abstraction	1	1 × from C5	(g)
Reduction products 200 K			
Dehydroxylation	20	7 × from C1	(a)
		9 × from C2	(b)
		5 × from C4	(c)
Ring-opening and protonation of ring oxygen	6	5 × scission between C5 and ring oxygen	(d)
		1 × scission between C1 and ring oxygen	(e)
H-atom abstraction	2	2 × from C3	(f)

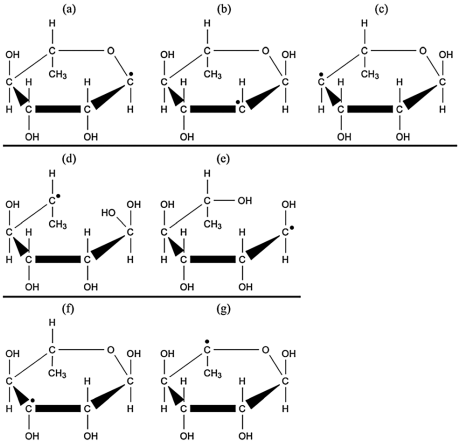

Fig. 4 Reduction product structures. (a)–(c) are dehydroxylation products, (d) and (e) are ring-opened structures, and (f) and (g) are H-atom abstraction products.

expelled the hydroxyl group attached to this carbon as a hydroxide anion (OH^-), leaving behind a neutral radical center. The ejected hydroxide would attract a proton along a preexisting hydrogen bond thereby effectively separating the negative charge from the radical site. Fig. 5 shows a diagram of this reaction. In most cases several proton transfers took place at once, thereby localizing the charge far away from the radical site. Out of the four possibilities, three different dehydroxylation products were observed, namely the C1, C2 and the C4-centered species. The hydroxyl group at C3 does not take part in a hydrogen bond chain, but rather the proton at that site is hydrogen bonded to the ring oxygen of a neighboring rhamnose molecule. It is likely that this structural feature is the reason why no such radical

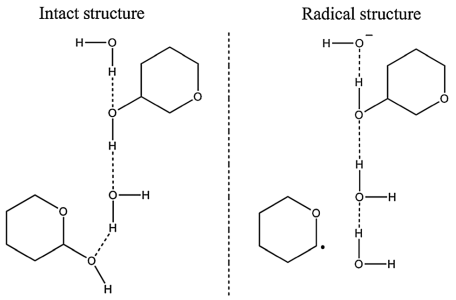

Fig. 5 Reductive dehydroxylation product formation. OH^- is emitted from radical site and absorbs a proton along a hydrogen bond to form water. The negative charge is moved further away *via* several proton shuffles along a hydrogen bond chain.

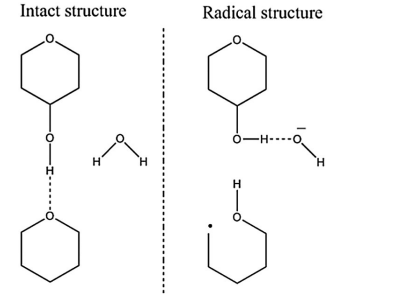

Fig. 6 Reductive ring-opened product formation. The negative radical molecule absorbs a proton across a hydrogen bond; the proton donor is neutralized by further proton absorption.

species was observed. Additionally one instance was observed of dehydroxylation from two different rhamnose molecules at once, this resulted in the spin being shared by two molecules, both containing positive charge as they each expelled a hydroxide anion.

Ring-opened structures were formed when spin localized on either C1 or C5 (structures (e) and (d) in Fig. 4) and the bond between the respective carbon atom and the ring oxygen was ruptured. The negative charge of these radicals was cancelled by protonation at the ring oxygen from the O3 position of an adjacent rhamnose molecule. The charge was moved even further away from the radical site *via* another proton shuffle from a crystal water. This reaction is shown in Fig. 6.

The H-atom abstraction products (structures (f) and (g) in Fig. 4) were formed when spin was localized on the hydrogen from a hydroxyl group in rhamnose. This hydrogen atom was ejected and the negative charge on the hydroxyl oxygen was cancelled by protonation *via* a hydrogen bond. In this situation both charge and spin migration occurred, though along different routes. This situation is described as the intermediate structure in Fig. 7. The lone hydrogen atom would then recombine with an aliphatic hydrogen abstracted from a different rhamnose molecule; thus forming a neutral hydrogen molecule and localizing the radical center on the H-atom abstracted carbon. This situation is depicted as the radical structure in Fig. 7. Two such radicals were observed in the simulations, one centered on C3 and one centered on C5.

3.2. Oxidation products

Five different oxidation products were observed. They are all alkoxy-type radicals, but they were formed *via* two routes: direct H-atom abstraction from radical center and ring-opening. All radical structures are illustrated in Fig. 8, and the frequency of occurrence for the different species are given in Table 2. It is clear that the oxidative radicals were more easily formed and stabilized at the lower temperature (100 K).

The structures (h)–(k) were formed as oxygen-centered cationic radicals expelled their surplus charge by transferring a hydroxyl

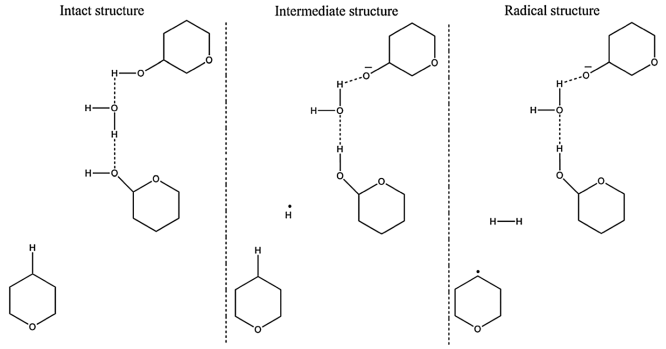

Fig. 7 Reductive H-atom abstraction product formation. Initially, a hydrogen atom is ejected from a hydroxyl group of a rhamnose molecule. The latter is protonated *via* a hydrogen bond. The lone hydrogen atom in turn abstracts another hydrogen from a carbon site on a neighboring rhamnose molecule. This leads to formation of H_2 and leaves the radical center on the H-atom abstracted carbon atom.

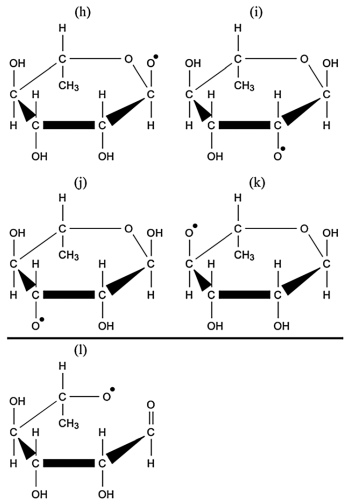

Fig. 8 Oxidation product structures. (h)–(k) are alkoxy radicals resulting from deprotonation on oxidized hydroxyl group, (l) is a ring-opened structure.

Table 2 Radical oxidation products and their frequency of occurrence

	Occurrences	Specification	Structure
Oxidation products 100 K			
O1-centered alkoxy	3	2 × stable 1 × unstable	(h)
O2-centered alkoxy	6	6 × stable	(i)
O4-centered alkoxy	11	3 × stable 8 × unstable	(k)
Ring oxygen-centered	1	Concomitant aldehyde formation at C1	(l)
Oxidation products 200 K			
O1-centered alkoxy	5	5 × unstable	(h)
O2-centered alkoxy	5	2 × stable 3 × unstable	(i)
O3-centered alkoxy	1	1 × stable	(j)
O4-centered alkoxy	4	1 × stable 3 × unstable	(k)

proton to a neighboring molecule *via* a hydrogen bond. In the case of the O1-, O2 and O4-centered alkoxy radicals (structures (h), (i) and (k) in Fig. 8), the hydroxyl groups take part in the infinite hydrogen bond networks in the crystal structure. The excess positive charge was in these cases effectively separated from the radical site by several proton shuffles along the hydrogen bond chains. This type of reaction is illustrated in Fig. 9.

Common for radicals (h), (i) and (k) is that they were not necessarily present throughout the rest of the MD run once they were formed. In some instances ejected protons moved back along the hydrogen bonds; thereby restoring the initial structure. This sometimes occurred even when the charge had been moved across two subsequent hydrogen bonds in the chain. In other instances it was found that the proton transfer pathway was so long the charge migrated to a periodic image of the radical site. This returned the chemical structure of the supercell to the original one, apart from the hydroxyl groups along the hydrogen bond chain, which were now rotated. In many instances this last type of recombination behavior occurred at several places in the crystal simultaneously. These two recombination reactions lead to several transient alkoxy radicals during the MDs run and a net reduction in the number of radicals formed. These transient radicals are included in Table 2.

The O3-centered alkoxy radical (radical structure (j) in Fig. 8) is the result of deprotonation from the O3 hydroxyl group. This hydroxyl group does not take part in the hydrogen bond networks in the crystal, and therefore does not benefit from the efficient way of separating charge and spin. In only one MD simulation, this radical was formed.

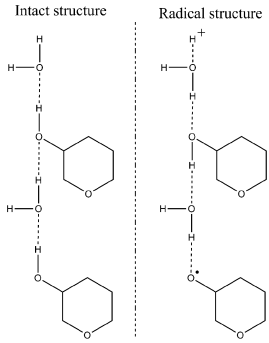

Fig. 9 Oxidative alkoxy deprotonation product formation. Protons are transferred along hydrogen bonds, separating the charge and spin.

There was also one occurrence of two stable O2-centered alkoxy radicals at once. These radicals have a 40–60 split of the electron spin density and both radicals carried negative charge slightly less than half an electron charge. It appears as the two molecules shared the electron hole, and that both expelled a whole proton to compensate for the positive charge.

In addition, one instance of H_2 molecule formation was seen in the cationic MD runs. This occurred when a deprotonation chain starting at O1 (of what became a stable alkoxy radical) ended up attracting a hydrogen anion from the C5 position of another rhamnose molecule in the cell. The rhamnose molecule giving up the hydrogen anion went through a ring-opening and a net deprotonation from O1 continuing the chain of positive charge transfer. A schematic of this process is given in the ESI.†

The ring oxygen-centered radical (structure (l) in Fig. 8) is the fifth kind of oxidation product observed. In this radical the ring was broken between the ring oxygen and C1 and the molecule was neutralized by deprotonation from O1 as illustrated in Fig. 10.

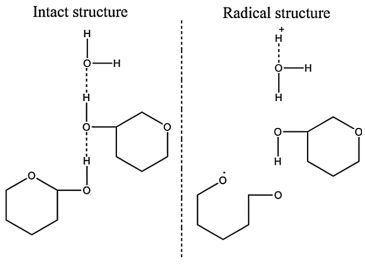

Fig. 10 Oxidative ring oxygen-centered product formation. Ring structure is broken and the charge is separated from the spin *via* several proton transfers along hydrogen bonds.

4. Evaluation of the formed products

4.1. Radical structures and hyperfine coupling tensors

Structures (b), (d)–(g), (k) and (l) were chosen as representative structures for their class and the MD runs were continued until 20 ps was reached. In this time, none of the radical structures evolved further, but rather seemed to be stable. The hydrogen molecules produced remained in the vicinity of where they were produced, but moved around and vibrated within this small area.

For the oxidation products, only structure (k), the O4-centered alkoxy radical, was found to have similar hfc tensors as the experimental evidence. This radical has been thoroughly examined before[13,14,16] and exhibits a very good agreement with experimental data. The couplings can be found in the ESI.† It is very assuring that previously verified radicals are formed during this process.

After careful examination of the calculated hfc tensors for all reduction radicals produced, only three, (d), (f) and (g), are found to have characteristics comparable to experimentally reported radicals to date. Out of the reduction products only structures (f) and (g) correspond to radical structures suggested by experimentalists on the basis of measured EMR properties,[9] whereas (d) has not yet been proposed. The calculated hfc tensors for all structures are given in the ESI.† For both structures (f) and (g), geometries were optimized and hfcs were calculated twice; once with the formed hydrogen molecule present in the crystal structure, and once without this molecule. The presence of the hydrogen molecule apparently did not affect the spin distribution or radical geometry significantly.

Structure (f), the C3-centered H-atom abstraction product, was observed in two different instances in this study, referred to as (f)-I and (f)-II. Mainly the orientation of the dissociated H_2 molecule differs between the conformations, as can be seen at the top left in Fig. 11. Both conformations have 78% spin on C3. The calculated hfcs for these two structures are given in Table 3, and it can be seen that they both exhibit one large coupling to H4 with isotropic value of 100 MHz and anisotropy of 12 MHz. Also there are couplings to H2 and HO2 which are

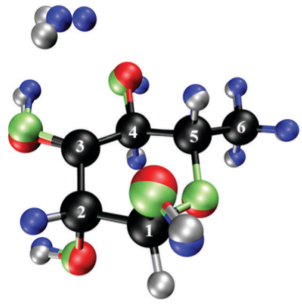

Fig. 11 The two different geometrical conformations of radical (f). Structure (f)-I is shown with black carbon atoms, red oxygen atoms and silver hydrogen atoms. Structure (f)-II is shown with black carbon atoms, green oxygen atoms and blue hydrogen atoms.

similar for the conformations, while there is a significant difference in the isotropic value of the coupling to HO3.

The isotropic value of the HO3 coupling seems to be a sensitive parameter both for the C–OH conformation and for the presence or absence of the H_2 molecule in the structure. Fig. 11 compares the geometrical differences between structures (f)-I and (f)-II. As can be seen from the figure, the orientations of the hydroxyl groups in the two structures are quite different, and the angle between the two C3–HO3 directions (HO3I–C3–HO3II) is 7°. It is believed that this difference in orientation is the cause of the discrepancy of 10 MHz in the HO3 isotropic coupling for the two structures. All HO3 couplings have anisotropies of about 30 MHz which increased slightly as the hydrogen molecule in the vicinity was removed. As can also be seen from the figure the hydrogen molecule orientation is very different, resulting in large differences in the hfcs of these atoms. The reorientation of the C3 hydroxyl group upon removal of the hydrogen molecule, was much smaller for each of the structures than the difference in orientation between the structures I and II.

The experimental evidence[9] for structure (f) consists of, at 65 K, one large and several smaller hfcs, see also Table 3. The larger one has isotropic value of 96.10 MHz, the full tensor of this coupling was determined after warming to 150 K. Of the smaller couplings, one (about 17–20 MHz) is due to an exchangeable proton, this coupling disappeared upon warming. Another coupling of the same magnitude remained. In comparing the calculated hfcs of the calculated structures to experimental data, it is found that the large H4 coupling of about 100 MHz corresponds well to the experimental observation of a coupling of 96.10 MHz. The experimentally determined tensor is compared to the H4 coupling tensor from the calculations in Table 3. It should be noted that in this case the DFT data are compared to the so-called Schonland conjugate of the experimentally determined tensor.[32,33] See the ESI† for details on why this is considered to be correct for this radical. From Table 3 it can be seen that there is good match between the experimental hfcs and theoretical tensors. As for the two smaller couplings: H2 seems to be a good candidate for the observed persisting coupling of about 20 MHz while HO3 could be the exchangeable coupling which disappears upon warming. As the 4 different computed radical structures ((f)-I and (f)-II with and without H_2 molecule present) resulted

Table 3 Calculated hfcs for the C3-centered H-atom abstraction product. Isotropic (A_{iso}) and anisotropic (A_{ani}) hyperfine couplings are in MHz. Principal directions are given with respect to the orthogonal crystallographic axes *a*bc*. Tensors are given for the systems with and without the H_2-molecule present in the crystal structure as well as the experimentally determined data assumed to result from this radical structure. The angular deviation indicates the angle (in degrees) between corresponding eigenvectors

		(1) H_2 molecule present in crystal					(2) H_2 molecule removed			(3) Experimental[9]		
Radical	Atom	A_{iso}	A_{ani}	*a**	*b*	*c*	Angular deviation (1)–(2)	A_{iso}	A_{ani}	Angular deviation (1)–(3)	A_{iso}	A_{ani}
f-I	H2	12.3	−5.8	−0.332	0.014	0.943	1	9.9	−5.7		20	
			−3.3	0.642	0.736	0.215	1		−3.3			
			9.0	−0.691	0.677	−0.253	1		9.0			
	H4	100.2	−5.2	−0.003	−0.374	0.927	2	97.8	−5.1	4	96.10	−4.96
			−1.4	−0.981	−0.179	−0.076	2		−1.6	4		−1.77
			6.7	0.195	−0.910	−0.366	0		6.7	1		6.73
	HO2	−4.2	−7.4	−0.126	0.992	0.018	1	−4.1	−7.4			
			0.2	0.428	0.037	0.903	1		0.2			
			7.1	0.895	0.122	−0.429	0		7.1			
	HO3	13.9	−11.0	−0.522	0.608	0.598	4	3.7	−12.1		17–20	
			−8.2	0.700	0.706	−0.107	1		−8.9			
			19.2	−0.487	0.362	−0.794	4		21.0			
	H(H_2)	13.5	−3.5	0.308	−0.951	0.011						
			−2.9	0.591	0.182	−0.786						
			6.4	0.746	0.248	0.619						
f-II	H2	7.2	−5.7	−0.378	0.019	0.926	2	6.1	−5.7		20	
			−3.3	0.662	0.705	0.256	2		−3.3			
			9.0	−0.647	0.709	−0.278	1		9.0			
	H4	101.5	−4.8	−0.213	−0.426	0.880	1	97.4	−4.8	9	96.10	−4.96
			−2.0	0.960	0.076	0.269	2		−2.0	9		−1.77
			6.8	−0.181	0.902	0.393	1		6.7	3		6.73
	HO2	−4.7	−8.0	−0.139	0.985	0.106	1	−4.6	−7.9			
			0.4	0.427	−0.037	0.904	1		0.4			
			7.6	0.894	0.171	−0.415	1		7.5			
	HO3	3.4	−11.2	−0.444	0.617	0.650	4	−0.8	−11.9		17–20	
			−8.2	0.762	0.642	−0.088	3		−8.8			
			19.4	−0.471	0.456	−0.755	3		20.7			
	H(H_2)	3.3	−3.7	−0.278	−0.807	0.522						
			−3.0	−0.455	0.589	0.668						
			6.7	−0.846	−0.052	−0.531						
	H(H_2)	5.3	−3.7	−0.504	0.831	0.236						
			−3.4	−0.414	−0.472	0.778						
			7.1	−0.758	−0.295	−0.582						

Table 4 Calculated hfcs for the C5-centered reduction products (d) and (g). Isotropic (A_{iso}) and anisotropic (A_{ani}) hyperfine couplings are in MHz. Principal directions are given with respect to the orthogonal crystallographic axes *a*bc*. Tensors are given for the systems produced in the MD runs (with and without the H_2-molecule present in the crystal structure (g)) as well as the experimentally determined data applicable for comparison. The angular deviation indicates the angle (in degrees) between corresponding eigenvectors

		(1) MD produced structure (H_2 molecule present for (g))					(2) H_2 molecule removed			(3) Experimental[9]		
Radical	Atom	A_{iso}	A_{ani}	*a**	*b*	*c*	Angular deviation (1)–(2)	A_{iso}	A_{ani}	Angular deviation (1)–(3)	A_{iso}	A_{ani}
d	H4	8.4	−5.8	−0.233	−0.901	0.365						
			−3.0	0.589	0.168	0.790						
			8.9	−0.773	0.400	0.492						
	H5	−48.2	−34.3	−0.439	−0.405	0.802					95	
			−3.3	0.713	0.387	0.585						
			37.6	−0.547	0.829	0.119						
	H6	103.7	−4.8	0.981	−0.188	−0.041					56	
			−3.2	0.189	0.906	0.379						
			8.1	0.034	0.379	−0.925						
	H6	91.8	−4.9	−0.028	0.668	0.744					56	
			−3.6	0.831	−0.398	0.388						
			8.4	0.555	0.629	−0.544						
	H6	2.0	−4.3	0.796	−0.073	−0.600					56	
			−3.6	0.571	0.419	0.706						
			7.8	−0.200	0.905	−0.376						
	HO4	−5.3	−9.1	−0.995	−0.042	−0.088						
			−1.5	−0.067	−0.365	0.929						
			10.6	−0.071	0.930	0.360						
	HO ring	9.4	−3.5	−0.730	0.574	0.372						
			−1.5	−0.427	−0.807	0.408						
			5.0	−0.534	−0.139	−0.834						
g	H4	99.0	−5.5	0.628	0.778	0.022	1	95.4	−5.4		95	
			−1.3	0.563	−0.474	0.677	4		−1.4			
			6.8	−0.537	0.413	0.735	4		6.8			
	H6	31.9	−4.7	−0.004	0.892	0.451	58	37.0	−4.7		56	
			−4.1	0.862	−0.225	0.453	57		−4.5			
			8.8	0.506	0.391	−0.769	3		9.2			
	H6	14.8	−4.9	0.069	0.028	0.997	14	14.6	−4.8		56	
			−4.0	0.780	−0.624	−0.036	14		−4.4			
			8.9	0.622	0.781	−0.065	3		9.2			
	H6	108.3	−4.1	0.140	0.480	0.866	4	122.9	−4.0		56	
			−2.6	0.987	−0.137	−0.083	4		−2.6			
			6.7	0.079	0.866	−0.493	2		6.6			
	H(H_2)	84.0	−3.1	0.134	0.392	0.910						
			−2.7	−0.324	−0.851	0.414						
			5.8	0.937	−0.350	0.013						
	H(H_2)	−11.2	−13.6	0.163	0.408	0.898						
			−11.2	−0.308	−0.844	0.439						
			24.8	0.937	−0.348	−0.012						

in large differences in isotropic value for the HO3 tensor, a reorientation of the –OH3 group could also explain the experimental data (as is also suggested previously[15]).

Structure (d), the C5-centered ring-opened structure, was observed in 6 MD simulations in this study. This structure has a spin density of 92% on C5. The hfcs are given in Table 4. The methyl group contains two large and one small coupling, for which the isotropic values average to 66 MHz. There is also one large α-coupling with isotropic value of −48 MHz and anisotropy of 70 MHz due to interaction with H5. Smaller couplings to H4, HO4 and the proton added to ring oxygen are also present.

Structure (g), the C5-centered H-atom abstraction product, was only observed in one MD run. The spin on this radical is localized with 81% on C5. Upon removal of the hydrogen molecule from the crystal structure, the geometry did not change much, but the spin density on C5 increased to 84%. The hfcs of the radicals, shown in Table 4, are dominated by two large isotropic couplings of about 100 MHz. Both are β-couplings, one to H4 and another to one of the methyl protons. The other two methyl protons are also interacting significantly with the unpaired spin. As the methyl group is likely to be rotating even at relatively low temperatures, the average value of these, being about 50–60 MHz, is more interesting. One of the H_2 protons exhibits a large coupling of 84 MHz, but whether or not this hydrogen molecule is present in the crystal structure with radical (g) does not seem to have large impact on the hfcs of the radical. The C6 methyl group couplings increased somewhat upon removal of the hydrogen molecule, but this is most likely linked to the concomitant increase in spin density on C5.

Also structure (g) was previously proposed to be observed experimentally.[9] The experimental evidence is an EPR spectrum which is a doublet of quartets, assumedly due to couplings to a proton and a rotating methyl group. Both couplings are relatively

isotropic. The magnitude of the experimentally determined proton coupling was about 95 MHz and the methyl group coupling was measured to about 56 MHz, but full hfc tensors were not determined for this radical. In the present study, only structures (d) and (g) display methyl group couplings of the right magnitude, as well as one other large coupling. These radicals are both C5-centered and the main difference between them is that (d) exhibits an α-proton coupling to H5, whereas (g) exhibits a β-proton coupling to H4. As the experimental evidence is of a relatively isotropic coupling,[9] the (d) candidate may likely be eliminated. A further verification of this radical candidate is not possible until more detailed experimental data are available.

4.2. Hydrogen gas formation

The formation of hydrogen gas (H_2) upon irradiation has been experimentally observed for a number of carbohydrates[30,31,34–36] as well as amino acids.[37] Hydrogen is generally found to be the major gaseous product formed. In particular, investigations on α-D-glucose and α-D-glucose monohydrate has shown that about 70% of the hydrogen gas formed is trapped inside the crystal lattice.[30,31] Similar studies on rhamnose do not exist to the best of our knowledge. The results in the present work indicate that the formation of hydrogen molecules is intrinsic for one type of radical formed, the H-atom abstraction products. According to our calculations on structure (f) it seems that trapped H_2 molecules lead to alterations in the hfcs of the radical even when the geometrical structure of the radical is not much influenced by the presence of H_2 in the lattice. The increased isotropic values of the hfcs of the radicals might therefore reveal H_2 even if protons of the hydrogen molecule itself do not possess sufficiently large hfcs for detection by EMR.

5. Conclusions

A method for exploring possible radical structures as resulting from radiation exposure has been presented. This method has the advantage of providing a selection of possible radiation damage products without bias by the expectations of the scientist. The method generates a number of different radical structures which need to be examined further and compared to experimental data. In this particular work dehydroxylation products as well as ring-opened structures were produced. These are not structures that would normally be explored to a large extent.

Starting from an intact crystal structure and introducing spin and charge to this, ionization events are mimicked. In an actual ionization event in nature, there will be a high localization of energy, and for this reason it is necessary to describe reactions over barriers that cannot be crossed using only the thermal energy available. Although the initial DFT ground state is one where the spin and charge is delocalized in the system, the time evolution of the system leads to a conformation where this is no longer the ground state. The failure of DFT to describe conical intersections properly is then exploited in the radical formation as the temperature rises for a brief time period and high reaction barriers can easily be crossed.

In a previous study[13] it was found that several alkoxy radicals are stable, but the relative energies may explain that the relative abundances of these species are such that only one radical is observable in experiments. The present simulations do not reproduce these relative abundances of radicals. The short-time increase in temperature at the moment of radical production in our simulations practically removes reaction barriers, as would also be expected from a physical ionization event. On the other hand, the thermal equilibration expected to allow for transformation of one type of radical into the other is not seen in the calculations. This is likely due to the short time span of the calculations.

The diversity of the radicals produced is caused by three initial conditions: the initial molecular geometries and atomic velocities in the MD-runs and the temperature of the thermostat. As four runs with different initial velocities were performed for each initial geometrical structure, the relative importance of these effects could be examined. It was clear that the initial velocities were decisive in which radicals were formed and where in the cell they were localized, more than the initial geometrical conformations.

The effect of temperature was opposite in the cases of reduction and oxidation products. A higher temperature increased the activity of proton transfer over the hydrogen bond network. In the case of cationic species this became an over-activity causing problems with radical formation as the charge migration sometimes looped due to the periodic boundary conditions. In anionic species on the other hand, the proton transfer activity was generally lower and the higher temperature was needed to gain sufficient charge transport for stabilization of radicals. These proton transfer reactions occur in nature, and contribute to charge–spin separation thereby stabilizing radicals, as was also seen in these simulations.

It is also satisfying that the method seems to produce all types of experimentally observed molecular radicals reported in literature on the system. The only radical not seen here is a C2-centered H-atom abstraction product.[9] There is of course the possibility that this event would have been observed if even more exhaustive sampling with the aid of MD simulations was performed. But as similar H-atom abstraction products are formed, the data at hand would already alert the scientist to the possibility of such a radical as well as the C3- and C5-centered versions. This possibility is not explored further in this work, as the C2-centered radical model has been confirmed by DFT simulation at an earlier stage.[15]

In the future it will be interesting to apply this computational procedure to other systems where there is experimental evidence for radicals which are at present unidentified, such as trehalose[3,4] and sucrose.[38] The method produces structures which have not previously been considered, and it is possible that this will lead to one or more structures that correspond with the experimental data.

Acknowledgements

The computational resources (Stevin Supercomputer Infrastructure) and services used in this work were provided by the

VSC (Flemish Supercomputer Center), funded by Ghent University, the Hercules Foundation and the Flemish Government – department EWI. A. Van Yperen-De Deyne acknowledges the Research Board of Ghent University (BOF) for funding. S. G. Aalbergsjø acknowledges PhD fellowship and travel grants from the University of Oslo.

References

1 H. Vrielinck, H. De Cooman, F. Callens and E. Sagstuen, in *Applications of EPR in Radiation Research*, ed. M. Shiotani and A. Lund, Springer, Berlin, 2014, to be published.
2 M. A. Tarpan, H. Vrielinck, H. De Cooman and F. Callens, *J. Phys. Chem. A*, 2009, **113**, 7994–8000.
3 H. De Cooman, M. A. Tarpan, H. Vrielinck, M. Waroquier and F. Callens, *Radiat. Res.*, 2013, **179**, 313–322.
4 M. A. Tarpan, H. De Cooman, E. O. Hole, M. Waroquier and F. Callens, *J. Phys. Chem. A*, 2012, **116**, 3377–3387.
5 H. De Cooman, E. Pauwels, H. Vrielinck, E. Sagstuen, M. Waroquier and F. Callens, *J. Phys. Chem. B*, 2010, **114**, 666–674.
6 E. Pauwels, in *Applications of EPR in Radiation Research*, ed. M. Shiotani and A. Lund, Springer, Berlin, 2014, to be published.
7 H. Tachikawa and T. Fukuzumi, *PCCP Phys. Chem. Chem. Phys.*, 2011, **13**, 5881–5887.
8 H. Tachikawa and T. Takada, *Chem. Phys.*, 2013, **415**, 76–83.
9 E. Sagstuen, M. Lindgren and A. Lund, *Radiat. Res.*, 1991, **128**, 235–242.
10 P. O. Samskog and A. Lund, *Chem. Phys. Lett.*, 1980, **75**, 525–527.
11 E. E. Budzinski and H. C. Box, *J. Chem. Phys.*, 1985, **82**, 3487–3490.
12 P. O. Samskog, A. Lund, G. Nilsson and M. C. R. Symons, *J. Chem. Phys.*, 1980, **73**, 4862–4866.
13 S. G. Aalbergsjø, E. Pauwels, H. De Cooman, E. O. Hole and E. Sagstuen, *PCCP Phys. Chem. Chem. Phys.*, 2013, **15**, 9615–9619.
14 E. Pauwels, R. Declerck, V. Van Speybroeck and M. Waroquier, *Radiat. Res.*, 2008, **169**, 8–18.
15 E. Pauwels, V. Van Speybroeck and M. Waroquier, *J. Phys. Chem. A*, 2006, **110**, 6504–6513.
16 E. Pauwels, T. Verstraelen and M. Waroquier, *Spectrochim. Acta, Part A*, 2008, **69**, 1388–1394.
17 S. Takagi and G. A. Jeffrey, *Acta Crystallogr., Sect. B: Struct. Crystallogr. Cryst. Chem.*, 1978, **34**, 2551–2555.
18 the CP2K developers group, *CP2K version 2.4 (Development Version)*, 2013.
19 A. D. Becke, *Phys. Rev. A: At., Mol., Opt. Phys.*, 1988, **38**, 3098–3100.
20 C. T. Lee, W. T. Yang and R. G. Parr, *Phys. Rev. B: Condens. Matter Mater. Phys.*, 1988, **37**, 785–789.
21 G. Lippert, J. Hutter and M. Parrinello, *Mol. Phys.*, 1997, **92**, 477–487.
22 J. VandeVondele, M. Krack, F. Mohamed, M. Parrinello, T. Chassaing and J. Hutter, *Comput. Phys. Commun.*, 2005, **167**, 103–128.
23 S. Goedecker, M. Teter and J. Hutter, *Phys. Rev. B: Condens. Matter Mater. Phys.*, 1996, **54**, 1703–1710.
24 C. Hartwigsen, S. Goedecker and J. Hutter, *Phys. Rev. B: Condens. Matter Mater. Phys.*, 1998, **58**, 3641–3662.
25 M. Krack, *Theor. Chem. Acc.*, 2005, **114**, 145–152.
26 G. Bussi, D. Donadio and M. Parrinello, *J. Chem. Phys.*, 2007, **126**, 7.
27 M. Krack and M. Parrinello, *Phys. Chem. Chem. Phys.*, 2000, **2**, 2105–2112.
28 G. Lippert, J. Hutter and M. Parrinello, *Theor. Chem. Acc.*, 1999, **103**, 124–140.
29 N. Godbout, D. R. Salahub, J. Andzelm and E. Wimmer, *Can. J. Chem.*, 1992, **70**, 560–571.
30 G. O. Phillips and P. Baugh, *Nature*, 1963, **198**, 282–283.
31 G. O. Phillips and P. J. Baugh, *J. Chem. Soc. A*, 1966, 370–377.
32 D. S. Schonland, *Proc. Phys. Soc.*, 1959, **73**, 788–792.
33 H. Vrielinck, H. De Cooman, M. A. Tarpan, E. Sagstuen, M. Waroquier and F. Callens, *J. Magn. Reson.*, 2008, **195**, 196–205.
34 M. Dizdaroglu, D. Henneberg, K. Neuwald, G. Schomburg and C. von Sonntag, *Z. Naturforsch., B: J. Chem. Sci.*, 1977, **32**, 213–224.
35 A. G. W. Bradbury and C. von Sonntag, *Z. Naturforsch., B: J. Chem. Sci.*, 1977, **32**, 725–726.
36 G. Löfroth and T. Gejvall, *Acta Chem. Scand., Ser. B*, 1974, **28**, 777–780.
37 T. Gejvall and G. Löfroth, *Radiat. Eff. Defects Solids*, 1975, **25**, 187–190.
38 H. De Cooman, J. Keysabyl, J. Kusakovskij, A. Van Yperen-De Deyne, M. Waroquier, F. Callens and H. Vrielinck, *J. Phys. Chem. B*, 2013, **117**, 7169–7178.

Paper VII

Determining the Storage, Availability and Reactivity of NH_3 with Cu-Chabazite-based Ammonia Selective Catalytic Reduction Systems

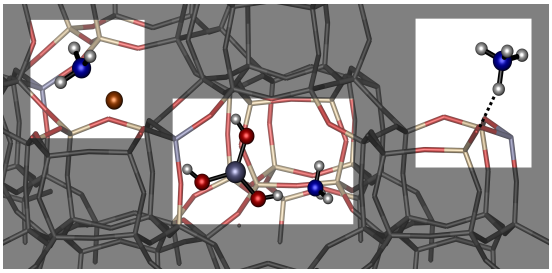

I. Lezcano-Gonzalez, U. Deka, B. Arstad, A. Van Yperen-De Deyne, K. Hemelsoet, M. Waroquier, V. Van Speybroeck, B. M. Weckhuysen and A. M. Beale
Physical Chemistry Chemical Physics **16**, 1639–1650 (2014)

PCCP

PAPER

View Article Online
View Journal | View Issue

Cite this: *Phys. Chem. Chem. Phys.*, 2014, **16**, 1639

Determining the storage, availability and reactivity of NH_3 within Cu-Chabazite-based Ammonia Selective Catalytic Reduction systems†

I. Lezcano-Gonzalez,[ab] U. Deka,[ab] B. Arstad,[c] A. Van Yperen-De Deyne,[de] K. Hemelsoet,[de] M. Waroquier,[de] V. Van Speybroeck,[de] B. M. Weckhuysen*[b] and A. M. Beale*[b]

Received 30th September 2013,
Accepted 27th November 2013

DOI: 10.1039/c3cp54132k

www.rsc.org/pccp

Three different types of NH_3 species can be simultaneously present on Cu^{2+}-exchanged CHA-type zeolites, commonly used in Ammonia Selective Catalytic Reduction (NH_3-SCR) systems. These include ammonium ions (NH_4^+), formed on the Brønsted acid sites, $[Cu(NH_3)_4]^{2+}$ complexes, resulting from NH_3 coordination with the Cu^{2+} Lewis sites, and NH_3 adsorbed on extra-framework Al (EFAl) species, in contrast to the only two reacting NH_3 species recently reported on Cu-SSZ-13 zeolite. The NH_4^+ ions react very slowly in comparison to NH_3 coordinated to Cu^{2+} ions and are likely to contribute little to the standard NH_3-SCR process, with the Brønsted groups acting primarily as NH_3 storage sites. The availability/reactivity of NH_4^+ ions can be however, notably improved by submitting the zeolite to repeated exchanges with Cu^{2+}, accompanied by a remarkable enhancement in the low temperature activity. Moreover, the presence of EFAl species could also have a positive influence on the reaction rate of the available NH_4^+ ions. These results have important implications for NH_3 storage and availability in Cu-Chabazite-based NH_3-SCR systems.

Introduction

The emission of nitrogen oxides (NO_x), produced through the combustion of fossil fuels, is a major concern for today's society, and is subject to stringent environmental and public health protection regulations. Until now, many efforts have been made to fulfil these legislative requirements, optimizing the performance of either combustion control or post-combustion abatement technologies. In particular Ammonia Selective Catalytic Reduction (NH_3-SCR) has emerged as an effective technology for reducing NO_x emissions from oxygen-rich exhausts, typical of diesel engines, to levels required by emission regulations.[1,2]

In the last few years, many metal-promoted zeolites have been shown to be active for the NH_3-SCR reaction, with BEA, FAU and MFI-type zeolites being the most extensively studied.[1,2] Recently, it has been reported that Cu^{2+}-exchanged zeolites based on the CHA topology exhibit a superior catalytic activity and hydrothermal stability over other zeolitic structures, particularly those of the SSZ-13 form, with a lower Al content.[3–6] These improvements are attributed to the preferential location of Cu^{2+} ions in the plane of the 6-ring of the double 6-ring (D6R) unit, coordinated to three framework oxygen atoms,[5–8] which are active for NH_3-SCR.[5–8]

In addition to the metallic active species, the overall framework acidity of the catalyst material has been suggested to be a decisive factor for NH_3-SCR activity; however, the role played by the different types of acid sites in NH_3-SCR is still not fully understood. It is generally assumed that NH_3 is activated on the Brønsted sites of the zeolite in the form of ammonium ions (NH_4^+), which further react with the surface NO_x species to form N_2 and H_2O.[9–11] However, it has also been proposed that Brønsted acidity may not be required for adsorbing or activating NH_3 and that the support acts mainly as a reservoir for NH_3, which can migrate to the active site.[12–14]

Overall, NH_3 storage capacity plays a crucial role in the NH_3-SCR reaction, with NO_x conversion efficiency being to a large extent determined by the amount of stored NH_3, especially at low temperatures.[15] Though zeolites present an exceptional NH_3 storage capacity when compared with commercial vanadia-based

[a] *Materials innovation institute (M2i), Mekelweg 2, 2628 CD Delft, The Netherlands*
[b] *Inorganic Chemistry and Catalysis Group, Debye Institute for Nanomaterials Science, Utrecht University, Universiteitsweg 99, 3584 CG, The Netherlands. E-mail: a.m.beale@uu.nl, b.m.weckhuysen@uu.nl*
[c] *SINTEF Materials and Chemistry, Forskningsveien 1, N-0314 Oslo, Norway*
[d] *Center for Molecular Modelling (CMM), Ghent University, Technologiepark 903, B-9052, Zwijnaarde, Belgium*
[e] *QCMM-alliance, Ghent-Brussels, Belgium*

† Electronic supplementary information (ESI) available: Details on the theoretical calculations; and XRD, ^{27}Al MAS NMR, UV-Vis-NIR DRS, EXAFS, N_2 adsorption and SEM data of Cu-SSZ-13 zeolites. See DOI: 10.1039/c3cp54132k

View Article Online

Paper PCCP

catalysts,[16] an optimal performance of the NH_3-SCR unit can only be achieved by adopting an appropriate approach for NH_3 storage control. NH_3 can be released from the SCR unit by thermal desorption, combustion or reaction with NO_x; NH_3 combustion leads to the unexpected release of NO_x and/or N_2O, whereas desorption results in undesirable NH_3 emissions to the atmosphere, termed 'NH_3 slip'.[15,16] In real vehicle operation, NH_3 slip usually occurs under transient conditions, *i.e.* when the engine operation is changed. Consequently, engine speed and load fluctuations, and thus variations in flow, temperature and feed gas compositions, have to be considered to achieve a precise control of the NH_3 injection rate.[15,16] An insufficient injection may result in unacceptably low NO_x conversions, whereas an injection rate that is too high may lead to unwanted NH_3 emissions during temperature fluctuations. This is of particular importance at high temperatures, since the maximum NH_3 storage capacity reduces with increasing temperature.[15,16]

To get a deeper understanding of NH_3 storage and availability in Cu-CHA NH_3-SCR systems, the type and nature of NH_3 species adsorbed on the acid sites of the zeolite need to be identified, as well as their contribution to NH_3 storage, slip and reaction. This knowledge is essential not only for meeting future legislative requirements, but also for achieving an optimal performance of the SCR unit, leading to the development of a suitable NH_3 storage control strategy.

In a very recent work,[17] the application of Diffuse Reflectance Infra-Red Fourier Transform Spectroscopy (DRIFTS) has shown the formation of two reacting ammonia species within a Cu-SSZ-13 zeolite: namely Brønsted and Lewis acid site-adsorbed NH_3, also observed within Cu-SAPO-34, a silicoaluminophosphate material based on the CHA topology.[14,18] Due to the lower adsorption temperature, weakly-bound NH_3 species were also observed on Cu-SAPO-34,[14] including NH_3 adsorbed on silanol groups, not present at the reaction temperature. Nevertheless, very little information was obtained on the type and nature of the species formed from the interaction with either the Cu^{2+} Lewis or the Brønsted acid sites; the characteristic features of the resulting complexes were not completely assigned, whereas the possible contribution of extra-framework Al (EFAl) species, also with Lewis acid character, to the Lewis acid site-adsorbed NH_3 was not considered[17,18] and therefore not investigated.[14] Furthermore, the Cu-SSZ-13 zeolite was activated under inert flow,[17] leading to Cu^{2+} self-reduction[19–21] and resulting in changes in the acid strength of the Brønsted acid sites, as observed for vacuum activated Cu-SSZ-13 samples.[21] Clearly, this could affect the adsorption properties of the zeolite.

In the present investigation, the type and nature of NH_3 species adsorbed on CHA-type zeolites and their evolution during standard SCR has been investigated by combining *in situ* Fourier Transform Infra-Red (FTIR) Spectroscopy with DFT-based simulations, as well as temperature programmed desorption (TPD) of NH_3. As catalysts, five CHA-type zeolites have been used, presenting different populations of acid sites, *i.e.* Brønsted acid sites, Cu^{2+} ions and/or EFAl species, characterised by X-ray diffraction (XRD), ^{27}Al MAS NMR, chemical analysis, UV-Vis-NIR DRS, X-ray absorption spectroscopy (XAFS), N_2 adsorption and scanning electron microscopy (SEM), as well as FTIR and theoretical calculations. The combination of theory and experiment on a systematic set of samples enabled us to unambiguously identify not two, but three types of NH_3 species within Cu-CHA-based zeolites (*i.e.* NH_4^+ ions formed on the Brønsted acid sites; $[Cu(NH_3)_4]^{2+}$ complexes and NH_3 adsorbed on EFAl species), with a complete assignment of the typical bending vibrations of these complexes. The results here presented give therefore, further insight into previous works, with a basis for future data interpretation. Moreover, based upon results outlined here, evidence is given concerning the role of these species on NH_3 storage, availability and reactivity, as well as suggestions with regard to the important problem of NH_3 slip. Importantly, a catalyst exhibiting an enhanced NH_3 availability is also presented.

Experimental

Catalysts

Two different H-form CHA-type zeolites were employed as parent materials; *i.e.* low silica H-CHA (Si/Al = 2.2) and high silica H-SSZ-13 (Si/Al = 15) zeolites. Low silica H-CHA zeolite was provided by Tosoh, whereas Al-containing SSZ-13 zeolite was synthesized as described previously, but using static conditions.[22] The sample was calcined in air with the following temperature program: 1 °C min^{-1} to 120 °C, held for 2.5 h; 2.2 °C min^{-1} to 350 °C, and 3 h at this temperature; and finally 0.8 °C min^{-1} to 580 °C, and held for 3 h. Identity and purity of the zeolite were verified by XRD (Bruker D2 phaser).

The studied Cu-zeolites were labelled as follows: Cu-SSZ-13(x), with x being the degree of Cu^{2+} exchange in %. Cu-SSZ-13(67) and Cu-CHA were prepared *via* wet ion exchange (WIE) of the calcined parent zeolite, using an aqueous solution of copper sulphate. Typically, 50 ml of a 0.1 M solution of $CuSO_4$ (Merck, 99%) was mixed with 1 g of the zeolite and magnetically stirred for 2 h at 80 °C. The product was then recovered by vacuum filtration, washed with deionised water, and dried at 120 °C overnight. The resulting sample was calcined in air with the following temperature program: 2 °C min^{-1} to 120 °C, held for 30 min; and finally 1 °C min^{-1} to 550 °C, and 4 h at this temperature. Cu-SSZ-13(100) was prepared *via* three successive ion exchanges of the parent Cu-SSZ-13(67), following the procedure reported above.

Catalyst characterisation

XRD patterns of as-synthesized, calcined and Cu-exchanged samples were recorded on a Bruker D2 X-ray powder diffractometer equipped with a Co Kα X-ray tube (λ = 1.7902 Å). The crystal size and morphology was analysed by SEM using a Tecnai FEI XL 30SFEG microscope. Pore volumes and BET surface areas were determined by nitrogen sorption measurements using a Micromeritics ASAP 2420. The chemical analysis was performed by coupled plasma optical emission spectrometry (ICP-OES, Perkin-Elmer 3300DV instrument). UV-Vis-NIR DRS was collected using a Varian Cary 500 UV-Vis-NIR spectrometer equipped with a DRS accessory to

View Article Online

PCCP Paper

allow collection in the diffuse reflectance mode. Spectra were collected between 5000–50 000 cm^{-1} with a data interval of 10 cm^{-1} and at a rate of 6000 cm^{-1} min^{-1}. XAFS measurements were performed at the Dutch-Belgian beamline (DUBBLE; BM26A) in the European Synchrotron Research Facility (ESRF), Grenoble, France. A detailed description of the beamline can be found elsewhere.[23] A Si(111) double crystal monochromator and Si/Pt mirrors were used for harmonic rejection. XAFS data (X-ray absorption near edge (XANES) and extended X-ray absorption fine structure (EXAFS)) at the Cu K-edge (8979 eV) was collected in transmission mode in quick scanning mode (XANES with 1 eV steps/500 ms integration time with scanning over the EXAFS region utilising steps of increasing size 1–4 eV and integration times 1–3 s resulting in a total acquisition time of ~40 min). Typically 3 scans were recorded per sample. The X-ray absorption data were background corrected using Athena (IFFEFIT software package).[24] The normalized data were k^3-weighed and a least-squares fitting analysis was performed in a k-range of 3–10 Å. The FTs of the k^3-weighed data were phase corrected and fit to the proposed theoretical model using the DL-EXCURV program.[25] ^{27}Al MAS NMR experiments were carried out on a Bruker Avance AV III 500 WB spectrometer using a 3.2 mm triple resonance MAS probe with the sample spinning at 20 kHz. The one-dimensional spectra were recorded upon single-pulse $\pi/12$ excitation with a pulse duration of 0.44 μs. The ^{27}Al chemical shifts are referenced to an aqueous solution of 1 M $Al(NO_3)_3$ (0 ppm). Simulation of the spectra was performed with DMFIT software.[26]

Infrared spectroscopy

FTIR spectra were collected with a Perkin-Elmer Spectrum One FTIR spectrometer, using self-supported wafers of *ca.* 5 mg. Spectra were obtained by accumulating 5 scans at a spectral resolution of 4 cm^{-1}. Prior to the experiment, the zeolite pellet was pre-treated for 12 h with 10% O_2 in He at 250 °C. After the pre-treatment, the catalyst was exposed to 1000 ppm NH_3 at 250 °C over a period of 30 min. Subsequently, the catalyst was exposed to He for 5 min, and then to a mixture of NO and O_2 (1000 ppm NO and 5% O_2) at 250 °C.

Temperature programmed desorption

Temperature programmed desorption of ammonia (NH_3-TPD) was performed making use of a mass spectrometer (MS, Hiden Analytical, HPR-20 QIC). 150 mg of sample was outgassed at 600 °C for 1 h with 10% O_2 in He, followed by NH_3 adsorption at 100 °C for 1 h (13 ml min^{-1}; 5% NH_3 in He). Subsequently, the sample was flushed with He for 1.5 h at 100 °C to remove physically adsorbed NH_3. NH_3 desorption was carried out by rising the temperature to 670 °C with a heating rate of 5 °C min^{-1}.

Catalyst testing

Catalytic tests were performed in a fixed bed plug flow set up. Typically, 150 mg of powdered catalyst material (sieve fractions of 0.425–0.150 mm) was loaded in a 1 cm OD quartz tubular reactor. Prior to the experiment, the zeolite sample was pre-treated for 1 h with 5% O_2 in He at 550 °C. After the pre-treatment, the desired reaction temperature was fixed and then, the catalyst exposed to a SCR feed composition of 1000 ppm NO, 1000 ppm NH_3 and 5% O_2, and He for balance, with a Gas Hourly Space Velocity (GHSV) of 100 000 h^{-1}. Steady-state measurements were performed at different temperatures, from 100 to 600 °C, using a stabilisation period of 30 min at each temperature and analysing the output gases by mass spectrometry (Hiden Analytical, HPR-20 QIC). All SCR gases were provided by Linde. To avoid condensation in the reaction system, all the gas lines were heated to 150 °C.

Theoretical calculations

First-principles simulations on Cu- and H-exchanged SSZ-13 zeolites were performed using the QUICKSTEP module in the CP2K software program.[27–29] For the majority of calculations, plane wave density functional theory (DFT) calculations were carried out using the Gaussian Plane Wave (GPW) method. The BLYP exchange–correlation functional,[30,31] in combination with a double-zeta MOLOPT basis set[32] and plain wave cutoff of 300 Ry was used. For the geometry optimisations, atoms near the reactive center (*i.e.* in the D6R) were treated with Gaussian Augmented Plane Waves (GAPW) and an Ahlrichs pTZV basis set.[33] Molecular Dynamics (MD) simulations were performed on all atoms. After 2 ps equilibration with the canonical sampling through velocity rescaling thermostat,[34] the more robust Nosé–Hoover thermostat[35] was used for 13 ps with a timestep of 0.5 fs for the Cu-containing zeolites while the protonated SSZ-13 were all simulated for 32 ps with the same time step. The temperature of the simulations was held to 600 K in accordance with experiment. All post-processing of the MD simulations was done using the program MD-tracks.[36] IR properties were calculated using a Fourier-based technique with input from the MD simulations.[37] More details are given in the ESI.† In addition, IR data resulting from a static Normal Mode Analysis (NMA) on the optimized geometries are included in the ESI.† The computed harmonic frequencies are compared with the experimental data; in order to get a good quantitative agreement, scaling factors can be applied.[38] In the present work, our main interest is a good qualitative correlation, and hence the reported theoretical data are non-scaled.

The unit cell parameters were taken from crystallographic data of pure siliceous SSZ-13 and kept fixed during the optimisation. The CHA unit cell contains 36 T-sites with corresponding oxygen atoms. For both the Cu-SSZ-13 and H-SSZ-13 simulations a double Si to Al substitution was assumed. This results in unit cells containing 109 ($1Cu^{2+}$) and 110 ($2H^+$) atoms without NH_3 adsorbed and cells containing 113 and 114 atoms when NH_3 is adsorbed to the active site. Model containing a $[Cu^{2+}(OH)^-]^{2+}$ and $[Cu(NH_3)_4]^{2+}$ complex in the center of the CHA cage were also considered.

Results and discussion

The catalysts

Table 1 summarises the chemical composition of the zeolite materials used here as catalysts. The elemental analysis of

View Article Online

Paper PCCP

Table 1 Chemical analysis of the zeolites used as catalyst materials in the present study

Sample	Si/Al	Cu loading (wt%)	I.E.[a] (%)	EFAl[b] (%)
H-SSZ-13	15	—	—	—
Cu-SSZ-13(67)	15	2.0	67	5.3
Cu-SSZ-13(100)	22	2.5	100	n.d.[c]
H-CHA	2.2	—	—	18
Cu-CHA	2.2	4.9	39	18

[a] Ion exchange level (I.E.); normalised to 100% for a Cu to Al ratio of 1 : 2. [b] Determined by ^{27}Al MAS NMR (see ESI; Fig. S1). [c] Not detected.

Cu-SSZ-13(67) and Cu-CHA zeolites reveal varying Cu^{2+}-exchange levels, which can be related to the different Si/Al ratio and hence, to the different population of Brønsted acid sites in the H-form parent materials. Furthermore, the ^{27}Al MAS NMR data show the presence of different amounts of EFAl species, attributed to the different synthesis method and/or Al content of the parent materials. No effect on the Si/Al ratios was found as a result of the Cu^{2+}-exchange treatments.

The results obtained for the Cu-SSZ-13(100) zeolite indicate an increase of 25% in the Cu content after the successive exchanges, reaching a final loading of 2.5 wt%, which corresponds to the maximum ion exchange level (I.E. = 100%) of the zeolite. In addition, the results show a slightly larger Si/Al ratio, indicating that mild dealumination takes place during successive exchanges with Cu^{2+}. It should be noted, however, that no EFAl species were detected by ^{27}Al MAS NMR (see Table 1 and Fig. S1, ESI†), probably due to acid leaching of these species during the successive exchanges, conducted at a pH of 3–4. Furthermore, the XRD patterns (see ESI;† Fig. S2) indicate that the crystallinity of the zeolite is maintained after the successive exchanges with Cu^{2+}.

To obtain further insight in the nature of the active sites, FTIR measurements of the dehydrated zeolites were performed and combined with DFT-based simulations of vibrational frequencies. Prior to the experiment, pre-adsorbed water molecules were removed by treating the zeolite materials for 12 h with 10% O_2 in He at 250 °C, thus preventing self-reduction of the Cu^{2+} ions.[19–21] Fig. 1 depicts the FTIR spectra of the dehydrated zeolites, acquired at 250 °C under flow conditions (10% O_2 in He). As clearly seen, the spectra show the presence of a very sharp peak, at 3735 cm^{-1}, that could be attributed to isolated internal silanol groups.[39,40] This peak becomes more evident for the Cu-SSZ-13(100) zeolite (Fig. 1c), consistent with mild dealumination occurring during the consecutive exchanges, as indicated above. No bands at 3675 cm^{-1}, corresponding to OH groups in partially extra-lattice positions,[40–43] were detected for the SSZ-13 zeolites (Fig. 1a–c), whereas for the high-silica CHA zeolites (Fig. 1d–e) this component may not be observable since it could be superimposed with other bands in the hydroxyl region.

A very broad band is found in the spectra of H-CHA and Cu-CHA zeolites, with a maximum at 3611 cm^{-1}, corresponding to Brønsted acidic OH groups. In contrast, two kinds of bridging hydroxyl groups can be observed in the spectra of the dehydrated H-SSZ-13, Cu-SSZ-13(67) and Cu-SSZ-13(100) zeolites, with bands

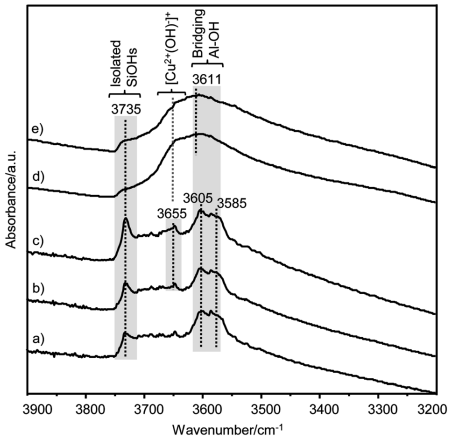

Fig. 1 FTIR spectra of H-SSZ-13 (a), Cu-SSZ-13(67) (b), Cu-SSZ-13(100) (c), H-CHA (d), and Cu-CHA (e) zeolites, activated with 10% O_2 in He, at 250 °C for 12 h.

at 3605 and 3585 cm^{-1}. It is known that CHA-type zeolites present four symmetrically non-equivalent acid OH groups, with approximately the same stability and acid strength;[43–47] three sites are part of an 8-ring connecting two cages, whereas the fourth group is in contact only with one cage. To further validate previous assignments, periodic models were constructed for the H-form SSZ-13 zeolite (see Fig. S5, ESI†), and the O(1) and O(2) sites, corresponding to the high- and low-frequency bands, respectively, were both considered; O(1) site belongs to two 4-ring and one 8-ring, whereas O(2) belongs to one 4-ring, one 6-ring and one 8-ring ring. From the MD simulations, the ν(OH) stretching frequencies for the O(1) and O(2) site were found at 3626 and 3562 cm^{-1}, respectively, in line with the experiment and with previous studies.[43–47]

Importantly, the FTIR spectrum of the zeolite with 100% exchange (see Fig. 1c), shows two intense bands of the bridging hydroxyl groups, at 3605 and 3585 cm^{-1}, comparable to those observed for the Cu-SSZ-13(67) zeolite, indicating that the Brønsted acid sites remain in the sample despite complete Cu^{2+}-exchange. This could be caused by the presence of a second type of Cu site (*i.e.* Cu oxides), not occupying the framework exchange positions, and thus requiring the presence of residual protons to ensure framework neutrality. However, the UV-Vis-NIR DRS and EXAFS data of the hydrated Cu-SSZ-13(100) zeolite (see ESI;† Fig. S7 and S8 and Table S2) show that almost all the Cu is present as isolated Cu^{2+} ions, with only a very small fraction of the Cu atoms not located in exchange positions, as CuO species. Therefore, the signal intensity attributable to Brønsted acidity in Cu-SSZ-13(100) zeolite is too large to be due to the presence of such small amount of extra-framework CuO and other possibilities should be considered, such as the presence of Cu species balanced by isolated Al atoms.[21,48–51]

In recent times, it has been proposed that two different Cu sites in CHA-type zeolites exist and that their occupation depends upon Cu exchange level; at low loadings, Cu^{2+} ions are located in the D6R units, whereas at high loadings the ions are located inside the large cages.[52–55] More recently, Giordanino *et al.* reported the presence of different Cu species on O_2 activated Cu-SSZ-13 samples (Si/Al = 13.1; Cu/Al = 0.444);[21] in addition to the well-known isolated Cu^{2+} ions, monovalent Cu^{+} and $[Cu^{2+}(OH)^{-}]^{+}$ species were also detected, for which Al pairs are not required to achieve charge compensation. The authors observed that the concentration of Brønsted sites was not affected by the activation treatment, obtaining similar intensities of the Brønsted acid sites for the samples activated in O_2 or in vacuum conditions.[21] Accordingly, no new bridging hydroxyls were created during the vacuum treatment to compensate the loss of positive charge as a result of Cu^{2+} self-reduction, and the authors concluded that not all the Cu^{2+} ions initially present were balancing the negative charge created by two Al atoms, being also probably in the form of monovalent $[Cu^{2+}(OH)^{-}]^{+}$ species.[21] The presence of $[Cu^{2+}(OH)^{-}]^{+}$ complexes was verified by using both CO and NO as probes, confirming the formation of Cu–OH···CO adducts and mono-nitrosyls, respectively. Additionally, the authors assigned the stretching OH band at 3657 cm^{-1} to the ν(OH) stretch of $[Cu^{2+}(OH)^{-}]^{+}$ complexes.[21]

Interestingly, the spectrum of the Cu-SSZ-13(100) zeolite (Fig. 1c) shows the presence of a broad band in the range from 3647 to 3666 cm^{-1}, centred at 3655 cm^{-1}, much more intense than for the Cu-SSZ-13(67) sample (Fig. 1b), suggesting the presence of monovalent $[Cu^{2+}(OH)^{-}]^{+}$ species. This could explain the excess of Brønsted acidity observed for Cu-SSZ-13(100) zeolite, for which the maximum cation exchange capacity has already been reached. To gain further insight into the origin of this band, the theoretical stretching frequency of the $[Cu^{2+}(OH)^{-}]^{+}$ complex in a CHA-type zeolite was also calculated. The computed FTIR spectrum resulting from a molecular dynamic investigation shows two peaks which represent different orientations of the OH group, corresponding to OH stretch vibrations around 3614 cm^{-1} and 3660 cm^{-1} (the optimized geometries of the complexes are shown in Fig. 2). During the simulation, the OH is mainly oriented away from the framework and no hydrogen bond is formed between the OH group and framework oxygen atoms (Fig. 2b). This corresponds to a vibrational peak at *ca.* 3660 cm^{-1}, in excellent agreement with the results here and those presented before.[21] Clearly, this result shows that not all the Cu^{2+} ions are balancing the negative charge created by two Al atoms, since some of the Cu species are present in the form of monovalent $[Cu^{2+}(OH)^{-}]^{+}$ complexes, thus resulting in a greater than expected number of Brønsted acid sites, as observed in the FTIR spectrum of the dehydrated Cu-SSZ-13(100) zeolite.

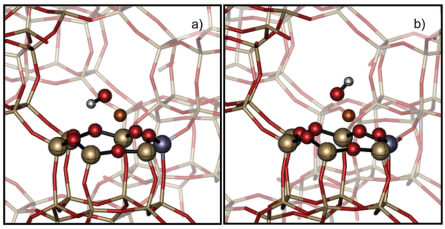

Fig. 2 Optimized structures for $[Cu^{2+}(OH)^{-}]^{+}$ complexes in SSZ-13 zeolite. Gold: Si, dark blue: Al, red: O, orange: Cu and white: H.

Identification of NH_3 species in CHA-type zeolites

As mentioned in the Introduction, the type of NH_3 species formed on Cu-SSZ-13 has been previously investigated by DRIFTS.[17] Zhu *et al.* identified two different NH_3 species; namely Brønsted acid site-adsorbed NH_3 and Lewis acid site-adsorbed NH_3. However, very little information was obtained on the type of complexes formed upon the interaction with either the Cu^{2+} or the Brønsted acid sites and the influence of EFAl species was not considered.[17] In addition, the zeolite sample was activated in flowing He, leading to some extent, to Cu^{2+} to Cu^{+} self-reduction.[19–21] This could also result in a different acid strength of the Brønsted acid sites, as previously observed for vacuum activated samples.[21] In this work, all the zeolite samples were activated with 10% O_2 in He, at 250 °C for 12 h, in order to avoid Cu^{2+} self-reduction.

The interaction of NH_3 with the bridging hydroxyl groups was modelled using OH groups at different framework positions, *i.e.* O(1) and O(2), representative of the high- and low-frequency bands, respectively (Fig. 3a and b), as described above. The optimized theoretical structures indicate that NH_3 molecules are protonated in both complexes, forming stable NH_4^{+} ions on the Brønsted hydroxyl groups of the zeolite. For the adsorption NH_3 on the Cu^{2+}-exchanged SSZ-13 zeolite, two different situations were considered; the adsorption of only one NH_3 molecule (NH_3@Cu^{2+} site; Fig. 3c), maintaining the interactions between the Cu^{2+} ions and the framework oxygen atoms, and a $[Cu(NH_3)_4]^{2+}$ complex

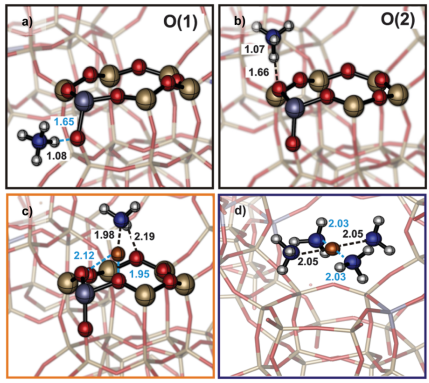

Fig. 3 Optimized structures of NH_3 on a Brønsted acid site at O(1) (a) and O(2) (b) framework positions; on a Cu^{2+} site (c) and of the $[Cu(NH_3)_4]^{2+}$ complex (d) in SSZ-13. Blue: N, gold: Si, dark blue: Al, red: O, orange: Cu and white: H. Distances are expressed in angstroms.

View Article Online

Paper PCCP

Table 2 Experimental and theoretical frequencies of NH_3 species formed on the acid sites of CHA-type zeolites

		ν_{theor} (cm^{-1})			
	ν_{exp} (cm^{-1})	O(1)	O(2)	Assignment	Ref.
NH_3@Brønsted site	3400–3100	3480–3200		$\nu(NH_4^+)$	11, 45, 56, 58
	1455–1448	1432	1455	$\delta(NH_4^+)_{as}$	11, 45–46, 57–58
	1401–1393	1370	1368	$\delta(NH_4^+)_s$	11, 45–46, 57–58
		ν_{theor} (cm^{-1})			
	ν_{exp} (cm^{-1})	$[Cu(NH_3)]^{2+}$	$[Cu(NH_3)_4]^{2+}$	Assignment	Ref.
NH_3@Cu^{2+} site	3400–3100	3480–3200		$\nu(NH_3)$ of NH_3 in $[Cu(NH_3)_4]^{2+}$	42, 56
	1619	1601	1606	$\delta(NH_3)_{as}$ of NH_3 in $[Cu(NH_3)_4]^{2+}$	42, 56–57
	—	1535	—	H-bonded $\delta(NH_3)_{as}$ in $[Cu\text{-}NH_3]^{2+}$	—
	1278	1271	1285	NH_3 wagging of NH_3 in $[Cu(NH_3)_4]^{2+}$	42, 56–57
NH_3@EFAl	1620[a]	[b]		Weakly adsorbed NH_3 on Lewis sites	59
	1332–1324	[b]		Strongly adsorbed NH_3 on EFAl	59

[a] Only detected in low silica H-CHA zeolite; overlapped in the spectra of the Cu-zeolites with the $\delta(NH_3)_{as}$ of NH_3 in $[Cu(NH_3)_4]^{2+}$. [b] Not modeled.

($(NH_3)_4$@Cu^{2+} site; Fig. 3d), centred in the zeolite cage, for which the Cu–O interactions are absent (see ESI†). Table 2 gives an overview of the assigned theoretical and experimental frequencies. The structures of the NH_3@Brønsted site (O1) and NH_3@Brønsted site (O2) complexes present two peaks in the bending region, corresponding to the symmetric and anti-symmetric vibrations of the chemisorbed NH_4^+ ions. In contrast, the structure of the NH_3@Cu^{2+} site complex presents a third IR active peak, at 1535 cm^{-1}, arising from the interaction between a hydrogen atom of NH_3 and a framework oxygen atom (see Fig. 3b). Due to the presence of different NH_3 molecules, the vibrational analysis of the $[Cu(NH_3)_4]^{2+}$ complex shows several contributing modes; the main theoretical absorbance bands, shown in Table 2, are very close to the experimental values previously obtained for this complex on Cu-containing zeolites.[42,56,57]

Fig. 4a displays the FTIR difference spectrum of the H-SSZ-13 zeolite acquired after NH_3 adsorption at 250 °C. As expected, the spectrum shows the disappearance of the bands of the bridging hydroxyl groups, at 3605 and 3585 cm^{-1}, together with the appearance of new features, at 3400–3100 and 1429 cm^{-1}, attributed to stretching[11,45,56,58] and bending[11,45,46,57,58] vibrations respectively, of NH_4^+ ions, resulting from NH_3 protonation over the Brønsted acidic hydroxyl groups (see Table 2). The band centred at 1429 cm^{-1} is a combination of two different contributions, at 1448 and 1393 cm^{-1}, which can be readily assigned to the anti-symmetric and symmetric bending vibrations of NH_4^+ ions respectively, in accordance with the theoretical calculations (see Table 1) and also with previous works.[11,45,46,57,58] Conversely, the spectra recorded for the Cu^{2+}-loaded SSZ-13 zeolites (Fig. 4b and c) show the presence of additional bands in the bending region, at 1619 and 1278 cm^{-1}, of NH_3 adsorbed over the Cu^{2+} Lewis sites of the zeolite, resulting in a $[Cu(NH_3)_4]^{2+}$ complex, in agreement with the calculated frequencies (Table 2). It is important to note that the ν(OH) stretch of $[Cu^{2+}(OH^-)]^+$ complexes is observed as a negative band after NH_3 adsorption, indicating that NH_3 molecules are also adsorbed on this particular site.

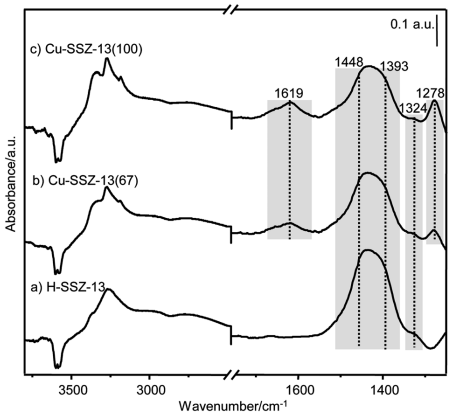

Fig. 4 FTIR difference spectra of NH_3 adsorbed on H-SSZ-13 (a), Cu-SSZ-13(67) (b), and Cu-SSZ-13(100) (c) zeolites at 250 °C. Note the presence of at least two different NH_3 species: NH_4^+ ions (1448 and 1393 cm^{-1}) and $Cu[(NH_3)_4]^{2+}$ complexes (1619 and 1278 cm^{-1}).

The interaction of NH_3 with EFAl species, also possessing Lewis acid character, can clearly be seen in the spectra of the low-silica CHA-type zeolites (Fig. 5), containing ~18% EFAl species (as seen by ^{27}Al MAS NMR; Table 1). Similarly to Cu-SSZ-13 zeolites, the spectrum of the Cu-CHA zeolite (Fig. 5b) shows the corresponding vibrations of NH_4^+ ions and $[Cu(NH_3)_4]^{2+}$ complexes, accompanied by an intense band, at 1327 cm^{-1}, attributed to NH_3 species strongly adsorbed on EFAl species.[59] In accordance, the spectrum of the H-form zeolite (Fig. 5a) also shows the presence of this band, together with the characteristic vibration of weakly adsorbed NH_3 on Lewis acid sites, at 1620 cm^{-1},[59] overlapped for Cu-CHA with the band of the $[Cu(NH_3)_4]^{2+}$ complex (Fig. 5b). Whilst the peak corresponding to strongly adsorbed NH_3 on EFAl is also present in the spectra of the Cu-SSZ-13(67) zeolite (1324 cm^{-1}, Fig. 4b),

View Article Online

PCCP Paper

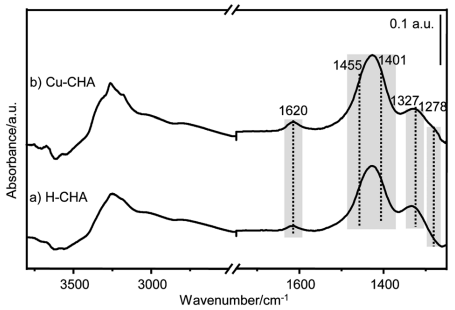

Fig. 5 FTIR difference spectra of NH_3 adsorbed on H-CHA (a), and Cu-CHA (b) zeolites at 250 °C. Note the presence of at least three different NH_3 species: NH_4^+ ions (1455 and 1401 cm^{-1}), $Cu[(NH_3)_4]^{2+}$ complexes (1620 and 1278 cm^{-1}) and NH_3 coordinated with extra-framework Al (EFAl) species (1620 and 1327 cm^{-1}).

with 5.3% of EFAl species (Table 1), the low intensity when compared with that of the Cu-CHA zeolite suggests that EFAl species barely contribute to the band at 1619 cm^{-1} for the SSZ-13 zeolites.

Therefore, three different types of NH_3 species have been found in CHA-type zeolites; NH_4^+ ions formed on the Brønsted acid sites, $[Cu(NH_3)_4]^{2+}$ complexes, resulting from NH_3 coordination with the Cu^{2+} Lewis sites, and, when present, NH_3 coordinated with EFAl species. Importantly, for completeness we observe that NH_3 molecules can also be physisorbed or weakly adsorbed at lower temperatures (see NH_3-TPD profiles below).

To provide further support to those assignments, NH_3-TPD measurements were performed. Consistent with the *in situ* FTIR results, the NH_3-TPD profiles of the high-silica Cu-SSZ-13 zeolites (Fig. 6) reveal two different desorption peaks above 250 °C (intermediate-temperature (IT) and high-temperature (HT) peaks; Fig. 6), corresponding to acid sites with different acid strength.

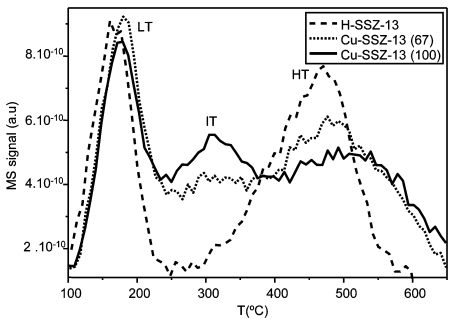

Fig. 6 NH_3-TPD profiles of H-SSZ-13, Cu-SSZ-13(67) and Cu-SSZ-13(100) zeolites. LT: low temperature peak; IT: intermediate temperature peak, and HT: high temperature peak.

In contrast, the profile of H-SSZ-13 shows only one desorption peak above this temperature (HT peak; Fig. 6). The low-temperature (LT) desorption peak, observed at 180 °C, corresponds to weakly bound NH_3,[60] and has been previously assigned either to NH_3 molecules solvating the NH_4^+ ions (*e.g.*, in $N_2H_7^+$ dimers) or to NH_3 desorbed from Lewis sites;[59,61] however, its identification is still a matter of controversy and its participation in the SCR reaction is ambiguous.[62] According to the desorption temperature observed for weakly bound NH_3 (180 °C), it appears that these species don't play any role in the present study; NH_3 adsorption was carried out at 250 °C for the *in situ* FTIR studies, so weakly bound NH_3 molecules are unlikely to be present on the catalyst surface at this temperature. Additionally, the high-temperature (HT) desorption peak, in the temperature range of 250–450 °C, is considered to be due to strongly bound NH_3, arising from protonated NH_3 formed over the Brønsted acid sites.[60]

After Cu^{2+}-exchange, the NH_3-TPD profile of Cu-SSZ-13(67) shows the presence of an extra desorption peak (IT peak) at 320 °C, attributed to NH_3 adsorbed over the Cu^{2+} sites, demonstrating that Cu^{2+}-exchange provides additional adsorption sites for NH_3, and consequently a reduction in the total number of Brønsted acid sites.[61] Accordingly, a significant decrease in the intensity of the HT peak is observed, together with a shift in the peak maximum to higher temperatures, indicating, as expected, a higher acid strength of the remaining Brønsted sites. Moreover, the broadening of the HT peak after ion exchange suggests an increase in heterogeneity of these sites after Cu^{2+}-exchange, with acid sites of varying strength being present.

In the case of the Cu-SSZ-13(100) zeolite, the higher Cu^{2+} loading is evidenced by a more pronounced increase in the intensity of the IT peak. However, despite the fact the maximum cation exchange level of the zeolite has been reached, the NH_3-TPD profile still shows an intense desorption peak at high temperatures, supporting the notion that some of the Cu^{2+} ions are present as monovalent complexes, for which Al pairs are not required for achieving charge balance. Nevertheless, the HT peak decreases in intensity, and is displaced slightly to higher temperatures, thus indicating a reduction in the number of the Brønsted sites accompanied by a small increase in their strength. This effect could be explained due to both an increase in the Cu^{2+} loading and the dealumination of the zeolitic framework that takes place during the consecutive exchanges with Cu^{2+}.

NH_3 availability and reactivity in CHA-type zeolites

The evolution of the different types of NH_3 species during SCR (250 °C; 1000 ppm NO and 5% O_2) was followed as a function of time by *in situ* FTIR, as outlined in Fig. 7 and 8. The results obtained for the Cu-SSZ-13(67) zeolite, show different reactivities for NH_3 species under SCR conditions; the spectrum recorded after 4 min (Fig. 7b) shows the disappearance of the NH_3 species adsorbed over Cu^{2+} ions to be almost complete, whereas the NH_4^+ ions formed over the Brønsted acid sites remain. The results are therefore consistent with those recently reported.[14,17]

View Article Online

Paper PCCP

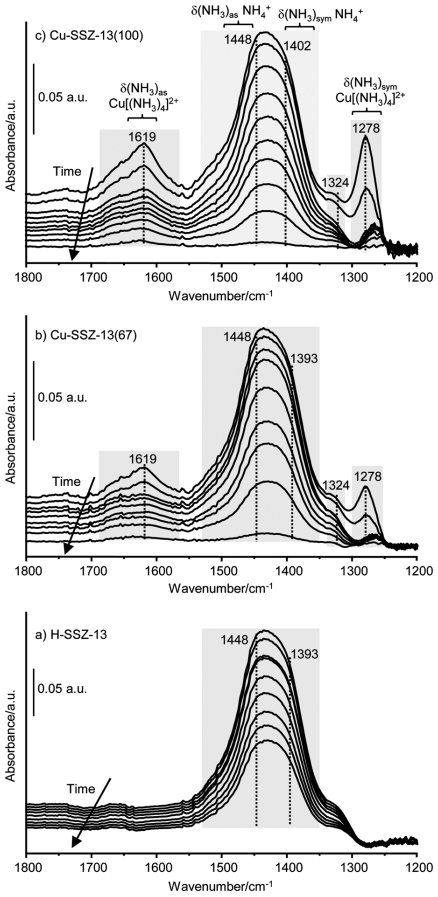

Fig. 7 NH_3 species reactivity during SCR (250 °C; 1000 ppm NO and 5% O_2) on H-SSZ-13 (a) and Cu-SSZ-13(67) (b) zeolites at 0 s, 35 s, 4 min, 1 h, 2 h, 3 h, 4 h, 5 h and 6 h of reaction time; and Cu-SSZ-13(100) (c) zeolite at 35 s, 2 min, 3 min, 4 min, 7 min, 9 min, 11 min, 14 min and 20 min of reaction time. Note the presence of at least two different NH_3 species: NH_4^+ ions (1448 and 1393 cm^{-1}) and $Cu[(NH_3)_4]^{2+}$ complexes (1619 and 1278 cm^{-1}).

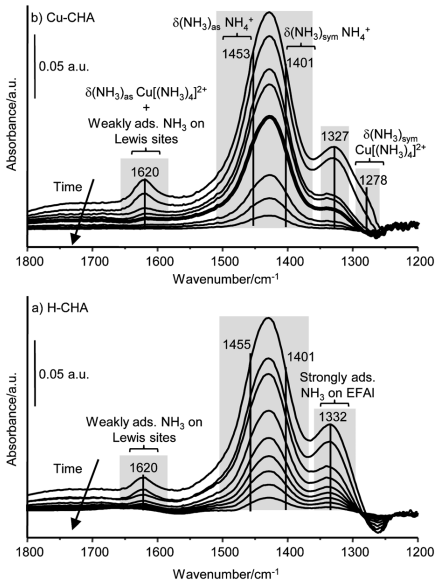

Fig. 8 NH_3 species reactivity during SCR (250 °C; 1000 ppm NO and 5% O_2) on H-CHA (a) and Cu-CHA (b) zeolites at 0 s, 35 s, 4 min, 1 h, 2 h, 3 h, 4 h, 5 h and 6 h of reaction time. Note the presence of at least three different NH_3 species: NH_4^+ ions (1455 and 1401 cm^{-1}), $Cu[(NH_3)_4]^{2+}$ complexes (1620 and 1278 cm^{-1}) and NH_3 coordinated with extra-framework Al (EFAl) species (1620 and 1332/1327 cm^{-1}).

Interestingly, the disappearance of NH_4^+ ions is much slower for the H-form zeolite, as evidenced by the spectrum recorded after 6 h (Fig. 7a). The reaction of NH_4^+ species is complete for the Cu-SSZ-13(67) zeolite after 6 h, while for the H-SSZ-13 zeolite the reaction takes more than 8 h, demonstrating the important role of the Cu^{2+} Lewis sites in the SCR reaction. These results suggest that the NH_4^+ ions formed at Brønsted acid sites barely contribute to the SCR process and may not be indispensable for the NH_3-SCR reaction, but function predominantly as NH_3 storage sites, as previously indicated.[12–14] This is likely to prove problematic at elevated temperatures (*e.g.*, temperature spikes), where NH_4^+ will be released (NH_3 slip) or else combusted (unexpected NO_x/N_2O release). Therefore, a reduced number of Brønsted sites would be favourable for the NH_3-SCR reaction.

Importantly, in the case of the Cu-SSZ-13(100) zeolite (Fig. 7c), the disappearance of NH_4^+ species is comparatively much faster than for Cu-SSZ-13(67), being complete after just 20 min of reaction. This result indicates that the availability of NH_4^+ ions can be particularly improved by submitting the zeolite to repeated exchanges with Cu^{2+}, most likely related with a modification of the acid strength and distribution of the acid sites during the repeated exchanges (see below). Since the differences in the chemical composition of the zeolites are not very pronounced (see Table 1), the enhanced reactivity of NH_4^+ ions cannot be definitively attributed to the higher amount of Cu present or the higher Si/Al ratio. Moreover, in view of the very low amounts of CuO detected within this sample (see ESI;† Fig. S7 and S8 and Table S2), the presence of these species cannot be considered as a possible reason of the enhanced reactivity.

In contrast to the results obtained for SSZ-13 zeolites, the spectra recorded for the Al-rich CHA materials (see Fig. 8), with ~18% of EFAl species, reveal very similar reactivities of NH_4^+ ions for both the H-form and the Cu^{2+}-exchanged zeolite; after

5 h of reaction, the spectrum recorded for the Cu-CHA zeolite shows almost complete disappearance of the NH_4^+ ions, whereas for the H-CHA zeolite the reaction is complete after almost 6 h. Comparison of these results with those obtained for the H-SSZ-13 and Cu-SSZ-13 zeolites, shown in Fig. 7, suggests that EFAl species, with Lewis acid character, could have a positive influence in the reaction rate of NH_4^+ ions for the low silica CHA zeolites, enhancing the availability of NH_3 molecules for the reaction. It is generally accepted that thermal and hydrothermal treatments of zeolites commonly lead to the abstraction of lattice Al atoms to form extra-framework Al (EFAl).[63] Depending on the experimental conditions and the zeolite type, a large number of Al atoms can be released from the framework, along with an enhancement of the Lewis acidity.[63] This is of particular importance for the SCR reaction, since hydrothermal ageing is one the main deactivation mechanisms.[64] To our knowledge, the influence of EFAl species in NH_3-SCR has received little attention so far.[57,65–67] Previous studies using NaY zeolites showed faster reaction rates and improved selectivity for nanocrystalline NaY, attributed to the increased external surface area, concentration of silanol groups and EFAl species on the external surface.[57,65] Moreover, investigation of the activity of H-ZSM-5 showed an enhanced reaction rate after mild steaming, suggesting the participation of EFAl species in the catalytic process.[66] In contrast, studies with dealuminated mordenites indicated a site-blocking effect due to the presence of polymeric EFAl species, which limit the accessibility to the sites responsible of the catalytic activity.[67] The results here obtained suggest a positive influence of the presence of EFAl species for the low silica CHA zeolites however, further experiments need to be performed to reach definitive conclusions, using different CHA zeolites with similar Si/Al ratios and Cu loadings, as well as varying amounts of EFAl species.

As previously mentioned, the characterisation results obtained for the high silica Cu^{2+}-loaded SSZ-13 zeolites (see above) showed very little differences between the catalysts, so no definitive conclusions could be made about the improved reactivity of the NH_4^+ ions. In an attempt to determine the influence of the ion exchange treatments on the reactivity of NH_4^+ ions, the two Cu^{2+}-containing SSZ-13 zeolites were further characterised by SEM and N_2 adsorption measurements. Moreover, activity tests were carried out under standard SCR conditions, using a GHSV of 100 000 h^{-1}.

Again, the N_2 adsorption measurements showed very similar results (see ESI;† Table S3); both Cu^{2+}-loaded zeolites present a typical type I isotherm, corresponding to a fully microporous material, so that the presence of an additional mesopore system in Cu-SSZ-13(100) produced as a consequence of the framework dealumination is not a possible reason of the enhanced reactivity. Identical results were also obtained by SEM (see ESI;† Table S3), ruling out a possible change in the crystal size and/or morphology after Cu exchange. In contrast, the catalytic tests performed, presented in Fig. 9, show a substantial improvement in the low temperature activity for the Cu-SSZ-13(100) sample. Both Cu-loaded zeolites present a

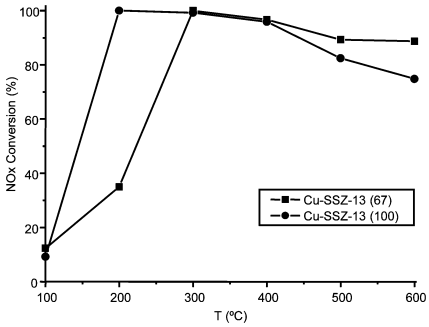

Fig. 9 NO_x conversion for Cu-SSZ-13(67) and Cu-SSZ-13(100) at different temperatures, using a GHSV of 100 000 h^{-1} and a feed composition of 1000 ppm NO, 1000 ppm NH_3 and 5% O_2.

notable activity over a wide temperature window however, in the case of the Cu-SSZ-13(100) zeolite, there is an important enhancement in NO conversion at low temperatures, from 30% in Cu-SSZ-13(67) to 100% in the Cu-SSZ-13(100) at 200 °C. A more pronounced drop in activity is found at temperatures up to 400 °C, attributed to the oxidation of NH_3 at high temperatures.[68] Clearly, these results are in contrast with those obtained by Kwak *et al.* for a series of Cu-SSZ-13 zeolites with different ion exchange levels;[69] just a slight increase in the activity at 200 °C was observed by increasing the ion exchange level from 20 to 40%, remaining almost constant at loadings above 40%. We note however, that the zeolites employed were synthesized by a different method, presenting a higher activity at 200 °C (~70%).[69] Therefore, the results here obtained give strong support to the idea that the enhanced reactivity is not related with the higher Cu loading of the Cu-SSZ-13(100) zeolite. In fact, similar results were recently reported by Martinez-Franco *et al.*, using Cu-SSZ-13 zeolites synthesized by one-pot methods.[70] The authors observed very different catalytic activities for Cu-SSZ-13 zeolites presenting the same chemical composition and similar crystal size, and pointed out a possible influence of the synthesis method, which could affect the Al distribution.[70]

Though work is in progress to shed further insight in the reasons behind the results here presented for the Cu-SSZ-13(100) zeolite, both the improved reactivity of NH_4^+ ions and the high activity at low temperatures could be indeed related to a different acid site distribution within the zeolitic crystals, leading to an enhanced NH_3 availability under SCR conditions. It is commonly accepted that Al atoms are not evenly distributed within the zeolite framework and that the probability of the presence of Al pairs decreases with the Al content. Hence, it is reasonable to think that the formation of $[Cu^{2+}(OH)^-]^+$ complexes is directly related with the Al content and its distribution within the zeolite crystals, as previously indicated.[21] Most likely, a particular Al distribution is achieved for the Cu-SSZ-13(100) zeolite crystals upon the consecutive exchanges

View Article Online

Paper PCCP

with Cu^{2+} (as well as the repeated calcinations), favouring the formation of $[Cu^{2+}(OH)^-]^+$ species and possibly influencing the acidic properties of the zeolite. It is known that the acid strength of the Brønsted sites is strongly influenced by the site location, but also by the Cu distribution; *i.e.* metal cations are considered as electron acceptors, so a Brønsted site located close to the metal cation becomes electron deficient, thus becoming a strong Brønsted site. Therefore, both Al and Cu distribution may have an important influence on the acidic strength of the Brønsted acid sites present in the Cu-SSZ-13(100) zeolite, enhancing the availability of NH_4^+ ions at low temperatures. Little information about the influence of exchange treatments on the acidic properties is available in the literature, so investigations are now being carried out to understand the influence of the different exchange protocols on the acid site distribution of the zeolite.

Conclusions

To gain further insight into NH_3 storage, availability and reactivity in Cu-Chabazite-based NH_3-SCR systems, the type and nature of NH_3 species adsorbed on CHA-type zeolites and their evolution under standard SCR conditions have been investigated by combining *in situ* FTIR spectroscopy with theoretical calculations. As catalysts, five CHA-type zeolites, with different populations of acid sites, have been used.

The zeolite samples under investigation have been characterised by several techniques, including chemical analysis, ^{27}Al MAS NMR, XRD, UV-Vis-NIR DRS or EXAFS. Additionally, the acid sites of the zeolites have also been characterised by combining FTIR measurements of the dehydrated samples (activated under O_2 flow) with theoretical calculations of vibrational frequencies. In particular, the results obtained for the Cu-SSZ-13(100) zeolite, with 100% of ion exchange degree, indicate that not all the Cu^{2+} ions are balancing the negative charge created by Al pairs, being also probably present in the form of monovalent $[Cu^{2+}(OH)^-]^+$ complexes, as previously observed by FTIR using CO and NO as probes[21] and hence resulting in an incomplete reduction in the number of Brønsted acid sites.

The most important conclusions reached in the present work are listed below as follows:

• Three different types of NH_3 species can be distinguished within Cu-Chabazite zeolites at 250 °C. They include NH_4^+ ions, resulting from NH_3 protonation over the Brønsted acid sites, $[Cu(NH_3)_4]^{2+}$ complexes formed on the Cu^{2+} Lewis sites and, when present, NH_3 adsorbed on EFAl species. Furthermore, NH_3 molecules could be also physisorbed or weakly adsorbed at low temperatures (<200 °C), although these species most likely do not play any role in the present study. These results are in contrast to those obtained in a previous work,[17] which showed the formation of only two reacting NH_3 species at 200 °C.

• The NH_4^+ ions formed on the Brønsted acid sites react very slowly in comparison to NH_3 coordinated to the Cu^{2+} ions and are likely to contribute little to the standard NH_3-SCR process. Therefore, Brønsted acid sites may not be indispensable, but act merely as NH_3 storage sites, as previously indicated by other research groups.[12–14] This could have serious implications, especially at elevated temperatures, where NH_4^+ ions are likely to become released (NH_3 slip) or else combusted (unexpected NO_x/N_2O release). Consequently, it is believed to be of particular importance to control NH_3 storage capacity to a level suitable to achieve high NO_x conversions, but not so high that it will lead to NH_3 slip at high temperatures; *i.e.* a reduced number of Brønsted sites, but with an optimal distribution and acid strength.

• The availability/reactivity of NH_4^+ ions can be however, notably improved by submitting the SSZ-13 zeolite to repeated exchanges with Cu^{2+}, leading to a substantial increase in the reaction rate of NH_4^+ species, together with an important enhancement in the low temperature activity of the zeolite, as demonstrated in Cu-SSZ-13(100). These differences are attributed to a particular Al and Cu distribution within the zeolite, favouring the formation of $[Cu^{2+}(OH)^-]^+$ species and influencing the acid strength of the remaining Brønsted sites. Within this context it has to be mentioned that the presence of EFAl species, with Lewis acid character, could also have a positive influence on the reaction rate of the NH_4^+ ions, as suggested by the low silica CHA zeolites, though more experiments are required to draw any firm conclusions.

Acknowledgements

This research was carried out under the Project number M.23.7.08301 in the framework of the Research Program of the Materials innovation institute M2i (www.m2i.nl). The authors would like to than NWO/FWO for DUBBLE beam time and Sachem inc. for kindly providing the template (Zeo-Gen2825) used in the synthesis of SSZ-13. Frank Mertens and Bart Wieland of DAF Trucks (Eindhoven, The Netherlands) are also thanked for their useful discussions and advice. This work was also supported by the Fund for Scientific Research Flanders (FWO), the Research Board of Ghent University (BOF) and from the European Research Council (ERC) under the European Community's Seventh Framework Programme [FP7(2007-2013) ERC grant agreement number 240483] and BELSPO in the frame of IAP P7/05. Computational resources and services used in this work were provided by the Stevin Supercomputer Infrastructure of Ghent University.

Notes and references

1 S. Brandenberger, O. Kröcher, A. Tissler and R. Althoff, *Catal. Rev. Sci. Eng.*, 2008, **50**, 492.
2 U. Deka, I. Lezcano-Gonzalez, B. M. Weckhuysen and A. M. Beale, *ACS Catal.*, 2013, **3**, 413.
3 J. H. Kwak, R. G. Tonkyn, D. H. Kim, J. Szanyi and C. H. F. Peden, *J. Catal.*, 2010, **275**, 187.
4 D. W. Fickel, E. D'Addio, J. A. Lanterbach and R. F. Lobo, *Appl. Catal., B*, 2011, **102**, 441.
5 S. T. Korhonen, D. W. Fickel, R. F. Lobo, B. M. Weckhuysen and A. M. Beale, *Chem. Commun.*, 2011, **47**, 800.

6 U. Deka, I. Lezcano-Gonzalez, S. J. Warrender, A. L. Picone, P. A. Wright, B. M. Weckhuysen and A. M. Beale, *Microporous Mesoporous Mater.*, 2013, **166**, 144.

7 D. W. Fickel and R. F. Lobo, *J. Phys. Chem. C*, 2010, **114**, 1633.

8 U. Deka, A. Juhin, E. A. Eilertsen, H. Emerich, M. A. Green, S. T. Korhonen, B. M. Weckhuysen and A. M. Beale, *J. Phys. Chem. C*, 2012, **116**, 4809.

9 R. Q. Long and R. T. Yang, *J. Am. Chem. Soc.*, 1999, **121**, 5595.

10 R. Q. Long and R. T. Yang, *J. Catal.*, 2002, **207**, 224.

11 J. Eng and C. H. Bartholomew, *J. Catal.*, 1997, **171**, 27.

12 S. Brandenberger, O. Kröcher, A. Wokaun, A. Tissler and R. Althoff, *J. Catal.*, 2009, **268**, 297.

13 Z. Liu, P. J. Millington, J. E. Bailie, R. R. Rajaram and J. A. Anderson, *Microporous Mesoporous Mater.*, 2007, **104**, 159.

14 D. Wang, L. Zhang, K. Kamasamudram and W. S. Epling, *ACS Catal.*, 2013, **3**, 871.

15 Y. Zhao, J. Hu, L. Hua, S. Shuai and J. Wang, *Ind. Eng. Chem. Res.*, 2011, **50**, 11863.

16 K. Kamasamudram, N. W. Currier, X. Chen and A. Yezerets, *Catal. Today*, 2010, **151**, 212.

17 H. Zhu, J. H. Kwak, C. H. F. Peden and J. Szanyi, *Catal. Today*, 2013, **205**, 16.

18 J. Wang, T. Yu, X. Wang, G. Qi, J. Xue, M. Shen and W. Li, *Appl. Catal., B*, 2012, **127**, 137.

19 S. C. Larsen, A. Aylor, A. T. Bell and J. A. Reimer, *J. Phys. Chem.*, 1994, **98**, 11533.

20 G. T. Palomino, P. Fisicaro, S. Bordiga, A. Zecchina, E. Giamello and C. Lamberti, *J. Phys. Chem. B*, 2000, **104**, 4064.

21 F. Giordanino, P. N. R. Vennestrøm, L. F. Lundegaard, F. N. Stappen, S. Mossin, P. Beato, S. Bordiga and C. Lamberti, *Dalton Trans.*, 2013, **42**, 12741.

22 M. Moliner, C. Franch, E. Palomares, M. Grill and A. Corma, *Chem. Commun.*, 2012, **48**, 8264.

23 S. Nikitenko, A. M. Beale, A. M. J. van der Eerden, S. D. M. Jacques, O. Leynaud, M. G. O'Brien, D. Detollenaere, R. Kaptein, B. M. Weckhuysen and W. Bras, *J. Synchrotron Radiat.*, 2008, **15**, 632.

24 M. Newville, *J. Synchrotron Radiat.*, 2001, **8**, 322.

25 N. Binsted, *EXCURV, CCLRC Daresbury Laboratory Computer Program*, 1998.

26 D. Massiot, F. Fayon, M. Capron, I. King, S. LeCalvé, B. Alonso, J.-O. Durand, B. Bujoli, Z. Gan and G. Hoatson, *Magn. Reson. Chem.*, 2002, **40**, 70.

27 J. VandeVondele, M. Krack, F. Mohamed, M. Parrinello, T. Chassaing and J. Hutter, *Comput. Phys. Commun.*, 2005, **167**, 103.

28 G. Lippert, J. Hutter and M. Parrinello, *Mol. Phys.*, 1997, **92**, 477.

29 G. Lippert, J. Hutter and M. Parrinello, *Theor. Chim. Acta*, 1999, **103**, 124.

30 A. D. Becke, *Phys. Rev. A: At., Mol., Opt. Phys.*, 1988, **38**, 3098.

31 C. T. Lee, W. T. Yang and R. G. Parr, *Phys. Rev. B: Condens. Matter Mater. Phys.*, 1988, **37**, 785.

32 A. Schafer, C. Huber and R. Ahlrichs, *J. Chem. Phys.*, 1994, **100**, 5829.

33 J. VandeVondele and J. Hutter, *J. Chem. Phys.*, 2007, **127**, 114105.

34 G. Bussi, D. Donadio and M. Parrinello, *J. Chem. Phys.*, 2007, **126**, 14101.

35 S. Nosé, *Mol. Phys.*, 1984, **52**, 255; S. Nosé, *J. Chem. Phys.*, 1994, **81**, 511.

36 T. Verstraelen, M. Van Houteghem, V. Van Speybroeck and M. Waroquier, *J. Chem. Inf. Model.*, 2008, **48**, 2414.

37 D. Lesthaeghe, P. Vansteenkiste, T. Verstraelen, A. Ghysels, C. E. A. Kirschhock, J. A. Martens, V. Van Speybroeck and M. Waroquier, *J. Phys. Chem. C*, 2008, **112**, 9186.

38 J. P. Merrick, D. Moran and L. Radom, *J. Phys. Chem. A*, 2007, **111**, 11683.

39 S. Bordiga, I. Roggero, P. Ugliengo, A. Zecchina, V. Bolis, G. Artioli, R. Buzzoni, G. Marra, F. Rivetti, G. Spano and C. Lamberti, *J. Chem. Soc., Dalton Trans.*, 2000, 3921.

40 A. Zecchina, S. Bordiga, G. Spoto, D. Scarano, G. Petrini, G. Leofanti, M. Padovan and C. Otero Arean, *J. Chem. Soc., Faraday Trans.*, 1992, **88**, 2959.

41 R. Buzzoni, S. Bordiga, G. Ricchiardi, C. Lamberti, A. Zecchina and G. Bellusi, *Langmuir*, 1996, **12**, 930.

42 J. Howard and J. M. Nicol, *J. Chem. Soc., Faraday Trans.*, 1989, **85**, 1233.

43 S. Bordiga, L. Regli, D. Cocina, C. Lamberti, M. Bjørgen and K. P. Lillerud, *J. Phys. Chem. B*, 2005, **109**, 2779.

44 S. Bordiga, L. Regli, C. Lamberti, A. Zecchina, M. Bjørgen and K. P. Lillerud, *J. Phys. Chem. B*, 2005, **109**, 7724.

45 K. Suzuki, G. Sastre, N. Katada and M. Niwa, *Phys. Chem. Chem. Phys.*, 2007, **9**, 5980.

46 M. Calligaris, G. Nardin, L. Randaccio and P. C. Chiaramonti, *Acta Crystallogr., Sect. B: Struct. Crystallogr. Cryst. Chem.*, 1982, **38**, 602.

47 C. Lo and B. L. Trout, *J. Catal.*, 2004, **227**, 77.

48 J. Dedecek, L. Capek, P. Sazama, Z. Sobalik and B. Wichterlova, *Appl. Catal., A*, 2011, **391**, 244.

49 L. Capek, J. Dedecek, P. Sazama and B. Wichterlova, *J. Catal.*, 2010, **272**, 44.

50 J. Dedecek, O. Bortnovsky, A. Vondrova and B. Wichterlova, *J. Catal.*, 2001, **200**, 160.

51 J. Dedecek and B. Wichterlova, *J. Phys. Chem. B*, 1997, **101**, 10233.

52 J. H. Kwak, H. Zhu, J. H. Lee, C. H. F. Peden and J. Szanyi, *Chem. Commun.*, 2012, **48**, 4758.

53 F. Gao, E. D. Walter, E. M. Karp, J. Luo, R. G. Tonkyn, J. H. Kwak, J. Szanyi and C. H. F. Peden, *J. Catal.*, 2013, **300**, 20.

54 F. Goltl, R. E. Bulo, J. Hafner and P. Sautet, *J. Phys. Chem. Lett.*, 2013, **4**, 2244.

55 F. Goltl and J. Hafner, *J. Chem. Phys.*, 2013, **136**, 064504.

56 S. Kieger, G. Delahay, B. Coq and B. Neveu, *J. Catal.*, 1999, **183**, 267.

57 S. Elzey, A. Mubayi, S. C. Larsen and V. H. Grassian, *J. Mol. Catal. A: Chem.*, 2008, **285**, 48.

58 A. Jentys, G. Warecka and J. A. Lercher, *J. Mol. Catal.*, 1989, **51**, 309.

59 M. Niwa, S. Nishikawa and N. Katada, *Microporous Mesoporous Mater.*, 2005, **82**, 105.
60 E.-Y. Choi, I.-S. Nam and Y. G. Kim, *J. Catal.*, 1996, **161**, 597.
61 G. V. A. Martins, G. Berlier, C. Bisio, S. Coluccia, H. O. Pastore and L. Marchese, *J. Phys. Chem. B*, 2008, **112**, 7193.
62 A. Sultana, T. Nanba, M. Sasaki, M. Haneda, K. Suzuki and H. Hamada, *Catal. Today*, 2011, **164**, 495.
63 R. D. Shannon, K. H. Gardner, R. H. Staley, G. Bergeret, P. Gallezot and A. Auroux, *J. Phys. Chem.*, 1985, **89**, 4778; A. Poppl, T. Rudolf and D. Michel, *J. Am. Chem. Soc.*, 1998, **120**, 4879.
64 J. H. Kwak, D. Tran, S. D. Burton, J. Szanyi, J. H. Lee and C. H. Peden, *J. Catal.*, 2012, **287**, 203.
65 G. Li, C. A. Jones, V. H. Grassian and S. C. Larsen, *J. Catal.*, 2005, **234**, 401.
66 S. A. Stevenson, J. C. Vartuli and S. B. Sharma, *J. Catal.*, 2002, **208**, 106.
67 M. Lezcano, A. Ribotta, E. Miro, E. Lombardo, J. Petunchi, C. Moreaux and J. M. Dereppe, *J. Catal.*, 1997, **168**, 511.
68 S. M. Jeong, S. H. Jung, K. S. Yoo and S. D. Kim, *Ind. Eng. Chem. Res.*, 1999, **38**, 2210.
69 J. H. Kwak, D. Tran, J. Szanyi, C. H. F. Peden and J. H. Lee, *Catal. Lett.*, 2012, **142**, 295.
70 R. Martinez-Franco, M. Moliner, J. R. Thogersen and A. Corma, *ChemCatChem*, 2013, **5**, 3316.

Electronic Supplementary Material (ESI) for Physical Chemistry Chemical Physics

Electronic Supporting Information:

^{27}Al MAS NMR of Cu-containing SSZ-13 zeolites

Figure S1 displays the ^{27}Al MAS NMR spectra acquired for the two Cu-loaded SSZ-13 zeolites. Both spectra are dominated by a signal at 58 ppm, corresponding to tetrahedrally-coordinated Al species. A very weak signal is found however, for the Cu-SSZ-13(67) zeolite, at c.a. 0 ppm, of octahedral Al, indicating the presence of very small amounts of extra-framework Al species (see Table 1).

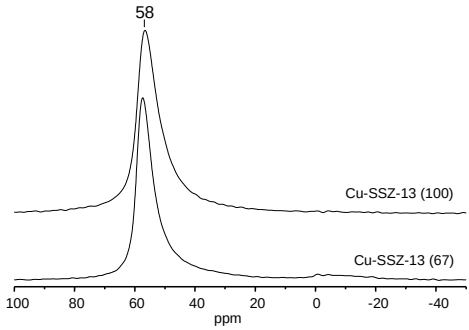

Figure S1. ^{27}Al MAS NMR spectra of Cu-SSZ-13 (67) and Cu-SSZ-13 (100) zeolites.

X-ray diffraction (XRD) of Cu-containing SSZ-13 zeolites

The XRD patterns (Figure S2) indicate that the crystallinity of the zeolite is maintained.

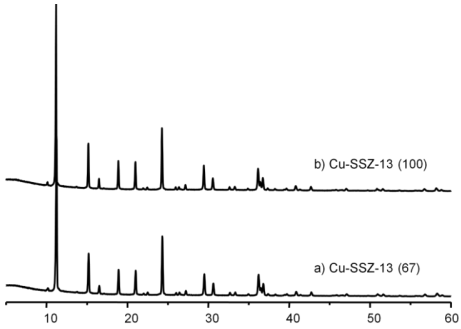

Figure S2. XRD patterns of Cu-SSZ-13 (67) (a) and Cu-SSZ-13 (100) (b) zeolites.

Electronic Supplementary Material (ESI) for Physical Chemistry Chemical Physics

Detailed information on the theoretical calculations

Cu-exchanged model

The static geometry optimization results in a four-folded coordination for the Cu-SSZ-13 system (see Figure S3) with Cu-O separations ranging from 2.04 to 2.30 Å and a significantly distorted local environment, i.e. the six-membered ring.

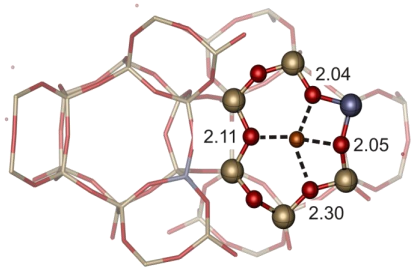

Figure S3. Optimized Cu-SSZ-13 structure with special indication of the local geometry of the metal ion. Relevant Cu-O distances are given in Å.

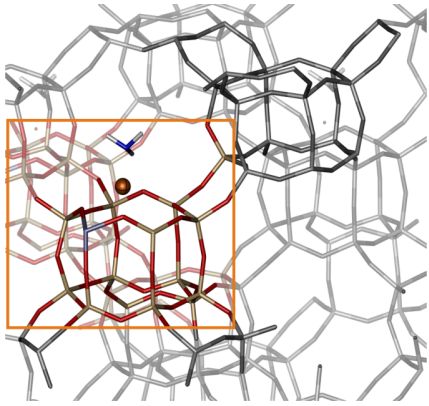

Figure S4. Periodic structure of a Cu-exchanged SSZ-13 zeolite used for the first-principles simulations.

Electronic Supplementary Material (ESI) for Physical Chemistry Chemical Physics

H-exchanged models

For the proton-exchanged SSZ-13 zeolites (H-SSZ-13), periodic models were constructed containing two acidic protons (due to the double Si to Al substitution) and hence 110 atoms (the periodic structure is depicted in Figure S5). Two framework positions were distinguished, in particular the O(1) and O(2) positions corresponding with the low- and high-frequency band, respectively.

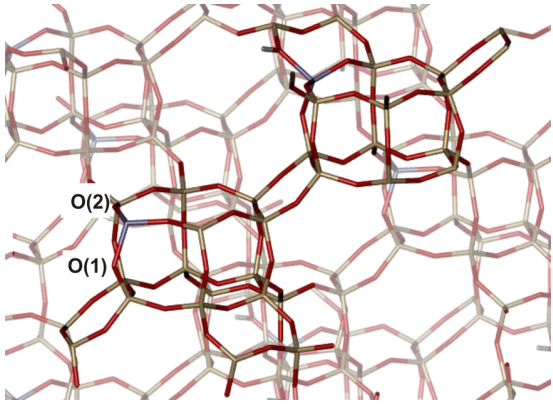

Figure S5. Periodic structure of a H-exchanged (proton not shown) SSZ-13 zeolite used for the first-principles simulations. Two different framework positions, O(1) and O(2), are indicated.

IR Simulations

After the geometry optimization, IR properties are calculated using two different methods: a static normal mode analysis (NMA) using the optimized geometry and a Fourier-based technique with input from molecular dynamics (MD) simulations. The NMA and MD simulations were performed applying the same computational details used for the geometry optimizations, however all atoms were described at the GPW level.

Electronic Supplementary Material (ESI) for Physical Chemistry Chemical Physics

Static NMA. A partial Hessian analysis was performed for the NMA calculations where only the relevant portion of the chemically active center - i.e. the Cu^{2+} ion, the ammonia molecule and a single six-membered ring in which the Lewis or Brønsted acid site is located - is taken into account, and all other atoms were fixed. For the $[Cu(NH_3)_4]^{2+}$ complex, the atoms of the six-membered ring were not included in the NMA analysis since they interact little with the complex. The focus of this study is on the region above 1200 cm^{-1} and hence there is no need to include global motions which are found at much lower wavenumbers.

Molecular Dynamics. The MD calculations were performed on all atoms. After 2 ps equilibration with the canonical sampling through velocity rescaling thermostat,[1] the more robust Nosé–Hoover thermostat[2] was used for 13 ps with a timestep of 0.5 fs for the Cu-containing zeolites while the protonated SSZ-13 were all simulated for 32 ps with the same time step. The temperature of the simulations was held to 600 K in accordance with experiment. All post-processing of the MD simulations was done using the program MD-tracks.[3]

To calculate the peak positions for the IR spectrum from the MD simulation, the velocity power spectrum (VPS) is determined by the Fourier transforms of the velocities, which are squared and summed.[4]

$$I_{VPS}(\omega) = \lim_{t\to\infty} \frac{1}{t} \sum_{i=1}^{N} \sum_{\alpha=x,y,z} \left| \int_0^t v_{i,\alpha}(t) \mathrm{e}^{-\mathrm{i}\omega t}\, dt \right|^2$$

This is related to the IR spectrum since this is the Fourier transform of the time derivative of the dipole moment $\mu_\alpha = \sum_i q_i R_{i\alpha}$.

$$I_{IR}(\omega) = \lim_{t\to\infty} \frac{1}{t} \sum_{\alpha=x,y,z} \left| \int_0^t \frac{d\mu_\alpha(t)}{dt} \mathrm{e}^{-\mathrm{i}\omega t}\, dt \right|^2$$

The derivative of the dipole moment is indeed very much related to the velocity. Hence, the VPS is related to the IR spectrum and contains even more information.

The theoretical spectra of the NH_3@Cu^{2+} site, NH_3@Brønsted site (O1), NH_3@ Brønsted site (O2) and $(NH_3)_4$@Cu^{2+} site spectra in the region 200-1200 cm^{-1} are compared in Figure S6.

Electronic Supplementary Material (ESI) for Physical Chemistry Chemical Physics

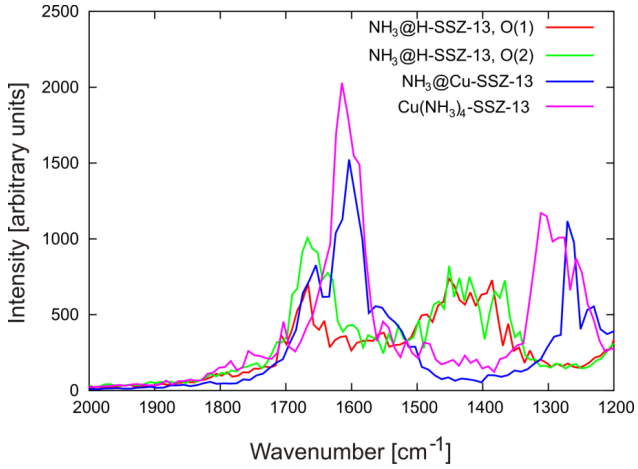

Figure S6. Theoretical spectra derived from MD simulations at 600 K of NH_3@Brønsted site (O1) (red), NH_3@Brønsted site (O2) (green), NH_3@Cu^{2+} site (blue) and $(NH_3)_4$@Cu^{2+} site (pink) in the region 2000-1200 cm^{-1}.

Table S1. Theoretical frequencies (in cm^{-1}) of the ammonia-adsorbed structures, depicted in Figure 3. Comparison between the NMA and MD-based results.

	$\nu_{theor,NMA}$ (cm^{-1})		$\nu_{theor,MD}$ (cm^{-1})		**Assignment**
	O(1)	**O(2)**	**O(1)**	**O(2)**	
NH_3@Brønsted site	-	1480	1432	1455	$\delta(NH_4^+)_{as}$
	-	1387	1370	1368	$\delta(NH_4^+)_s$
	$[Cu(NH_3)]^{2+}$	**$[Cu(NH_3)_4]^{2+}$**	**$[Cu(NH_3)]^{2+}$**	**$[Cu(NH_3)_4]^{2+}$**	
NH_3@Cu^{2+} site	1632	1621	1601	1606	$\delta(NH_3)_{as}$
	1537		1535		hydrogen-bonded $\delta(NH_3)_{as}$ in $[Cu\text{-}NH_3]^{2+}$
	1261	1291	1271	1285	NH_3 wagging

Electronic Supplementary Material (ESI) for Physical Chemistry Chemical Physics

UV-Vis-NIR DRS Spectroscopy of Cu-containing SSZ-13 zeolites

The UV-Vis spectrum acquired for the Cu-SSZ-13(67) zeolite, depicted in Figure S7, shows the presence of isolated Cu^{2+} ions (ca. 12000 d–d and 47500 cm^{-1} charge transfer (CT) O → Cu),[5] whereas for the Cu-SSZ-13(100) zeolite a new band appears at 40000 cm^{-1}, attributed to the formation of isolated CuO particles.[6]

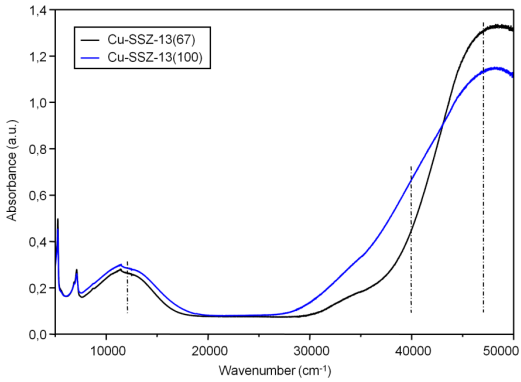

Figure S7. UV-Vis spectra of Cu-SSZ-13 (67) (black line) and Cu-SSZ-13 (100) (blue line) zeolites.

Cu-K edge EXAFS of Cu-containing SSZ-13 zeolites

Comparison of the EXAFS data (see Figure S8 and Table S2) shows a decrease in the intensity of the feature at ~1.96 Å for the Cu-SSZ-13(100) zeolite, indicating a slight reduction in the number of isolated Cu^{2+} ions,[7] together with the appearance of a new feature at ~3 Å. This new feature is due to a Cu-Cu contribution, and indicates the presence of small amounts of CuO in the Cu-SSZ-13(100) sample,[8] in accordance with the previous UV-Vis results.

Electronic Supplementary Material (ESI) for Physical Chemistry Chemical Physics

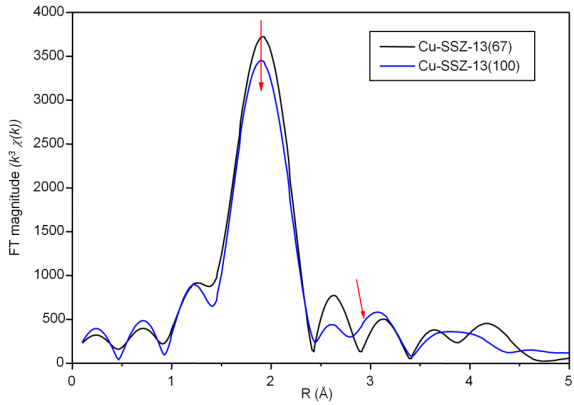

Figure S8. Fourier transform of $k^3\chi(k)$ EXAFS data for Cu-SSZ-13 (67) (black line) and Cu-SSZ-13 (100) (blue line) (solid line) zeolites.

Table S2. EXAFS parameters for Cu–O derived from a first shell fit of the data in k-space. Estimated errors (fitting) are listed in brackets below (±)

	R (Å)	***N***	**$2\sigma^2$ (Å^2)**	**E_f (eV)**	**R-factor**
Cu-SSZ-13 (67)	1.96	3.1	0.009	-1.15	
	(0.02)	(0.305)	(0.006)	(1.007)	24.18
Cu-SSZ-13 (100)	1.95	3.0	0.007	-0.45	
	(0.02)	(0.385)	(0.009)	(1.455)	23.37

R-factor values are calculated using the following formula:

$$R_{exafs} = \sum_{i}^{N} 1\ \sigma_i\left(\left|\chi_i^{exp}(k) - \chi_i^{th}(k)\right|\right) \text{ x } 100\%$$

Electronic Supplementary Material (ESI) for Physical Chemistry Chemical Physics

N_2 sorption measurements of Cu-containing SSZ-13 zeolites

As shown in Table S3, N_2 sorption measurements basically show the same results; both Cu-loaded zeolites present a typical type I isotherm, corresponding to a fully microporous material, so that the presence of an additional mesopore system in Cu-SSZ-13(100), produced as a consequence of framework dealumination, can also be ruled out.

Table S3. BET surface area and micropore volume, determined by N_2 adsorption, and crystal size, obtained from Scanning Electron Microscopy (SEM) images, of Cu-SSZ-13 (67) and Cu-SSZ-13 (100) zeolites.

	A_{BET} (m^2/g)	$V_{\mu p}$ (cm^3/g)	Crystal size (μm)
Cu-SSZ-13 (67)	775	0.27	8-10
Cu-SSZ-13 (100)	765	0.26	8-10

Scanning Electron Microscopy (SEM) of Cu-containing SSZ-13 zeolites

Identical results were also obtained by SEM (see Table S3), ruling out the presence of smaller crystallites in Cu-SSZ-13(100) or a change in morphology, which could be also a possible reason of the enhanced reactivity.

Electronic Supplementary Material (ESI) for Physical Chemistry Chemical Physics

References

1. G. Bussi, D. Donadio and M. Parrinello, *J. Chem. Phys.*, 2007, **126**, 14101.

2. S. Nosé, *Mol. Phys.*, 1984, **52**, 255; S. Nosé, *J. Chem. Phys.*, 1984, **81**, 511.

3. T. Verstraelen, M. Van Houteghem, V. Van Speybroeck and M. Waroquier, *J. Chem. Inf. Model.*, 2008, **48**, 2414.

4. M. Van Houteghem, T. Verstraelen, D. Van Neck, C. Kirschhock, J. A. Martens, M. Waroquier and V. Van Speybroeck. *J. Chem. Theo. Comput.*, 2011, **7**, 1045, and references herein.

5. M. H. Groothaert, J. A. Bokhoven, A. A. Battiston, B. M. Weckhuysen and R. A. Schoonheydt, *J. Am. Chem. Soc.*, 2003, **125**, 7629.

6. A. El-Trass, H. ElShamy, I. El-Mehasseb and M. El-Kemary, *Appl. Surf. Sci.*, 2012, **258**, 2997.

7. S. Bordiga, E. Groppo, G. Agostini, J. A. van Bokhoven and C. Lamberti, *Chem. Rev.*, 2013, **113**, 1736.

8. W. Grunert, N.W. Hayes, R.W. Joyner, E.S. Shpiro, M.R.H. Siddiqui and G.N. Baeva, *J. Phys. Chem.*, 1994, **98**, 10832.

Paper VIII

Mn-salen@MIL101(Al): a Heterogeneous enantioselective catalyst synthesized using a 'bottle around the ship' approach

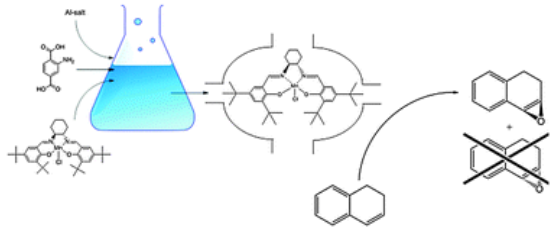

T. Bogaerts, A. Van Yperen-De Deyne, Y-Y. Liu, F. Lynen, V. Van Speybroeck, P. Van Der Voort *Chemical Communications* **49**, 8021–2023, (2013)

ChemComm

RSC Publishing

COMMUNICATION

View Article Online
View Journal | View Issue

Mn-salen@MIL101(Al): a heterogeneous, enantioselective catalyst synthesized using a 'bottle around the ship' approach†

Cite this: *Chem. Commun.*, 2013, **49**, 8021

Received 14th June 2013,
Accepted 11th July 2013

DOI: 10.1039/c3cc44473b

www.rsc.org/chemcomm

Thomas Bogaerts,[ab] Andy Van Yperen-De Deyne,[a] Ying-Ya Liu,[b] Frederic Lynen,[c] Veronique Van Speybroeck*[a] and Pascal Van Der Voort*[b]

An enantioselective catalyst, consisting of a chiral Mn(III)salen complex entrapped in the MIL-101 metal organic framework, is reported. For the first time, we assemble a robust MOF-cage around a chiral complex. The heterogeneous catalyst shows the same selectivity as the homogeneous complex and is fully recyclable. Theoretical calculations provide insight into this retention of selectivity.

Chiral epoxides are valuable intermediates in the chemical industry. The high ring strain makes them very reactive and their enantioselectivity can be transferred to the products. Various methods have been proposed to enantioselectively synthesize these epoxides.[1] One of these methods is the use of the Jacobsen salen catalyst.[2] Such manganese complexes enable the epoxidation of unfunctionalized olefins (shown in Scheme 1) with selectivities one would expect from enzymes. In order for this system to be sustainable, an efficient recovery of this catalyst is required. Moreover deactivation of the manganese salen complex, that occurs readily *via* the formation of dimeric species,[3] must be prevented. All these issues can be solved by immobilizing the complex on a solid material. Various processes for anchoring chiral complexes to a support have already been proposed.[4] We propose a simple immobilization procedure where the salen complex is encapsulated in a metal organic framework without any covalent bonds.

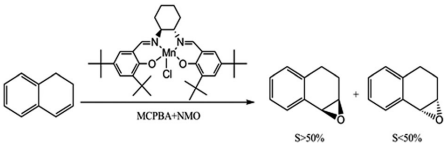

Scheme 1 The enantioselective epoxidation of dihydronaphthalene with the salen complex used in this study.

Metal organic frameworks (MOFs) are porous crystalline materials consisting of metal (-oxide) building blocks connected with organic linkers. Using various metals, linkers and synthesis procedures, a wide array of structures are available. In this study NH_2-MIL101(Al) is used as the carrier material. This MOF was first reported by Kapteijn *et al.*[5] The use of MOFs as catalyst supports has been investigated previously.[6] MIL-101 type MOFs (MIL stands for Materials Institute Lavoisier) are known for the highly porous structure consisting of large cages (2.9–3.4 nm) connected by windows of 1.2 and 1.6 nm[7] diameter. The goal is to form the MOF around the complex, building a so-called 'bottle around the ship'. The dimensions of the Jacobsen salen complex (approximately 1.7 × 1.2 × 0.5 nm) allow it to reside in the cages without being able to pass through the windows, thus effectively immobilizing the complex. In contrast to using salen-type ligands as struts for the MOF[8] the proposed method only makes use of easily available chemicals. "Ship in a bottle" methodologies for producing salen-type complexes have been proposed[9] however they do not involve MOFs and require several reaction steps. In this communication we propose another approach, denoted as "bottle around a ship", in which the encapsulation procedure consists of a one-pot single-step synthesis. The linker and the commercially available salen complex were simultaneously dissolved in DMF after which $AlCl_3$ was added stepwise. While crystals are formed, the color of the solution changes from deep-red to a paler red-brownish color. This points to the decrease in concentration of the salen complex in the solution, meaning a fraction gets trapped in the pores.

Comparing the powder XRD pattern of pure NH_2-MIL101(Al) with the encapsulated catalyst shows minimal differences as shown in Fig. 1. This shows that the addition of the salen complex to the synthesis mixture has no effect on the formed structure. The Langmuir surface area, measured by N_2-sorption, was 2603 $m^2\ g^{-1}$ and 2413 $m^2\ g^{-1}$ for the empty and loaded structure respectively. The pore volume decreased from 0.984 $cm^3\ g^{-1}$ to 0.953 $cm^3\ g^{-1}$.

[a] *Center for Molecular Modelling (CMM), Ghent University, Technologiepark 903, 9052 Zwijnaarde, Belgium. E-mail: Veronique.vanspeybroeck@ugent.be*
[b] *Center for Ordered Materials, Organometallics and Catalysis (COMOC), Department of Inorganic and Physical Chemistry, Ghent University, Krijgslaan 281-S3, 9000 Ghent, Belgium. E-mail: pascal.vandervoort@ugent.be*
[c] *Separation Science group, Department of Organic Chemistry, Ghent University, Krijgslaan 281-S4bis, 9000 Ghent, Belgium*

† Electronic supplementary information (ESI) available. See DOI: 10.1039/c3cc44473b

View Article Online

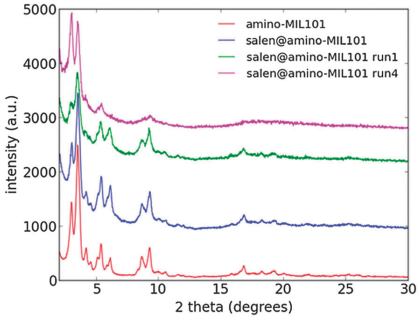

Fig. 1 Powder XRD patterns for the pure NH_2-MIL101(Al), salen@NH_2-MIL101(Al) and salen@NH_2-MIL101(Al) after one and four catalytic runs. The encapsulation of the complex does not significantly changes the crystal structure. The retained crystallinity after various catalytic runs shows the stability of the catalyst.

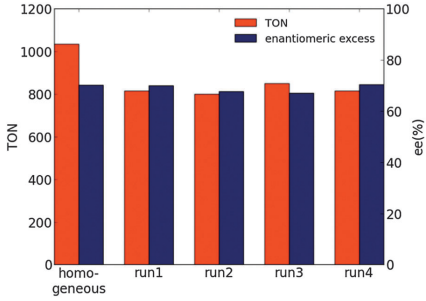

Fig. 2 TON and enantioselectivity for the salen@NH_2-MIL101(Al) compared to homogeneous catalysis with the salen complex for the same conditions. It appears the encapsulation procedure has no effect on the selectivity of the catalyst.

XRF analysis resulted in a loading of 0.02 mmol g^{-1} or one out of six cages containing a salen complex. This small loading is in good agreement with the limited decrease in internal volume. Given the high activity of the manganese–salen catalyst, a low loading is preferred to minimize pore blocking and diffusion limitations which lower the catalytic activity. To assess the behaviour of this encapsulated catalyst it was tested in a typical epoxidation of dihydronaphthalene with *meta*-chloroperoxybenzoic acid (MCPBA) and *N*-methylmorpholine N-oxide (NMO) as an axial ligand for the salen complex and adding toluene as an internal standard. This combination has been proven to be an effective oxidant to use in combination with the Mn(III) salen complex, both homogeneous as immobilized.[10,11] The product distribution was analyzed by chiral HPLC. In a homogeneous medium the salen catalyst yielded a conversion of 82% with a %ee of 70. The heterogeneous catalyst showed a lower conversion of 69% when approximately the same amount of manganese was used (Table 1). However the enantioselectivity remained unchanged at a %ee of 70. This shows that the proposed encapsulation procedure has a minimal impact on the catalytic behaviour of the complex. After the catalytic run the solid catalyst is filtered off, and investigation of the crystallinity with XRD showed that the structure remained unchanged. The manganese content in the filtrate was analysed by XRF and was found to be below the detection limit of the device, showing none of the complex was leached out. This indicates that the catalyst is truly heterogeneous and stable in the reaction medium. To test the reusability of the catalyst, the powder was washed with dichloromethane and reused for another run, this was repeated three times. During the four runs the turn over number (TON) remained constant (see Fig. 2), proving this catalyst can be reused without significant loss in activity.

Table 1 Details on the amount of added catalyst in the experimental procedure

Catalyst	Weight (mg)	Mn (mmol)	Mn/substrate
Salen homogeneous	4	0.0062	1/1261
Salen@NH_2-MIL101(Al)	330	0.0066	1/1216

Moreover the selectivity remains constant showing the catalyst is very stable and possesses excellent reusability. Blank reactions using the pristine MOF and the mixture without any catalyst yielded only marginal conversion after two hours. In order to obtain more insight into the bottle around the ship approach, *ab initio* calculations were performed. They allow us to make a realistic prediction of the dimensions of the Mn salen complex and its transition state, which can be compared with the cage size of a MIL101 structure. Here we will use a full DFT level of theory instead of using force fields in order to get a more detailed picture. The DFT method used is the OPBE functional, which has shown to yield accurate energies when comparing spin states of organometallic complexes,[12] which is important since the Mn–salen complex has a small energy separation between the different spin states.[13] All optimizations were done with a 6-31+G(d) basis set for H,C,O,N and a 6-311++G(2df,2p) basis set for Cl and Mn. Computations were done using the gaussian09 suite of programs.[14] Calculations were done on the (*S*,*S*)-variant of the salen complex, the axial ligand was omitted for computational feasibility. Starting from an oxidized manganese complex, which is an experimentally proven intermediate,[3] the proposed methodology showed that a system with a spin multiplicity of three is most favourable and this will be used further. For the first transition state (Scheme S1 of the ESI†), two

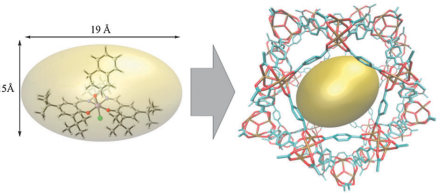

Fig. 3 Schematic representation of the transition state contained in the small (2.9 nm diameter) cage of MIL101. Hydrogens and amine-groups are omitted for clarity. The space needed for transition state to be contained in the cage is represented by and ellipsoid with radii of 19 and 15 Å. This fits readily in the MIL101 cage.

View Article Online

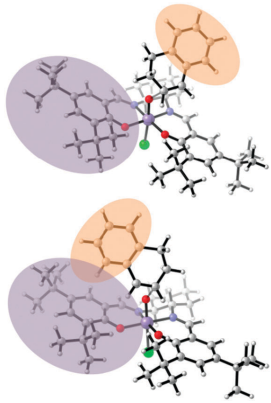

Fig. 4 Transition state for the two possible approaches of dihydronaphthalene leading to the (1*R*,2*S*)-enantiomer (left) and the (1*S*,2*R*)-enantiomer (right). The first approach suffers from more steric hindrance than the latter.

possible approaches leading to a different enantiomer were calculated. Both transition state dimensions were 1.7 × 1.2 × 1.0 nm, taking NMO as an axial ligand into account this would increase to approximately 1.7 × 1.5 × 1.0 nm. This means both transition states fit readily in the cages (Fig. 3).

Upon closely analyzing the mechanism of oxygen transfer, as presented in various theoretical contributions,[15] it appears that the first transition state determines the resulting selectivity. Once the first C–O bond is formed the second one can only form on the same side. Since both transition states fit in the cages of the host without any interaction, the observed selectivity should be the same as the Jacobsen catalyst under homogeneous conditions, as can be observed from the experiments. Using the two approaches one can also rationalize reasons for the selectivity of the salen complex. The transition state leading to (1*R*,2*S*)-epoxydihydronaphthalene is clearly less favorable since the steric bulk of the substrate is directed towards the side of the complex facing upwards (Fig. 4). The (1*S*,2*R*)-approach does not suffer from this steric hindrance. This demonstrates that the folded structure of the salen complex is very important to induce selectivity of the substrate in the approaches. The free energy difference at 273 K between the transition states is 10 kJ mol^{-1} which can explain the preference for the formation of (1*S*,2*R*)-epoxydihydronaphthalene. To assess the influence of the cage we performed a single point calculation with a MIL-101 cage surrounding the transition states. The Jacobsen complex was modeled on the same level of theory as described before, the MOF cage was modeled with the universal force field (details in ESI†). The electronic energy difference between the transition states was 12 kJ mol^{-1}, which confirms the results described above.

In summary, we proposed a novel "bottle around the ship" encapsulation procedure for heterogenizing an enantioselective manganese complex in the pores of NH_2-MIL101(Al). The catalyst synthesis occurs in a single step using readily available chemicals which allows easy scale-up. The metal organic framework is used as a micro-reactor containing a single active complex, with limited influence of the walls. This results in a catalyst with good activity and a selectivity comparable to the homogeneous complex. The unchanged selectivity after heterogenization is due to the 'soft' encapsulation strategy. The trapping of the active complex without any covalent or coordinative bonds keeps the structure in the optimal shape needed for achieving the high selectivity. This catalyst was tested for up to four runs with a minimal decrease in activity and retention of the selectivity. This allows for the easy separation and the reuse of this catalyst without loss as was the case for the homogeneous variant. *Ab initio* calculations allow computing the dimensions of the important steps in the reaction, rationalizing the unchanged selectivity after encapsulation. The transition state which determines the selectivity fits the pores of the host unhindered, allowing the reaction to exhibit the same behaviour as with the homogeneous catalyst.

The research was financed by UGent GOA grant 01G00710, the European Research Council for funding through the European Community's Seventh Framework Programme (FP7(2007-2013) ERC grant agreement no.\240483) and the Research Board of Ghent University (BOF). Computational resources and services were provided by Ghent University (*Stevin Supercomputer Infrastructure*).

Notes and references

1 Q. H. Xia, H. Q. Ge, C. P. Ye, Z. M. Liu and K. X. Su, *Chem. Rev.*, 2005, **105**, 1603–1662.
2 W. Zhang, J. L. Loebach, S. R. Wilson and E. N. Jacobsen, *J. Am. Chem. Soc.*, 1990, **112**, 2801–2803.
3 K. Srinivasan, P. Michaud and J. K. Kochi, *J. Am. Chem. Soc.*, 1986, **108**, 2309–2320.
4 J. M. Fraile, J. I. Garcia, C. I. Herrerias, J. A. Mayoral and E. Pires, *Chem. Soc. Rev.*, 2009, **38**, 695–706.
5 P. Serra-Crespo, E. V. Ramos-Fernandez, J. Gascon and F. Kapteijn, *Chem. Mater.*, 2011, **23**, 2565–2572.
6 J. Canivet, S. Aguado, Y. Schuurman and D. Farrusseng, *J. Am. Chem. Soc.*, 2013, **135**, 4195–4198.
7 G. Ferey, C. Mellot-Draznieks, C. Serre, F. Millange, J. Dutour, S. Surble and I. Margiolaki, *Science*, 2005, **309**, 2040–2042.
8 S.-H. Cho, B. Ma, S. T. Nguyen, J. T. Hupp and T. E. Albrecht-Schmitt, *Chem. Commun.*, 2006, 2563–2565.
9 B. Li, S. Y. Bai, P. Wang, H. Q. Yang, Q. H. Yang and C. Li, *Phys. Chem. Chem. Phys.*, 2011, **13**, 2504–2511.
10 M. Palucki, G. J. McCormick and E. N. Jacobsen, *Tetrahedron Lett.*, 1995, **36**, 5457–5460.
11 L. Canali, D. C. Sherrington and H. Deleuze, *React. Funct. Polym.*, 1999, **40**, 155–168.
12 M. Swart, A. R. Groenhof, A. W. Ehlers and K. Lammertsma, *J. Phys. Chem. A*, 2004, **108**, 5479–5483.
13 J. S. Sears and C. D. Sherrill, *J. Chem. Phys.*, 2006, **124**, 144314.
14 M. J. Frisch, G. W. Trucks, H. B. Schlegel, G. E. Scuseria, M. A. Robb, J. R. Cheeseman, G. Scalmani, V. Barone, B. Mennucci, G. A. Petersson, H. Nakatsuji, M. Caricato, X. Li, H. P. Hratchian and A. F. Izmaylov, *et al.*, *Gaussian 09*, 2009.
15 L. Cavallo and H. Jacobsen, *Inorg. Chem.*, 2004, **43**, 2175–2182.

Paper IX

Solution enthalpy of Po and Te in solid lead-bismuth eutectic

K. Rijpstra, A. Van Yperen-De Deyne, J. Neuhausen, V. Van Speybroeck, S. Cottenier *Journal of Nuclear Materials*, **450**, 287–291 (2014)

Journal of Nuclear Materials 450 (2014) 287–291

Contents lists available at ScienceDirect

Journal of Nuclear Materials

journal homepage: www.elsevier.com/locate/jnucmat

Solution enthalpy of Po and Te in solid lead–bismuth eutectic

Kim Rijpstra [a], Andy Van Yperen-De Deyne [a], Jörg Neuhausen [b], Veronique Van Speybroeck [a], Stefaan Cottenier [a,c,*]

[a] Center for Molecular Modeling, Ghent University, Technologiepark 903, BE-9052 Zwijnaarde, Belgium
[b] Laboratory for Radio- and Environmental Chemistry, Paul Scherrer Institute, OFLB/101, CH-5232 Villigen PSI, Switzerland
[c] Department of Materials Science and Engineering, Ghent University, Technologiepark 903, BE-9052 Zwijnaarde, Belgium

HIGHLIGHTS

- First-principles calculations can help planning difficult experiments with ^{210}Po.
- Po and Te do not dissolve into the bulk matrix of solid LBE.
- Formation of rock salt PbPo and PbTe is more exothermic than dissolution in bulk.
- Te-behaviour is predictive for Po-behaviour.
- Relativistic effects lead to a less negative solution enthalpy of Po in LBE.

GRAPHICAL ABSTRACT

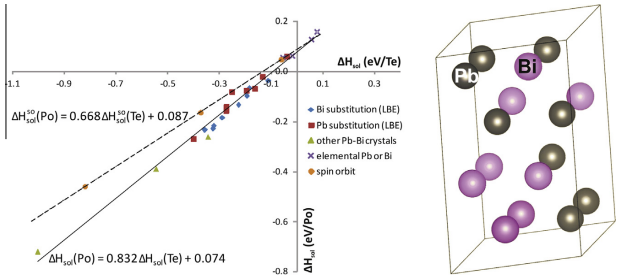

ARTICLE INFO

Article history:
Available online 11 July 2013

ABSTRACT

It is examined to which extent first-principles calculations can be used to collect *a priori* information on the solution enthalpy and solubility of Po in solid lead–bismuth eutectic (LBE). Such information can be helpful to limit the number of complicated experiments that are required to measure these properties. It is found that in the thermodynamic limit and at 0 K, Po does not dissolve in solid LBE. Its solution enthalpy is negative, in particular in Pb-rich environments, but competing compound-forming reactions are more exothermic. A clear correlation is found between the calculated solution enthalpies for Te in LBE and for Po in LBE, suggesting that Te-experiments can be used to map the expected behaviour for Po. The role of spin–orbit coupling as the major relativistic effect on the solution enthalpies of these heavy atoms is inspected.

1. Introduction

The molten phase of a lead–bismuth eutectic (LBE) is going to be used as coolant in planned experimental generation IV fission reactors [1]. Neutron capture by ^{209}Bi will inevitably lead to the presence of a non-negligible amount of radiotoxic ^{210}Po in the coolant. For safety assessments, it is essential to know how this Po will interact with its environment in several operation and accident scenarios. Eventually, this has to be examined experimentally. However, exactly due to its radiotoxicity, Po-experiments are subject to major safety constraints and are therefore not straightforward to perform. In order to minimize the number of experiments, it would be convenient to know in advance as well as possible what to expect. This is a situation where predictive computational modelling can play a role. Indeed, it is well-established that many properties of molecules [2] and solids [3–5] can be predicted by solving the fundamental equations provided by quantum physics. In the case of solids, this is most often done in the framework of Density Functional Theory (DFT). The solution enthalpy of impurity elements in metals is one example of a prop-

* Corresponding author at: Center for Molecular Modeling, Ghent University, Technologiepark 903, BE-9052 Zwijnaarde, Belgium. Tel.: +32 92646563.
E-mail address: Stefaan.Cottenier@ugent.be (S. Cottenier).

0022-3115/$ - see front matter © 2013 Elsevier B.V. All rights reserved.
http://dx.doi.org/10.1016/j.jnucmat.2013.07.004

erty that can be determined by DFT [6–12]. In this work, we will address the solution enthalpy of Po in solid LBE. We will do this in two ways: by directly predicting the solution enthalpy of a Po atom in solid LBE, and indirectly by dissolving the same amount of Te in exactly the same LBE-environment. The latter 'virtual experiment' will reveal a correlation between Po- and Te-behaviour, suggesting that it is possible to obtain information on Po in LBE by performing experiments on Te in LBE.

2. Computational details

All calculations in this work were done within the framework of Density Functional Theory [13–16], using the Perdew–Burke–Ernzerhof exchange–correlation functional [17]. The numerical method used to solve the scalar-relativistic [18] Kohn–Sham equations for periodic solids is the Projector Augmented Wave (PAW) method [19,20] as implemented in the VASP package [21,3] (6-electron PAW potential for Te, d-electrons included for Pb, Bi and Po). Spin–orbit coupling as the major relativistic effect beyond the scalar-relativistic level was added for the calculations described in Section 5. The cut-off energy for the basis set size was taken to be 290 eV. The k-grids were Γ-centered Monkhorst–Pack grids, with a density of 125,000 k-points/Å^{-3}. Both basis set size and k-point density were tested for numerical convergence. All unit cells were fully relaxed under the constraint of zero applied pressure and all calculated energies therefore correspond to enthalpies. No entropic effects were taken into account, such that all quantities refer to the ground state (0 K). The calculations reported in this paper are equivalent to 10 cpu-years of single-core computing.

3. Elemental solids and LBE-model

Five solids will play a major role in this work: the elemental solids Te, Pb, Bi and Po, and a Pb-Bi mixture. In order to demonstrate the validity of the computational method for this kind of solids, we list in Table 1 some predicted basic structural properties for the elemental solids. The computational settings as described in Section 2 were used. The bare calculated results were corrected for a systematic deviation as described in Ref. [5], and also the error estimates (1σ standard deviations) were taken from the latter work. The agreement between calculated and experimental values is reassuring for the validity of this computational method for this kind of solids. Furthermore, Table 1 demonstrates that spin–orbit coupling has a non-negligible effect on the properties of solids of heavy elements (see also Section 5).

Solid state DFT calculations require a unit cell as input, which is then periodically repeated to fill space. For an intrinsically disordered material as solid LBE, this straightforward approach is not possible. If it is the aim to describe the details of a disordered solid as faithfully as possible, one can resort to a set of elaborations or modifications of DFT that are meant for disordered alloys [22]: special quasi-random structures (SQS) [23], cluster expansion [24] or the coherent potential method (CPA) [25]. Our aim, however, is to inspect whether and how the local stoichiometry of the nearest-neighbour shell affects the solution behaviour of Po. We therefore take the simpler approach to describe a Pb–Bi alloy by a 'disordered supercell'. A unit cell of the underlying high-symmetry crystal structure is multiplied by a small integer factor in all three dimensions (in our case $2 \times 2 \times 2$, see Fig. 1(a)), and all atom sites are randomly occupied by a predefined number of Pb and Bi atoms. Subsequently the shape and volume of the cell as well as the positions of the atoms are allowed to adjust themselves in order to adopt the lowest-energy configuration under the condition of no applied pressure [12]. Applying the same procedure to a $3 \times 3 \times 3$ cell would require 100 times more computation time, and – as will be argued in Section 4 – is bound to lead to the same conclusions as are obtained from the $2 \times 2 \times 2$ cell. For the same reason, only one random choice of the Pb/Bi-occupation is considered (see Section 4).

Which underlying crystal structure has to be taken for LBE? A glance at the Pb–Bi phase diagram in Fig. 2 shows the relevant ones. Elemental Pb has the fcc structure (cF4, Cu-type), and elemental Bi has a rhombohedral structure (hR6, As-type). Around the concentration range of 70% Pb, the Pb–Bi mixture adopts the

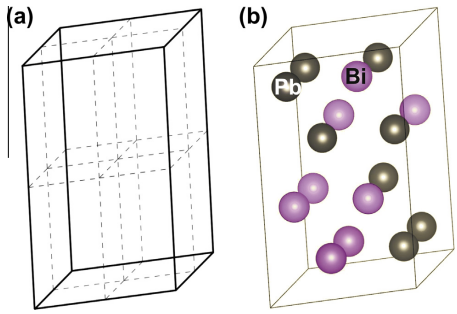

Fig. 1. (a) A $2 \times 2 \times 2$ supercell of the hexagonal close packed primitive cell. (b) The randomly chosen Pb- and Bi-occupation that served as a model for a configurationally disordered Pb/Bi-alloy in this work.

Table 1
Equilibrium volume per atom (Å^3) and equilibrium bulk modulus (GPa) for the bulk phases of Te, Pb, Bi and Po: experimental values (as listed in [5], extrapolated to 0 K and corrected for zero point motion), and calculated values (using the methods and settings described in Section 2) without (no SO) and with (SO) spin–orbit coupling. The calculated values have been corrected for the systematic deviations introduced by the PBE functional and an estimate of the expected uncertainty on the calculated value is given (see Ref. [5] for the procedure). Without spin–orbit coupling, all calculated volumes and bulk moduli agree with experiment within the error bar on the computed value, except for the bulk modulus of Po. When spin–orbit coupling is added, the latter disagreement is repaired.

	V_0 (Å^3/atom)			B_0 (GPa)		
	Exp.	no SO	SO	Exp.	no SO	SO
Te	33.30	33.70 (1.1)	–	26.2	18.7 (15)	–
Pb	29.86	30.86 (1.1)	31.03 (1.1)	46.3	41.9 (15)	38.1 (15)
Bi	35.13	35.62 (1.1)	36.85 (1.1)	32.1	27.3 (15)	24.3 (15)
Po	36.93	36.16 (1.1)	38.04 (1.1)	27.4	48.2 (15)	37.3 (15)

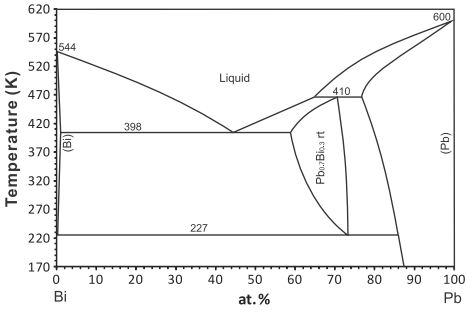

Fig. 2. The Pb–Bi phase diagram as given in Ref. [26] (picture redrawn from AtomWork [27,28]).

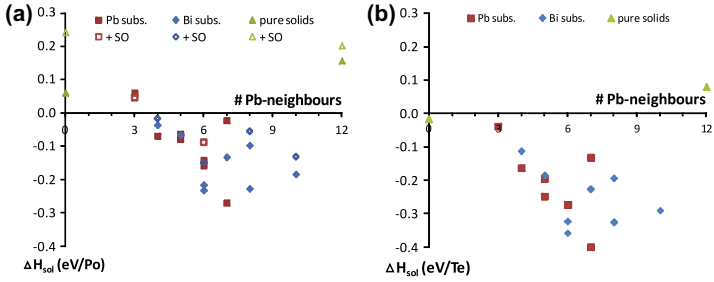

Fig. 3. (a) Solution enthalpy for Po at all 16 positions in our LBE model, as well as in pure Bi and pure Pb. These solution enthalpies are plotted with respect to the number of Pb-neighbours in the first coordination shell of Po. Open symbols are data points for which spin–orbit coupling has been taken into account. (b) Idem, but for Te instead of Po.

hcp structure (hP2, Mg-type). This hcp phase has a rather large homogeneity range. The solubility range of Pb in rhombohedral Bi is much smaller. In the broad concentration range between 1 at.% and 57 at.% Pb, the material will consist of a mixture of almost pure Bi microcrystals and hcp $Pb_{0.7}Bi_{0.3}$ microcrystals. Dissolving Po in LBE therefore means dissolving it in almost pure Bi and in hcp $Pb_{0.7}Bi_{0.3}$ (grain boundary effects are neglected). We want to examine how Po interacts with its immediate environment in Pb–Bi alloys. In order to sample as much as possible different nearest neighbour environments in a relatively small supercell, we take as our model system hcp-Pb_8Bi_8. This means: 8 Pb-atoms and 8 Bi atoms are randomly distributed over the 16 sites in a $2 \times 2 \times 2$ hcp supercell (Fig. 1(b)).

4. Dissolving Po and Te in LBE

How much energy does it cost to put one Po atom in (the Pb–Bi microcrysals of) a LBE matrix? To answer this, we examine the reaction

$$\underbrace{Pb_8Bi_8}_{\text{LBE}} + Po^{\text{solid}} \leftrightarrow \underbrace{Pb_8Bi_7Po}_{\text{LBE+Po}} + Bi^{\text{solid}} \quad (1)$$

which describes solid Po (α-Po, simple cubic) in contact with LBE (modelled by our 16-atom hexagonal cell), reacting to form solid bismuth and LBE with Po substituting for a Bi atom. A similar reaction can be written for Po substituting for Pb. The reaction enthalpy for Eq. (1) happens to be identical to the solution enthalpy of Po in LBE:

$$\Delta H^i_{\text{sol}} = \left[H(LBE + Po)_i + \mu_{\text{Pb(Bi)}}\right] - \left[H(LBE) + \mu_{\text{Po}}\right] \quad (2)$$

It expresses the total enthalpy cost to remove one Po-atom from a Po-reservoir with chemical potential μ_{Po}, to put it at a Pb (or Bi) site in LBE, and to bring the replaced Pb-atom (or Bi-atom) to a Pb-reservoir (or Bi-reservoir) with chemical potential μ_{Pb} (or μ_{Bi}). For the reservoirs (or chemical potentials μ), one usually takes the enthalpy per atom in the elemental solids, i.e. as determined by the calculations described in Section 3.

One after the other, all 16 Pb or Bi atoms in our model LBE are replaced by a Po atom, after which the supercell is allowed in all cases to relax completely. This results in 16 different values for the enthalpy $H(LBE + Po)_i$ ($1 \leqslant i \leqslant 16$). These 16 solution enthalpies are plotted in Fig. 3(a) as a function of the number of Pb atoms in the first coordination shell of Po. The same picture shows the solution enthalpy for Po in rhombohedral Bi and fcc-Pb as well. The solution enthalpy for Po in Pb is positive, indicating that at 0 K Po will not dissolve spontaneously in Pb. For Po in Bi, the (scalar-relativistic) solution enthalpy is slightly positive as well. For Po in LBE, there is a rough trend with respect to the number of Pb neighbours: Po has a positive solution enthalpy when it goes to sites with few Pb neighbours, and a negative solution enthalpy when it goes to sites with many Pb neighbours. This negative solution enthalpy means that the reaction in Eq. (1) will proceed exothermally to the right if Po ends up in an environment with a lot of Pb-atoms. It does not mean, however, that Po will effectively dissolve into the solid Pb/bi-microcrystals in LBE in Nature. For this to happen, there should be no alternative reaction that is even more exothermal. As solid PbPo is experimentally known to exist in the rocksalt structure [29], a straightforward alternative that should be examined is

$$\underbrace{Pb_8Bi_8}_{\text{LBE}} + Po^{\text{solid}} \leftrightarrow \underbrace{Pb_7Bi_7}_{\text{LBE}} + PbPo^{\text{solid}} + Bi^{\text{solid}} \quad (3)$$

The reaction enthalpy for this reaction is calculated to be −0.60 eV/Po, which is clearly lower than the lowest value of −0.27 eV/Po in Fig. 3(a) (or Eq. (1)). As a consequence, Po will not dissolve spontaneously into solid LBE.[1] Either it will react with LBE to form rocksalt PbPo and rhombohedral Bi, or it will follow other reaction paths that have even more negative reaction enthalpies (involving, for instance, ternary Pb–Bi–Po phases). This conclusion is consistent with experimental observations that Po inside solid Pb [30] and solid LBE [31,32] migrates to the surface and/or to grain boundaries [33].

Exactly the same procedure was followed to determine the solution enthalpy of Te in LBE. This results in Fig. 3(b) for a reaction similar to Eq. (1). The solution enthalpy for Te in solid Pb is positive, consistent with the low solubility range of Te in Pb [34]. At the Bi-side, the solution enthalpy is slightly negative. Yet, in low-temperature experiments Te will not dissolve in rhombohedral Bi, as it is more favourable to form Bi_4Te_3 [35]. This too is consistent with the low solubility range of Te in Bi (0.2 at.% at most [36]). The solution enthalpy of Te in the Pb/Bi-microcrystals of LBE is considerably negative (down to −0.40 eV/Te), and Te prefers Pb-rich environments in LBE, just as Po does. Te is not expected to dissolve effectively into LBE, however, as also here at least one competing reaction can be found with a lower reaction enthalpy: the analogue of Eq. (3) with PbTe has a reaction enthalpy of −0.96 eV/Te. PbTe is indeed the phase that is found experimentally [37–39].

At this point, one can exploit a particular feature of first principles calculations: the ability to do very controlled 'experiments' in

[1] As −0.60 eV is considerably lower than −0.27 eV, this conclusion will not be affected by taking a different random occupation for the 16-atom LBE cell, or by taking a larger supercell to model LBE.

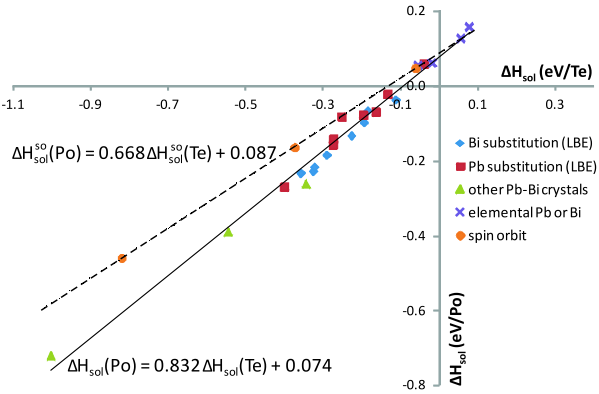

Fig. 4. Correlation between the solution enthalpies of Po and Te in LBE (1/16), elemental Pb (various concentrations), and in elemental Bi (1/24). Additionally, the same correlation for full subsitution of either Pb or Bi by Po or Te is given for PbBi (NaCl-structure) and for Bi_4Pb_3. Every data point corresponds to a different local environment for Po/Te. In the two calculations that lead to every data point, all atomic positions were independently optimized (=the distance between Te and its neighbours is allowed to be different from the distance between Po and its neighbours). The dashed line is a similar fit through three well-separated data points, now taking spin–orbit coupling into account (from left to right: Bi-substitution in PbBi [NaCl], Pb-substitution in PbBi [NaCl], 25% of Po/Te in fcc-Pb).

a way that is not achievable in a lab. Using the 2×18 data points in both Fig. 3(a) and (b), we can compare the enthalpy cost of putting either Po or Te in *the same* atomistic environment (i.e. identical coordination symmetry, different bond lenghts). If these two data sets are plotted with respect to each other, an excellent linear correlation emerges (Fig. 4). In order to test whether or not this correlation depends on the particular $2 \times 2 \times 2$ LBE-model we have chosen, data points for reaction enthalpies of other crystals in contact with solid Te or solid Po were calculated: Te/Po as impurity in fcc Pb (concentrations of 3.1%, 6.25% and 25%), Te/Po as impurity in rhombohedral Bi (4.2%), substitution of all Pb in hypothetical Bi_4Pb_3 by Te/Po, and substitution of either all Pb or all Bi in hypothetical rocksalt PbBi by Te/Po. As Fig. 4 shows, these data points obtained in very different crystals perfectly follow the linear correlation. This strongly suggests that this linear correlation is a genuine property, and not an artefact due to the limited $2 \times 2 \times 2$ LBE supercell or the single random configuration. The linear correlation in Fig. 4 implies that Te is more strongly bound to the LBE matrix than Po is: environments that bind Te by less than 0.09 eV per solute atom, do not bind Po any longer (less than 0.14 eV per solute atom if spin–orbit coupling is considered). The latter is consistent with experimental observations in solid PbTe and solid PbPo (rock salt structure): whereas PbTe melts at 1195 K [40], PbPo decomposes already between 820 and 900 K [41,42] or sublimes around 1000 K [29]. Another corroborating observation is the evaporation rate of Po from LBE, which is larger than the one of Te from LBE [43].

Knowing this correlation, it would be possible to predict the solution enthalpy of Po in any LBE-like environment without making a DFT calculation, provided one has calculated the solution enthalpy of Te in that same environment. By extension, this applies to experiment as well: performing experiments on Te in LBE provides information that in principle could be translated to Po in LBE.

5. Influence of spin–orbit coupling

The common way to perform DFT calculations is to do it at the scalar-relativistic level [18]. This includes, for instance, the speed dependence of the mass of the electron. For heavy atoms, relativistic effects beyond the scalar-relativistic level cannot be entirely neglected. The dominant effect is spin–orbit coupling, which can be added in a perturbative way to scalar-relativistic calculations. Table 1 demonstrates the impact of spin–orbit coupling on the equilibrium volume and bulk modulus of the pure phases of Pb, Bi and Po: without spin–orbit coupling, all calculated volumes and bulk moduli agree with experiment within the error bar on the computed value, except for the bulk modulus of Po. When spin–orbit coupling is added, the latter disagreement is repaired. Therefore, we did apply spin–orbit coupling to some of the Po-substitutions in LBE. The result is that the scalar-relativistic solution enthalpies are shifted in the direction of more positive values by a varying amount, that has the order of magnitude of 0.1 eV per solute atom (open symbols in Fig. 3(a)). This shows that the Po solution enthalpy is less negative than the scalar-relativistic calculations suggested. However, the qualitative conclusions are not affected (no dissolution in the pure materials, Pb-rich environments preferred in LBE). For three well-separated points in Fig. 4, all calculations were repeated with spin–orbit coupling (including the geometry optimization). This allows to determine the linear correlation with spin–orbit coupling taken into account (dashed line in Fig. 4). It is this line which should be used to convert experimental solution enthalpies for Te into predicted solution enthalpies for Po.

6. Conclusions

Starting from a simple model system for solid LBE and using only information obtained from first-principles calculations, we predict that at low temperatures Po will not dissolve in the matrix of solid LBE (grain boundary solution was not studied). Although its solution enthalpy is negative (and most so in Pb-rich environments), competing compound-forming reactions are more exothermic. Similar calculations for Te in LBE show that Te is bound stronger by the LBE matrix than Po is. Solution enthalpies for Te in LBE correlate strongly with solution enthalpies for Po in LBE. This suggests that Te experiments can be used to map the expected behaviour for Po, a procedure that can reduce the number of required Po experiments.

Acknowledgements

This work is supported by the European Commission through the FP7 project SEARCH (Safe ExploitAtion Related CHemistry for HLM reactors, Project Nr. 295736) and by the Research Board of Ghent University. The authors acknowledge helpful discussions with Alexander Aerts (SCK-CEN, Mol), Emilio Andrea Maugeri and Matthias Rizzi (both PSI, Villigen). Three anonymous referees have contributed valuable suggestions. Stefaan Cottenier acknowledges financial support from OCAS NV by an OCAS-endowed chair at Ghent University. Calculations were carried out using the Stevin Supercomputer Infrastructure at Ghent University, funded by Ghent University, the Hercules Foundation, and the Flemish Government (EWI Department).

References

[1] H.A. Abderrahim, P. Baeten, D. De Bruyn, R. Fernandez, Energy Conversion and Management 63 (2012) 4–10.
[2] Pekka Pyykkö, John F. Stanton (Eds.), Chemical Reviews 112 (2012) 1–672.
[3] J. Hafner, Journal of Computational Chemistry 29 (2008) 2044.
[4] K. Schwarz, P. Blaha, S. Trickey, Molecular Physics 108 (2010) 3147.
[5] K. Lejaeghere, V. Van Speybroeck, G. Van Oost, S. Cottenier, Critical Reviews in Solid State Physics and Materials Science 39 (2014) 1.
[6] D. Jiang, E.A. Carter, Physical Review B 67 (2003) 214103.
[7] C. Wolverton, V. Ozolins, M. Asta, Physical Review B 69 (2004) 144109.
[8] C. Wolverton, V. Ozolins, Physical Review B 73 (2006) 144104.
[9] F. Soisson, C. Fu, Physical Review B 76 (2007) 214102.
[10] P. Erhart, B. Sadigh, A. Caro, Applied Physics Letters 92 (2008) 141904.
[11] A. Harutyunyan, N. Awasthi, A. Jiang, W. Setyawan, E. Mora, T. Tokune, K. Bolton, S. Curtarolo, Physical Review Letters 100 (2008) 195502.
[12] K. Lejaeghere, S. Cottenier, S. Claessens, M. Waroquier, V.V. Speybroeck, Physical Review B 83 (2011) 184201.
[13] P. Hohenberg, W. Kohn, Physical Review 136 (1964) B864.
[14] W. Kohn, L.J. Sham, Physical Review 140 (1965) A1133.
[15] R. Martin, Electronic Structure, Basic Theory and Practical Methods, Cambridge University Press, 2004.
[16] S. Cottenier, Density Functional Theory and the Family of (L)APW-Methods: A Step-By-Step Introduction, (Instituut voor Kern- en Stralingsfysica, KULeuven, Belgium), 2002. <http://www.wien2k.at/reg_user/textbooks> (ISBN: 90-807215-1-4).
[17] J.P. Perdew, K. Burke, M. Ernzerhof, Physical Review Letters 77 (1996) 3865.
[18] D. Koelling, B. Harmon, Journal of Physics C: Solid State Physics 10 (1977) 3107.
[19] P.E. Blöchel, Physical Review B 50 (1994) 17953.
[20] G. Kresse, D. Joubert, Physical Review B 59 (1999) 1758.
[21] G. Kresse, J. Furthmüller, Physical Review B 54 (1996) 11169.
[22] M.H.F. Sluiter en, Y. Kawazoe, Europhysics Letters 57 (2002) 526–532.
[23] A. Zunger, S. Wei, L. Ferreira, J. Bernard, Physical Review Letters 65 (1990) 353–356.
[24] S. Müller, Journal of Physics: Condensed Matter 15 (2003) R1429.
[25] P.E.A. Turchi, M. Sluiter, F.J. Pinski, D.D. Johnson, D.M. Nicholson, G.M. Stocks, J.B. Staunton, Physical Review Letters 67 (1991) 1779–1782.
[26] T.B Massalski, H. Okamoto, P.R. Subramanian, L. Kacprzak, Binary Alloys Phase Diagrams, second ed., ASM International, 1990, pp. 772–773.
[27] National Institute for Materials Science (NIMS), AtomWork, 2012. <http://crystdb.nims.go.jp/>.
[28] Y. Xu, M. Yamazaki, P. Villars, Japanese Journal of Applied Physics 50 (2011) 11RH02.
[29] W. Witteman, A. Giorgi, D. Vier, Journal of Physical Chemistry 64 (1960) 434.
[30] A. Zastawny, J. Bialon, T. Sosinski, Applied Radiation and Isotopes 40 (1989) 19.
[31] T. Miura, T. Obara, H. Sekimoto, Applied Radiation and Isotopes 61 (2004) 1307.
[32] J. Neuhausen, D. Schumann, R. Dressler, B. Eichler, S. Heinitz, B. Hammer, F. von Rohr, L. Zanini, V. Boutellier, M. Rthi, J. Eikenberg, E. Noah, Proceedings of the DAE-BRNS Symposium on Nuclear and Radiochemistry NUCAR-2011, vol. 44, Visakhapatnam, 2011.
[33] G. Tammann, A. von Löwis of Menar, Zeitschrift für anorganische und allgemeine Chemie 205 (1932) 145.
[34] V. Kutznetsov, V. Zlomanov, Inorganic Materials 25 (1989) 923.
[35] K. Yamana, K. Kihara, T. Matsumoto, Acta Crystallographica B 35 (1979) 147.
[36] S. Chizhevskaya, L. Shelimova, V. Zemskov, V. Kosyakov, D. Malakhov, Inorganic Materials 30 (1994) 1.
[37] R. Blachnik, F. Romermann, A. Schlieper, Zeitschrift fur Metallkunde 88 (1997) 301.
[38] R. Oshea, J. Donovan, E. Peretti, Transactions of the Metallurgical Society of AIME 221 (1961) 1266.
[39] R. Oshea, E. Peretti, Transactions of the American Society of Metals Quarterly 56 (1963) 153.
[40] W. Gierlotka, J. Lapsa, D. Jendrzejczyk-Handzlik, Journal of Alloys and Compounds 479 (2009) 152.
[41] J. Goode, Mound Laboratory Report 1952/55; N.S.A. 10, 1956.
[42] T. Miura, T. Obara, H. Sekimoto, Annals of Nuclear Energy 34 (2007) 926.
[43] J. Neuhausen, U. Köster, B. Eichler, Radiochimica Acta 92 (2004) 917.

Appendix A

High Performance Computing

During this PhD research, the available computational infrastructure at the Ghent University evolved drastically. At the start, a combination of group infrastructure (*tier-3*) and one institution wide computer cluster (*tier-2*) was available. Nowadays, the *tier-2* infractructure was increased by a factor 4. Additionally, the Flemish Government and the Hercules foundation finance the construction and maintenance of a new *tier-1* high performance computer (HPC), available for all Flemish universities, research institutes and industry. A virtual supercomputer center is created to manage the available infrastructure on the different Flemish universities: the Flemish Supercomputer Center (VSC, *Vlaamse Supercomputer Centrum*). [156] The Partnership

Figure A.1: Top layers of computational infrastructure in Europe.

for Advanced Computing in Europe (PRACE) created an infrastructure of HPC resources on the European level (*tier-0*) and is in collaboration with national HPC centres.[157] These different layers are represented in Figure A.1.

		year	cores	network	clock	RAM/node
tier-3	moldyn47-49,51	2006	16	Ethernet	2.00 GHz	8.8 GB
	moldyn52-55	2008	32	Ethernet	2.83 GHz	11 GB
tier-2	gengar	2008	1536	IB DDR	2.5 GHz	16 GB
	gastly	2009	448	Ethernet	2.26 GHz	12 GB
	haunter	2010	1336	Ethernet	2.26 GHz	12 GB
	gulpin	2011	1088	IB 2xQDR	2.4 GHz	64 GB
	dugtrio	2011	192	IB 2xQDR	3.06 GHz	96 GB
	raichu	2012	1024	Ethernet	2.6 GHz	32 GB
	delcatty	2013	2560	IB FDR	2.6 GHz	64 GB
tier-1	muk	2013	8848	IB FDR	2.6 GHz	64 GB

Table A.1: Overview of the computational infrastructure used in this work (2009-2014).[158]

In this dissertation, *tier-3*, *tier-2* and *tier-1* infrastructure were used. Table A.1 summarizes the most important specifications of the clusters. The *tier-3* infrastructure is still valuable for small test simulations, while the various *tier-2* infrastructures are applicable for simulations on larger systems or high-throughput calculations. Each of the clusters has its own specific purposes: the ones with infiniband (IB) network connection are ideally suited to cope with very demanding calculations (*e.g.* solving linear response equations for Rh in NaCl and sucrose crystals, molecular dynamics of Cu-SSZ-13 and rhamnose single crystals), while the clusters with slower connections are suited for a massive amount of smaller jobs (*e.g.* TD-DFT calculations on a large set of MD snapshots, benchmark of g-tensor calculations on diatomic molecules, dissociation energy calculation of Po-containing molecules).

The introduction of the *tier-1* infrastructure allowed performing much longer *ab initio* MD simulations on larger systems, performing more calculations on snapshots from this MD or coping with much larger systems. In **Paper II** in particular, the *tier-1* infrastructure was used to calculate the excitation energies on the MD snapshots. For these simulations and for simulations on the Cu-SSZ-13 system (paper in preparation), a project was granted for 4267 node days.

During the pilot phase of the *tier-1* cluster, the CMM — as one of the largest users of the *tier-2* infrastructure — was allowed to benchmark the system and the quantum chemistry codes to be installed on the machine, in particular CP2K, VASP, Gaussian. For this dissertation, CP2K was thouroughly

benchmarked over all VSC clusters. Figure A.2 shows the single core calculation time for simulating a short MD simulation on 64 water molecules, performed at the different clusters, clearly showing a speedup for the more recent clusters.

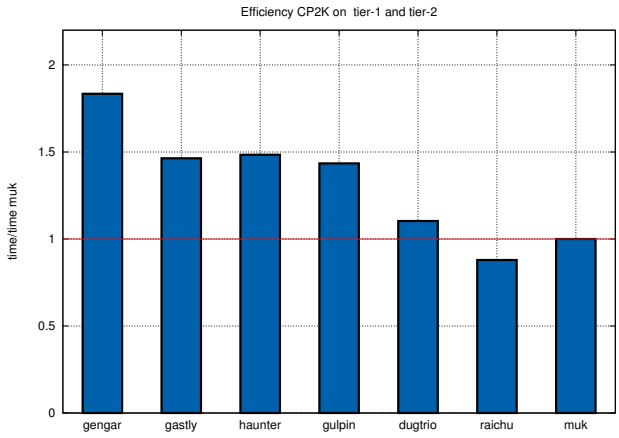

Figure A.2: Efficiency of the *tier-2* clusters, scaled by the computation time for the same calculation on the *tier-1* cluster (muk).

In Figure A.3, the scaling behaviour of CP2K with respect to the number of cores is presented for different system sizes. The considered systems are periodic boxes with increasing size, filled with a number of water molecules, varying between 32 and 1024. From these tests, it becomes clear that increasing the number of cores is only beneficial for large applications, while for small systems the efficiency decreases from one point on.

Within CP2K, new algorithms towards linear scaling of the calculation time with system size became available quite recently.[84, 159] This aspect was also investigated. The timings between traditional methods and the linear scaling implementations are compared in Figure A.4. From the point at which the traditional codes cannot cope with the large systems (around 40000 basis functions) — due to memory issues for example — the linear scaling methods reach the same efficiency as before. They allow, however, to simulate larger systems systems up to 16384 water molecules (393216 basis functions).

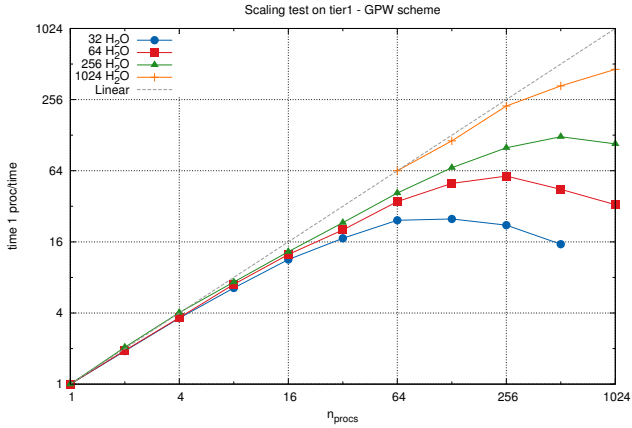

Figure A.3: Scaling behaviour of CP2K with respect to system size.

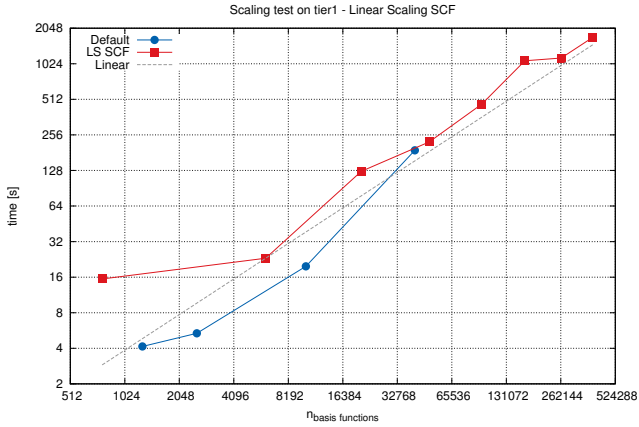

Figure A.4: Comparison between the timings of the traditional algorithms (blue) used in CP2K and the linear scaling algorithms (red) which became available recently.

Bibliography

[1] The Official Web Site of the Nobel Prize. http://www.nobelprize.org/, 2014.

[2] The Nobel Prize in Physics 1902. http://www.nobelprize.org/nobel_prizes/physics/laureates/1902/, 2014.

[3] The Nobel Prize in Chemistry 2007. http://www.nobelprize.org/nobel_prizes/chemistry/laureates/2007/, 2014.

[4] Isaac Newton. *Opticks, or a treatise of the reflections, refractions, inflections and colours of light.* William Innys, 1730.

[5] Joseph Fraunhofer. Bestimmung des Brechungs- und des Farben-Zerstreuungs - Vermögens verschiedener Glasarten, in Bezug auf die Vervollkommnung achromatischer Fernröhre. *Denkschriften der Königlichen Akademie der Wissenschaften zu München*, 5:193–226, 1814-1815.

[6] Gustav Kirchoff. Ueber die Fraunhofer'schen Linien. *Annalen der Physik*, 185:148–150, 1860.

[7] Johann Jakob Balmer. Notiz über die Spectrallinien des Wasserstoffs. *Annalen der Physik*, 261(5):80–87, 1885.

[8] Theodore Lyman. An Extension of the Spectrum in the Extreme Ultra-Violet. *Nature*, 93:241, 1914.

[9] Niels Bohr. I. On the constitution of atoms and molecules. *Philosophical Magazine Series 6*, 26(151):1–25, 1913.

[10] David J. Griffiths. *Introduction to Quantum Mechanics (2nd ed.).* Prentice Hall, 2004.

[11] Pieter Zeeman. The Effect of Magnetisation on the Nature of Light Emitted by a Substance. *Nature*, 55:347, 1897.

[12] George E. Uhlenbeck and Samuel Goudsmit. Spinning Electrons and the Structure of Spectra. *Nature*, 117:264–265, 1926.

[13] Paul A. M. Dirac. The Quantum Theory of the Electron. *Proceedings of the Royal Society of London A*, 117:610–624, 1928.

[14] Harry G. Hecht. *Magnetic Resonance Spectroscopy*. John Wiley, 1967.

[15] E. Zavoisky. Relaxation of liquid solution for perpendicular fields. *Journal of Physics-USSR*, 9:211–216, 1945.

[16] Neil Manning Atherton. *Principles of Electron Spin Resonance*. Ellis Horwood Limited, 1993.

[17] Anatole Abragam and Brebis Bleaney. *Electron Paramagnetic Resonance of Transition Ions*. Dover Publications, Inc., 1986.

[18] John E. Harriman. *Theoretical Foundations of Electron Spin Resonance*. Academic Press, 1978.

[19] George W. Chantry. *Modern Aspects of Microwave Spectroscopy*. Academic Press Inc, 1979.

[20] Gerhard Herzberg. *Molecular Spectra and Molecular Structure*. D. Van Nostrand Company, Inc., 1950.

[21] Clifton E. Meloan. *Elementary Infrared Spectroscopy*. MacMillan, 1963.

[22] Werner A. Bingel. *Theory of Molecular Spectra*. Chichester, 1970.

[23] Fred Basolo and Ralph G. Pearson. *Mechanisms of Inorganic Reactions: a Study of Metal Complexes in Solution*. Wiley, 1967.

[24] Martin Klessinger and Josef Michl. *Excited States and Photochemistry of Organic Molecules*. VCH, 1995.

[25] Karen Hemelsoet, Qingyun Qian, Thierry De Meyer, Kristof De Wispelaere, Bart De Sterck, Bert M. Weckhuysen, Michel Waroquier, and Veronique Van Speybroeck. Identification of Intermediates in Zeolite-Catalyzed Reactions by In Situ UV/Vis Microspectroscopy and a Complementary Set of Molecular Simulations. *Chemistry – A European Journal*, 19(49):16595–16606, 2013.

[26] Thierry De Meyer, Karen Hemelsoet, Lien Van der Schueren, Ewald Pauwels, Karen De Clerck, and Veronique Van Speybroeck. Investigating the Halochromic Properties of Azo Dyes in an Aqueous Environment by Using a Combined Experimental and Theoretical Approach. *Chemistry - A European Journal*, 18(26):8120–8129, 2012.

[27] Jörg Grunenberg. *Computational Spectroscopy: Methods, Experiments and Applications*. Wiley-VCH, 2010.

[28] Inge L. C. Buurmans and Bert M. Weckhuysen. Heterogeneities of individual catalyst particles in space and time as monitored by spectroscopy. *Nature Chemistry*, 4:1755–4330, 2012.

[29] Robert G. Parr and Weitao Yang. *Density-Functional Theory of Atom and Molecules*. Oxford University Press, 1989.

[30] Pierre Hohenberg and Walter Kohn. Inhomogeneous Electron Gas. *Physical Review*, 136:B864–B871, 1964.

[31] Christopher J. Cramer. *Essentials of Computational Chemistry: Theories and Models*. Wiley-VCH, 2004.

[32] Miguel A. Marques, Carsten A. Ullrich, Fernando Nogueira, Angel Rubio, Kieron Burke, and Eberhard K. U. Gross. *Time-dependent density functional theory*. Springer, 2006.

[33] Carsten A. Ullrich. *Time-Dependent Density-Functional Theory, Concepts and Applications*. Oxford University Press, 2012.

[34] Carlo Adamo and Denis Jacquemin. The calculations of excited-state properties with Time-Dependent Density Functional Theory. *Chemical Society Reviews*, 42:845–856, 2013.

[35] Vincenzo Barone and Antonino Polimeno. Integrated computational strategies for UV/Vis spectra of large molecules in solution. *Chemical Society Reviews*, 36:1724–1731, 2007.

[36] Vincenzo Barone, Julien Bloino, Susana Monti, Alfonso Pedone, and Giacomo Prampolini. Fluorescence spectra of organic dyes in solution: a time dependent multilevel approach. *Physical Chemistry Chemical Physics*, 13:2160–2166, 2011.

[37] ADF2010, SCM, Theoretical Chemistry, Vrije Universiteit, Amsterdam, The Netherlands. http://www.scm.com.

[38] Frank Neese. The ORCA program system. *Wiley Interdisciplinary Reviews: Computational Molecular Science*, 2(1):73–78, 2012.

[39] Vladimir G. Malkin, Olga. L. Malkina, Roman Reviakine, Alexei V. Arbuznikov, Martin Kaupp, Bernd Schimmelpfennig, Irina Malkin, Michal Repiský, Stanislav Komorovský, Peter Hrobárik, Elena Malkin, Trygve Helgaker, and Kenneth Ruud. ReSpect program (current version 2.2).

[40] Jürg Hutter, Marcella Iannuzzi, Florian Schiffmann, and Joost VandeVondele. cp2k: atomistic simulations of condensed matter systems. *Wiley Interdisciplinary Reviews: Computational Molecular Science*, 4(1):15–25, 2014.

[41] Vienna Ab-Initio Simulation Package (VASP).

[42] QuantumESPRESSO.

[43] Chris J. Pickard and Francesco Mauri. First-principles theory of the EPR g tensor in solids: Defects in quartz. *Physical Review Letters*, 88(8):086403, 2002.

[44] Valéry Weber, Marcella Iannuzzi, Samuele Giani, Jürg Hutter, Reinout Declerck, and Michel Waroquier. Magnetic linear response properties calculations with the Gaussian and augmented-plane-wave method. *Journal of Chemical Physics*, 131:014106, 2009.

[45] Eugene S. Kadantsev and Tom Ziegler. Implementation of a DFT-Based Method for the Calculation of the Zeeman g-Tensor in Periodic Systems with the Use of Numerical and Slater-Type Atomic Orbitals. *Journal of Physical Chemistry A*, 113(7):1327–1334, 2009.

[46] Piotr Pietrzyk, Tomasz Mazur, Katarzyna Podolska-Serafin, Mario Chiesa, and Zbigniew Sojka. Intimate Binding Mechanism and Structure of Trigonal Nickel(I) Monocarbonyl Adducts in ZSM-5 Zeolite–Spectroscopic Continuous Wave EPR, HYSCORE, and IR Studies Refined with DFT Quantification of Disentangled Electron and Spin Density Redistributions along σ and π Channels. *Journal of the American Chemical Society*, 135(41):15467–15478, 2013.

[47] L. Ateş, Ö. Dereli, E. Türkkan, Ü. Sayin, F. Sevgi, R. Tapramaz, and M. Birey. EPR study of gamma-irradiated diaminoglyoxime single crystals. *Journal of Molecular Structure*, 1005(1-3):8–11, 2011.

[48] Francesco Napoli, Mario Chiesa, Elio Giamello, Maria Fittipaldi, Cristiana Di Valentin, Federico Gallino, and Gianfranco Pacchioni. N_2-Radical Anions Trapped in Bulk Polycrystalline MgO. *Journal of Physical Chemistry C*, 114(11):5187–5192, 2010.

[49] Bernd A. Hess, Christel M. Marian, Ulf Wahlgren, and Odd Gropen. A mean-field spin-orbit method applicable to correlated wavefunctions. *Chemical Physics Letters*, 251(5-6):365–371, 1996.

[50] Frank Neese. Efficient and accurate approximations to the molecular spin-orbit coupling operator and their use in molecular g-tensor calculations. *Journal of Chemical Physics*, 122:034107, 2005.

[51] Giovanni Ciccotti and William G. Hoover. *Molecular-Dynamics Simulation of Statistical-Mechanical Systems*. North-Holland Physics Publishing, 1986.

[52] Dominik Marx and Jürg Hutter. Ab Initio Molecular Dynamics: Theory and Implementation. In J. Grotendorst, editor, *Modern Methods and Algorithms of Quantum Chemistry*, volume 3 of *NIC Series*, pages 329–477, 2000.

[53] Daan Frenkel and Berend Smit. *Understanding Molecular Simulation*. Academic Press, 2002.

[54] Hamid Aït Abderrahim, Peter Baeten, Didier De Bruyn, and Rafael Fernandez. MYRRHA - A multi-purpose fast spectrum research reactor. *Energy Conversion and Management*, 63:4–10, 2012.

[55] Eberhard K. U. Gross, Erich Runge, and Olle Heinonen. *Many-Particle Theory*. CRC Press, 1991.

[56] Peter Schwerdtfeger. *Relativistic Electronic Structure Theory*. Elsevier, 2002.

[57] Roy McWeeny. *Methods of Molecular Quantum Mechanics (2nd ed.)*. London: Academic, 1989.

[58] Wim H. Dickhoff and Dimitri Van Neck. *Many-Body Theory Exposed! Propagator Description of Quantum Mechanics in Many-Body Systems*. World Scientific Publishing Company, 2006.

[59] Rodney J. Bartlett. Many-Body Perturbation Theory and Coupled Clusters Theory for Electron Correlation in Molecules. *Annual Review of Physical Chemistry*, 32:359 – 401, 1981.

[60] W. Kohn and L. J. Sham. Self-Consistent Equations Including Exchange and Correlation Effects. *Physical Review*, 140:A1133–A1138, 1965.

[61] Llewellyn H. Thomas. The calculation of atom fields. *Proceedings Cambridge Philosophical Society*, 23:542–548, 1927.

[62] Enrico Fermi. Un Metodo Statistico per la Determinazione di alcune Prioprietà dell'Atomo. *Rendiconti Accademia Nazionale dei Linceiok*, 6:602–607, 1927.

[63] Paul A. M. Dirac. Note on Exchange Phenomena in the Thomas Atom. *Proceedings Cambridge Philosophical Society*, 26(03):376–385, 1930.

[64] John C. Slater. A Simplification of the Hartree-Fock Method. *Physical Review*, 81:385–390, 1951.

[65] Tobias Schwabe and Stefan Grimme. Double-hybrid density functionals with long-range dispersion corrections: higher accuracy and extended applicability. *Physical Chemistry Chemical Physics*, 9:3397–3406, 2007.

[66] Walter Greiner. *Quantum Mechanics: Special Chapters*. Springer, 2006.

[67] Leslie L. Foldy and Siegfried A. Wouthuysen. On the Dirac theory of spin 1/2 particles and its non-relativistic limit. *Physical Review*, 78:29–36, 1950.

[68] Gregory Breit. Dirac's Equation and the Spin-Spin Interactions of Two Electrons. *Physical Review*, 39:616–624, 1932.

[69] Zeno V. Chraplyvy. Reduction of Relativistic Two-Particle Wave Equations to Approximate Forms. I. *Physical Review*, 91:388–391, 1953.

[70] Zeno V. Chraplyvy. Reduction of Relativistic Two-Particle Wave Equations to Approximate Forms. II. *Physical Review*, 92:1310–1315, 1953.

[71] W. A. Barker and F. N. Glover. *Physical Review*, 99:317, 1955.

[72] Andy Van Yperen-De Deyne. Theoretische en computationele aspecten van zero-field splitting berekeningen aan transitiemetaaldefecten in ionaire roosters. Master's thesis, Ghent University, 2009.

[73] Erik van Lenthe, Evert-Jan Baerends, and Jaap G. Snijders. Relativistic regular two-component Hamiltonians. *Journal of Chemical Physics*, 99:4597, 1993.

[74] Abbas Farazdel and Vedene H. Smith Jr. Invalidity of the Ubiquitous Mass-Velocity Operator in Quasirelativistic Theories. *International Journal of Quantum Chemistry*, 29:311–314, 1986.

[75] Christoph van Wüllen. Molecular density functional calculations in the regular relativistic approximation. method, application to coinage metal diatomics, hydrides, fluorides and chlorides, and comparison with first-order relativistic calculations. *Journal of Chemical Physics*, 109:392–399, 1998.

[76] Jürgen Gauss. *Modern Methods and Algorithms of Quantum Chemistry*. John von Neumann-Institut für Computing, 2000.

[77] Paul Geerlings, Stijn Fias, Zino Boisdenghien, and Frank De Proft. Conceptual DFT: chemistry from the linear response function. *Chemical Society Reviews*, pages –, 2014.

[78] Hans Hellman. *Einführung in die Quantenchemie*. 1937.

[79] Richard P. Feynman. Forces in Molecules. *Physical Review*, 56(4):340, 1939.

[80] Frank Neese. Prediction of electron paramagnetic resonance g values using coupled perturbed Hartree-Fock and Kohn-Sham theory. *Journal of Chemical Physics*, 115(24):11080–11096, 2001.

[81] Erich Runge and E. K. U. Gross. Density-Functional Theory for Time-Dependent Systems. *Physical Review Letters*, 52:997–1000, 1984.

[82] Mark E. Casida. *Time-Dependent Density Functional Response Theory for Molecules*, chapter 5, pages 155–192.

[83] Mark E. Casida. Time-Dependent Density-Functional Theory for molecules and molecular soids. *Journal of Molecular Structure: THEOCHEM*, 914:3–18, 2009.

[84] Rustam Z. Khaliullin, Joost VandeVondele, and Jürg Hutter. Efficient Linear-Scaling Density Functional Theory for Molecular Systems. *Journal of Chemical Theory and Computation*, 9(10):4421–4427, 2013.

[85] Joost VandeVondele, Matthias Krack, Fawzi Mohamed, Michele Parrinello, Thomas Chassaing, and Jürg Hutter. QUICKSTEP: Fast and accurate density functional calculations using a mixed Gaussian and plane waves approach. *Computer Physics Communications*, 167(2):103–128, 2005.

[86] ORCA. http://cec.mpg.de/forum/.

[87] CP2K Open Source Molecular Dynamics. http://www.cp2k.org/.

[88] Walther Gerlach and Otto Stern. Das magnetische Moment des Silberatoms. *Zeitschrift für Physik*, 9(1):353–355, 1922.

[89] Martin Kaupp, Michael Bühl, and Vladimir G. Malkin. *Calculation of NMR and EPR Parameters*. WILEY-VCH4, 2004.

[90] Reinout Declerck. *Development and Implementation of Theoretical Methods for the Calculation of EPR Parameters in Periodic Simulations*. PhD thesis, Ghent University, 2008.

[91] Ewald Pauwels, Reinout Declerck, Veronique Van Speybroeck, and Michel Waroquier. Evidence for a Grotthuss-like mechanism in the formation of the rhamnose alkoxy radical based on periodic DFT calculations. *Radiation Research*, 169:8 – 18, 2008.

[92] Ewald Pauwels, Reinout Declerck, Toon Verstraelen, Bart De Sterck, Christopher W. M. Kay, Veronique Van Speybroeck, and Michel Waroquier. Influence of Protein Environment on the Electron Paramagnetic Resonance Properties of Flavoprotein Radicals: A QM/MM Study. *Journal of Physical Chemistry B*, 114:16655 – 16665, 2010.

[93] Ewald Pauwels, Veronique Van Speybroeck, and Michel Waroquier. Study of Rhamnose Radicals in the Solid State Adopting a Density Functional Theory Cluster Approach. *Journal of Physical Chemistry A*, 110:6504 – 6513, 2006.

[94] Erik van Lenthe, Ad van der Avoird, and Paul E. S. Wormer. Density Functional calculations of molecular hyperfine interactions in the zero order regular approximation for relativistic effects. *Journal of Chemical Physics*, 108:4783 – 4796, 1998.

[95] Frank Neese. Metal and ligand hyperfine ccoupling in transition metal complexes: the effect of spin-orbit coupling as studied by coupled perturbed Kohn-Sham theory. *Journal of Chemical Physics*, 118:3939, 2003.

[96] Alexei V. Arbuznikov, Juha Vaara, and Martin Kaupp. Relativistic spin-orbit effects on hyperfine coupling tensors by density-functional theory. *The Journal of Chemical Physics*, 120(5):2127–2139, 2004.

[97] Olav Vahtras, Oleksandr Loboda, Boris Minaev, Hans Ågren, and Kenneth Ruud. Ab initio calculation of zero-field splitting parameters. *Chemical Physics*, 279:133 – 142, 2002.

[98] Sebastian Sinnecker and Frank Neese. Spin-Spin Contributions to the Zero-Field Splitting Tensor in Organic Triplets, Carbenes and Biradicals - A Density Functional and Ab Initio Study. *Journal of Physical Chemistry A*, 110:12267 – 12275, 2006.

[99] Dmitry Ganyushin and Frank Neese. First-Principles calculations of zero-field splitting parameters. *Journal of Chemical Physics*, 125:024103, 2006.

[100] Frank Neese. Calculation of the zero-field splitting tensor on the basis of hybrid density functional and Hartree-Fock theory. *Journal of Chemical Physics*, 127:164112, 2007.

[101] Frank Neese and Edward I. Solomon. Calculation of Zero-Field Splittings, g-Values, and the Relativistic Nephelauxetic Effect in Transition Metal Complexes. Application to High-Spin Ferric Complexes. *Inorganic Chemistry*, 37(26):6568–6582, 1998.

[102] Shiro Koseki, Michael W. Schmidt, and Mark S. Gordon. MCSCF/6-31G(D,P) calculations of one-electron spin-orbit-coupling constants in diatomic-molecules. *Journal of Physical Chemistry*, 96(26):10768–10772, 1992.

[103] Henk Vrielinck, Freddy Callens, Marieta Zdravkova, and Paul Matthys. ENDOR identification of a Rh^{+} centre in solution-grown NaCl. *Journal of the Chemical Society, Faraday Transactions*, 94:2999–3002, 1998.

[104] Henk Vrielinck, Kris Sabbe, Freddy Callens, and Paul Matthys. Detection of charge compensating cation vacancies near Rh^{2+} complexes in AgCl and NaCl using Q-band ENDOR. *Physical Chemistry Chemical Physics*, 3:1709 – 1716, 2001.

[105] Henk Vrielinck, Freddy Callens, and Paul Matthys. EPR spectrum and formation properties of a cubic Rh^{+} centre in NaCl. *Physical Chemistry Chemical Physics*, 4:2434 – 2437, 2002.

[106] Peter V. Sushko, Alexander L. Shluger, Roger C. Baetzold, and C. Richard A. Catlow. Embedded cluster calculations of metal complex impurity defects: properties of the iron cyanide in NaCl. *Journal of Physics: Condensed Matter*, 12:8257 – 8266, 2000.

[107] Franky Stevens, Henk Vrielinck, Freddy Callens, Ewald Pauwels, and Michel Waroquier. Density-functional study on S_2^- defects in alkali halides. *Physical Review B*, 66:134103, 2002.

[108] Hendrik De Cooman, Ewald Pauwels, Henk Vrielinck, Anna Dimitrova, Nicola Yordanov, Einar Sagstuen, Michel Waroquier, and Freddy Callens. Radiation-induced defects in sucrose single crystals, revisited: A combined electron magnetic resonance and density functional theory study. *Spectrochimica Acta, Part A: Molecular and Biomolecular Spectroscopy*, 69:1372 – 1383, 2008.

[109] Hendrik De Cooman, Ewald Pauwels, Henk Vrielinck, Einar Sagstuen, Sabine Van Doorslaer, Freddy Callens, and Michel Waroquier. ENDOR

and HYSCORE analysis and DFT-assisted identification of the third major stable radical in sucrose single crystals X-irradiated at room temperature. *Physical Chemistry Chemical Physics*, 11:1105 – 1114, 2009.

[110] Peter H. Berens and Kent R. Wilson. Molecular Dynamics and Spectra. I. Diatomic rotation and vibration. *Journal of Chemical Physics*, 74:4872, 1981.

[111] Martin Thomas, Martin Brehm, Reinhold Fligg, Peter Vöhringer, and Barbara Kirchner. Computing vibrational spectra from ab initio molecular dynamics. *Physical Chemistry Chemical Physics*, ASAP, 2013.

[112] Yitzhak Katznelson. *An Introduction to Harmonic Analysis*. Cambridge University Press, 2004.

[113] Sebastián Gonçalves and Hernan Bonadeo. Vibrational density of states from molecular-dynamics calculations. *Physical Review B*, 46:12019 – 12021, 1992.

[114] Mark E. Tuckerman. *Ab initio* molecular dynamics: basic concepts, current trends and novel applications. *Journal of Physics: Condensed Matter*, 14:1297 – 1355, 2002.

[115] Marco Bernasconi, Pier L. Silvestrelli, and Michele Parrinello. Ab Initio Infrared Absorption Study of the Hydrogen-Bond Symmetrization in Ice. *Physical Review Letters*, 81(6):1235 – 1238, 1998.

[116] Anna Putrino and Michele Parrinello. Anharmonic Raman Spectra in High-Pressure Ice from Ab Initio Simulations. *Physical Review Letters*, 88(17):176401, 2002.

[117] Marc Van Houteghem. A Study of Liquids on an Atomic Scale: Molecular Dynamics on Organic Solvents. Master's thesis, Ghent University, 2008.

[118] Eckart Henssge, Denis Dumont, Dieter Fisher, and Daniel Bougeard. Analysis of infrared and Raman spectra calculated by molecular dynamics. *Journal of Molecular Structure*, 482-483:491 – 496, 1998.

[119] Marc Van Houteghem, Toon Verstraelen, Dimitri Van Neck, Christine Kirschhock, Johan A. Martens, Michel Waroquier, and Veronique Van Speybroeck. Atom Velocity Projection Method: A New Analysis Method for Vibrational Spectra in Terms of Internal Coordinates for a Better Understanding of Zeolite Nanogrowth. *Journal of Chemical Theory and Computation*, 7:1045 – 1061, 2011.

[120] M. Martinez, Marie-Pierre Gaigeot, Daniel Borgis, and Rodolphe Vuilleumier. Extracting effective normal modes from equilibrium dynamics at finite temperature. *Journal of Chemical Physics*, 125:144106, 2006.

[121] Walter Rudin. *Real and Complex Analysis*. McGraw-Hill, 1987.

[122] Masaoki Iwasaki and Hirofumi Shinjoh. A comparative study of "standard", "fast" and NO_2 SCR reactions over Fe/zeolite catalyst. *Applied Catalysis A: General*, 390(1-2):71 – 77, 2010.

[123] Masakazu Iwamoto, Hiroshi Furukawa, Yoshihiro Mine, Fumihide Uemura, Shin-ichi Mikuriya, and Shuichi Kagawa. Copper(II) ion-exchanged ZSM-5 zeolites as highly active catalysts for direct and continuous decomposition of nitrogen monoxide. *Journal of the Chemical Society, Chemical Communications*, pages 1272–1273, 1986.

[124] Dustin W. Fickel, Elizabeth D'Addio, Jochen A. LAuterbach, and Raul F. Lobo. The ammonia selective catalytic reduction activity of copper-exchanged small-pore zeolites. *Applied Catalysis B: Environmental*, 102:441 – 448, 2011.

[125] Ja Hun Kwak, Russell G. Tonkyn, Do Heui Kim, JÃąnos Szanyi, and Charles H.F. Peden. Excellent activity and selectivity of Cu-SSZ-13 in the selective catalytic reduction of NOx with NH3. *Journal of Catalysis*, 275(2):187 – 190, 2010.

[126] Toon Verstraelen, Paul W. Ayers, Veronique Van Speybroeck, and Michel Waroquier. Hirshfeld-E partitioning: AIM charges with an improved trade-off between robustness and accurate electrostatics. *Journal of Chemical Theory and Computation*, 9:2221–2225, 2013.

[127] Feng Gao, Ja Hun Kwak, Janos Szanyi, and Charles H.F. Peden. Current understanding of Cu-exchanged chabazite molecular sievers for use as commercial diesel engine DeNO$_x$ catalysts. *Topics in Catalysis*, 56:1441–1459, 2013.

[128] Upakul Deka, Ines Lezcano-Gonzalez, Bert M. Weckhuysen, and Andrew M. Beale. Local Environment and Nature of Cu Active Sites in Zeolite-Based Catalysts for the Selective Catalytic Reduction of NOx. *ACS Catalysis*, 3(3):413–427, 2013.

[129] Florian Göltl and Jürgen Hafner. Structure and properties of metal-exchanged zeolites studied using gradient-corrected and hybrid functional. I. Structure and energetics. *Journal of Chemical Physics*, 136:064501, 2012.

[130] Filippo Giordanino, Elisa Borfecchia, Kirill A. Lomachenko, Andrea Lazzarini, Giovanni Agostini, Erik Gallo, Alexander V. Soldatov, Pablo Beato, Silvia Bordiga, and Carlo Lamberti. Interaction of NH_3 with Cu-SSZ-13 catalyst: A complementary FTIR, XANES and XES study. *Thai Journal of Physical Chemistry Letters*, 5:1552 – 1559, 2014.

[131] Ewald Pauwels, James Asher, Martin Kaupp, and Michel Waroquier. Cluster or periodic, static or dynamic-the challenge of calculating the g tensor of the solid-state glycine radical. *Physical Chemistry Chemical Physics*, 13:18638–18646, 2011.

[132] Florian Göltl and Jürgen Hafner. Structure and properties of metal-exchanged zeolites studied using gradient-corrected and hybrid functional. II. Electron structure and Photoluminescence spectra. *Journal of Chemical Physics*, 136:064502, 2012.

[133] Florian Göltl and Jürgen Hafner. Structure and properties of metal-exchanged zeolites studied using gradient-corrected and hybrid functional. III. Energetics and vibrational spectroscopy of adsorbates. *Journal of Chemical Physics*, 136:064503, 2012.

[134] Stefan Grimme, Jens Antony, Stephan Ehrlich, and Helge Krieg. A consistent and accurate ab initio parametrization of density functional dispersion correction (DFT-D) for the 94 elements H-Pu. *Journal of Chemical Physics*, 32:1456, 2011.

[135] Dana Nachtigallová, Ota Bludský, Carlos Otero Areán, Roman Bulánek, and Petr Nachtigall. The vibrational dynamics of carbon monoxide in a confined space - CO in zeolites. *Physical Chemistry Chemical Physics*, 8:4849–4852, 2006.

[136] Vincent F. Kispersky, A. Jeremy Kropf, Fabio H Ribeiro, and Jeffrey T. Miller. Low absorption vitreous carbon reactors for operando XAS: a case study on Cu/Zeolites for selective catalytic reduction of NOx by NH_3. *Physical Chemistry Chemical Physics*, 14:2229, 2012.

[137] Satu T. Korhonen, Dustin W. Fickel, Raul F. Lobo, Bert M. Weckhuysen, and Andrew M. Beale. Isolated Cu^{2+} ions: active sites for selective catalytic reduction of NO. *Chemical Communications*, 47:800–802, 2011.

[138] Gemma Turnes Palomino, Paola Fisicaro, Silvia Bordiga, Adriano Zecchina, Elio Giamello, and Carlo Lamberti. Oxidation States of Copper Ions in ZSM-5 Zeolites. A Multitechnique Investigation. *Journal of Physical Chemistry B*, 104:4064 – 4073, 2000.

[139] F.L. Hirshfeld. Bonded-atom fragments for describing molecular charge densities. *Theoretica chimica acta*, 44(2):129–138, 1977.

[140] Patrick Bultinck, Christian Van Alsenoy, Paul W. Ayers, and Ramon Carbó-Dorca. Critical analysis and extension of the Hirshfeld atoms in molecules. *The Journal of Chemical Physics*, 126(14):–, 2007.

[141] Ewald Pauwels. *First-principles study of radiation-induced radicals in solid-state amino-acids and sugars: confrontation of density-functional calculations with experimental results*. PhD thesis, Ghent University, 2003-2004.

[142] Hendrik De Cooman. *A combined EMR and DFT study of radiation-induced defects in sucrose and glucose 1-phosphate*. PhD thesis, Ghent University, 2008-02009.

[143] Ewald Pauwels. *Uncovering radiation chemis1try in the solid state through periodic density-functional calculations: confrontation with experimental results and beyond*, chapter 18, page to be published. 2014.

[144] Ewald Pauwels, Toon Verstraelen, and Michel Waroquier. Effect of temperature on the EPR properties of a rhamnose alkoxy radical: A DFT molecular dynamics study. *Spectrochimica Acta, Part A: Molecular and Biomolecular Spectroscopy*, 69:1388 – 1394, 2008.

[145] Einar Sagstuen, Mikael Lindgren, and A. Lund. Electron Trapping and Reactions in Rhamnose by ESR and ENDOR. *Radiation Research*, 128:235 – 242, 1991.

[146] Per-Olof Samskog and Anders Lund. The alkoxy radical RCHO formed in irradiated single crystals of rhamnose. *Chemical Physics Letters*, 75:525 – 527, 1980.

[147] Per-Olof Samskog, Anders Lund, Goesta Nilsson, and Martyn C. R. Symons. Primary reactions of localized electrons in rhamnose crystals studied by pulse radiolysis and ESR spectroscopy. *The Journal of Chemical Physics*, 73(10):4862–4866, 1980.

[148] Hiroto Tachikawa and Takahiro Fukuzumi. Ionization dynamics of aminopyridine dimer: a direct ab initio molecular dynamics (MD) study. *Physical Chemistry Chemical Physics*, 13:5881–5887, 2011.

[149] MYRRHA: Multi-purpose hybrid research reactor for high-tech applications. http://myrrha.sckcen.be/, 2014.

[150] Kim Rijpstra. *Density functional theory as a tool to get more out of experimental data: case-studies for Al-Zn-O and for the interaction between Po and Pb-Bi-eutectic*. PhD thesis, Ghent University, 2013-2014.

[151] Joerg Neuhausen, Ulli Köster, and Bernd Eichler. Investigation of evaporation characteristics of polonium and its lighter homologues selenium and tellurium from liquid pb-bi-eutecticum. *Radiochim. Acta*, 92:917–923, 2004.

[152] Michael Dolg. Effective core potentials. In J. Grotendorst, editor, *Modern Methods and Algorithms of Quantum Chemistry*, volume 3 of *NIC Series*, pages 507–540, 2000.

[153] Joseph Ivanic, Jack R. Collins, and Stanley K. Burt. Theoretical Study of the Low Lying Electron States of oxoX(salen) (X= Mn, Mn^{-}, Fe and Cr^{-} Complexes. *The Journal of Physical Chemistry A*, 108:2314–2323, 2004.

[154] John S. Sears and C. David Sherrill. The elelectron structure of oxo-Mn(salen): Single-reference and multireference approaches. *Journal of Chemical Physics*, 124:1441414, 2006.

[155] Tait Takatani, John S. Sears, and C. David Sherrill. Assessing the Performance of Density Functional Theory for the Electron Structure of Metal-Salens: The d^6-Metals. *Journal of Physical Chemistry A*, 113:9231 – 9236, 2009.

[156] Vlaams Supercomputer Centrum. https://vscentrum.be/.

[157] Partnership for Advanced Computing in Europe. http://www.prace-ri.eu/.

[158] Centrale Rekeninfrastructuur - HPC. https://www.ugent.be/hpc/.

[159] Urban Borstnik, Joost VandeVondele, Valéry Weber, and Jürg Hutter. Sparse matrix multiplication: The distributed block-compressed sparse row library. *Parallel Computing*, 40(5-6):47 – 58, 2014.

List of publications

1. A. Van Yperen-De Deyne, E. Pauwels, V. Van Speybroeck and M. Waroquier, *Accurate spin-orbit and spin-other-orbit contributions to the g-tensor for transition metal containing systems*, PCCP **14**, 10690 – 10704 (2012)

2. A. Van Yperen-De Deyne, T. De Meyer, E. Pauwels, A. Ghysels, K. De Clerck, M. Waroquier, V. Van Speybroeck and K. Hemelsoet, *Exploring the vibrational fingerprint of the electronic excitation energy via molecular dynamics*, J. Chem. Phys. **140**, 134105 (2014)

3. A. Van Yperen-De Deyne, K. Rijpstra, M. Waroquier, V. Van Speybroeck, S. Cottenier, *Binary and Ternary Po-containing Molecules Relevant for LBE-coolant in Reactors*, *to be submitted*

4. N. Sakhabutdinova, A. Van Yperen-De Deyne, E. Pauwels, V. Van Speybroeck, H. Vrielinck, F. Callens and M. Waroquier, *Assessment of Periodic and Cluster-in-Vacuo Models for First Principles Calculations of EPR Parameters of Paramagnetic Defects in Crystals: Rh^{2+} Defects in NaCl as Case Study*, J. Phys. Chem. A **114**, 1721–1733 (2011)

5. H. De Cooman, J. Keysabyl, J. Kusakovskii, A. Van Yperen-De Deyne, M. Waroquier, F. Callens and H. Vrielinck, *Dominant Stable Radicals in Irradiated Sucrose: g Tensors and Contribution to the Powder Electron Paramagnetic Resonance Spectrum*, J. Phys. Chem. B **117**, 7169–7178 (2013)

6. S. G. Aalbergsjø, E. Pauwels, A. Van Yperen-De Deyne, V. Van Speybroeck and E. Sagstuen, *Automated generation of radical species in crystalline carbohydrate using ab initio MD simulations*, PCCP (2014) *accepted*

7. I. Lezcano-Gonzalez, U. Deka, B. Arstad, A. Van Yperen-De Deyne, K. Hemelsoet, M. Waroquier, V. Van Speybroeck, B. M. Weckhuysen and

A. M. Beale, *Determining the Storage, Availability and Reactivity of NH_3 with Cu-Chabazite-based Ammonia Selective Catalytic Reduction Systems*, PCCP **16**, 1639–1650 (2014)

8. T. Bogaerts, A. Van Yperen-De Deyne, Y-Y. Liu, F. Lynen, V. Van Speybroeck, P. Van Der Voort, *Mn-salen@MIL101(Al): a Heterogeneous enantioselective catalyst synthesized using a 'bottle around the ship' approach*, Chem. Comm. **49**, 8021–2023, (2013)

9. K. Rijpstra, A. Van Yperen-De Deyne, J. Neuhausen, V. Van Speybroeck, S. Cottenier, *Solution enthalpy of Po and Te in solid lead-bismuth eutectic*, J. Nucl. Mat. **450**, 287–291 (2014)

KINPOR

First principle chemical kinetics in nanoporous materials

http://molmod.ugent.be/erc

This research was supported by the Research Board of Ghent University and the Seventh Framework Programme through the FP7 SEARCH project and the FP7 ERC grant agreement number 240483.

The computational resources and services used in this work were provided by Ghent University (Stevin), the Hercules Foundation (Tier-1 Flemish Supercomputer Infrastructure) and the Flemish Government - department EWI.